

UNIVERSITY OF OKLAHOMA

GRADUATE COLLEGE

INVESTIGATIONS OF THE MECHANICAL PROPERTIES AND  
MICROSTRUCTURE OF THE ATRIOVENTRICULAR HEART VALVE LEAFLETS

A THESIS

SUBMITTED TO THE GRADUATE FACULTY

in partial fulfillment of the requirements for the

Degree of

MASTER OF SCIENCE

By

SAMUEL VICTOR JETT

Norman, Oklahoma

2019

INVESTIGATIONS OF THE MECHANICAL PROPERTIES AND  
MICROSTRUCTURE OF THE ATRIOVENTRICULAR HEART VALVE LEAFLETS

A THESIS APPROVED FOR THE  
SCHOOL OF AEROSPACE AND MECHANICAL ENGINEERING  
GALLOGLY COLLEGE OF ENGINEERING  
UNIVERSITY OF OKLAHOMA

BY

Dr. Chung-Hao Lee, Chair

Dr. David Baldwin

Dr. Chenkai Dai

© Copyright by SAMUEL VICTOR JETT 2019  
All Rights Reserved.

Dedicated to my parents and family.

## TABLE OF CONTENTS

<b>Table of Contents .....</b>	<b>v</b>
<b>List of Figures.....</b>	<b>xii</b>
<b>List of Tables .....</b>	<b>xxvii</b>
<b>Acknowledgements .....</b>	<b>xxx</b>
<b>Abstract of the Thesis .....</b>	<b>xxxi</b>
<b>CHAPTER 1. INTRODUCTION .....</b>	<b>1</b>
1.1 Motivation.....	1
1.1.1 Valvular heart disease prevalence and treatments .....	1
1.1.2 Necessities for improving VHD treatment outcomes .....	2
1.2 Objective and Scope .....	3
1.2.1 Mechanical studies on HV leaflets .....	3
1.2.2 Development of a dynamic tissue microstructure imaging system ...	4
<b>CHAPTER 2. LITERATURE REVIEW .....</b>	<b>5</b>
2.1 Introduction to the HV Function, Anatomy, and Diseases .....	5
2.1.1 HV function .....	5

2.1.2 Anatomy of the atrioventricular valves.....	6
2.1.3 Valvular heart disease and current treatments .....	8
2.2 Mechanical Characterizations of the HV Leaflet Tissues.....	10
2.2.1 Uniaxial and biaxial mechanical testing procedures.....	10
2.2.2 Prior studies on the mechanical behaviors of the AHV leaflets .....	12
2.3 Microstructural Characterizations of the HV Leaflets.....	15
2.3.1 Layered microstructure of the HV leaflet .....	16
2.3.2 Collagen fiber morphology and composition .....	17
2.3.3 Techniques for quantifying collagen fiber architecture (CFA).....	18
2.3.4 Quantifications of the CFAs of heart valve leaflets.....	22
<b>CHAPTER 3. CHARACTERIZATION OF THE MECHANICAL BEHAVIORS OF THE AHV LEAFLETS .....</b>	<b>26</b>
3.1 Introduction to the AHV Mechanics.....	26
3.2 Methods.....	27
3.2.1 Tissue acquisition.....	27
3.2.2 Tissue preparation.....	28
3.2.3 Biaxial mechanical testing protocols .....	30

3.2.4 Tissue stress and strain calculations .....	31
3.2.5 Quantification of the anatomical structure of valve apparatus .....	33
3.2.6 Histological analysis .....	33
3.2.7 Statistical analysis .....	34
3.3 Results.....	35
3.3.1 Baseline testing .....	35
3.3.2 Loading-rate effect on the biaxial mechanical properties.....	38
3.3.3 Temperature effect on the biaxial mechanical properties .....	40
3.3.4 Comparison of the mechanical responses between species .....	43
3.3.5 Anatomical quantification of the valve apparatus .....	44
3.3.6 Histological analysis .....	45
3.4 Discussion .....	47
3.4.1 Baseline testing .....	47
3.4.2 Effects of various loading rates on the mechanical responses.....	49
3.4.3 Effects of temperature on the mechanical responses .....	49
3.4.4 Motivation for porcine-ovine HV comparison .....	50
3.4.5 Comparisons of the mechanical responses between species.....	50

3.4.6 Comparisons of anatomy and microstructure between species .....	51
3.4.7 Discussion of the histological results.....	52
3.4.8 Study limitations .....	53
3.4.9 Concluding remarks .....	54

**CHAPTER 4. SPATIAL VARIATION IN THE MECHANICAL PROPERTIES OF  
THE MVAL AND TVAL TISSUES.....56**

4.1 Region-Specific AHV Tissue Mechanics .....	56
4.2 Methods.....	57
4.2.1 Tissue acquisition & sectioning .....	57
4.2.2 Tissue sample preparation.....	57
4.2.3 Biaxial mechanical testing .....	58
4.2.4 Tissue strain & stress calculations .....	60
4.2.5 Statistical analysis .....	61
4.3 Results.....	61
4.3.1 Thickness of leaflet regions .....	61
4.3.2 Biaxial mechanical testing .....	62
4.3.3 Stress relaxation testing results .....	69

4.4 Discussion .....	70
4.4.1 Overall findings and comparisons with previous work .....	70
4.4.2 Study limitations .....	72
4.4.3 Concluding remarks .....	73
<b>CHAPTER 5. PSFDI SYSTEM DEVELOPMENT.....</b>	<b>74</b>
5.1 Introduction to Collagen Fiber Quantification Techniques .....	74
5.2 Methods.....	77
5.2.1 Theory of birefringent collagen scattering.....	77
5.2.2 Spatial frequency domain imaging (SFDI) theory.....	80
5.2.3 Polarized spatial frequency domain imaging system.....	81
5.2.4 Analyzing the CFA in soft tissues .....	83
5.3 Results.....	86
5.3.1 Collagen microstructural imaging for bovine tendon tissues .....	86
5.3.2 Collagen microstructural imaging for MV leaflet tissues.....	88
5.3.3 Quantified transmural CFA for the MVAL tissues.....	94
5.2.4 Discussion .....	96
5.4.1 Evaluation of the integrated system's capabilities.....	96

5.4.2 Relationship between CFA and tissue mechanics in the MVAL.....	99
5.4.3 Concluding remarks .....	100
<b>CHAPTER 6. CONCLUSION.....</b>	<b>101</b>
6.1 Summary of Thesis Contributions .....	101
6.2 Recommendations for Future Work.....	102
6.2.1 Microstructure and mechanics studies .....	102
6.2.2 Biomaterials testing .....	104
6.1.2 Interval imaging project.....	104
6.2.3 Machine learning approaches to relate tissue CFA to mechanics..	105
<b>APPENDIX A: NOMENCLATURE AND SYMBOLS.....</b>	<b>107</b>
<b>APPENDIX B: STATISTICAL ANALYSIS OF BIAXIAL TESTING DATA.....</b>	<b>110</b>
<b>APPENDIX C: DERIVATIONS OF PSFDI FUNDAMENTAL EQUATIONS.....</b>	<b>126</b>
C.1 Derivation of pSFDI reflected intensity (Eq. (5.1)) from birefringent scattering theory .....	126
C.2 Illustration of AC image penetration depth relationship (Eq. (5.2)) from the SFDI theory.....	130
<b>APPENDIX D: BIAXIAL MECHANICAL TESTING PROCEDURES .....</b>	<b>134</b>

D.1 Tissue Acquisition and Preparation .....	134
D.2 Tissue Mounting .....	136
D.3 Biaxial Testing Procedures .....	137
D.3.1 Study agnostic tools and utilities .....	137
D.3.2 Study specific testing procedures.....	140
<b>APPENDIX E: PSFDI TESTING AND DATA ANALYSIS PROCEDURES.....</b>	<b>143</b>
E.1 pSFDI System Calibration.....	143
E.2 pSFDI System Testing.....	145
E.3 pSFDI Post-Processing and Data Analysis.....	148
<b>REFERENCES.....</b>	<b>152</b>

## LIST OF FIGURES

- Figure 2.1.** Schematic diagram of the *four heart chambers* and the **four heart valves**, with the passage of the oxygenated blood through the left side of the heart and the deoxygenated blood through the right side of the heart. The image was modified from Harvard Health Publications..... 5
- Figure 2.2.** Schematic of the anatomical components of the MV and TV apparatus—annulus, chordae tendineae, and leaflets (papillary muscles not shown). The image was adapted from the Basic Medical Key..... 6
- Figure 2.3.** Schematic of the closure of an atrioventricular heart valve and the differences between the valvular geometry at diastole (*left*) and systole (*right*). The image was adapted from Antranik..... 7
- Figure 2.4.** Schematic of a biaxial testing system for anisotropic mechanics characterization of heart valve leaflet tissue samples: (a) the mounting of the tissue sample and the application of force-controlled biaxial testing, and (b) tissue sample at the undeformed and loaded configurations with fiducial markers used for strain tracking.  $F_x$  and  $F_y$  are applied forces along the  $x$ - and  $y$ -directions, respectively. ..... 11
- Figure 2.5.** Biaxial testing results of the MV leaflets: (a) the loading portion of a stress-strain relationship for MVAL (*unfilled*) and MVPL (*filled*) tissues in the circumferential (*circles*) and radial (*triangles*) directions under *equibiaxial strains*, and (b) a typical loading and unloading cycle of the MVPL under

equibiaxial stretching (*circles*: circumferential direction, *triangles*: radial direction). The images were modified from [38]..... 13

**Figure 2.6.** The mechanical response of the TVAL tissues (n=10) under various biaxial loading protocols ( $T_{C,max}:T_{R,max}$ ) where  $T_C$  and  $T_R$  are the membrane tensions applied in the circumferential and radial directions, respectively: (a) 100:100 N/m, (b) 100:80 N/m, (c) 80:100 N/m, (d) 100:50 N/m, and (e) 50:100 N/m. Bars show standard error in testing results over n=10 TVAL samples. The image was modified from [48]..... 14

**Figure 2.7.** Microscopy images of a TV posterior leaflet cross section (T: Transmural, C: Circumferential) stained by Movat's Pentachrome to color VICs and elastin fibers in *black*, hydrated PGs and GAGs in *blue*, and collagen fibers in *yellow*. ..... 16

**Figure 2.8.** Collagen fibers within the MVAL tissue, visualized transmurally with second harmonic generation imaging through two-photon microscopy: (a) unloaded tissue, (b) tissue under equibiaxial planar tension of 150 N/m. T: Transmural, C: Circumferential. (a) and (b) are at equivalent scale. The images were modified from Lee *et al.* (2015) [63]..... 18

**Figure 2.9.** Comparison of collagen contrast in the colon tissue stained with type-I collagen antibody and examined with (a) standard microscopy methods and (b) polarized light microscopy. The images were adapted from [66]. ..... 19

**Figure 2.10.** Representative SHG images of MVAL microstructure at various spatial points, demonstrating collagen fibers (cyan) and GAGs (green). The images were adapted from [56]..... 20

**Figure 2.11.** Schematic of the SALS domain mapping of collagen fiber structures: (a) the fundamental basis for the SALS technique (image adapted from [69]), and (b) representative mapping of the collagen fiber orientation (vector plot) and fiber dispersion (via degree of alignment, 0: randomly aligned fibers , 1: perfectly aligned fibers) for the ocular lamina cribrosa tissue (image adapted from [70]). ..... 21

**Figure 2.12.** Quantifications of collagen fiber preferred orientation (dashed lines: –) and degree of local fiber alignment (colorbar) for the pulmonary and aortic valve leaflets: (a) raw images of the leaflets, (b) the collagen fiber architecture prior to loading, and (c) the fiber architecture under 90 mmHg transvalvular fixation pressure. The images were modified from [73]. ..... 23

**Figure 2.13.** pSFDI depth-modulated imaging and CFA extraction of an ovine aortic valve leaflet compared to equivalent SALS result. (a-c) Imaging arrangement, (d-f) raw intensity images, (g-i) extracted fiber orientation maps, (j-l) extracted normalized orientation index (NOI) maps, indicating the fiber dispersion. Note that (d, e, g, h, j, k) were limited to the superficial 250  $\mu\text{m}$  of the tissue. The images were modified from [80]. ..... 25

**Figure 3.1.** (a) dissected porcine heart showing the MV (top) and TV (bottom), with labels describing key anatomical components (ruler shows inches). (b) Schematic of

the excised leaflet and the central bulk region (top), and the mounted tissue specimen on the biaxial mechanical testing system (C: circumferential direction; R: radial direction)..... 28

**Figure 3.2.** (a) Image of the biaxial mechanical testing system (BioTester), (b) image of the mounted tissue, (c) schematic of the valve leaflet specimen before and after prescribed loading, and (d) illustration of the force-controlled protocols employed in both the baseline and temperature-controlled tests ( $F_{max}$ : the maximum applied load, — : the applied tension in the circumferential direction, and --- : the applied tension in the radial direction). ..... 29

**Figure 3.3.** Mean  $\pm$  SEM of the 1st-PK stress versus stretch results of the porcine MVAL and MVPL tissues (n=6) at room temperature (22 °C) under: (a) equibiaxial tension ( $T_{C,max}:T_{R,max} = 1:1$ ), (b)  $T_{C,max}:T_{R,max} = 0.5:1$ , (c)  $T_{C,max}:T_{R,max} = 1:0.5$ , (d)  $T_{C,max}:T_{R,max} = 0.75:1$ , and (e)  $T_{C,max}:T_{R,max} = 1:0.75$ ..... 36

**Figure 3.4.** Mean  $\pm$  SEM of the 1st-PK stress versus stretch results of the porcine TVAL, TVPL, and TVSL tissues (n=6) at room temperature (22 °C) under (a) equibiaxial tension ( $T_{C,max}:T_{R,max} = 1:1$ ), (b)  $T_{C,max}:T_{R,max} = 0.5:1$ , (c)  $T_{C,max}:T_{R,max} = 1:0.5$ , (d)  $T_{C,max}:T_{R,max} = 0.75:1$ , and (e)  $T_{C,max}:T_{R,max} = 1:0.75$ . .... 37

**Figure 3.5.** Representative biaxial mechanical testing results of each porcine atrioventricular leaflet under equibiaxial tension ( $T_{C,max}:T_{R,max} = 1:1$ ) at room temperature (22 °C), showing the effect of varied loading rates on the

quantified 1st-PK stress versus stretch relationship: (a) MVAL, (b) MVPL, (c) TVAL, (d) TVPL, and (e) TVSL.....	39
--	----

**Figure 3.6.** Representative biaxial mechanical testing results of each porcine atrioventricular leaflet under  $T_{C,\max}:T_{R,\max} = 0.5:1$  at room temperature (22 °C), showing the effect of varied loading rates on the quantified 1st-PK stress versus stretch relationship: (a) MVAL, (b) MVPL, (c) TVAL, (d) TVPL, and (e) TVSL..... 39

**Figure 3.7.** Representative biaxial mechanical testing results of each porcine atrioventricular leaflet under  $T_{C,\max}:T_{R,\max} = 1:0.5$  at room temperature (22 °C), showing the effect of varied loading rates on the quantified 1st-PK stress versus stretch relationship: (a) MVAL, (b) MVPL, (c) TVAL, (d) TVPL, and (e) TVSL..... 40

**Figure 3.8.** Representative biaxial mechanical testing results of each porcine atrioventricular leaflet under  $T_{C,\max}:T_{R,\max} = 1:1$ , showing the effect of temperature on the quantified 1st-PK stress versus stretch relationship: (a) MVAL, (b) MVPL, (c) TVAL, (d) TVPL, and (e) TVSL..... 41

**Figure 3.9.** Representative biaxial mechanical testing results of each porcine atrioventricular leaflet under  $T_{C,\max}:T_{R,\max} = 0.5:1$ , showing the effect of temperature on the quantified 1st-PK stress versus stretch relationship: (a) MVAL, (b) MVPL, (c) TVAL, (d) TVPL, and (e) TVSL..... 42

**Figure 3.10.** Representative biaxial mechanical testing results of each porcine atrioventricular leaflet under  $T_{C,\max}:T_{R,\max} = 1:0.5$ , showing the effect of temperature on the quantified 1st-PK stress versus stretch relationship: (a) MVAL, (b) MVPL, (c) TVAL, (d) TVPL, and (e) TVSL ..... 42

**Figure 3.11.** Comparisons of the biaxial mechanical responses of representative atrioventricular valve leaflet tissues under  $T_{C,\max}:T_{R,\max} = 1:1$  at 37 °C between different species and ages (adult porcine, adult ovine/sheep, and juvenile ovine/lamb). ..... 43

**Figure 3.12.** Histological sections of all the MV and TV leaflets (MVAL, MVPL, TVAL, TVPL, and TVSL) stained with Masson's trichrome. Four morphologically distinct layers of the leaflets (atrialis: A, spongiosa: S, ventricularis: V, fibrosa: F) were identified ..... 46

**Figure 4.1.** Dissected porcine hearts showing (a) the MV and (b) the TV with the anterior leaflet highlighted for both atrioventricular HVs. (c) Schematic of a valve anterior leaflet with the six tested regions. Experimental images of (d) the biaxial mechanical tester (BioTester) used in this study and (e) a mounted tissue sample with labelled components of the biaxial mechanical testing system. ..... 58

**Figure 4.2.** Mean  $\pm$  SEM of membrane tension versus total tissue stretch results for the six MVAL tissue regions under equibiaxial loading ( $T_{C,\max}:T_{R,\max} = 1:1$ ). The

labels (a-f) correspond to the region label defined in Figure 4.1c. N.S.: non-statistically significant. ....	62
---	----

**Figure 4.3.** Mean  $\pm$  SEM of membrane tension versus total tissue stretch results for the six TVAL tissue regions under equibiaxial loading ratio ( $T_{C,\max} : T_{R,\max} = 1:1$ ). ....

The labels (a-f) correspond to the region label defined in Figure 4.1c. N.S.: non-statistically significant. ....	63
---	----

**Figure 4.4.** Mean  $\pm$  SEM of anisotropy index for peak stretch of the six regions of the (a) MVAL and (b) TVAL. The labels (A-F) correspond to the regions defined in Figure 4.1c. ....

**Figure 4.5.** Mean  $\pm$  SEM of the preconditioning stretches ( $\lambda_C^{0-1}$  and  $\lambda_R^{0-1}$ ) of (a) the six MVAL tissue regions and (b) the six TVAL tissue regions under equibiaxial loading in both the C (left) and R (right) directions. (\*) denotes statistically significant ( $p<0.05$ ) difference between groups and (\*\*) denotes nearly statistically significant ( $0.05<p<0.10$ ) difference between groups; otherwise, not statistically significant ( $p>0.10$ ). ....

**Figure 4.6.** Mean  $\pm$  SEM of the mechanical stretches ( $\lambda_C^{1-peak}$  and  $\lambda_R^{1-peak}$ ) of all six (a) MVAL and (b) TVAL tissue regions in both the C (left) and R (right) directions under the equibiaxial loading. (\*) denotes statistically significant ( $p<0.05$ ) difference and (\*\*) denotes nearly statistically significant ( $0.05<p<0.10$ ) difference between groups; otherwise, not statistically significant ( $p>0.10$ ). ....

**Figure 4.7.** Mean  $\pm$  SEM of the normalized membrane tension versus time results from the stress relaxation testing for all the six MVAL tissue regions. .... 69

**Figure 4.8.** Mean  $\pm$  SEM of the normalized membrane tension versus time results from the stress relaxation testing for all the six TVAL tissue regions. .... 70

**Figure 5.1.** (a) Schematic of a co-polarized pSF DI system, showing the **optical components** and *passage of light*, including scattering from the fibrous tissue microstructure. (b) Illustration of the birefringent reflected intensity response with an example fiber with orientation angle  $\theta_{fiber}=90^\circ$  and a polarizer angle  $\theta_{polarizer}$  defined on the polar axis with the same reference. .... 78

**Figure 5.2.** Trimetric and side views of the integrated pSF DI and biaxial testing system. Arrows in the side view indicate the passage of light through the system. . . 82

**Figure 5.3.** Microstructural quantifications from the pSF DI system. (a) DC images for 3 bovine tendon tissue samples, with expected  $\theta_{fiber}$  according to the tendon's preferential axial direction, i.e.,  $120^\circ$ ,  $60^\circ$ , and  $20^\circ$ . Red circles indicate single pixel locations where: (b) DC intensity responses, together with the 3-term Fourier series fit (Eq. (5.1)) for quantifying the  $\theta_{fiber}$ , are presented. (c) Colormaps of the predicted  $\theta_{fiber}$  for each tendon tissue sample. .... 86

**Figure 5.4.** Dynamic microstructural quantifications from the integrated biaxial-pSF DI system. (a) Experimental raw images of bovine tendon tissue specimen (thickness = 1.25 mm), and predictions of (b)  $\theta_{fiber}$  and (c) DOA at 0% and 3% uniaxial strains. (d) DC intensity responses, obtained by spatially

averaging over the region outlined in red, considering 0%, 1%, 2%, and 3% uniaxial strains..... 87

**Figure 5.5.** Dynamic microstructural quantifications from the integrated biaxial-pSF DI system. (a) Schematic of the porcine MVAL specimen (thickness = 0.75 mm) mounted to the BioTester and the DC image showing the biaxially-loaded region. (C: Circumferential, R: Radial). Predictions of  $\theta_{fiber}$  (vector field) and DOA for the MVAL tissue (b) after preconditioning, and (c-d) under various biaxial loads..... 89

**Figure 5.6.** Distributions of the  $\theta_{fiber}$  and DOA predictions from MVAL testing in Figure 5.5. (a) Testing image of the MVAL with the region of interest (ROI) outlined in red and loading labelled. Histograms of (b) the  $\theta_{fiber}$  distributions with the corresponding bimodal von Mises distribution fit (Eq. (5.4)) and (c) the DOA distributions with the corresponding bimodal normal distribution fit (Eq. (5.6)). The parameters of the fit are summarized in Table 5.2), where the distributions were obtained from all the pixels in the ROI..... 90

**Figure 5.7.** Depth-modulated microstructural predictions from the integrated biaxial-pSF DI system. (a) Histological image illustrating the 4 morphologically distinct layers of a typical porcine MVAL tissue (image modified from [147]). Predictions of  $\theta_{fiber}$  from the AC intensities for a porcine MVAL tissue sample (thickness=0.87 mm) at various penetration depths associated with different spatial frequencies ( $f_x$ ) determined based on Eq. (5.3): (b) after

preconditioning, and (c) under equibiaxial loading of 1000 mN. Predictions from the DC intensities are included to compare orientation predictions extracted from the full optical thickness..... 95

**Figure 6.1.** (a-d) CFA predictions and (e) mechanical response curves for a TVSL tissue specimen subjected to loading ratios ( $F_C:F_R$ , mN) of (a) 0:0, after preconditioning, (b) 500:500, (c) 125:500, and (d) 500:125. White streamlines show  $\theta_{fiber}$ , while DOA is represented via colormap. Note that tissues were imaged at the maximum load of each mechanical curve..... 103

**Figure 6.2.** Depiction of CFA quantification at 10 distinct kinematic states over the physiological mechanical loading interval for a representative heart valve leaflet tissue. .... 105

**Figure B1.** Statistical analyses of the MVAL from the loading rate effect group (n=6), with plots showing trends in (a) the preconditioning stretches, (b) mechanical stretches, and (c) the peak stretches. All bars show mean  $\pm$  SEM. (N.S.: no statistically significant difference,  $p>0.10$ , #: nearly statistically significant difference,  $p<0.10$ , and \*: statistically significant difference,  $p<0.05$ ) .... 111

**Figure B.2.** Statistical analyses of the MVPL from the loading rate effect group (n=6), with plots showing trends in (a) the preconditioning stretches, (b) mechanical stretches, and (c) the peak stretches. All bars show mean  $\pm$  SEM. (N.S.: no statistically significant difference,  $p>0.10$ , #: nearly statistically significant difference,  $p<0.10$ , and \*: statistically significant difference,  $p<0.05$ ) .... 112

**Figure B.3.** Statistical analyses of the TVAL from the loading rate effect group (n=6), with plots showing trends in (a) the preconditioning stretches, (b) mechanical stretches, and (c) the peak stretches. All bars show mean  $\pm$  SEM. (N.S.: no statistically significant difference,  $p>0.10$ )..... 113

**Figure B.4.** Statistical analyses of the TVPL from the loading rate effect group (n=6), with plots showing trends in (a) the preconditioning stretches, (b) mechanical stretches, and (c) the peak stretches. All bars show mean  $\pm$  SEM. (N.S.: no statistically significant difference,  $p>0.10$ )..... 114

**Figure B.5.** Statistical analyses of the TVSL from the loading rate effect group (n=6), with plots showing trends in (a) the preconditioning stretches, (b) mechanical stretches, and (c) the peak stretches. All bars show mean  $\pm$  SEM. (N.S.: no statistically significant difference,  $p>0.10$ )..... 115

**Figure B.6.** Statistical analyses of the MVAL from the temperature effect group (n=6), with plots showing trends in (a) the preconditioning stretches, (b) mechanical stretches, and (c) the peak stretches. All bars show mean  $\pm$  SEM. (N.S.: no statistically significant difference,  $p>0.10$ )..... 118

**Figure B.7.** Statistical analyses of the MVPL from the temperature effect group (n=6), with plots showing trends in (a) the preconditioning stretches, (b) mechanical stretches, and (c) the peak stretches. All bars show mean  $\pm$  SEM. (N.S.: no statistically significant difference,  $p>0.10$ )..... 119

**Figure B.8.** Statistical analyses of the TVAL from the temperature effect group (n=6), with plots showing trends in (a) the preconditioning stretches, (b) mechanical stretches, and (c) the peak stretches. All bars show mean  $\pm$  SEM. (N.S.: no statistically significant difference,  $p>0.10$ )..... 120

**Figure B.9.** Statistical analyses of the TVPL from the temperature effect group (n=6), with plots showing trends in (a) the preconditioning stretches, (b) mechanical stretches, and (c) the peak stretches. All bars show mean  $\pm$  SEM. (N.S.: no statistically significant difference,  $p>0.10$ )..... 121

**Figure B.10.** Statistical analyses of the TVSL from the temperature effect group (n=6), with plots showing trends in (a) the preconditioning stretches, (b) mechanical stretches, and (c) the peak stretches. All bars show mean  $\pm$  SEM. (N.S.: no statistically significant difference,  $p>0.10$ )..... 122

**Figure C.1.** Diagrams exploring the relationship between  $f_x$  and  $\delta_{eff}^{AC}$ . The varied attenuation of three spatial frequency ( $f_{x,1-3}$ ) intensity patterns showing the AC penetration depths ( $\delta_{eff,1-3}^{AC}$ ) according to Eq. (C.14) from the (a) trimetric and (b) side view. (c) Plot comparing estimated penetration depths from the exact model (Eq. (C.13)) for selected tissues [156, 157] and the approximate model (Eq. (C.14)), highlighting the  $f_x$  range used in this study (Fig. 5.7)..... 132

**Figure D.1.** Depictions of the appropriate cut line positions on (a) a porcine heart with atria removed and (b) a schematic of the atrioventricular heart valves. (c, d) show

the mitral and tricuspid valves, respectively, fully opened and allowing leaflet excision ..... 134

**Figure D.2.** Illustrations of the sample sectioning and mounting procedures for leaflet tissues. (a-c) show schematic representations of the excised leaflet, the sample sectioning and marking process, and the sample mounting procedure, respectively, while (d-f) show images from the same respective procedures. Small ticks in (d) show mm. ..... 135

**Figure D.3.** Decomposition of the LabJoy testing graphical interface. (a) Shows, from left to right, the *Start*, *Stop*, *Reset Actuators*, *Zero Load Cells*, *Move to Size*, and *Move to Force* buttons, while (b) highlights input boxes for specification of desired size in x, y directions. (c) includes a dynamic overhead visualization of the testing sample, while (d) encloses real-time graphs of the sample temporal applied forces and deformations, and (e) displays outputs of the current sample applied forces and sizes in the x- and y-directions. .... 138

**Figure D.4.** Example test file from the baseline/force-controlled biaxial mechanical study (cf. *Section 3.3.1*). (a) highlights the settings applied to the entire test, such as the testing temperature, camera settings, and display settings, while (b) contains the specific details for the testing sequence. ..... 140

**Figure E.1.** Calibration of the DLP projector lens. (a) shows the projection focal distance adjustment via linear translation of the lens, while (b,c) depict examples of unresolved and properly resolved projections, respectively, of an example image. ..... 144

**Figure E.2.** Calibration of the camera lens. (a) shows the working distance adjustment ring of the lens, while (b) shows the aperture adjustment ring, permitting control of image brightness. (c) depicts an underexposed and unresolved image, (d) shows a properly resolved and illuminated image, and (e) depicts a resolved but overexposed image. .... 145

**Figure E.3.** Image of the LabVIEW testing control program interface. (a) shows output of the automated testing folder generation, while (b, c, d) show the boxes allowing input of the test name, spatial frequency, and camera, respectively. (e) displays the real-time testing images at each phase shift, and (f) shows the state of the rotational polarizer mount, while (g) allows input of step size and final polarizer angle (typically 5° and 180°, respectively). .... 146

**Figure E.4.** Image of the data analysis interface. (a) denotes the user input box to specify lists of the test names and spatial frequencies of the tests to be analyzed during **Step 1** of the analysis, while (b) shows the corresponding **Step 1** output, including indications of the program state and resulting figures. (c) displays the input for **Step 2** of the analysis, and (d) provides an interactive textual cropping tool for the user to specify the region of interest. .... 149

**Figure E.5.** Results from **Step 1** of the analysis for a TVPL tissue under equibiaxial loading. (a) shows the fiber orientations (–) on a background of *DOA*, while (b, c) illustrate 4 spatial points and the DC intensity curves (Intensity vs Polarization angle) at these points. .... 150

**Figure E.6.** Results from **Step 2** of the analysis for a TVPL tissue under equibiaxial loading. (a) denotes the sample's region of interest (ROI) over a combined DC image, while (b) shows the fiber orientations (white lines) on a background of *DOA*. (c,d) show histograms of the fiber orientation and *DOA*, respectively, while (e) shows the combined distributions of fiber orientation and *DOA*. ..... 151

## LIST OF TABLES

<b>Table 3.1.</b> Circumferential and radial stretches of porcine AHVs (n=6) at selected stress levels (% of maximum 1st-PK stress) under equibiaxial tension protocol ( $T_{C,\max}:T_{R,\max} = 1:1$ ). Values are reported as mean $\pm$ SEM. ....	35
<b>Table 3.2.</b> Anatomical measurements for chordae and leaflet tissues of both porcine and ovine atrioventricular heart valves (n=6, each valve leaflet). All quantities are reported as mean $\pm$ SEM. ....	45
<b>Table 3.3.</b> The thickness and collagen fiber content obtained from the histology sections of porcine MV and TV leaflets. All quantities except for collagen content (generated from image analysis) are reported as mean $\pm$ SEM with 3 repeated measurements. ....	46
<b>Table 4.1.</b> Total tissue stretch, anisotropy index, preconditioning stretch, mechanical stretch from biaxial mechanical tests, and the engineering strain from stress relaxation tests for each MVAL region. Values are reported as mean (SEM). ....	67
<b>Table 4.2.</b> Tissue total stretch, anisotropy index, preconditioning stretch, mechanical stretch from biaxial mechanical tests, and the engineering strain from stress relaxation tests for each TVAL region. Values are reported as mean (SEM). ....	68
<b>Table 5.1.</b> Comparison of collagen fiber quantification techniques [68, 72, 73, 128-130]. ....	75

<b>Table 5.2.</b> Bulk distributions of the CFA in the MVAL (cf. Fig. 5.5 and Fig. 5.6). Bimodal fiber orientation and <i>DOA</i> fitting are described by Eqns. (5.4) & (5.6), respectively.....	92
---	----

<b>Table B.1.</b> Statistical analysis of the loading rate effect group on the preconditioning ( $\lambda_C^{0-1}$ and $\lambda_R^{0-1}$ ), mechanical ( $\lambda_C^{1-peak}$ and $\lambda_R^{1-peak}$ ), and the peak stretches ( $\lambda_C^{0-peak}$ and $\lambda_R^{0-peak}$ ) of the MVAL and MVPL tissues (n=6). Quantities are presented as mean $\pm$ SEM.....	116
--	-----

<b>Table B.2.</b> Statistical analysis of the loading rate effect on the preconditioning, mechanical, and peak stretches of the TVAL, TVPL, and TVSL tissues (n=6) (mean $\pm$ SEM).....	117
--	-----

<b>Table B.3.</b> Statistical analysis of the temperature effect group on the preconditioning ( $\lambda_C^{0-1}$ and $\lambda_R^{0-1}$ ), mechanical ( $\lambda_C^{1-peak}$ and $\lambda_R^{1-peak}$ ), and peak stretches ( $\lambda_C^{0-peak}$ and $\lambda_R^{0-peak}$ ) of the MVAL and MVPL tissues (n=6). All quantities are presented as mean $\pm$ SEM.....	123
---	-----

<b>Table B.4.</b> Statistical analysis of the temperature effect on the preconditioning, mechanical, and peak stretches of TVAL, TVPL, and TVSL tissues (n=6) (mean $\pm$ SEM).....	124
---	-----

<b>Table B.5.</b> Statistical analysis results of the species effect group on the preconditioning ( $\lambda_C^{0-1}$ and $\lambda_R^{0-1}$ ), mechanical ( $\lambda_C^{1-peak}$ and $\lambda_R^{1-peak}$ ), and peak stretches ( $\lambda_C^{0-peak}$
--

and  $\lambda_R^{0-peak}$ ) of the MVAL tissue (n=6). All quantities are presented as mean  
 $\pm$  SEM..... 125

**Table B.6.** Statistical analysis results of the species effect group on the preconditioning ( $\lambda_C^{0-1}$  and  $\lambda_R^{0-1}$ ), mechanical ( $\lambda_C^{1-peak}$  and  $\lambda_R^{1-peak}$ ), and peak stretches ( $\lambda_C^{0-peak}$  and  $\lambda_R^{0-peak}$ ) of the TVAL tissue (n=6). All quantities are presented as mean  
 $\pm$  SEM..... 125

**Table E.1.** Spatial frequency index values, with corresponding penetration depths and  
*actual* spatial frequency values. Index values are input to the testing script to  
permit control of *actual* spatial frequency and penetration depth. .... 147

## ACKNOWLEDGEMENTS

I would like to thank my thesis advisor, Dr. Chung-Hao Lee, for his support throughout the past two and a half years of research. I'm sincerely grateful for the countless hours he invested toward helping me learn, grow, and mature during my research journey. I also want to thank my lab colleagues in the BBDL, and especially my close friends Devin Laurence and Rob Kunkel. Working and spending time with you has been a pleasure and privilege, and I feel fortunate to have met such motivated, talented, and genuine individuals. My family has been there for me before and will be there for me after this research journey, and I am eternally grateful for their support and love. Many other people and groups have helped me through this research journey, and I would like to thank them—the AME office staff, for helping to smoothly resolve every purchase, application, and research issue; the machine shop staff, for providing hardware support for projects; the open-source software community, for devoting countless unrecognized hours to help aspiring programmers and developers build their projects; Dr. Kuang-Hua Chang from AME, for striving to help his students to learn and grow; my Koda community, for helping me keep research in perspective; my roommates, for being like a second family to me. Thank you to all these people, and the many others who have helped me along this journey.

## ABSTRACT OF THE THESIS

### INVESTIGATIONS OF THE MECHANICAL PROPERTIES AND MICROSTRUCTURE OF THE ATRIOVENTRICULAR HEART VALVE LEAFLETS

by

Samuel Victor Jett

Master of Science in Mechanical Engineering

University of Oklahoma, Norman, OK, 2019

Dr. Chung-Hao Lee, Chair

Atrioventricular heart valves (AHVs), namely the mitral and tricuspid valves, regulate unidirectional blood flow from the atria to the ventricles in the left and right sides of the hearts, respectively. These valves can be afflicted by diseases which degrade the tissue microstructure and cause blood backflow, or *valve regurgitation*. This regurgitation causes poorer prognoses and higher mortality rates for patients. However, no current treatments for valve regurgitation offer an ideal solution, though recent research efforts have focused on developing novel treatment techniques with improved long-term therapeutic outcomes. For these applications, a comprehensive understanding of the mechanical behaviors and microstructure of the native heart valve leaflet tissues is essential. This thesis research used biaxial mechanical testing methods to provide novel insights into the complexity of the AHV leaflet mechanics, revealing: (i) the characteristic nonlinear and anisotropic mechanical response of the AHV leaflets, with radial stretches 30.7% higher than

circumferential stretches on average across all AHV leaflets, (ii) the higher stiffness of the mitral valve leaflets (avg. circumferential- and radial-direction stretches of 1.224 and 1.599, respectively, under physiological loading) compared to their more compliant tricuspid counterparts (avg. circumferential- and radial-direction stretches of 1.298, 1.708, respectively, under physiological loading), (iii) the minimal loading-rate response of the AHV leaflets and the anisotropic changes in tissue response with varied testing temperature, and (iv) the regional variance in the mechanical properties of the AHV anterior leaflets, with increased mechanical anisotropy in the center of the tissues and more isotropic mechanics nearer to the leaflet boundaries (avg. *anisotropy index* of 1.087 in central regions vs. 1.017 in edge regions). To complement these tissue mechanics studies, a polarization-based quantitative imaging device was developed to assess the reorientation of microstructural collagen fibers in response to mechanical loading. The device was applied to assess the representative mitral valve anterior leaflet, *for the first time* illuminating the spatial heterogeneity and load-dependence of the leaflet collagen microstructures, with observed average degree of optical anisotropy, which describes the degree of collagen fiber alignment, increasing from 0.042 in an unloaded tissue to 0.086 in a tissue under predicted physiological loading. These investigations and this novel system provide an essential first step toward elucidating the mechanics-microstructure relationship in the AHV leaflets. At the same time, our studies contribute to an improved understanding of valve leaflet tissue function, with the overarching goal of advancing treatment options for patients with valve regurgitation.

# CHAPTER 1. INTRODUCTION

## 1.1 Motivation

### 1.1.1 Valvular heart disease prevalence and treatments

Valvular heart disease (VHD) encompasses a variety of conditions afflicting one or more of the four heart valves (HVs). VHD is prevalent in an estimated 2.5% of the typical population in the United States, and although severity varies, even minor VHD contributes to poorer prognoses for patients [1, 2]. Therefore, the efficient diagnosis and optimal treatment of VHD is of utmost importance. A study by Iung *et al.* in 2011 found that VHD treatments accounted for 20% of all cardiovascular surgical procedures, and the frequency of VHD treatment is only expected to increase as patient populations age [3]. A substantial variety of unique protocols exist to treat different VHD phenotypes. For many patients, much of the treatment difficulty arises from rigorously matching the patient's specific valvular disease, valve morphology, and cardiovascular geometry to the appropriate treatment. In addition to these pre-operative difficulties, the existing treatments have many challenges and suboptimal side-effects for patients. Although the efficacy differs, the accepted treatments generally exhibit one or more of the following shortcomings:

- (1) A lack of treatment longevity, with some patients requiring repeat surgery to address subsequent degeneration of the previously-treated valve [4];
- (2) An invasive implementation, with traditional approaches requiring full open-heart surgery, and subsequent recovery time of 6-8 weeks;
- (3) Irregular blood-flow, inducing a need for lifelong anticoagulant medication and causing further alterations to the cardiovascular complex

Given these shortcomings, research studies seek to develop novel treatment techniques for VHD. In the following section, we explore a set of frontier approaches for VHD treatment and assess the requirements for further development of these solutions.

### **1.1.2 Necessities for improving VHD treatment outcomes**

One research technique proposed for informing pre-operative planning and thereby improving patient-treatment matching is *patient-specific computational modeling*. This process entails construction of a finite element model of the patient's heart geometry, which permits the evaluation of various treatment techniques based on expected valvular tissue stress concentration, valvular hemodynamics, and functional behavior [5]. These high-fidelity computational models rely on appropriate mechanical constitutive models of the valvular tissue behavior, and for certain valve tissues, the experimental data has not been captured. Furthermore, microstructural-based material models have recently shown promise for improving predictions of tissue-level mechanical behaviors [6, 7]. To facilitate the development of these models of the valvular tissue, there is a need for more extensive evaluation of the microstructures of the valvular tissues.

Tissue engineering of HVs shows promise as a new VHD therapy, free from the current limitations. The first step in development of a tissue-engineered valve is synthesis of the bulk microstructure of the replacement valve. This acellular construct, known as a scaffold, is then “seeded” by cells from the organ transplant patient, and later surgically implanted into the patient. Currently, this technique is not validated for clinical trials, but receives significant research effort, and is often seen as the future of valvular treatments [8, 9]. A modern challenge in tissue engineering is the synthesis of an appropriate biomimetic

scaffold material to replicate *in vivo* tissue function [10-12]. For this synthesis, a thorough understanding of the biomechanics and the *dynamic tissue microstructure* of the native valve is essential. Current imaging systems are incapable of providing this quantification, which could improve the development and analysis of tissue engineered HV constructs.

Although patient-specific computational modeling and tissue engineering of HVs show promise as future treatment techniques, their outcomes are limited by the current understanding of tissue biomechanics and microstructures within the heart valve leaflets. To provide needed support for the next-generation therapeutic goals, the goals of this research are: (i) to elucidate the mechanics of the native heart valve tissues, and (ii) to provide novel insight into the functional dynamic microstructure of the heart valve tissues.

## **1.2 Objective and Scope**

### **1.2.1 Mechanical studies on HV leaflets**

One of the objectives of this thesis is to characterize the mechanical properties of the specific porcine mitral and tricuspid valve (MV and TV) leaflets. We believe these leaflet-specific quantifications will be valuable for improving understanding and ability to model the biomechanics of the MV and TV. Additionally, we seek to quantify the impact of testing parameters—sample deformation rate, testing temperature, donor animal, and region of sample selection—on the observed mechanical properties of the material. We believe this thorough analysis of valvular tissue mechanics will help future groups to appropriately represent the mechanical behaviors of the valve tissues in constitutive models of material behavior and high-fidelity computational models of organ-level function.

### **1.2.2 Development of a dynamic tissue microstructure imaging system**

The mechanical behaviors of tissues are a combination of the mechanical contributions of their internal constituents. Therefore, for a more complete understanding of tissue biomechanics, an in-depth knowledge of tissue microstructure is required. However, existing characterizations of *dynamic* and *load-dependent microstructures* of HV leaflets are inadequate. To better understand the load-dependence of tissue microstructure, our group sought to develop a novel optical-mechanical system capable of quantifying the load-dependent collagen microstructure in tissues subjected to arbitrary mechanical loading. Our objective in developing this system is to further understand the microstructural basis for the observed mechanical behaviors of the HV tissues.

The remainder of this thesis is organized as follows. In Chapter 2, the function and anatomy of the heart valve leaflets are explored, and a review of mechanical testing and microstructural collagen imaging techniques for the heart valve leaflet tissues is presented. Chapter 3 discusses comprehensive quantifications of the mechanical properties of the MV and TV leaflet tissues. To complement these baseline investigations, Chapter 4 offers quantifications of the *spatially-varied* mechanical properties and stress-relaxation behaviors of the selected MV and TV leaflet tissues. In Chapter 5, the development of an optical-mechanical system to quantify the collagen fiber microstructure within HV tissues is discussed. Characterization of the dynamic collagen microstructures within tendon and mitral valve leaflets is also presented, as examples of the capabilities of the system. Chapter 6 provides the concluding discussion about the findings in this study and the suggested future research extensions.

## CHAPTER 2. LITERATURE REVIEW

### 2.1 Introduction to the HV Function, Anatomy, and Diseases

#### 2.1.1 HV function

The unidirectional blood flow through the four chambers of the heart is enforced via the regulatory action of the four heart valves: the aortic and mitral valves on the left side of the heart, and the pulmonary and tricuspid valves on the right side of the heart (Fig. 2.1).

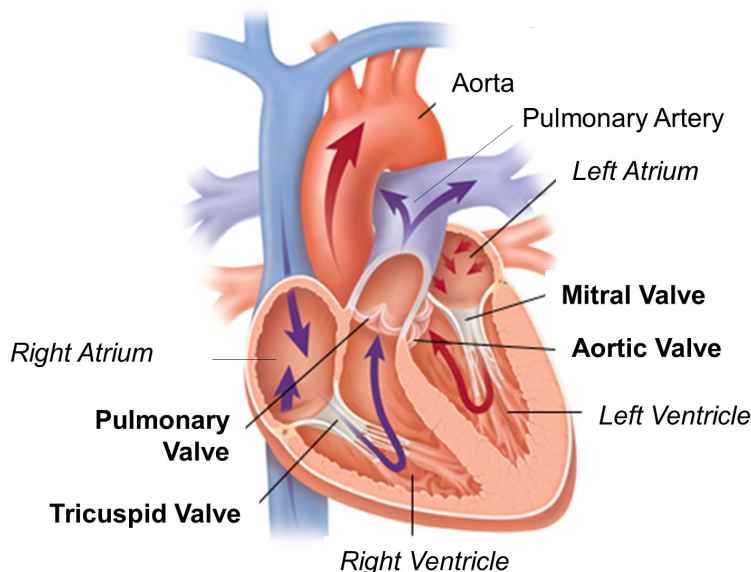


**Figure 2.1.** Schematic diagram of the *four heart chambers* and the **four heart valves**, with the passage of the **oxygenated blood** through the left side of the heart and the **deoxygenated blood** through the right side of the heart. The image was modified from [Harvard Health Publications](#).

These valves are classified into two families according to their position and morphology: the mitral valve (MV) and the tricuspid valve (TV) are described as the *atrioventricular* valves based on their anatomic location between the atria and ventricles, and the pulmonary valve (PV) and aortic valve (AV) are known as the *semilunar* valves owing to their half-

moon geometry. The aortic valve enforces the exit of the oxygenated blood from the left ventricle to the aorta via its position at the aortic root. Similarly, the pulmonary valve regulates the deoxygenated blood flow from the right ventricle to the pulmonary artery. The atrioventricular valves demonstrate a comparable functional and positional parallelism—regulating the unidirectional flow from the atria to ventricles in the left and right heart. Despite these categorizations, each of the heart valves is subjected to distinct loading conditions, contributing to the unique anatomy and microstructure of each valve.

### 2.1.2 Anatomy of the atrioventricular valves

The atrioventricular valves regulate the unidirectional blood flow through the motion of membranous, collagenous tissues known as the leaflets, which are enclosed by ring-like structures known as the valve *annuli* (singular: annulus) (Fig. 2.2).

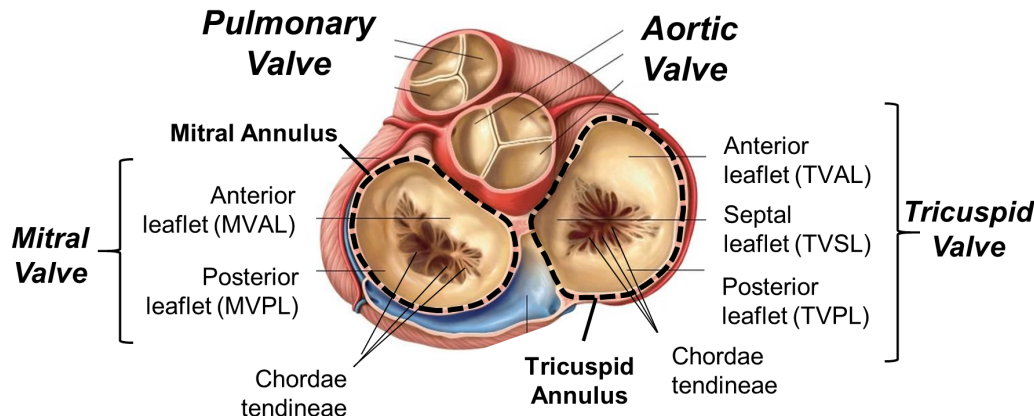


**Figure 2.2.** Schematic of the anatomical components of the MV and TV apparatus—annulus, chordae tendineae, and leaflets (papillary muscles not shown). The image was adapted from the [Basic Medical Key](#).

The complex morphologies of the valve annuli are associated with the functional openings of the atrioventricular valves [13]. Subsequently, significant efforts have been devoted to

better understanding the impacts of the annular geometry changes on the overall AHV function [14-16]. Internal to the annuli are the AHV leaflets. The MV is composed of two anatomically distinct leaflets, namely the anterior leaflet (MVAL) and the posterior leaflet (MVPL), whereas the TV contains three leaflets: the anterior leaflet (TVAL), the posterior leaflet (TVPL), and the septal leaflet (TVSL) (Fig. 2.2). These leaflets attach around their superior edge to the valve annulus, and distally to the chordae tendineae network. The leaflets exhibit unique and frequently asymmetric shapes, allowing for the complete closure of the valvular orifice during systole. The leaflets also demonstrate substantial variance across species and population, making a general geometric description challenging [17-19]. During systole of the cardiac cycle, these leaflets close to enforce the unidirectional blood flow from the ventricles to the arteries (Fig. 2.3).

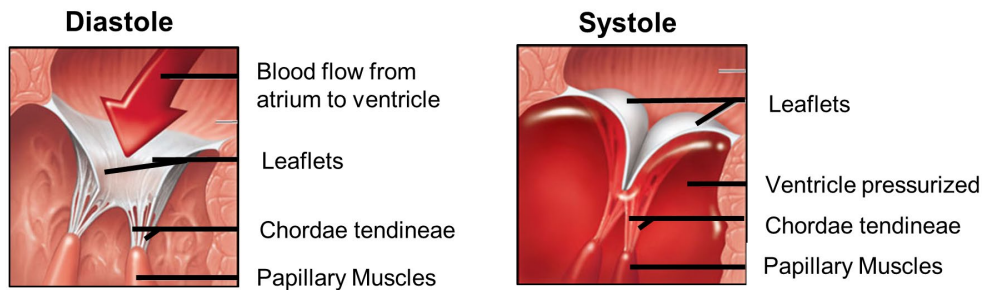


**Figure 2.3.** Schematic of the closure of an atrioventricular heart valve and the differences between the valvular geometry at diastole (*left*) and systole (*right*). The image was adapted from [Antranik](#).

In valve closure, the leaflets are mechanically reinforced by a network of structurally robust tendons known as chordae tendineae. These chordae tendineae connect the valve leaflets to the papillary muscles of the ventricular wall (Fig. 2.3) [20]. The papillary muscles, another key anatomical component of the AHVs, provide an anchor for the attachment of multiple chordae tendineae groups and help prevent leaflet prolapse via contraction at the

onset of systole [21]. The right ventricle contains three such anchors for the securing of chords connecting to the TV, while the left ventricle generally contains two anchors located inferior to the leaflet commissures. Collectively, these four anatomical components comprise each AHV apparatus. Although the components have typical positions, the biomechanics and geometries of the valve apparatus often change throughout the lifetime of an individual, in some occasions accompanying the onset of disease.

### **2.1.3 Valvular heart disease and current treatments**

A variety of diseases can impact the healthy function of the atrioventricular valves. Valve disease consequences can be broadly categorized into two groups: valve regurgitation and valve stenosis. In valve regurgitation, the AHVs lose their ability to close fully, resulting in the blood backflow, or *regurgitation*, from the ventricle to the atrium. This consequence can result from valvular component degradation, known as *organic* regurgitation, or changes to the surrounding ventricular or valvular geometry, in which case it is known as *functional* regurgitation [22]. In many cases of functional regurgitation, the ventricle enlarges, causing dilation of the annulus and preventing the leaflets from complete closure [23]. Conversely, a common etiology associated with organic regurgitation, particularly in the mitral valve, is myxomatous valve disease, which describes a lengthening of the leaflets and/or chordae tendineae through changes to the tissue microstructure. Other causes of organic regurgitation include leaflet tearing or chordae rupture, which can result from infectious conditions such as rheumatic fever or endocarditis [24]. Organic regurgitation frequently manifests in leaflet prolapse—a ballooning of the leaflets above the valvular annulus during systole, or leaflet flail—a condition wherein the leaflets are unstable during systole and “flail” in the regurgitant stream. Both prolapse and flail behaviors typically

indicate a valve which requires treatment before further degradation [25]. Valve stenosis is an opposite condition from regurgitation, in which the valve is unable to open completely to allow blood flow. The flow impairment in stenosis typically occurs through a stiffening or thickening of the leaflet tissues. In the developed world, stenosis of varying degree is typically present in the aortic valve in elderly patients, due to a progressive calcification of the valves. However, in less developed regions, complications due to rheumatic fever cause scarring and subsequent stenosis of the mitral valve in a younger population [26].

Treatments for valve diseases depend on the severity and mechanism of the disease. Most treatments for functional regurgitation entail the suturing of a synthetic *annuloplasty* ring onto the valvular annulus to restore functional geometry. For organic valve regurgitation, a repair or replacement procedure can be advocated. In valves with isolated degradation, such as individual chordae rupture or contained myxomatous disease, the advised treatment is typically an excision of degraded components followed by insertion of an annuloplasty ring to allow valve closure [27]. For more severely degraded valves, as observed in profuse myxomatous disease or acute valve calcification, valve replacement is required. Current replacement options for the mitral and tricuspid valves include bi-leaflet mechanical valves, or tri-leaflet xenogeneic *bioprosthetic* valves crafted from biologically-inactive bovine pericardial tissues. In addition to traditional surgically-implemented repair or replacement options, recent treatments have focused on transcatheter treatment methods, although these approaches have not yet gained widespread clinical adoption [28, 29].

Regardless of whether a repair or replacement method is employed, treatments for these valvular conditions do not offer ideal outcomes for patients. Existing approaches typically require an invasive open-heart procedure with an extensive recovery period. Moreover,

existing treatments for valve diseases can fail to fully remedy the condition, and symptoms can recur post-operation [30, 31]. Similarly, mechanical valve replacements require patients to take lifelong blood thinning medication to prevent hemolysis, whereas bioprosthetic valve replacements can degrade and fail, requiring subsequent operation [32]. To improve outcomes and diagnoses for valvular disease, many groups have examined the mechanics and microstructures of the native mitral and tricuspid valvular components, with special emphasis on the valve leaflet biomechanics.

## 2.2 Mechanical Characterizations of the HV Leaflet Tissues

### 2.2.1 Uniaxial and biaxial mechanical testing procedures

A variety of methods have been developed to investigate the mechanical properties of the AHV leaflet tissues. Traditional techniques for soft tissue characterization stemmed from the seminal works by Fung *et al.* (1970, 1983) [33, 34], including the implementation of a preconditioning protocol to restore the tissue's *in vivo* functional behaviors. Owing to recent advances in hardware and improved understanding of the functional role of valve tissue, these foundational techniques have further been modified and adapted to capture tissue's mechanical properties in a more comprehensive manner.

Originally, uniaxial mechanical testing was employed to quantify the mechanical properties of the aortic valve tissues and the xenogeneic valve replacement materials under tensile loading [35, 36]. An early study by Sauren *et al.* (1983) also examined how the mechanical properties of the heart valve leaflets changed with applications of cyclic loading in an early fatigue mechanical tests implemented for heart valve tissues. These results were complemented by the flexural studies on strips of the native aortic valve

tissues, as well as the comparisons between the bending behaviors of the native valve tissues and their corresponding replacement materials [37]. However, these uniaxial and “strip” mechanical testing techniques were unable to adequately capture the material anisotropy arising from the tissue’s collagen fiber network. Therefore, a biaxial mechanical testing system was developed to characterize the mechanical properties of the heart valve leaflet tissues under various biaxial loading protocols (Fig. 2.4) [38].

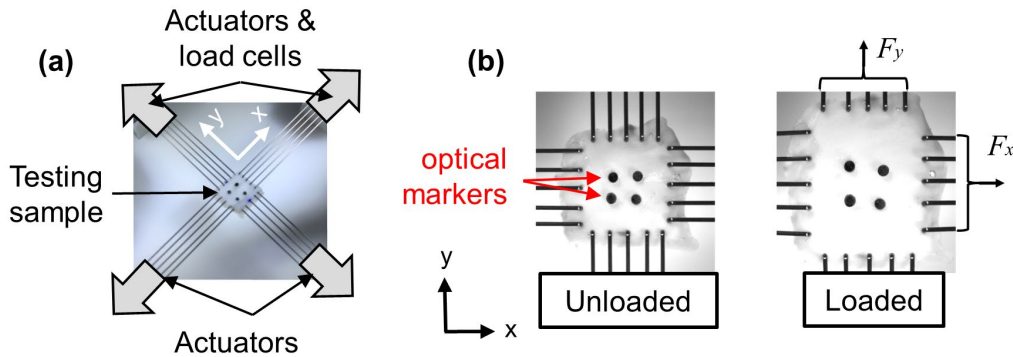


**Figure 2.4.** Schematic of a biaxial testing system for anisotropic mechanics characterization of heart valve leaflet tissue samples: (a) the mounting of the tissue sample and the application of force-controlled biaxial testing, and (b) tissue sample at the undeformed and loaded configurations with fiducial markers used for strain tracking.  $F_x$  and  $F_y$  are applied forces along the  $x$ - and  $y$ -directions, respectively.

Through biaxial testing, the directional-coupling and anisotropy of the mechanical responses of the heart valves leaflets could be revealed. These phenomena inspired further investigations using the biaxial mechanical techniques, leading to an experimental framework by Sacks *et al.* (2000) for developing heart valve constitutive models to predict membrane tissue mechanics under the finite element computational modeling framework [39, 40]. Concurrently with this development in the constitutive modeling theory, extensive biaxial mechanical testing was performed on native and glutaraldehyde-treated aortic valve

tissues [41]. Moreover, over the past two decades, further studies were performed to explore the mechanical behaviors of the HV leaflets, including analyses of the layer-specific properties, the loading-rate dependence of the mechanical properties of the aortic valve leaflet, the creep and stress-relaxation behaviors of the MVAL, and the impacts of various chemical and biological treatments on the tissue mechanics of the HV leaflets [42-46]. Despite these extensive experimental efforts to characterize the biaxial mechanical properties of the aortic and mitral valve leaflet tissues, the mechanical properties of the TV leaflet tissues have been relatively underrepresented in literature [47, 48]. This lack of investigation has been due to the clinical insignificance of right-sided heart diseases, especially compared to the aortic valve and mitral valve conditions [3]. However, recent clinical evidence has shown that tricuspid regurgitation is prevalent in 18% of heart failure victims, and that it can worsen prognoses for cardiac disease patients if left untreated [49]. Also, because of the substantial anatomical differences between the leaflets of the four heart valves, the mechanical properties of the specific valve leaflets may not be readily extrapolated across valves being studied. For these reasons, characterization of the mechanical behaviors of the tricuspid valve leaflet tissues is a relevant goal of the heart valve biomechanics research.

### **2.2.2 Prior studies on the mechanical behaviors of the AHV leaflets**

The original biaxial testing of MV tissues revealed many phenomena in both the MVAL and the MVPL [38]. May-Newman *et al.* (1995) found that both mitral valve leaflets, i.e., the MVAL and MVPL, exhibit a distinct material anisotropy, with higher stretches in the tissue's radial (R) direction compared to the responses in the circumferential (C) direction (Fig. 2.5a). They also observed an elastic mechanical response with minimal hysteresis

during loading and unloading cycles (Fig. 2.5b). Furthermore, it was observed that both the MVAL and the MVPL exhibited a nonlinear stiffening response with increased loading (Fig. 2.5).

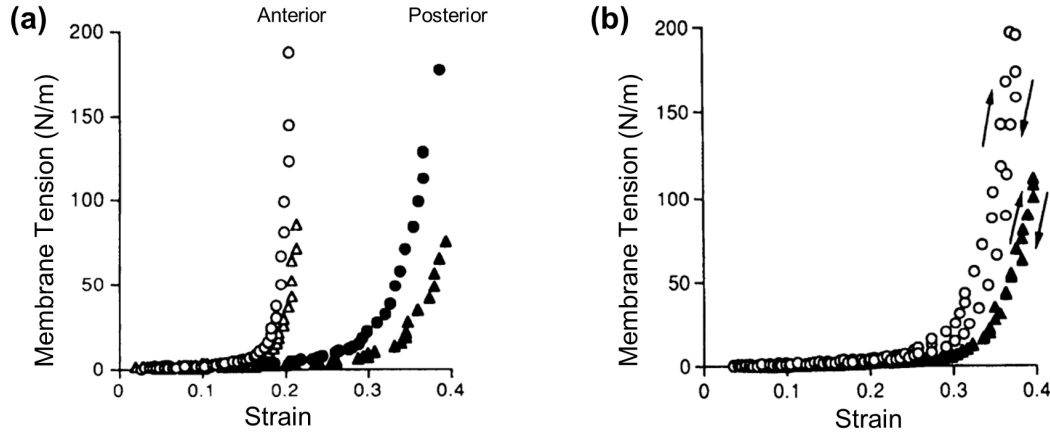


**Figure 2.5.** Biaxial testing results of the MV leaflets: (a) the loading portion of a stress-strain relationship for MVAL (*unfilled*) and MVPL (*filled*) tissues in the circumferential (*circles*) and radial (*triangles*) directions under *equibiaxial strains*, and (b) a typical loading and unloading cycle of the MVPL under equibiaxial stretching (*circles*: circumferential direction, *triangles*: radial direction). The images were modified from [38].

Subsequent studies of the mechanical behavior of the MV leaflet tissues include the investigations of the time-dependent viscoelasticity, i.e., the stress relaxation and creep behaviors [44, 45]. These studies showed that the MVAL exhibits a stress relaxation response which is typical of soft connective tissues, and that the lack of creep in the MVAL was atypical among collagenous soft tissues. These findings motivated the MVAL material classification as *anisotropic quasi-elastic*, indicating that the viscoelasticity in leaflet mechanics becomes negligible as loading approaches the *in vivo* deformation rates. In a later study, the age-dependence of the mechanical behaviors of the mitral leaflets was examined, and a general trend of tissue stiffening and thickening was observed with an

increasing specimen age [50]. More recently, aged human mitral valve samples were obtained and mechanically tested. These first human tissue results showed an increased mechanical stiffness with patient age, accompanying tissue calcification in all the leaflet samples [51]. These important characterizations of *ex vivo* mechanics of the MV leaflet tissues, especially as they relate to tissue microstructure and the functional valvular geometry, have been discussed in extensive reviews of the MV mechanics [52, 53]. In contrast, the mechanics of the TV leaflet tissues have traditionally merited little attention; a recent study by Khoiy and Amini (2016) was the first to examine the mechanical properties of each TV leaflet through biaxial mechanical testing methods [48] (Fig. 2.6).

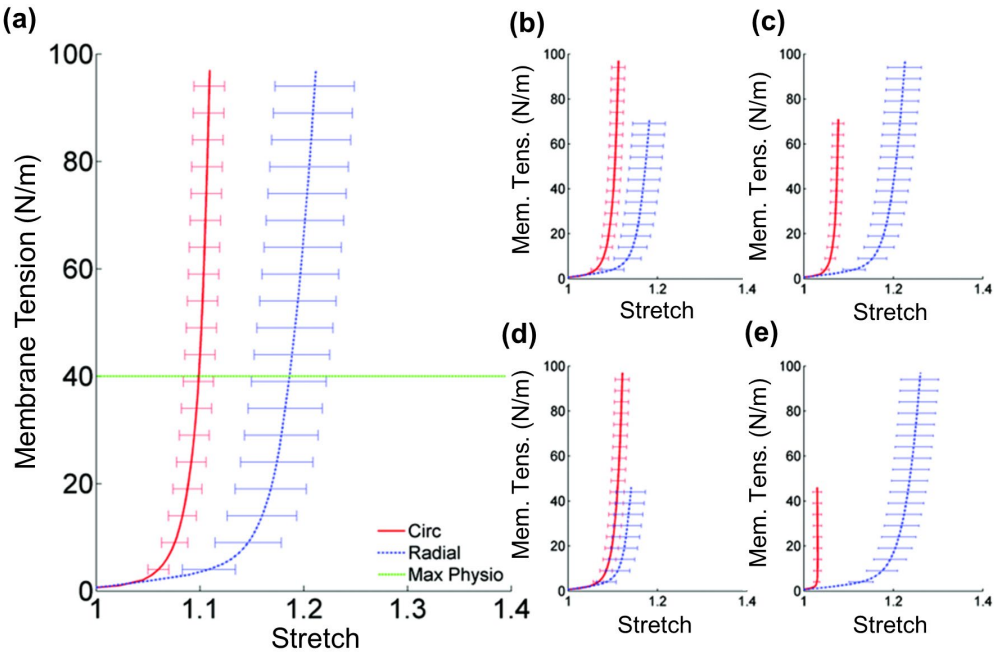


**Figure 2.6.** The mechanical response of the TVAL tissues ( $n=10$ ) under various biaxial loading protocols ( $T_{C,max}:T_{R,max}$ ) where  $T_C$  and  $T_R$  are the membrane tensions applied in the circumferential and radial directions, respectively: (a) 100:100 N/m, (b) 100:80 N/m, (c) 80:100 N/m, (d) 100:50 N/m, and (e) 50:100 N/m. Bars show standard error in testing results over  $n=10$  TVAL samples. The image was modified from [48].

These results demonstrate the mechanical coupling between the two tissue directions, i.e., the deformation in one tissue direction depends on the loading in both directions. Besides this mechanical-coupling, nonlinear and anisotropic mechanical behaviors were found in each of the TV leaflets (Fig. 2.6). They also observed distinct mechanical responses in each TV leaflet, with increased material anisotropy in the TVPL, and slightly more extensibility in the TVSL than in the TVAL. Aside from the study by Khoiy and Amini (2016), only one other study focused on the TV tissue biomechanics [47]. The study compared the mechanical properties of the leaflet tissues from excised human AHVs, finding more extensible and thinner tissues in the right-sided TV leaflets compared to their left-sided counterparts (the MV leaflets). They also observed cross-donor and age-dependent variances in leaflet mechanical properties. However, due to the difficulty of acquiring human tissues, a broad age range was examined, complicating the extraction of a “healthy” tissue’s mechanical response. Despite these efforts to characterize the mechanical properties of the AHV leaflet tissues, there is a need for understanding of the link between the tissue mechanics and underlying microstructure, particularly in the TV leaflet tissues.

### **2.3 Microstructural Characterizations of the HV Leaflets**

The HV leaflet tissues are broadly classified as *membranous fibrous connective tissues*. Morphologically, the *membrane* classification arises from the planar shape of the leaflet tissues, like skin tissue or blood vessels. The *fibrous connective tissue* denotes that the tissues are composed of cells, typically referred to as valvular interstitial cells (VICs), interspersed throughout a fibrous extracellular matrix (ECM). The ECM, synthesized by the embedded VICs, composes the bulk of connective tissue and is the primary contributor to the mechanical behaviors of the tissues. In the heart valve leaflet tissues, the ECM

consists of four primary constituents—glycosaminoglycans (GAGs), proteoglycans (PGs), elastin fibers, and collagen fibers—organized in complex spatial and depth-varied architectures [54].

### 2.3.1 Layered microstructure of the HV leaflet

Heart valve leaflet tissues are composed of four morphologically distinct layers, with an example depicted for the MVAL in Figure 2.7 [52]: the atrialis, spongiosa, fibrosa, and the ventricularis.

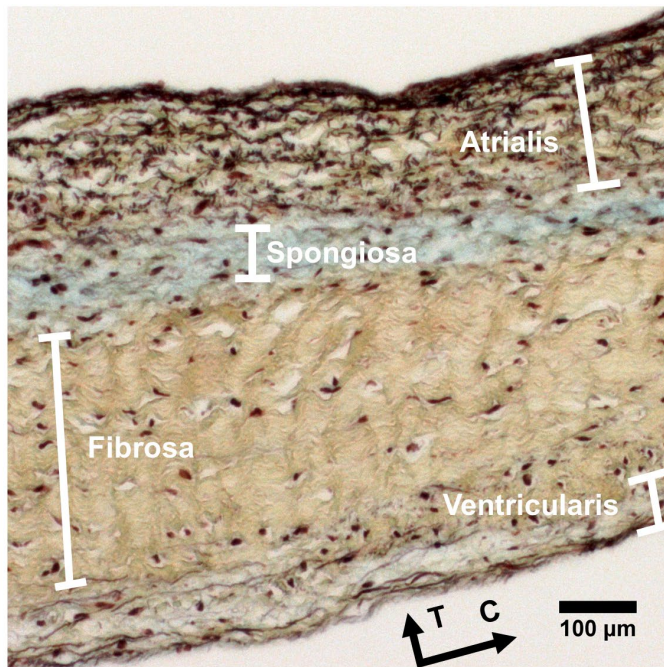


**Figure 2.7.** Microscopy images of a TV posterior leaflet cross section (T: Transmural, C: Circumferential) stained by Movat’s Pentachrome to color VICs and elastin fibers in *black*, hydrated PGs and GAGs in *blue*, and collagen fibers in *yellow*.

The atrialis layer, located on the atrial surface of the MV and TV leaflets, is a thin endothelial layer composed primarily of elastin. Inferior to the atrialis layer is the spongiosa—a layer loosely bound to its neighbors and composed predominantly of PGs

and GAGs [55]. The fibrosa, which is the thickest leaflet layer and located inferior to the spongiosa layer, is composed primarily of densely-packed type-I collagen fibers [56]. Inferior to the collagen-dense fibrosa layer, the ventricularis is a thin epithelial membrane located on the ventricular surface of the AHV leaflets; it is composed primarily of radially-oriented elastin fibers and less organized collagen fibers.

The four layers contribute distinctly to the AHV leaflet tissue biomechanics and function. The fibrosa layer is known to dictate the nonlinear and anisotropic leaflet mechanical behaviors through its dense internal collagen fiber composition [57]. It is believed that the radially-oriented elastin fibers within the ventricularis and atrialis allow the leaflets to recover their original geometries rapidly and elastically in the valve's mechanical loading environment [58]. The function of the spongiosa is perhaps the least understood, with some groups arguing that it reduces shear strain by acting as a lubricant between the atrialis and fibrosa [59, 60]. For the duration of this review, we focus on the fibrosa layer due to its deterministic relationship with the leaflet tissue's mechanical properties.

### **2.3.2 Collagen fiber morphology and composition**

Collagen is a prevalent structural protein, composing 25-35% of protein mass within the body [61]. In heart valve tissues, the protein exhibits a nested internal organization down to a molecular level, but for mechanical applications most interest concerns the fiber scale (1-10  $\mu\text{m}$ ). Collagen fibers within the heart valve leaflets exhibit an intrinsic dynamic property known as "crimp", which permits the fibers to behave like springs under tensile loading [62] (Fig. 2.8). On a population scale, the fibers in heart valve tissues exhibit

complex dynamically-structured networks. These dynamic fiber networks are responsible for the leaflet tissue mechanical strength and load-bearing capacity.

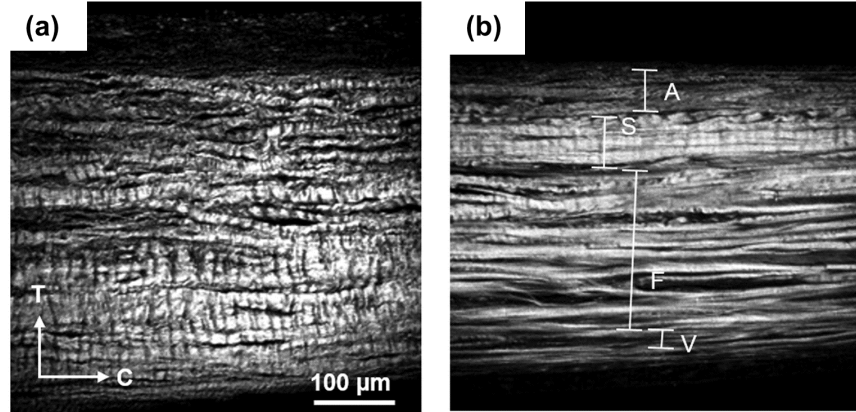


**Figure 2.8.** Collagen fibers within the MVAL tissue, visualized transmurally with second harmonic generation imaging through two-photon microscopy: (a) unloaded tissue, (b) tissue under equibiaxial planar tension of 150 N/m. T: Transmural, C: Circumferential. (a) and (b) are at equivalent scale. The images were modified from Lee *et al.* (2015) [63].

### 2.3.3 Techniques for quantifying collagen fiber architecture (CFA)

A variety of optical techniques have been employed to examine the collagen fiber architecture (CFA) in planar tissues, such as heart valve leaflets. These techniques utilized different mechanisms to establish image contrast for quantifying the fiber structures, including *reflectance and transmission differences* between material constituents (often enhanced via histological staining), *nonlinear optical responses*, *birefringent scattering properties*, and *front/back scattering properties* of fibers and fiber families. In the following, imaging modalities that have been commonly adopted to quantify the CFA will be discussed.

Reflectance and transmission differences are the simplest image contrast mechanism. In a medium with significant reflectance and/or transmission differences between fibrous structures and others, a simple magnified image of the tissue will provide an adequate contrast for visualization of the fiber structures, such as through stained histology images. However simple reflectance or transmission differences in collagenous tissues generally may not be sufficient to adequately visualize fiber structures, so can be supplemented by other contrast mechanisms [64, 65] (Figure 2.9).

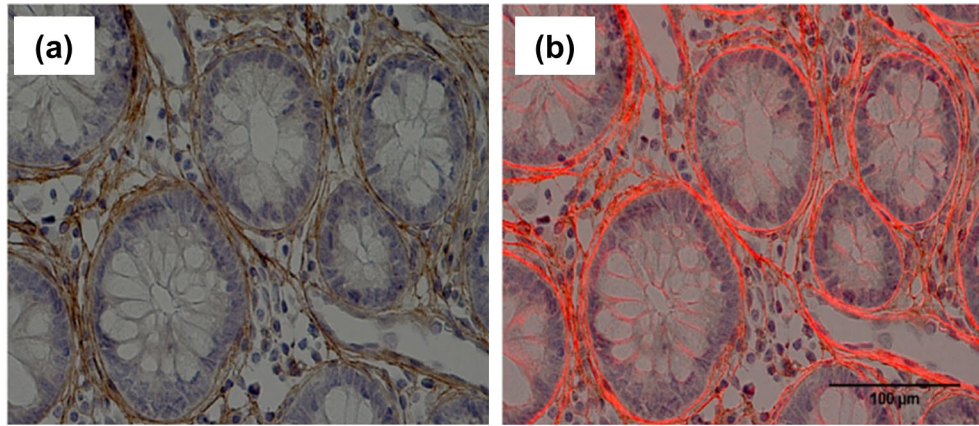


**Figure 2.9.** Comparison of collagen contrast in the colon tissue stained with type-I collagen antibody and examined with (a) standard microscopy methods and (b) polarized light microscopy. The images were adapted from [66].

As depicted in Figure 2.9, the contrast of the CFA can be enhanced through the addition of polarization elements. The improved contrast arises via capturing the birefringent, or polarization-dependent, optical properties of the cylindrical collagen fibers. The augmentation of standard microscopes to capture the birefringent properties, such as the phase retardance and diattenuation, of the CFA is commonly referred to as polarized light microscopy (PLM). Because fibrous microstructural elements are the predominant

birefringent actors in a tissue sample, this practice allows the isolation of the CFA from the other microstructural constituents.

Another standardized method to quantify the collagen fiber structures is known as second harmonic generation (SHG) imaging. SHG utilizes the combination of simultaneously incident photons in a nonlinear medium to create a reflected photon has twice the frequency and half the wavelength of the initial photon (i.e., the second harmonic). The SHG imaging technique uses gating to capture only the photons that have been upconverted to the second harmonic, thus employing the *nonlinear optical properties* of collagen fibers as a contrast mechanism. Although the instrumentation required for SHG imaging is complex, the technique permits high-resolution, high-contrast imaging of the localized CFA features. As such, it has been widely used for characterizing the CFAs within tissues, such as the cornea, tendons and heart valve leaflets [67, 68] (Fig. 2.10).

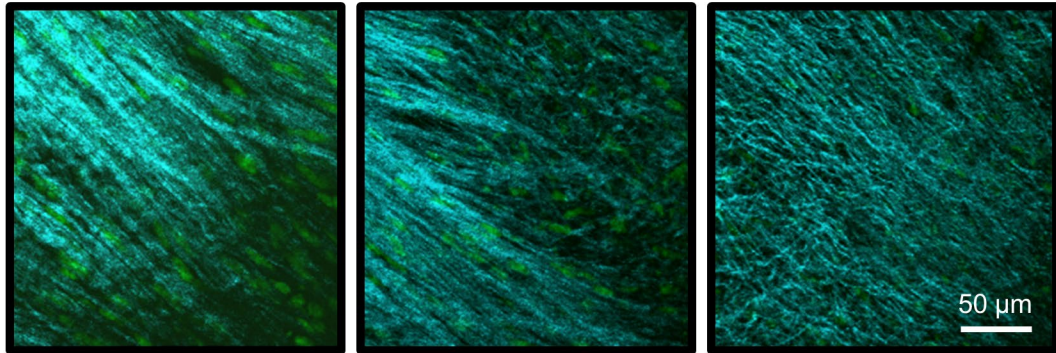


**Figure 2.10.** Representative SHG images of MVAL microstructure at various spatial points, demonstrating collagen fibers (cyan) and GAGs (green). The images were adapted from [56].

For many biomedical applications, a characterization of fiber structures over a wide field is required, for which a decrease in the image resolution is an acceptable compromise to

allow mapping the CFA over a field of view (FOV) at the tissue scale. In general, the wide-field CFA can be described by two local parameters: the fiber orientation and the fiber dispersion, which can be considered two-dimensional properties by assuming homogeneous properties across a third dimension (typically the thickness). Small angle light scattering (SALS) is a class of methods for producing two-dimensional maps of CFA via the *front/back scattering* properties of collagen fibers. SALS uses transmitted laser illumination to quantify the CFA in planar tissues. The transmitted light assumes an elliptical profile due to the laser's interaction with the oriented tissue CFA. Through rasterized laser illumination and analyses on the transmitted light profiles, the predominant local collagen fiber orientation and dispersion can be extracted (Fig. 2.11).

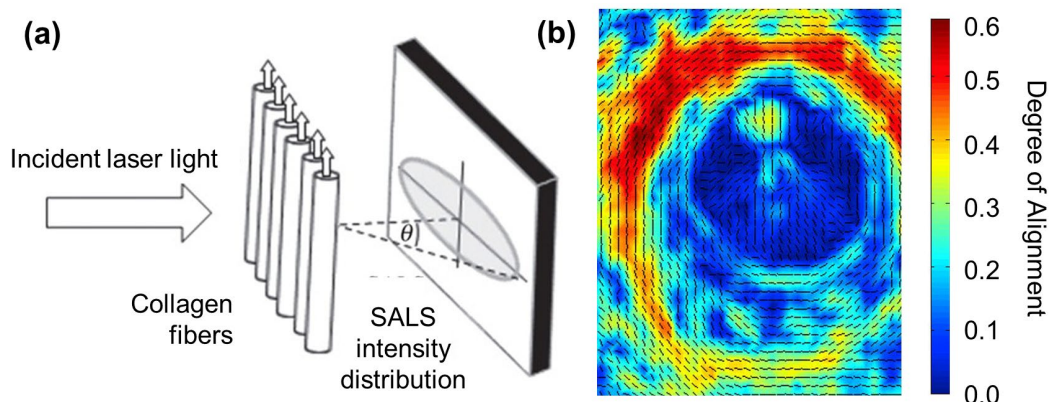


**Figure 2.11.** Schematic of the SALS domain mapping of collagen fiber structures: (a) the fundamental basis for the SALS technique (image adapted from [69]), and (b) representative mapping of the collagen fiber orientation (vector plot) and fiber dispersion (via degree of alignment, 0: randomly aligned fibers , 1: perfectly aligned fibers) for the ocular lamina cribrosa tissue (image adapted from [70]).

Inherent to SALS techniques is the assumption of structural heterogeneity through the thickness, which can propagate errors when estimating the CFA for multilayered samples.

Additionally, SALS is limited in spatial resolution by the diameter of the incident beam and the time-cost of raster scanning larger tissue samples. Despite these limitations, the technique has been used widely for analysis of membrane tissues such as arteries, tendons, leaflets, and many ocular tissues [71, 72].

#### **2.3.4 Quantifications of the CFAs of heart valve leaflets**

Several studies have examined the CFAs of the semilunar valve leaflets [73-77]; however, relatively fewer efforts have focused on quantification of the CFA of the tricuspid valve leaflets. One of the observed properties of the semilunar leaflet's CFA is the tendency of collagen fibers to prefer orientation in the circumferential direction. This fiber orientation affinity contributes to the valve tissue's stiffer mechanical response in the circumferential direction (Fig. 2.5). In quantifying the CFA, it is important to note that tissue microstructures will change with applied load. Toward this end, recent studies have examined the “*dynamic*” CFA of the aortic and pulmonary valve leaflets [73, 74]. Typically, these dynamic CFA quantifications utilize *tissue fixation techniques* combined with SALS; in this process, the leaflets are chemically fixed under specified loads and subsequently imaged by SALS technique [73, 78]. Representative results of the AV and PV leaflets via this procedure are shown in Figure 2.12.

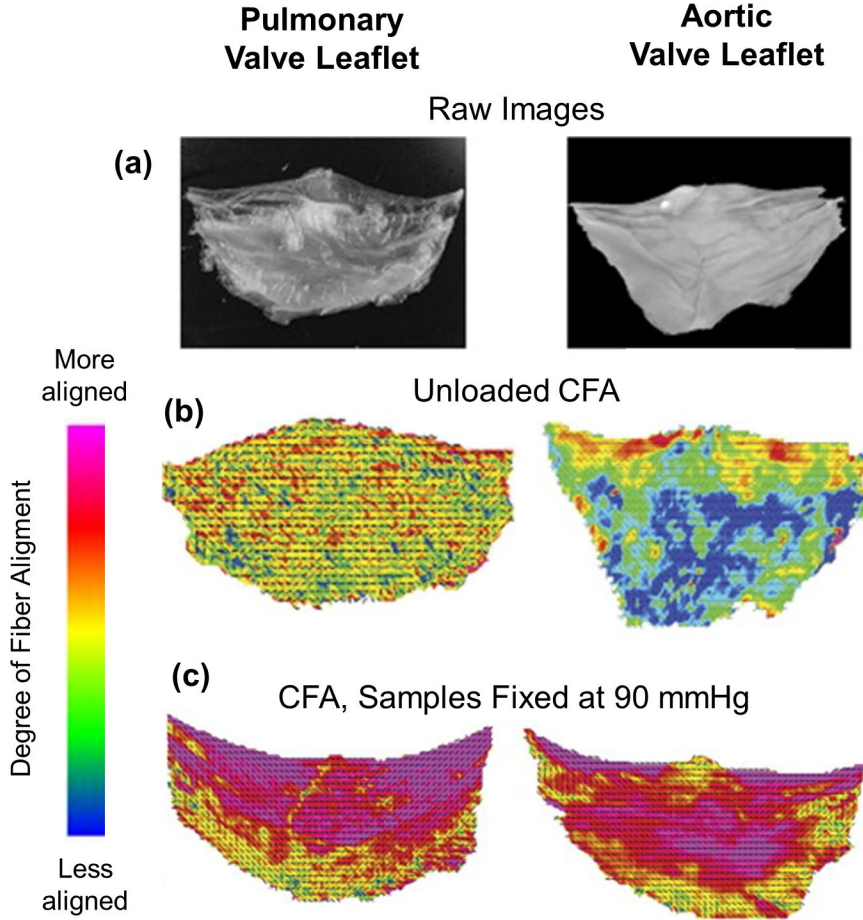


**Figure 2.12.** Quantifications of collagen fiber preferred orientation (dashed lines: –) and degree of local fiber alignment (colorbar) for the pulmonary and aortic valve leaflets: (a) raw images of the leaflets, (b) the collagen fiber architecture prior to loading, and (c) the fiber architecture under 90 mmHg transvalvular fixation pressure. The images were modified from [73].

In the loaded pulmonary and aortic valve leaflet tissues, the fibers demonstrate an extended U-shape, running from the annular attachment at each leaflet edge to the coaptation point and back to the annulus. Moreover, the fibers are substantially more aligned in loaded tissues. However, an important consequence of the fixation-SALS experimental approach is the inability to test *the same tissue* under a variety of mechanical loading protocols, because the requisite chemical treatment irrevocably “fixes” the tissue’s CFA.

A recent technique developed by Yang *et al.* (2014) [77] aimed to address the shortcomings of the SALS modality. The technique, named polarized spatial frequency domain imaging (pSF DI), entails the use of spatial frequency domain imaging (SF DI) combined with reflectance-based polarized light imaging to perform wide-field, non-destructive depth-modulated quantifications of the CFA in connective tissues [79, 80]. An example of the depth-discernment and CFA quantification capability of pSF DI compared to the full-thickness result using the SALS technique is shown in Figure 2.13.

The recent study by Goth *et al.* (2019) using the pSF DI modality found unique transmural fiber dispersion in the HV leaflets, with more aligned fibers in the fibrosa layer (Figure 2.13 j) than the ventricularis layer (Figure 2.13k). Alavi *et al.* (2015) also observed the existence of both layer-specific and load-dependent CFAs in the atrioventricular heart valve leaflets through SHG imaging [56]. Although their study helps to extend microstructural understanding in the atrioventricular leaflets, the analysis was depth-limited to the superficial 60  $\mu\text{m}$  of the tissue, i.e., less than 10% of the full leaflet thickness, and spatially limited by the narrow FOV of SHG imaging. Therefore, considerable work is still warranted in understanding how the CFAs in the HV leaflets change under various physiological loading conditions.

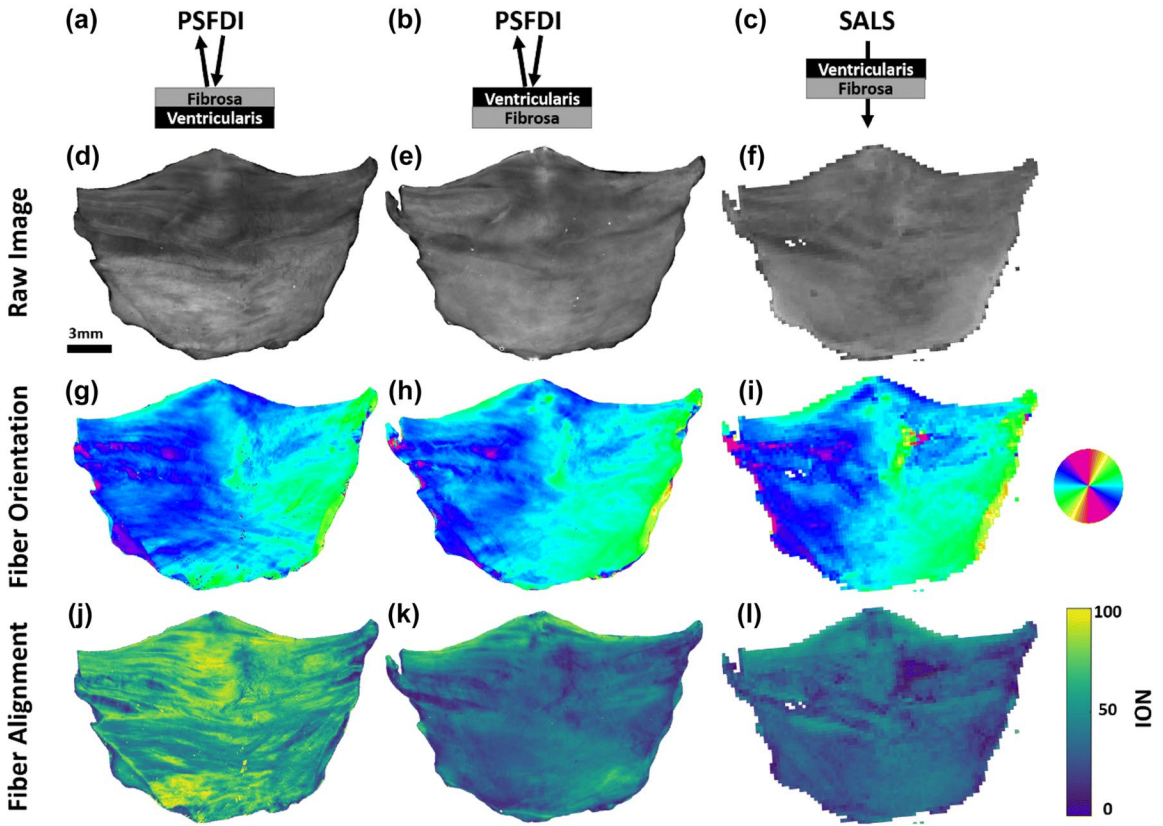


**Figure 2.13.** pSF DI depth-modulated imaging and CFA extraction of an ovine aortic valve leaflet compared to equivalent SALS result. (a-c) Imaging arrangement, (d-f) raw intensity images, (g-i) extracted fiber orientation maps, (j-l) extracted normalized orientation index (NOI) maps, indicating the fiber dispersion. Note that (d, e, g, h, j, k) were limited to the superficial 250  $\mu\text{m}$  of the tissue. The images were modified from [80].

## CHAPTER 3. CHARACTERIZATION OF THE MECHANICAL BEHAVIORS OF THE AHV LEAFLETS

### 3.1 Introduction to the AHV Mechanics

In healthy individuals, blood circulates through the heart with minimal backflow (or regurgitation) via proper opening and closing of the atrioventricular valves. However, valvular heart diseases, such as valve stenosis, valve prolapse, chordae rupture, leaflet damage and/or congenital defects, can affect the overall function of the valve and eventually lead to significant regurgitation [1, 81-83]. The regurgitation increases the strain on the heart and is a corollary and precedent to the development of other, more threatening, heart conditions.

To improve our understanding of the functional degradation in diseased HVs, it is important to understand the mechanics of the valvular soft tissues. Despite the prior studies on heart atrioventricular valve leaflet biomechanical responses, mechanical testing results can vary significantly based on specific experimental procedures [84]. Therefore, it would be useful to compare leaflet material properties from both the MV and TV from the same heart under a unified mechanical quantification procedure. Moreover, the relationship between mechanics of the MV and TV is important towards understanding the connection between the MV surgical intervention and the subsequent development of functional tricuspid regurgitation observed in clinical studies [85-87].

Hence, the objective of this chapter is to utilize biaxial testing experiments to compare the unique material response of each MV and TV leaflet. Porcine atrioventricular leaflets were also tested at various loading rates and temperature levels to characterize the dependence of tissue response on these selected experimental parameters. In addition, the stretch

responses of leaflets from juvenile ovine and adult ovine hearts were characterized and compared to understand the effects of species and animal age on testing results. Lastly, an anatomical study was conducted to examine chordae distributions in porcine and ovine valves, and histological methods were employed to study and examine the layered microstructure of the porcine atrioventricular valve leaflets.

## **3.2 Methods**

### **3.2.1 Tissue acquisition**

To characterize the material properties of porcine atrioventricular HV leaflets, porcine heart tissues from physically healthy pigs (80-140 kg, 1-1.5 years of age) were acquired from a local USDA-approved abattoir (Country Home Meat Company, Edmond, OK). To further compare the leaflet mechanical behaviors between different species and ages, adult ovine hearts (65-90 kg, 2-5 years of age) and juvenile ovine hearts (35-60 kg, 6-12 months of age) were also obtained. The heart tissues were frozen within 12 hours post-mortem in a standard freezer at -14 °C for storage purposes. This tissue storage procedure was based on the previous studies which found that freezing has a minimal impact on the mechanics of collagenous tissues such as skin tissue and arteries [88-90]. In preparation for testing, the hearts were thawed and leaflets from both the MV and TV were dissected (Fig. 3.1a). The excised leaflets were preserved in phosphate-buffered saline (PBS) and refrigerated at 4 °C to maintain material properties until testing [91].

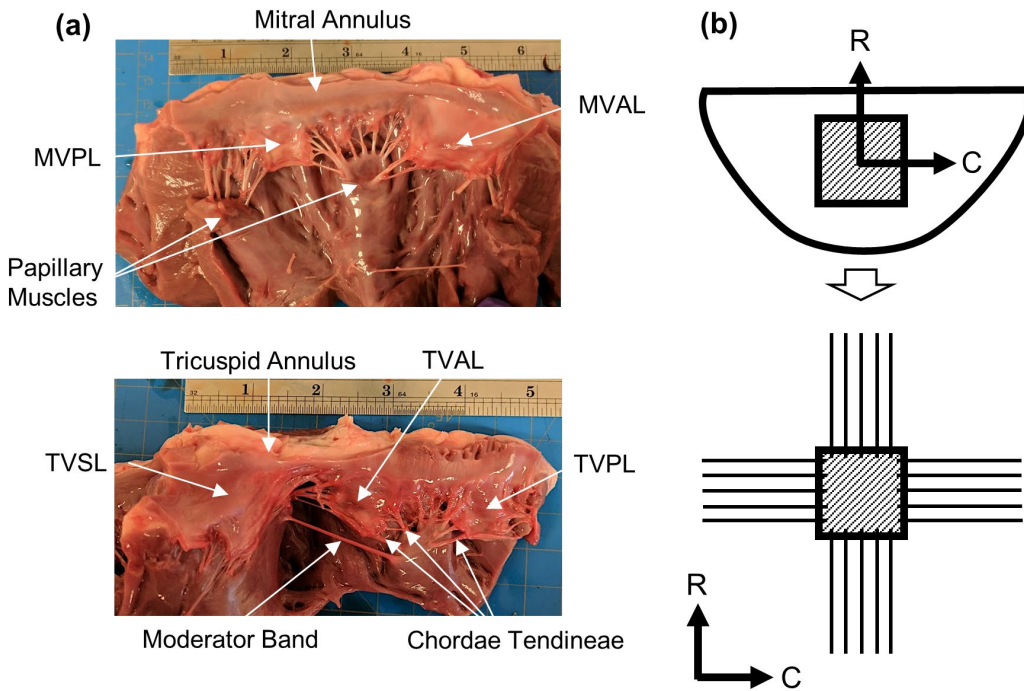


**Figure 3.1.** (a) dissected porcine heart showing the MV (top) and TV (bottom), with labels describing key anatomical components (ruler shows inches). (b) Schematic of the excised leaflet and the central bulk region (top), and the mounted tissue specimen on the biaxial mechanical testing system (C: circumferential direction; R: radial direction).

### 3.2.2 Tissue preparation

For biaxial mechanical testing, a square specimen ( $8 \times 8$  mm) was dissected from the central or belly region of each of the 5 atrioventricular heart valve leaflets: the MVAL, MVPL, TVAL, TVPL, and TVSL (Fig. 3.1b). The thickness of the specimen was measured at 3 different locations using digital calipers (WestWard Company, Lake Forest, IL) to determine an average tissue thickness. The tissue specimen was then mounted on a commercial biaxial mechanical testing system—BioTester (CellScale, Waterloo, ON, Canada), equipped with a load cell capacity of 1.5 N (Fig. 3.2a). The primary axes of the testing system were aligned with the tissue's circumferential and radial directions (Fig.

3.1b), and four BioRakes were used to facilitate a 6.5 x 6.5mm effective testing region (Fig. 3.2b). Four glass beads (with diameters of 300-500  $\mu\text{m}$ ) were affixed to the specimen in a square configuration (Fig. 3.2c) for measuring the in-plane deformation and strain using a non-contact image-based technique as described in [40]. To ensure the tissue remained hydrated, the specimen was submerged in a bath of PBS solution for the duration of the testing process.

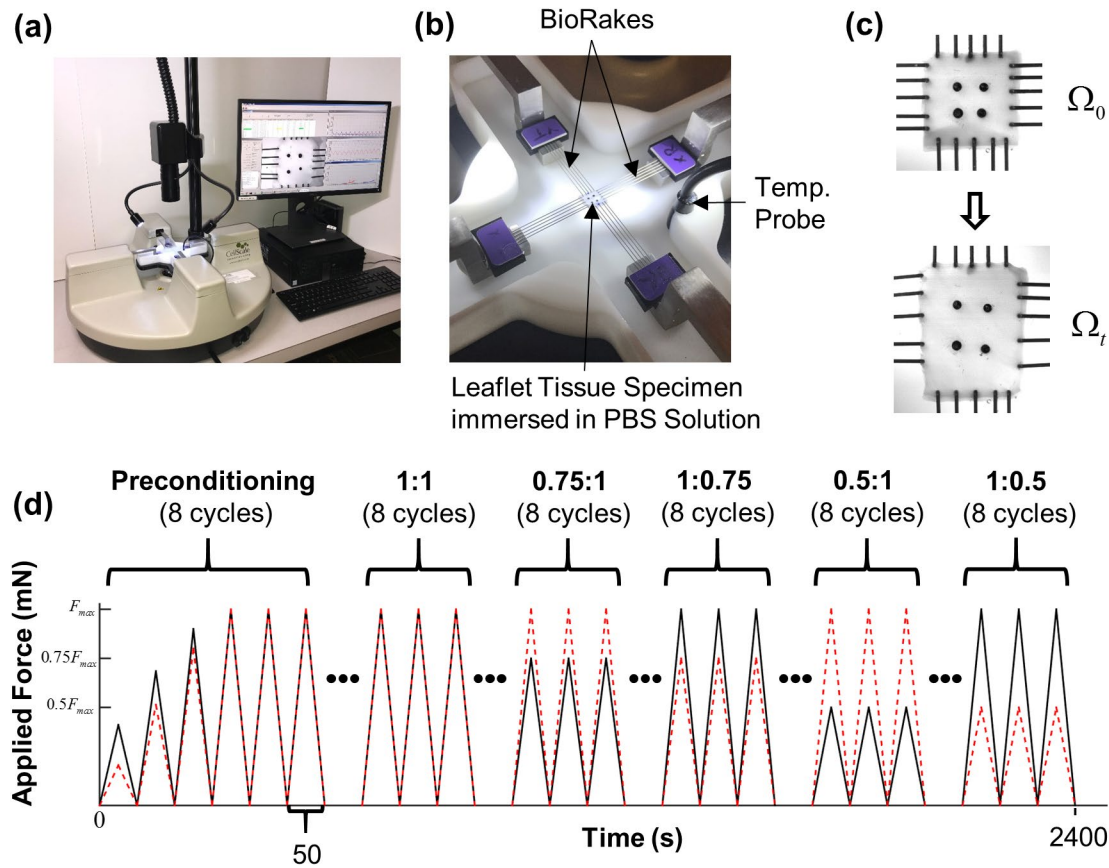


**Figure 3.2.** (a) Image of the biaxial mechanical testing system (BioTester), (b) image of the mounted tissue, (c) schematic of the valve leaflet specimen before and after prescribed loading, and (d) illustration of the force-controlled protocols employed in both the baseline and temperature-controlled tests ( $F_{max}$ : the maximum applied load, — : the applied tension in the circumferential direction, and --- : the applied tension in the radial direction).

### 3.2.3 Biaxial mechanical testing protocols

Force-controlled biaxial mechanical testing was performed on 4 experimental groups: (i) the baseline testing group (porcine tissues) with a loading rate of 4.42 N/min at room temperature (22 °C), (ii) the loading-rate effect group (porcine tissues) with three loading rates of 2.29 N/min, 4.42 N/min, and 7.92 N/m at room temperature (22°C), (iii) the temperature effect group (porcine tissues) with a loading rate of 4.42 N/min at three temperature levels (27 °C, 32 °C and 37 °C), and (iv) the species and age group (porcine, adult ovine, and juvenile ovine tissues) with a loading rate of 4.42 N/min at the physiological temperature (37 °C). The sample size of each atrioventricular heart valve leaflet for each of these groups was n=6.

For each biaxial mechanical test, the physiological stress levels of the MV and TV leaflets were estimated to be  $P_{max} = 240$  kPa and  $P_{max} = 115$  kPa, respectively, where  $P$  is the first Piola-Kirchhoff (1<sup>st</sup>-PK) stress. This maximum stress assumption is based on the Laplace's law assuming coapted leaflets with spherical geometry and mean radius of curvature of 2 cm [48], and the transvalvular pressure gradients of 100 mmHg [92] and 40 mmHg [48] for the coapted MV and TV, respectively. Then, the maximum applied membrane tensions in both the circumferential and radial directions were calculated based on measured thickness of the leaflet tissue, i.e.  $T_{(C,R)max} = P_{max} \cdot t_s$ , where  $t_s$  is the specimen average thickness. Similarly, the maximum applied force in each direction were computed as  $F_{(C,R)max} = T_{(C,R)} \cdot L = P_{max} \cdot t_s$ , where  $L$  is the initial loaded region edge length.

Each test began with a preconditioning protocol, during which estimated membrane tensions  $T_{C,max}$  and  $T_{R,max}$  were applied for 8 repeated loading-unloading cycles (Fig. 3.2d),

considering a preload of 1% of  $T_{C,\max}$  and  $T_{R,\max}$ , to restore the dissected tissue to its respective *in vivo* functional configuration [93, 94]. The ascending applied loading preconditioning method is typical in the field, while the 8 cycles were found to be adequate due to the observed convergence of the mechanical response curves. Then, biaxial testing with various loading ratios ( $T_{C,\max}:T_{R,\max} = 1:1, 0.75:1, 1:0.75, 0.5:1$ , and  $1:0.5$ ) was conducted (Fig. 3.2d). Data from the unloading portion of the last cycle of each loading protocol were used in the tissue stress and strain analyses as described in the next subsection and presented in the results in *Section 3.3*. In addition to the monitored forces and BioRake separation distance in both directions, a series of 1280 x 960 pixel images were collected by a high-resolution CCD camera (The Imaging Source LLC, Charlotte, NC) at 15 Hz. The images were used for non-contact planar strain calculations described in the next section.

### **3.2.4 Tissue stress and strain calculations**

Digital image correlation (DIC) based techniques have been widely utilized in the biomechanics society to track the deformations of a tissue specimen while avoiding the Saint-Venant edge effects on tissue deformation [95]. For this process, four fiducial markers (glass beads) were placed in the central delimited region (3mm x 3mm) of the valve leaflet specimen (Fig. 3.2c). A series of images of the tissue specimen were collected by the high-resolution CCD camera, and the time-dependent positions of the four fiducial markers were analyzed based on the acquired images using the DIC-based capability in the LabJoy software of the BioTester system:

$$\mathbf{x}_I(t) = \mathbf{X}_I + \mathbf{d}_I(t), \quad I = [1, 2, 3, 4], \quad (3.1)$$

where  $\mathbf{X}_I$  and  $\mathbf{x}_I$  are the two-dimensional marker positions at the undeformed (reference) configuration ( $\Omega_0$ ) and at the deformed configuration ( $\Omega_t$ ), respectively, and  $\mathbf{d}_I$ 's are the displacement vectors of the fiducial markers, i.e.,  $\mathbf{d}_I(t) = [u_I(t), v_I(t)]^T$ , where  $u_I(t)$  and  $v_I(t)$  are the displacements of marker  $I$  at time  $t$  in the  $x$ - and  $y$ -directions, respectively.

To compute the in-plane strains of the tissue specimen, a four-node bilinear finite element was developed based on the 4 markers, and the deformation gradient tensor  $\mathbf{F}$  was computed using an in-house MATLAB program (R2016a, The MathWorks, Natick, MA) based on the previously developed strain-calculation technique [40, 96]:

$$\mathbf{F} = \mathbf{F}(\mathbf{X}, t) = \frac{\partial \mathbf{x}}{\partial \mathbf{X}} = \begin{bmatrix} \sum_{I=1}^4 B_{xI} u_I(t) & \sum_{I=1}^4 B_{yI} u_I(t) \\ \sum_{I=1}^4 B_{xI} v_I(t) & \sum_{I=1}^4 B_{yI} v_I(t) \end{bmatrix}, \quad (3.2)$$

where  $B_{xI}'s$  and  $B_{yI}'s$  are the shape function derivatives associated with node  $I$  with respect to the  $x$  and  $y$  coordinates, respectively. Note the  $x$ - and  $y$ -coordinates were aligned with the tissue's circumferential and radial directions, respectively (Fig. 3.1b and Fig. 3.2b). The right Cauchy-Green deformation tensor  $\mathbf{C}$  and the Green strain tensor  $\mathbf{E}$  could then be computed:

$$\mathbf{C} = \mathbf{F}^T \mathbf{F}, \text{ and } \mathbf{E} = \frac{1}{2} (\mathbf{C} - \mathbf{I}), \quad (3.3)$$

where  $\mathbf{I}$  is the 2<sup>nd</sup>-order identity tensor. The circumferential and radial stretches,  $\lambda_C$  and  $\lambda_R$ , were determined by the square roots of the principal values of  $\mathbf{C}$ . Next, the first Piola-Kirchhoff (1<sup>st</sup>-PK) stress tensor  $\mathbf{P}$  was computed using the specimen average thickness,  $t_s$ , and the applied membrane tensions,  $T_C$  and  $T_R$ , as follows:

$$\mathbf{P} = \frac{1}{t_s} \begin{bmatrix} T_C & 0 \\ 0 & T_R \end{bmatrix}. \quad (3.4)$$

### **3.2.5 Quantification of the anatomical structure of valve apparatus**

To complement the mechanical response data from biaxial mechanical testing, we further investigated the anatomical features of both the porcine and adult ovine atrioventricular HVs (n=6). In brief, we measured the number of chordae and each chord's length, then classified the chordae according to their respective supported leaflet. Adapting the classification convention of Toma *et al.* (2016) [97], tertiary chordae were not measured, and no distinction was captured between primary and secondary chordae. The length of each chord was measured from proximal attachment at the papillary muscles to distal attachment at the ventricular leaflet surface. We also measured each leaflet's thickness in 3 separate locations using digital calipers with a resolution of 0.01 mm.

### **3.2.6 Histological analysis**

To examine the microstructural organization of the ECM components in the valve leaflets, specimens from all five atrioventricular valve leaflets were fixed in 10% formalin at room temperature. These tissue specimens were then dehydrated in graded solutions of alcohol and embedded in paraffin. Samples of 5-7  $\mu\text{m}$  thickness were sectioned and stained with Masson's trichrome stain. For the morphological characterization, all stained sections were examined with a halogen illumination microscope (AmScope, Irvine, CA) at a magnification of 2X. Images of leaflets were captured using a 10 Mega Pixel camera and analyzed with ImageJ software (National Institute of Health, Bethesda, MD). A single image of each valve leaflet was captured from the stained sections and thickness was

measured at three random locations in the collected image. Further, the color deconvolution and image threshold plugins in ImageJ [98] were used to quantify the collagen content in each leaflet specimen.

### 3.2.7 Statistical analysis

Previous studies have demonstrated a difference between the stretch responses due to the preconditioning effect and the applied loading to the tissue [99]. To capture these distinctions, we compared three different stretch metrics across directions for the same tissue (circumferential versus radial) and between the five atrioventricular valve leaflets.

For each leaflet type, the *peak stretches* ( $\lambda_C^{0-peak}$  and  $\lambda_R^{0-peak}$ ) were defined as the circumferential and radial stretch values at the peak stress from the equibiaxial tension protocol as. The peak stretches were further decomposed into two constituents: (i) the *preconditioning stretches* ( $\lambda_C^{0-1}$  and  $\lambda_R^{0-1}$ ), defined as the tissue stretch from the mounting configuration ( $\Omega_0$ ) to the post-preconditioning state ( $\Omega_1$ ), and (ii) the *mechanical stretches* ( $\lambda_C^{1-peak}$  and  $\lambda_R^{1-peak}$ ), defined as the tissue stretch from the post-preconditioning configuration ( $\Omega_1$ ) to the peak loading state.

These stretch measures in all three experimental groups (baseline, loading-rate effect, temperature effect, and species effect) were evaluated via a one-way ANOVA with the null hypothesis of equivalent stretches across study groups to examine the differences in the leaflet mechanical responses. Similarly, in the anatomical study, the leaflet thicknesses, leaflet-specific chordae lengths, and leaflet-specific chordae quantities were all compared using the standard one-way ANOVA method. A *p*-value <0.05 was considered as statistically significant and a *p*-value <0.10 as nearly significant.

### 3.3 Results

#### 3.3.1 Baseline testing

Results for the MV and TV leaflets under loading protocols ( $T_{C,\max}:T_{R,\max} = 1:1, 0.5:1, 1:0.5, 0.75:1$ , and  $1:0.75$ ) are presented in Figure 3.3 and Figure 3.4, respectively. Table 3.1 **Error! Reference source not found.** provides the mean  $\pm$  standard error of the mean (SEM) of the stretches for the MV and TV leaflets at the specified stress values for the equibiaxial loading protocol ( $T_{C,\max}:T_{R,\max} = 1:1$ ).

**Table 3.1.** Circumferential and radial stretches of porcine AHVs (n=6) at selected stress levels (% of maximum 1st-PK stress) under equibiaxial tension protocol ( $T_{C,\max}:T_{R,\max} = 1:1$ ). Values are reported as mean  $\pm$  SEM.

% of $P_{11,\max}$	$\lambda$	MVAL	MVPL	TVAL	TVPL	TVSL
0%	$\lambda_C^{0-peak}$	$1.061 \pm 0.049$	$1.087 \pm 0.032$	$1.089 \pm 0.023$	$1.120 \pm 0.041$	$1.168 \pm 0.035$
	$\lambda_R^{0-peak}$	$1.358 \pm 0.042$	$1.429 \pm 0.069$	$1.434 \pm 0.050$	$1.511 \pm 0.035$	$1.476 \pm 0.066$
25%	$\lambda_C^{0-peak}$	$1.207 \pm 0.058$	$1.192 \pm 0.031$	$1.172 \pm 0.026$	$1.270 \pm 0.058$	$1.331 \pm 0.023$
	$\lambda_R^{0-peak}$	$1.551 \pm 0.054$	$1.572 \pm 0.081$	$1.569 \pm 0.072$	$1.735 \pm 0.037$	$1.641 \pm 0.035$
50%	$\lambda_C^{0-peak}$	$1.219 \pm 0.061$	$1.204 \pm 0.032$	$1.194 \pm 0.026$	$1.292 \pm 0.059$	$1.355 \pm 0.023$
	$\lambda_R^{0-peak}$	$1.572 \pm 0.055$	$1.589 \pm 0.082$	$1.624 \pm 0.084$	$1.766 \pm 0.040$	$1.664 \pm 0.088$
75%	$\lambda_C^{0-peak}$	$1.225 \pm 0.062$	$1.212 \pm 0.034$	$1.204 \pm 0.026$	$1.303 \pm 0.060$	$1.367 \pm 0.023$
	$\lambda_R^{0-peak}$	$1.583 \pm 0.055$	$1.599 \pm 0.082$	$1.640 \pm 0.087$	$1.780 \pm 0.040$	$1.676 \pm 0.089$
100%	$\lambda_C^{0-peak}$	$1.231 \pm 0.063$	$1.217 \pm 0.034$	$1.210 \pm 0.027$	$1.310 \pm 0.060$	$1.374 \pm 0.023$
	$\lambda_R^{0-peak}$	$1.591 \pm 0.055$	$1.606 \pm 0.082$	$1.651 \pm 0.089$	$1.788 \pm 0.040$	$1.685 \pm 0.089$

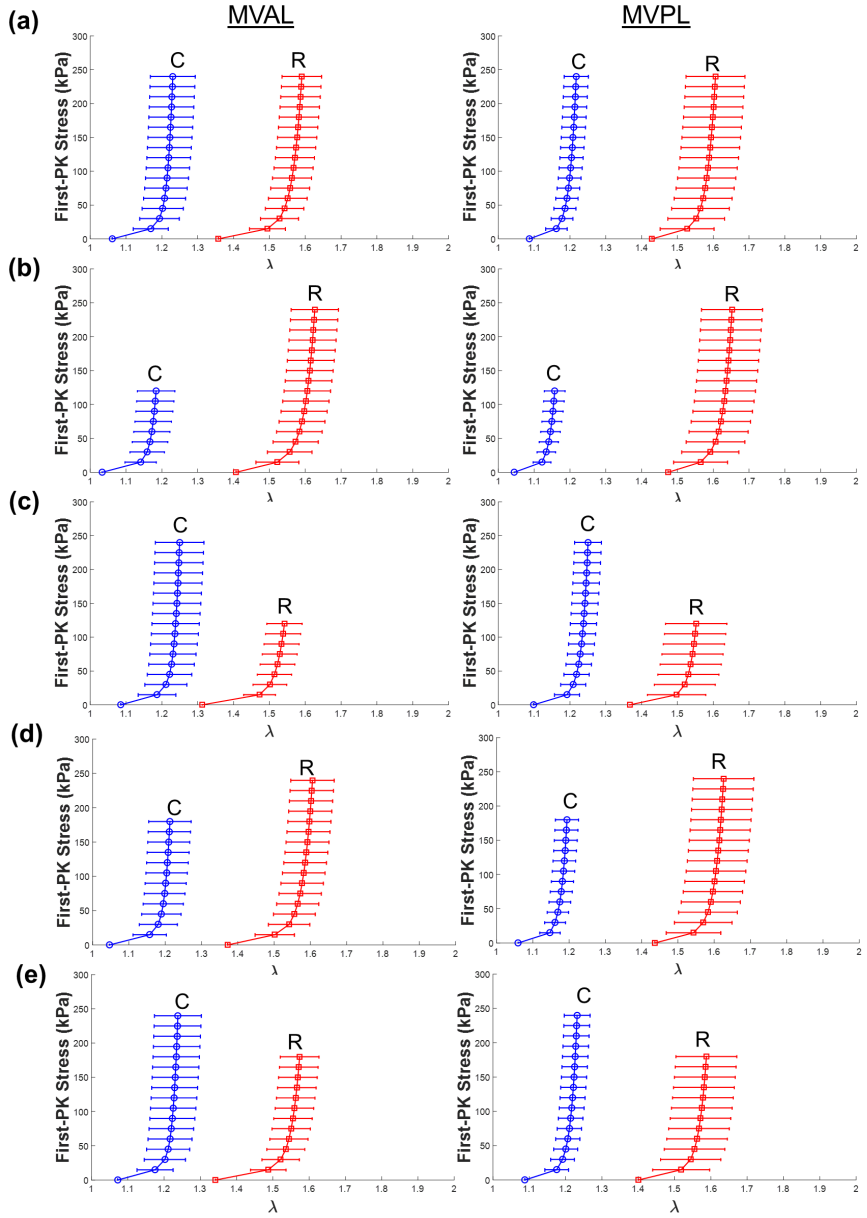


**Figure 3.3.** Mean  $\pm$  SEM of the 1st-PK stress versus stretch results of the porcine MVAL and MVPL tissues ( $n=6$ ) at room temperature ( $22^{\circ}\text{C}$ ) under: (a) equibiaxial tension ( $T_{C,\text{max}}:T_{R,\text{max}} = 1:1$ ), (b)  $T_{C,\text{max}}:T_{R,\text{max}} = 0.5:1$ , (c)  $T_{C,\text{max}}:T_{R,\text{max}} = 1:0.5$ , (d)  $T_{C,\text{max}}:T_{R,\text{max}} = 0.75:1$ , and (e)  $T_{C,\text{max}}:T_{R,\text{max}} = 1:0.75$ .

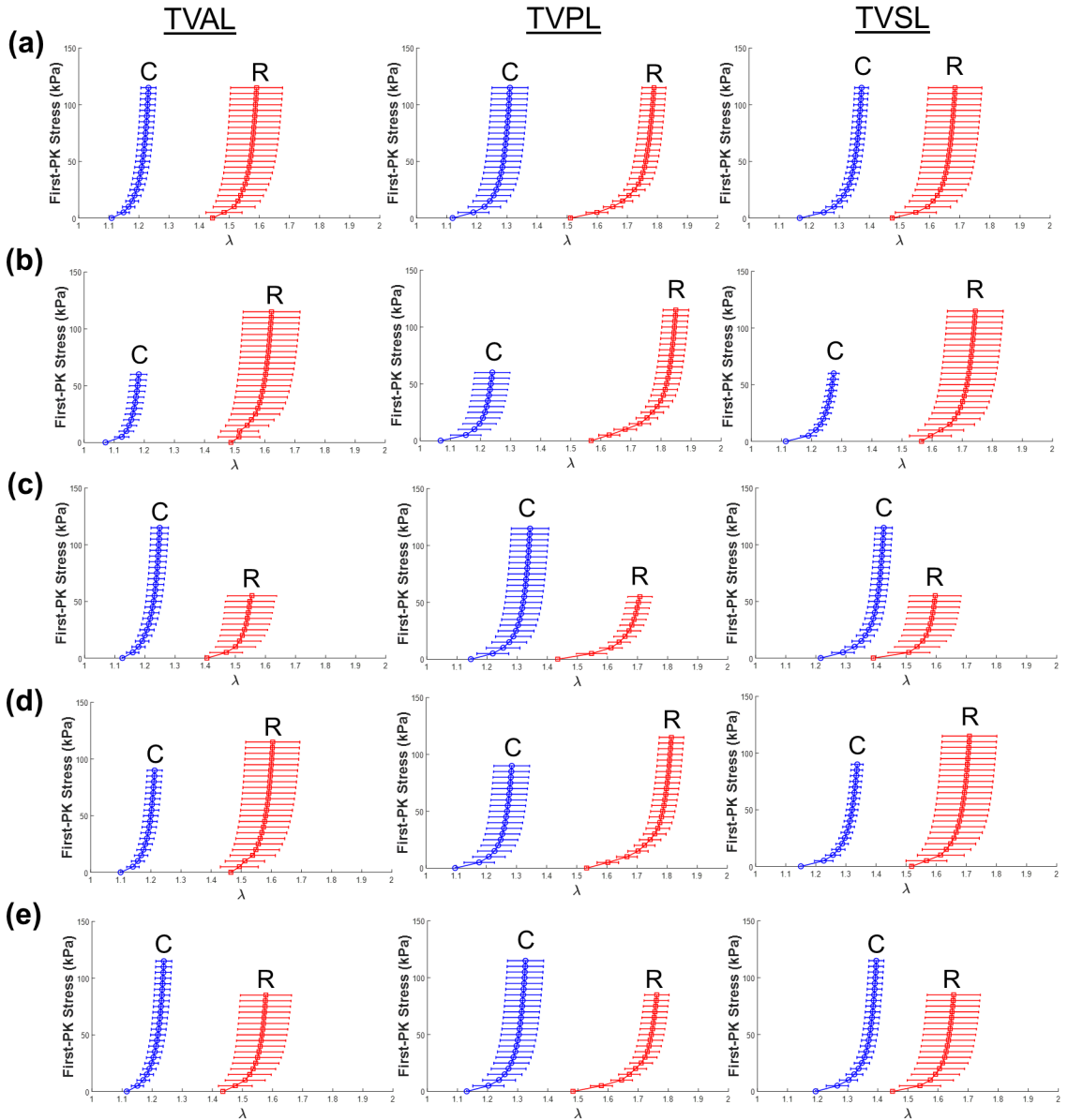


**Figure 3.4.** Mean  $\pm$  SEM of the 1st-PK stress versus stretch results of the porcine TVAL, TVPL, and TVSL tissues ( $n=6$ ) at room temperature ( $22^{\circ}\text{C}$ ) under (a) equibiaxial tension ( $T_{C,\max}:T_{R,\max} = 1:1$ ), (b)  $T_{C,\max}:T_{R,\max} = 0.5:1$ , (c)  $T_{C,\max}:T_{R,\max} = 1:0.5$ , (d)  $T_{C,\max}:T_{R,\max} = 0.75:1$ , and (e)  $T_{C,\max}:T_{R,\max} = 1:0.75$ .

Through the statistical analysis, it was found that both the MV and TV leaflets exhibited anisotropic material behavior with the peak stretches smaller in the circumferential direction than in the radial direction ( $p<0.012$  for all leaflets, cf. Figure 3.3a and Figure 3.4a). Our results also revealed some statistically significant differences in the mechanical responses of the AHV leaflets. Specifically, the MVPL and TVAL were stiffer in the circumferential direction than the TVSL ( $p=0.050$ ), and the TVPL was more compliant in the radial direction than the MVAL ( $p=0.024$ ).

### **3.3.2 Loading-rate effect on the biaxial mechanical properties**

Representative results of our loading rate effect group from the equibiaxial loading protocol ( $T_{C,\max}:T_{R,\max} = 1:1$ ) for all MV and TV leaflets are presented in Figure 3.5. Representative results from the same group under other loading protocols  $T_{C,\max}:T_{R,\max} = 0.5:1$  and  $1:0.5$  are shown in Figure 3.6 and Figure 3.7, respectively. Statistical analysis results of the circumferential and radial stretches of each AHV leaflet in response to varied loading rates are included in **Appendix B**.

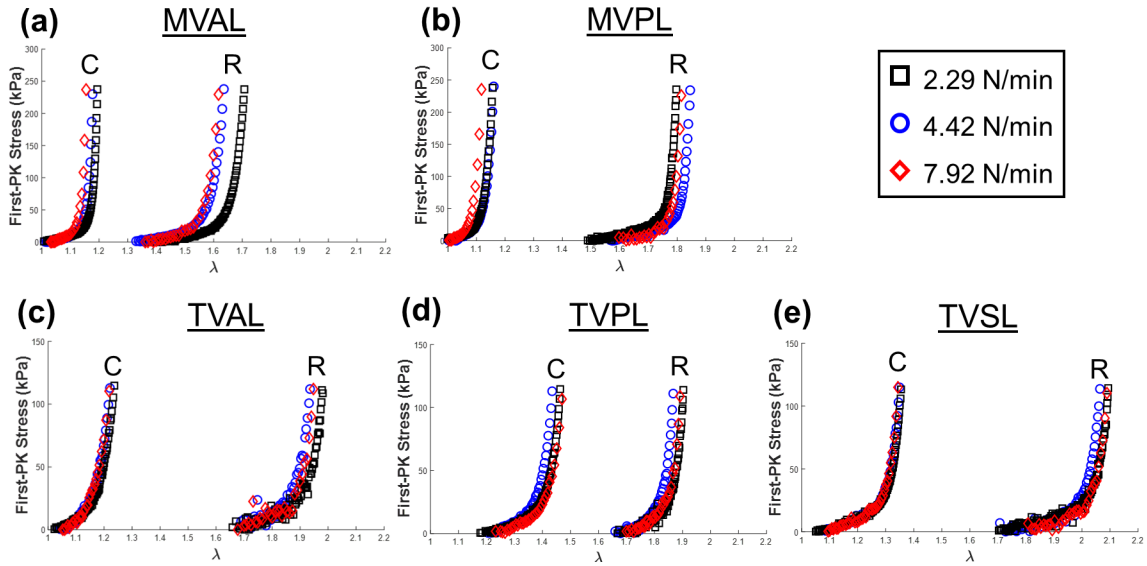


**Figure 3.5.** Representative biaxial mechanical testing results of each porcine atrioventricular leaflet under equibiaxial tension ( $T_{C,\max}:T_{R,\max} = 1:1$ ) at room temperature (22 °C), showing the effect of varied loading rates on the quantified 1st-PK stress versus stretch relationship: (a) MVAL, (b) MVPL, (c) TVAL, (d) TVPL, and (e) TVSL.

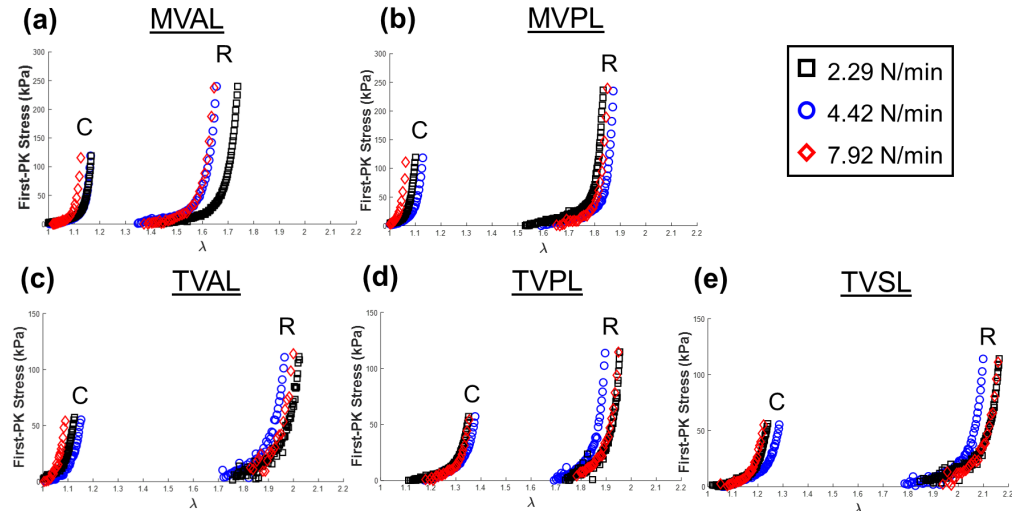


**Figure 3.6.** Representative biaxial mechanical testing results of each porcine atrioventricular leaflet under  $T_{C,\max}:T_{R,\max} = 0.5:1$  at room temperature (22 °C), showing the effect of varied loading rates on the quantified 1st-PK stress versus stretch relationship: (a) MVAL, (b) MVPL, (c) TVAL, (d) TVPL, and (e) TVSL.

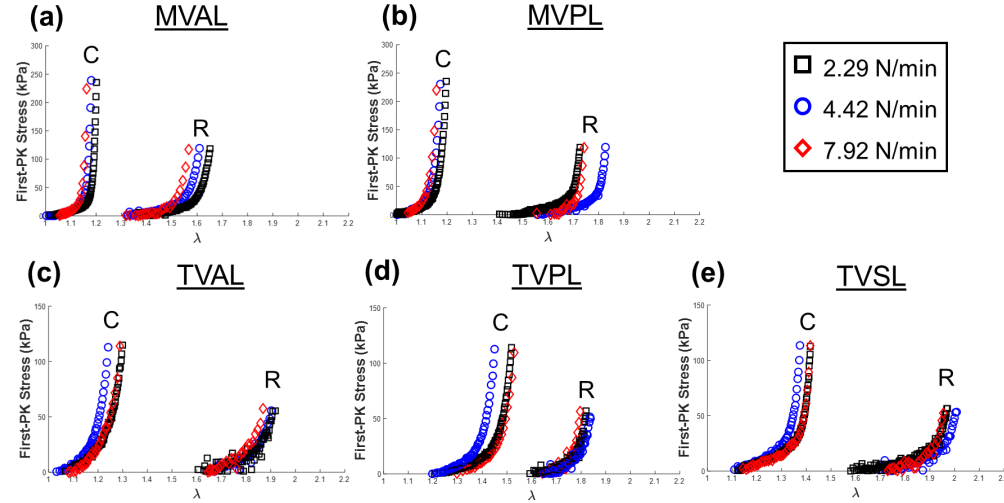


**Figure 3.7.** Representative biaxial mechanical testing results of each porcine atrioventricular leaflet under  $T_{C,\max}:T_{R,\max} = 1:0.5$  at room temperature ( $22^\circ\text{C}$ ), showing the effect of varied loading rates on the quantified 1st-PK stress versus stretch relationship: (a) MVAL, (b) MVPL, (c) TVAL, (d) TVPL, and (e) TVSL.

Three observations could be drawn from the statistical analysis results: (1) the preconditioning stretches increase as the loading rate increases in both the circumferential and radial directions; (2) the mechanical stretches decrease as the loading rate increases in both directions; (3) as the loading rate increases, the peak stretch in the circumferential direction decreases while the peak stretch in the radial direction. The observed trends were not statistically significant but were generally persistent across all the MV and TV leaflets.

### 3.3.3 Temperature effect on the biaxial mechanical properties

The mechanical responses under the equibiaxial tension protocol with varied temperature levels were presented in Figure 3.8 for the representative MV and TV leaflets. Similarly, the representative results associated with other loading protocols ( $T_{C,\max}:T_{R,\max} = 0.5:1$  and  $1:0.5$ ) are shown in Figure 3.9 and Figure 3.10, respectively. The corresponding statistical

analysis results of the circumferential and radial direction stretches of each AHV leaflet at varied testing temperatures are included in **Appendix B**. No statistically significant results were found; however, a general increase in extensibility with increased testing temperature was observed. Additionally, three observations were drawn from the analysis of the temperature effect results: (1) an increase in temperature led to the decrease in the circumferential preconditioning stretch but an increase in the radial preconditioning stretch; (2) the mechanical stretches had no noticeable or statistically significant correlation to the increase in temperature in both the circumferential and radial directions; (3) through comparison of the peak stretches, we found that an increase in the temperature corresponded to a decrease in the circumferential peak stretch but an increase in the radial peak stretch. These trends were generally consistent across all the MV and TV leaflets, but not prevalent enough to attain statistical significance.

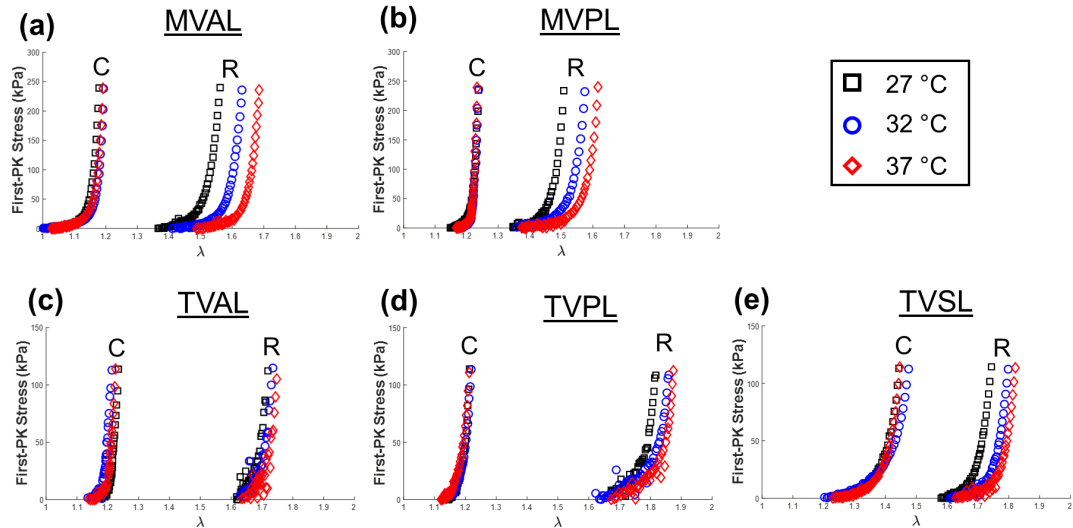


**Figure 3.8.** Representative biaxial mechanical testing results of each porcine atrioventricular leaflet under  $T_{C,\max}:T_{R,\max} = 1:1$ , showing the effect of temperature on the quantified 1st-PK stress versus stretch relationship: (a) MVAL, (b) MVPL, (c) TVAL, (d) TVPL, and (e) TVSL.

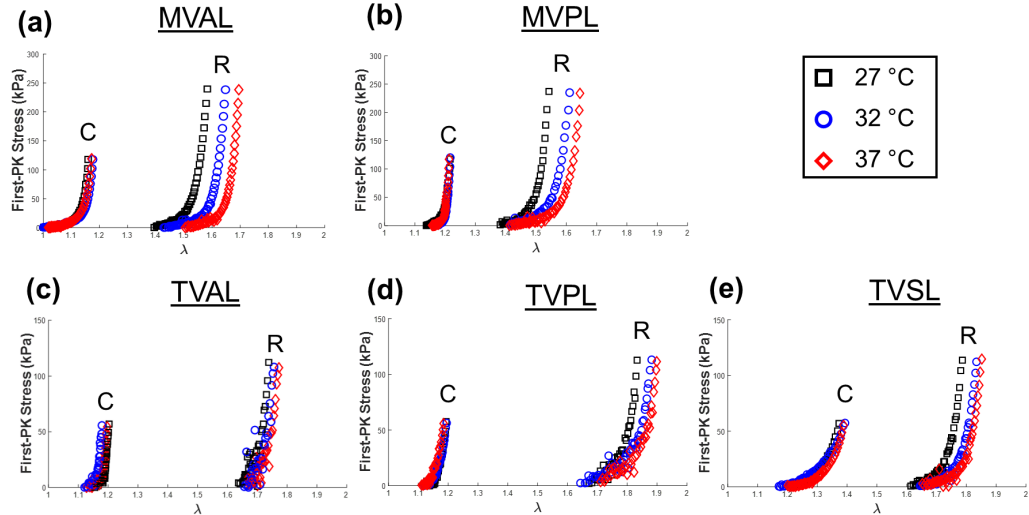


**Figure 3.9.** Representative biaxial mechanical testing results of each porcine atrioventricular leaflet under  $T_{C,\max}:T_{R,\max} = 0.5:1$ , showing the effect of temperature on the quantified 1st-PK stress versus stretch relationship: (a) MVAL, (b) MVPL, (c) TVAL, (d) TVPL, and (e) TVSL.

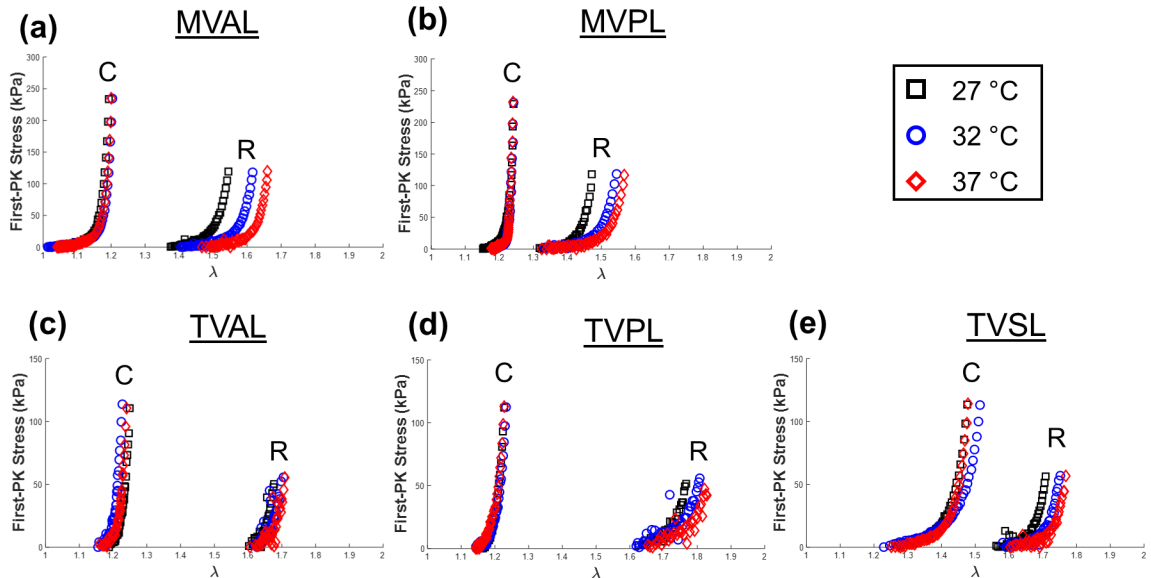


**Figure 3.10.** Representative biaxial mechanical testing results of each porcine atrioventricular leaflet under  $T_{C,\max}:T_{R,\max} = 1:0.5$ , showing the effect of temperature on the quantified 1st-PK stress versus stretch relationship: (a) MVAL, (b) MVPL, (c) TVAL, (d) TVPL, and (e) TVSL.

### 3.3.4 Comparison of the mechanical responses between species

The averaged mechanical responses ( $n=6$ ) for the MVAL and TVAL under equibiaxial loading from porcine, adult ovine, and juvenile ovine hearts are presented in Figure 3.11, respectively. Further information about the statistical comparisons of the peak stretches, preconditioning stretches, and the mechanical stretches between any two of these species is presented in **Appendix B**.

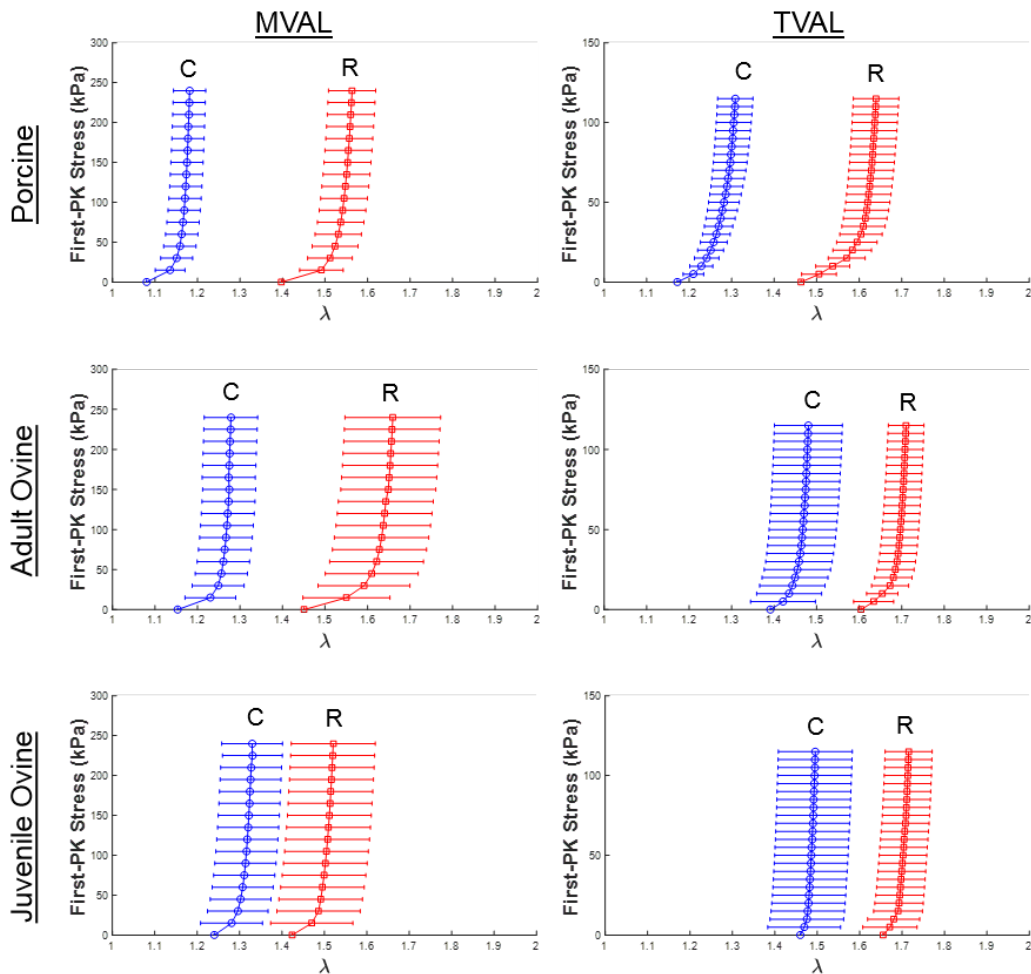


**Figure 3.11.** Comparisons of the biaxial mechanical responses of representative atrioventricular valve leaflet tissues under  $T_{C,\max}:T_{R,\max} = 1:1$  at 37 °C between different species and ages (adult porcine, adult ovine/sheep, and juvenile ovine/lamb).

The cross-species (porcine versus ovine) and within-species (juvenile ovine versus adult ovine) observed behaviors were specific to MVAL or TVAL and did not support conclusions across leaflets. Through interpreting the statistical analysis results, we found three leaflet-specific relations: (1) the preconditioning stretches were lower for the porcine TVAL than the adult ovine TVAL in both the circumferential ( $p=0.028$ ) and radial directions ( $p=0.057$ ); (2) the mechanical stretches were notably lower for the juvenile ovine MVAL than the adult ovine MVAL in the radial direction ( $p=0.052$ ) but showed no consistent trends in the circumferential direction ( $p=0.614$ ); (3) In the MVAL, the peak stretch was lower for the porcine tissue than the juvenile ovine tissue in the circumferential direction but higher in the radial direction. The results also showed the more isotropic behavior of the juvenile ovine leaflets compared to the porcine and adult ovine tissues (Fig. 3.11).

### **3.3.5 Anatomical quantification of the valve apparatus**

The measurements of the anatomical and structural features of porcine and adult ovine atrioventricular valves are shown in Table 3.2. It was found that the porcine MVAL was significantly thicker than each porcine TV leaflet ( $p<0.040$ ), and the porcine MVPL was thicker than the porcine TVPL and TVSL ( $p<0.006$ ). The similarity in the length of the chordae anchoring porcine and ovine valve leaflets was also observed, as reflected in the MVAL where chordae anchoring porcine leaflets had a length  $17.5 \pm 1.32$  mm, while those anchoring the ovine leaflet had a comparable length of  $17.9 \pm 1.12$  mm (Table 3.2). Conversely, we found that the porcine MV and TV had more chordae than the ovine MV and TV ( $p<0.001$  and  $p=0.002$ , respectively). These similarities in chordae lengths and significant differences in chordae quantities are explored further in *Section 3.4.6*.

**Table 3.2.** Anatomical measurements for chordae and leaflet tissues of both porcine and ovine atrioventricular heart valves (n=6, each valve leaflet). All quantities are reported as mean  $\pm$  SEM.

Anatomical Measurements		Mitral Valve		Tricuspid Valve		
		MVAL	MVPL	TVAL	TVPL	TVSL
Porcine	<b>Leaflet Thickness (mm)</b>	0.79 $\pm$ 0.10	0.70 $\pm$ 0.06	0.52 $\pm$ 0.06	0.46 $\pm$ 0.04	0.37 $\pm$ 0.02
	<b>Number of Chordae</b>	10.0 $\pm$ 0.50	20.5 $\pm$ 1.20	11.2 $\pm$ 1.30	11.8 $\pm$ 1.00	12.3 $\pm$ 1.80
	<b>Chordae Length (mm)</b>	17.5 $\pm$ 1.32	14.1 $\pm$ 0.70	10.8 $\pm$ 0.80	11.3 $\pm$ 1.30	11.3 $\pm$ 0.77
Adult Ovine	<b>Leaflet Thickness (mm)</b>	0.40 $\pm$ 0.03	0.36 $\pm$ 0.02	0.28 $\pm$ 0.03	0.26 $\pm$ 0.02	0.27 $\pm$ 0.03
	<b>Number of Chordae</b>	4.7 $\pm$ 0.50	10.2 $\pm$ 0.80	6.8 $\pm$ 0.50	8.2 $\pm$ 0.50	8.7 $\pm$ 0.90
	<b>Chordae Length (mm)</b>	17.9 $\pm$ 1.12	14.8 $\pm$ 0.59	10.5 $\pm$ 0.79	10.9 $\pm$ 0.82	12.1 $\pm$ 0.83

### 3.3.6 Histological analysis

The Masson's trichrome-stained MV and TV leaflets from a representative porcine heart are shown in Figure 3.12. The average thickness obtained from the histology images of each leaflet are presented in Table 3.3.

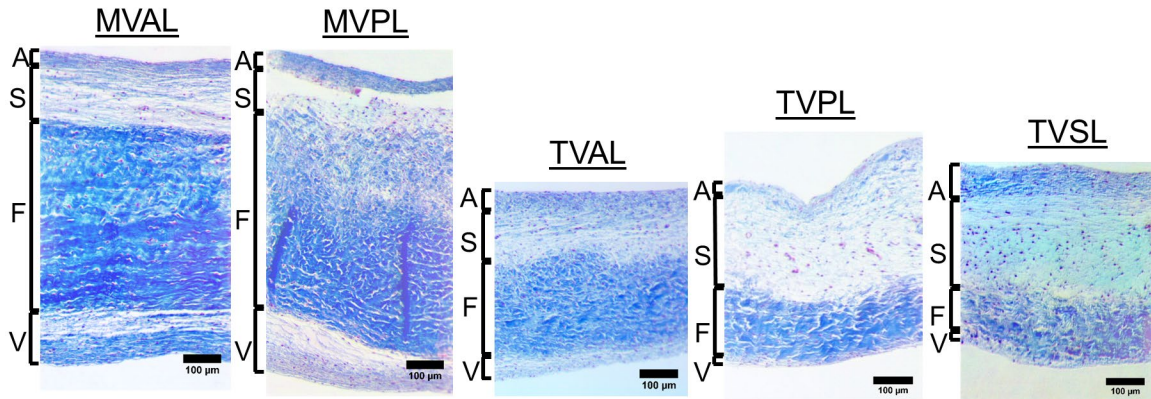


**Figure 3.12.** Histological sections of all the MV and TV leaflets (MVAL, MVPL, TVAL, TVPL, and TVSL) stained with Masson's trichrome. Four morphologically distinct layers of the leaflets (atrialis: A, spongiosa: S, ventricularis: V, fibrosa: F) were identified.

**Table 3.3.** The thickness and collagen fiber content obtained from the histology sections of porcine MV and TV leaflets. All quantities except for collagen content (generated from image analysis) are reported as mean  $\pm$  SEM with 3 repeated measurements.

		Mitral Valve		Tricuspid Valve		
		MVAL	MVPL	TVAL	TVPL	TVSL
Thickness (μm)	A	43.74 $\pm$ 4.22	54.84 $\pm$ 7.07	54.11 $\pm$ 5.32	50.27 $\pm$ 5.16	74.29 $\pm$ 4.78
	S	135.21 $\pm$ 8.23	99.85 $\pm$ 6.93	108.53 $\pm$ 5.59	221.26 $\pm$ 7.40	260.31 $\pm$ 9.26
	F	477.82 $\pm$ 6.41	556.35 $\pm$ 11.72	250.77 $\pm$ 9.69	154.01 $\pm$ 10.95	149.21 $\pm$ 6.62
	V	121.14 $\pm$ 7.64	141.44 $\pm$ 15.18	35.93 $\pm$ 3.72	20.17 $\pm$ 2.78	20.82 $\pm$ 2.24
	Intact	777.92 $\pm$ 13.46	852.49 $\pm$ 7.00	449.33 $\pm$ 3.63	445.71 $\pm$ 7.51	504.62 $\pm$ 9.55
Collagen Content (%)		77.65	69.13	68.51	45.16	32.30

The MV leaflets were distinctly thicker than the TV leaflets to sustain a higher transvalvular pressure level [100]. The characteristic four layers of the leaflets: ventricularis, spongiosa, fibrosa, and atrialis were histologically distinguishable in all the five leaflets (Fig. 3.12). The fibrosa layer is primarily composed of a dense layer of collagen and comprises ~60% of the total thickness of the MV leaflets. Similarly, the

histology image suggested the fibrosa is the dominant layer of the TVAL. Interestingly, we found the spongiosa, composed of non-fibrous constituents such as GAGs, was the thickest layer in the TVPL and TVSL. The ventricularis layer, facing the ventricle in each atrioventricular leaflet, was twice as thick in the MVAL as the TVAL, whereas it was seven-times thicker in the MVPL than in the TVPL. Histology image-based collagen quantification of the valve leaflets indicated the MVAL and MVPL have 77.7%, and 69.1% collagen fiber contents, respectively, whereas the TVAL and TVPL have 68.5%, 45.2% collagen fiber content, respectively (Table 3.3). Interestingly, we also found the collagen fiber content is lower in the TVSL (~32%) than in other leaflets.

## 3.4 Discussion

### 3.4.1 Baseline testing

Our baseline testing confirmed the previously quantified anisotropic, nonlinear elastic mechanical response of HV leaflets (Figure 3.3 and Figure 3.4), through the presence of a toe portion of the curve (near the low-stress region) and a highly stiff, nearly asymptotic region as the force approached the maximum physiological stress experienced by the leaflets. All leaflets tested were significantly stiffer in the circumferential direction ( $p<0.010$ ). Specifically, the average stretches under equibiaxial loading differed between the circumferential and radial directions by 0.360 for the MVAL, 0.389 for the MVPL, 0.441 for the TVAL, 0.444 for the TVPL, and 0.284 for the TVSL (Table 3.1). In general, the TV leaflets were more compliant than the MV leaflets at their respective physiological loadings in both tissue directions.

In a prior study, planar biaxial testing was performed on porcine MV tissues and stretches of 1.2 and 1.4 were found for the MVAL in the circumferential and radial directions under an equibiaxial loading protocol [45], whereas stretches of  $1.232 \pm 0.154$  and  $1.592 \pm 0.136$  were found in our study for the MVAL in the same directions (Table 3.1). Recent studies have shown that testing parameters, such as the mounting mechanism, the spacing of attachment points and the specimen size, could have an impact on the biaxial mechanical testing results [84]. Such discrepancy between our results and those of Grashow *et al.* (2006), particularly in the radial direction, may be attributed to procedural differences such as different tissue mounting mechanisms (rigid BioRake fixture in our study versus suture hooks in the study by Grashow *et al.* (2006)) and different methods used to estimate and model the maximum *in vivo* loading, i.e., the applied forces computed through measured thickness based on estimated  $P_{max}$  used in our study versus applied forces based on estimated  $T_{max}$  in the study by Grashow *et al.* (2006).

Our observed stretches of the TV leaflets were similar to those reported by Khoiy and Amini (2016) [48]. In their study, the TVPL showed the most anisotropy, with the TVAL and TVSL exhibiting similar, but lower, amounts of mechanical anisotropy. In general, our results agreed with these findings for the TV leaflets. Khoiy and Amini (2016) also found the TVPL was the most compliant leaflet in the radial direction. Our study agreed with their finding, with the observed radial peak stretches of  $1.651 \pm 0.089$  for the TVAL,  $1.788 \pm 0.040$  for the TVPL, and  $1.685 \pm 0.089$  for the TVSL (Table 3.1). Importantly, both studies found the same anisotropic and nonlinear mechanical behaviors of the TV leaflets.

### **3.4.2 Effects of various loading rates on the mechanical responses**

An interesting result of the loading rate testing group is the decrease in mechanical stretch of the tissue in both directions with an increased loading rate. These results support the viscoelastic nature of heart valve leaflets [101], and agree with the time-dependent stress relaxation as observed in leaflet tissues [42]. However, our results prove contrary to those of a prior study by Grashow *et al.* (2006), where a variety of loading rates were examined and no *significant* dependence of mechanical properties on loading rate was observed [45]. One possible reason for this discrepancy is Grashow *et al.* (2006) examined the peak stretch of the tissue, while we examined the decomposed components of the peak stretch. As for the MVAL, we observed minor differences in the peak stretch between the loading rates of 2.29 N/min and 7.92 N/min in the circumferential direction ( $p=0.844$ ) and radial direction ( $p=0.614$ ). Based on these peak stretches, it is reasonable to conclude that there was no significant viscoelastic effect. However, by decomposing the peak stretch and examining the mechanical stretch, the statistical comparisons showed the tissue is stiffer under the loading rate of 7.92 N/min than the rate of 2.29 N/min in both the circumferential direction ( $p=0.334$ ) and the radial direction ( $p=0.077$ ). These comparisons of mechanical stretches could shed light on the tissue's native response to varied loading rates, as decoupled from the preconditioning effect.

### **3.4.3 Effects of temperature on the mechanical responses**

In the result of temperature group, we found distinct trends between the circumferential direction and the radial direction. Specifically, it was found that the preconditioning and peak stretches decreased in the circumferential direction but increased in the radial

direction with increased temperature. A general lack of temperature dependence in the mechanical stretches ( $\lambda_C^{1-peak}$  and  $\lambda_R^{1-peak}$ ) of the atrioventricular valve leaflet tissues was also observed, which illustrated how the temperature dependence observed in the peak stretches was primarily an indicator of similar temperature effects in the preconditioning stretches. These findings are potentially useful for informing protocols where maintenance of valve tissue at body temperature would not be feasible. In such experiments, we expect valve tissue's mechanical response would be relatively unimpacted by the non-physiological temperature.

#### **3.4.4 Motivation for porcine-ovine HV comparison**

Both porcine and ovine hearts are commonly employed in animal studies as analogous to human hearts [102]. A proper comparison between human and ovine or porcine hearts first requires an intimate understanding of the mechanics and anatomy of the non-sapiens heart. To that end, the biaxial mechanical responses of porcine, adult ovine, and juvenile ovine atrioventricular leaflet tissues were compared (Fig. 3.11), and the specific anatomical features of the MV and TV from both porcine and ovine hearts were examined (Table 3.2).

#### **3.4.5 Comparisons of the mechanical responses between species**

The mechanical responses of the MVAL and TVAL of the porcine, adult ovine, and juvenile ovine heart were examined (Fig. 3.11) to capture the distinct tissue response between different species and between the juvenile and adult ovine animals.

In this study group, it was found that the preconditioning stretches were lower for the porcine HVs than the ovine valves, and the mechanical stretches of the porcine heart were

generally higher than the mechanical stretches of the ovine hearts, particularly in the TVAL (Fig. 3.11). It was also observed that the peak stretches for the adult ovine TVAL were higher than those of the porcine TVAL in both the circumferential direction ( $p=0.090$ ) and the radial direction ( $p=0.180$ ). These differences between the porcine and ovine MV and TV imply the necessity to consider the mechanics of the specific analogous heart valve in computational models, rather than assuming similar properties based on similar function.

With regards to within-species examinations, it was found that the juvenile ovine MVAL behaved in a more isotropic manner compared to the adult ovine heart, whereas the TVAL showed little stretch response differences between the adult and juvenile ovine hearts (Fig. 3.11). In addition, some discrepancy between the juvenile and adult ovine MVAL mechanical responses and similarity between the juvenile and adult ovine TVAL mechanical responses were observed. These findings suggest possible differences in the development rates between the MV and TV, and motivate further examinations of HV growth and remodeling over the organism maturation period [103].

### **3.4.6 Comparisons of anatomy and microstructure between species**

Our anatomical comparison allowed a glimpse into the differences and similarities between valvular structures of different species (Table 3.2). Substantial differences in leaflet thickness between the porcine and ovine valve was observed, with the porcine MVAL thickness of  $0.79 \pm 0.10$  mm and the ovine MVAL thickness of  $0.40 \pm 0.03$  mm, but similar average chordae lengths between the porcine and ovine valves (Table 3.2). These leaflet thicknesses are interpreted as proportional to the valvular capacity to bear pressure load, assuming healthy valve tissue. As such, it is intriguing that the MVs of the different species

exhibit such similar chordae lengths, despite the apparent difference in load-bearing capacity/necessity [100]. In addition, it was found that the chordae quantity generally correlated with the leaflet thickness. For example, the porcine TVAL possessed  $11.2 \pm 1.30$  anchoring chordae to support a leaflet of thickness  $0.52 \pm 0.06$  mm, while the ovine TVAL had only  $6.8 \pm 0.50$  anchoring chordae to support a leaflet of thickness  $0.28 \pm 0.05$  mm. This relationship could provide insight into the growth and development process of chordae tendineae in the atrioventricular heart valves.

To examine the chordae quantities within human heart valves, Lam *et al.* (1970) and Silver *et al.* (1971) conducted anatomical studies on the human MV and TV, respectively [17, 18]. They found human hearts have, on average, 25 chordae in both the mitral and tricuspid valves. Our study revealed average chordae quantities of  $30.5 \pm 1.7$  and  $35.3 \pm 2.8$  chords for porcine mitral and tricuspid valves, respectively, and  $14.9 \pm 1.3$  and  $23.7 \pm 1.9$  chords for the adult ovine mitral and tricuspid valves, respectively. These differences in chordae quantities between species suggest unique valvular density and distribution of chordae tendineae within human, porcine, and ovine atrioventricular valves. The error presented in the chordae quantities also alludes to the differences in physiological structures across specimens, and the inability to determine a precise expected value for the chordae quantity within a healthy valve.

#### **3.4.7 Discussion of the histological results**

Valve leaflets are composed of collagen, elastin, GAGs, and PGs. The corresponding nonlinear anisotropic mechanical response of the valve leaflets is mainly determined by these constituents in the ECM. Studying the microstructural organization of leaflets is

crucial to understanding the physiological functions of the leaflets. In this study, we investigated the distinct thicknesses of the individual leaflet layers, as well as the collagen composition in the MV and TV leaflets based on quantitative histology analyses. The intact layer thickness measured from the histological images (Table 3.3) was in the same range as the thickness obtained from anatomical measurements (Table 3.2). The histological measurements allowed us to precisely quantify the discrepancies in the thickness of intact and individual layers of the MV and TV leaflets (Table 3.3). The measurements also showed the MV leaflets have relatively thicker collagen-rich fibrosa and ventricularis layers compared to TV leaflets (Fig. 3.12). The atrialis layer, which is facing the atrium in each leaflet, occupies  $6.42 \pm 1.36\%$  of the total thickness of the MVPL and  $11.32 \pm 2.31\%$  of the total thickness of the TVPL (Table 3.3). Although both atrioventricular valves are located in between the atrium and the ventricle, their respective leaflets are subjected to distinct hemodynamic loading conditions and transvalvular pressure gradients. Such functional discrepancies lead to the difference in the microstructural organization of the MV and TV leaflets as observed in this study. In addition, the high collagen fiber content and the collagen-rich fibrosa layer in the MV leaflets may serve as a primary load bearing layer to sustain higher pressures during cardiac cycles compared to the TV counterparts.

### **3.4.8 Study limitations**

Biaxial testing methods are notoriously limited in their ability to capture and account for in-plane shear stresses [39]. In our study, planar shear stresses were found to be negligible compared to their direct stress counterparts, and so were not included in the results. This is standard practice in biaxial testing experiments [104]. In addition, we encountered difficulty in determining an average sample thickness due to the roughness and non-

uniformity of the HV leaflets, particularly in regions with chordae attachments [105]. To address this obstacle, three thickness measurements from different regions of the testing sample were averaged. Still, the measurement of tissue thickness with calipers can result in lower than expected values due to tissue compressibility. A more optimal thickness measurement approach could employ optical coherence tomography (OCT) or a similar non-contact method to provide a more robust measurement. Another potential limitation of our study was the use of frozen tissues. Although this is a standard practice in biaxial mechanical testing experiments [42, 45], the effect of freezing on the mechanics of HV tissues has not been rigorously studied. Within the biaxial mechanical testing process, other factors such as the load cell resolution, the force-control algorithm, and the tissue interaction with the PBS solution can cause scattering in the observed sample mechanical responses. We saw this scatter in the low-loading regime for the tricuspid tissues, especially for the representative effect study results (e.g., Figs. 3.5-3.10(c,d,e) for TV leaflets). In addition to these experimental limitations, the natural variance in biological material property and structure led to substantial discrepancies in biaxial testing and anatomical study results. This challenge persists across many biological domains and leads to larger errors in experimental results compared to other fields.

### **3.4.9 Concluding remarks**

In this Chapter, the response of each porcine atrioventricular leaflet has been thoroughly characterized. Our comprehensive results suggest the porcine MVAL and MVPL exhibit similar levels of material anisotropy, and the porcine TVPL is the most compliant in both the circumferential and radial directions and the most anisotropic among the three tricuspid leaflets. These findings also suggest the necessity of employing different constitutive

model parameters to describe the distinct mechanical behavior of each individual atrioventricular valve leaflet, rather than assuming homogeneous mechanical properties between leaflets. Moreover, we have demonstrated an increased loading rate is associated with a stiffer mechanical response, and increased temperature yields directionally-specific differences in the tissue stretches. A novel quantification of the distinct mechanical responses of porcine and ovine leaflets was also provided, along with the quantification of the difference in leaflet mechanical response between different species and between juvenile and adult ovine animals. The work presented in this Chapter is also *the first of its kind* to examine the anatomic chordae distributions within porcine and ovine atrioventricular valves to quantify the structural differences between MV and TV.

## CHAPTER 4. SPATIAL VARIATION IN THE MECHANICAL PROPERTIES OF THE MVAL AND TVAL TISSUES

### 4.1 Region-Specific AHV Tissue Mechanics

With recent advances in computer power and numerical methods, it becomes possible for computational models to provide key insights into the behaviors and function of the atrioventricular HVs. It is expected that predictive computer simulations could be employed in determining possible failure mechanisms of current treatments and in supplementing patient-specific surgery planning. Current computational models incorporate valvular tissue material properties primarily based upon experimental data of the bulk tissue-level mechanical properties [42, 45, 106-108]. Although the heterogeneity of the HV microstructure has been qualitatively examined via organ-level computational studies [7, 109, 110], no existing efforts have attempted to characterize how this collagen network contributes to spatially-varied tissue mechanics. Therefore, most existing computational models assumed spatially homogeneous material properties, which may not accurately represent the leaflet tissues. Hence, there is a critical need to investigate the spatial variance in the MV and TV mechanical properties for enhancing existing computational models.

The goal of this research is to address this need through novel characterizations of the regional mechanical properties and stress relaxation behaviors of both the MV and TV leaflets. Specifically, the anterior leaflets (MVAL and TVAL) were selected to represent each atrioventricular valve based on their anisotropic, highly-nonlinear nature [45, 48, 111]. Mechanical testing with various biaxial mechanical loading and stress relaxation

protocols was conducted for each of the six tissue regions of the MVAL and TVAL to examine the regional variance/similarity in the tissue's mechanical properties.

## 4.2 Methods

### 4.2.1 Tissue acquisition & sectioning

Healthy, adult porcine hearts (80-140 kg, 1-1.5 years of age) were obtained from a local USDA approved slaughterhouse (Country Home Meat Co., Edmond, OK). Hearts were obtained on the same day of excision from the animal, promptly cleaned of clots, and placed in a freezer at -14 °C. This freezing-based storage procedure was adopted according to previous studies, which demonstrated a minimal effect of freezing on the mechanical properties of collagenous tissues [88-90]. For dissection, hearts were thawed and the MV and TV anterior leaflets were excised (Fig. 4.1a-b). Next, the leaflets were laid flat and further sectioned into six regions of a 6 x 6 mm dimension (Fig. 4.1c): regions B and E are denoted as the *central regions*, whereas regions A, C, D, and F are classified as the *edge regions*. The sectioned tissue samples were then stored in PBS solution and refrigerated in a 4 °C environment for testing within two days of dissection.

### 4.2.2 Tissue sample preparation

At the time of testing, the sectioned tissues' thicknesses were recorded at three locations using digital calipers (Westward 1AAU4) and averaged. The specimens were then mounted, using BioRakes to facilitate an effective loaded region of 4 x 4 mm, onto a commercial biaxial mechanical testing system (BioTester–CellScale, Canada) equipped with 1500 mN load cells (Fig. 4.1d). The circumferential and radial tissue directions were aligned with the testing system's x- and y-directions (Fig. 4.1e).

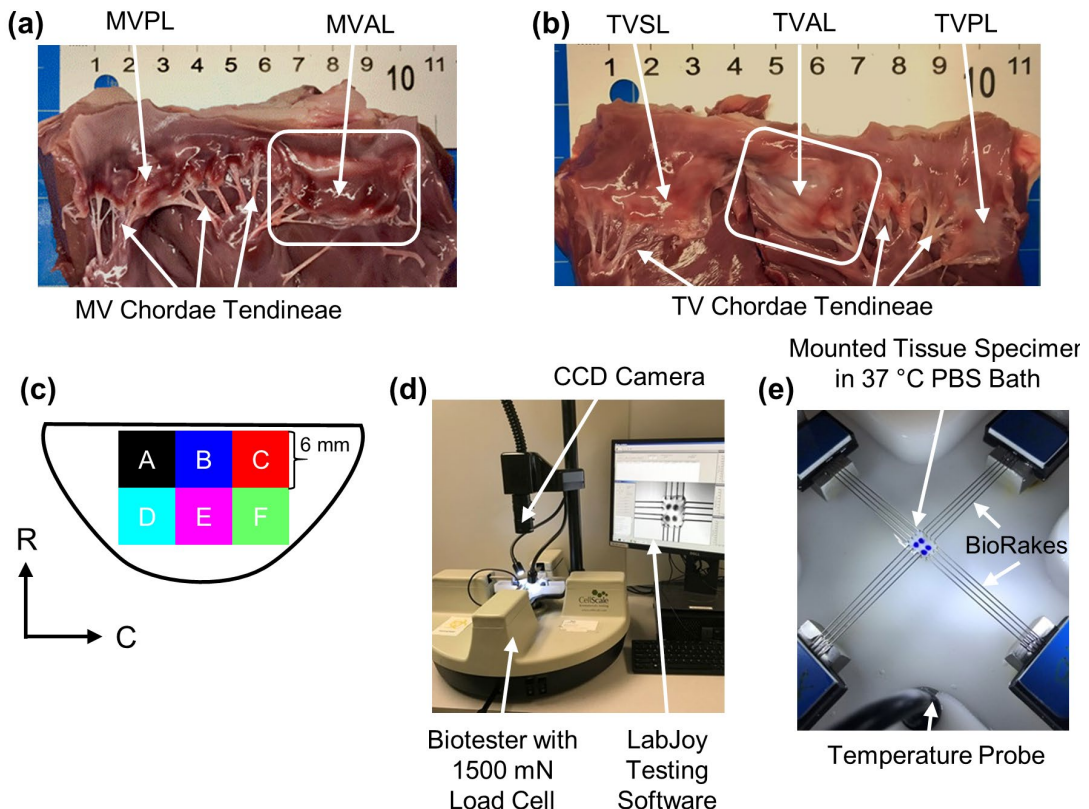


**Figure 4.1.** Dissected porcine hearts showing (a) the MV and (b) the TV with the anterior leaflet highlighted for both atrioventricular HVs. (c) Schematic of a valve anterior leaflet with the six tested regions. Experimental images of (d) the biaxial mechanical tester (BioTester) used in this study and (e) a mounted tissue sample with labelled components of the biaxial mechanical testing system.

Four fiducial markers were placed in an array via a surgical pen on the central region of the tissue for optical tracking-based strain calculations (cf. *Sections 3.2.4, 4.2.4*). The tissue was submerged in a 37 °C PBS bath to emulate the valve’s physiological conditions.

#### 4.2.3 Biaxial mechanical testing

Following the experimental procedure developed in our previous study [111], biaxial mechanical testing was performed to investigate the differences and similarities in the

mechanical responses of the MVAL and TVAL tissue regions. In brief, the maximum applied membrane tension in the C and R-directions ( $T_{C,\max}$  and  $T_{R,\max}$ ) of 100 N/m and 50 N/m were used for the MVAL and TVAL, respectively [48, 92]. A two-step force-controlled biaxial testing procedure was used to characterize the mechanical behavior of the MVAL and TVAL tissue regions. First, a preconditioning protocol was used to restore the valve leaflet tissue to its *in vivo* configuration, in which  $T_{C,\max}$  and  $T_{R,\max}$  were applied in each direction at a rate of 2.29 N/min for 8 repeated loading/unloading cycles with a preload as 2.5% of  $T_{C,\max}$  and  $T_{R,\max}$ . Next, five varying loading ratios ( $T_{C,\max} : T_{R,\max} = 1:1$ , 0.75:1, 1:0.75, 0.5:1, and 1:0.5) with 8 loading/unloading cycles were employed to investigate all possible physiological tissue deformations. Throughout the test, the BioRake separation distance and force were continuously recorded, and a series of 1280 x 960 pixel images were collected at 15 Hz using a high-resolution CCD camera. Data from the unloading portion of the last cycle of each loading protocol were used in the tissue stress and strain analyses as described in the next subsection, and in the results presented in *Section 4.3*. In addition, a biaxial stress-relaxation test was employed to observe the regional variance in the stress decaying response. For this testing, tissue specimens were loaded to  $T_{C,\max}$  and  $T_{R,\max}$  using the maximum displacements recorded previously. Then, the specimens were held to relax over 15 minutes. The force readings were retrieved at a rate of 5 Hz for the subsequent stress reduction analysis. Although 3-hour stress relaxation experiments have been previously adopted for the semilunar valve leaflets by Huang *et al.* (2015) [112] and the MV leaflets by Sacks *et al.* (2004, 2006) [44, 108], the majority of stress reduction occurs within the first 800 seconds. Hence, the 15-minute stress-relaxation

period was chosen as sufficient to observe noticeable differences in the relaxation behaviors between the regions of both the MVAL and TVAL tissues.

#### 4.2.4 Tissue strain & stress calculations

These tissue optical strain-tracking procedures follow the practices discussed in our previous manuscript, allowing for the computation of the deformation gradient,  $\mathbf{F}$  (cf. *Section 3.2.4*) [111]. The stretches in each direction were then computed by taking the square roots of the principle values of the right Cauchy deformation tensor,  $\mathbf{C} = \mathbf{F}^T \mathbf{F}$ , and the membrane tension was then computed by

$$\begin{bmatrix} T_C & 0 \\ 0 & T_R \end{bmatrix} = \frac{1}{L} \begin{bmatrix} F_C & 0 \\ 0 & F_R \end{bmatrix}, \quad (4.1)$$

where  $F_C$  and  $F_R$  are the recorded force in the C and R-direction, respectively, and  $L$  is the effective edge length. Various stress measures can be readily computed using the membrane tension values and the associated specimen's thickness:  $\mathbf{P} = \text{diag}([\mathbf{P}_{CC}, \mathbf{P}_{RR}]) = (1/t_s) \cdot \text{diag}([T_C, T_R])$ ,  $\mathbf{S} = \mathbf{F}^{-1} \mathbf{P}$ , and  $\boldsymbol{\sigma} = J^{-1} \mathbf{P} \mathbf{F}^T$  [113, 114], for making comparisons with results in other studies. Here,  $\mathbf{P}$  is the 1<sup>st</sup>-PK stress tensor,  $\mathbf{S}$  is the 2<sup>nd</sup>-PK stress tensor,  $\boldsymbol{\sigma}$  is the Cauchy stress tensor, and  $J = \det(\mathbf{F})$  is the Jacobian of  $\mathbf{F}$ . Finally, an anisotropy index ( $AI$ ), defined as the ratio of the peak stretch in the radial direction to the circumferential stretch, i.e.,  $AI = \lambda_R^{0\text{-peak}} / \lambda_C^{0\text{-peak}}$ , was used quantitatively compare regional anisotropy.

For analyses of the decaying stress responses from stress relaxation testing, force readings were converted to membrane tensions. The reported membrane tension values were

normalized by the peak values with respect to each direction for evaluating the percent relaxation over the 15-minute duration.

#### 4.2.5 Statistical analysis

For quantitative comparisons, the *peak tissue stretches* ( $\lambda_C^{0-peak}$  and  $\lambda_R^{0-peak}$ ) obtained from the mechanical testing results were further broken into two parts as described in our previous work [111]: *(i)* the *preconditioning stretches* ( $\lambda_C^{0-1}$  and  $\lambda_R^{0-1}$ ), which are defined as the tissue deformations due to the preconditioning effect, and *(ii)* the *mechanical stretches* ( $\lambda_C^{1-peak}$  and  $\lambda_R^{1-peak}$ ) which denote the tissue deformations in response to mechanical loading with respect to the post-preconditioning configuration. These decomposed stretch measures, along with the *AI* derived from the peak stretches, were compared between regions A-F using the standard one-way ANOVA. A *p*-value <0.05 was considered as statistically significant and a *p*-value <0.10 as nearly significant.

### 4.3 Results

#### 4.3.1 Thickness of leaflet regions

The measured thickness was generally consistent for the six regions with maximum variations of 0.106 mm for the MVAL and 0.104 mm for the TVAL. Thickness measurements for the MVAL were:  $0.633 \pm 0.033$  mm (region A),  $0.600 \pm 0.045$  mm (region B),  $0.657 \pm 0.041$  mm (region C),  $0.554 \pm 0.039$  mm (region D),  $0.551 \pm 0.045$  mm (region E), and  $0.584 \pm 0.061$  mm (region F). As for the TVAL, thicknesses were:  $0.309 \pm 0.028$  mm (region A),  $0.287 \pm 0.038$  mm (region B),  $0.378 \pm 0.032$  mm (region C),  $0.301 \pm 0.039$  mm (region D),  $0.368 \pm 0.048$  mm (region E), and  $0.391 \pm 0.041$  mm (region F).

### 4.3.2 Biaxial mechanical testing

Biaxial mechanical testing provided insight into the variance in stretch across the MVAL and TVAL tissue regions. Equibiaxial testing results ( $T_{C,\max} : T_{R,\max} = 1:1$ ) for the MVAL and TVAL total tissue stretch are reported in Figure 4.2 and Figure 4.3. Quantitative comparisons of the anisotropy index are summarized in Figure 4.4, while comparisons of the preconditioning and mechanical stretches are summarized in Figure 4.5 and Figure 4.6, respectively. Compiled quantitative mechanics metrics for the MVAL regions are shown in Table 4.1, and similar results for the TVAL regions are shown in Table 4.2.

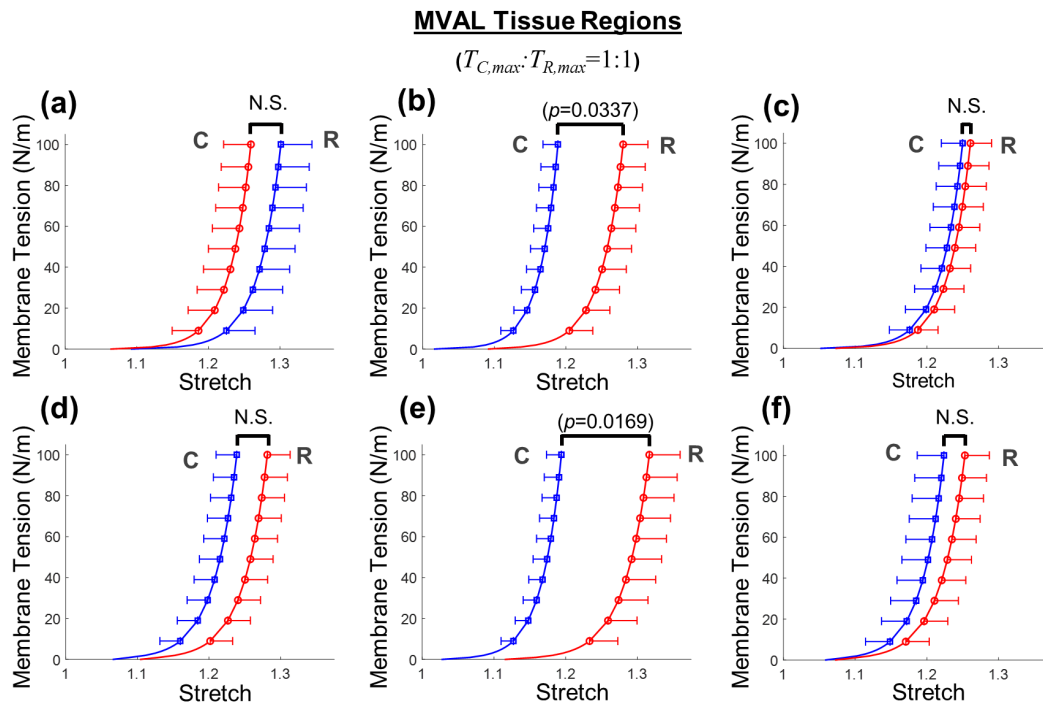


**Figure 4.2.** Mean  $\pm$  SEM of membrane tension versus total tissue stretch results for the six MVAL tissue regions under equibiaxial loading ( $T_{C,\max} : T_{R,\max} = 1:1$ ). The labels (a-f) correspond to the region label defined in Figure 4.1c. N.S.: non-statistically significant.

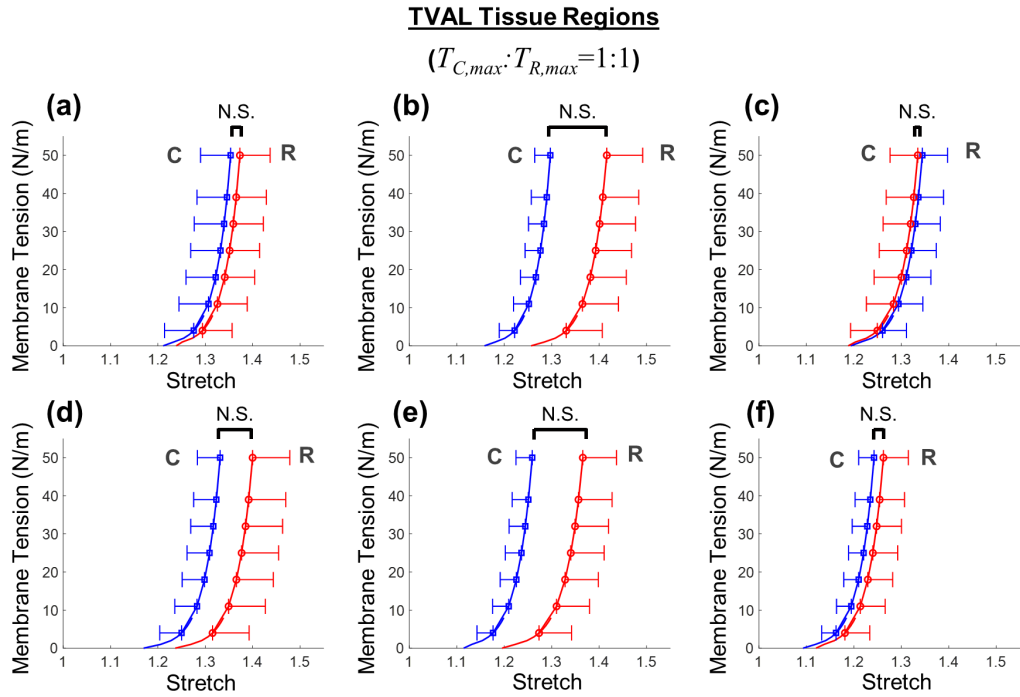


**Figure 4.3.** Mean  $\pm$  SEM of membrane tension versus total tissue stretch results for the six TVAL tissue regions under equibiaxial loading ratio ( $T_{C,max} : T_{R,max} = 1:1$ ). The labels (a-f) correspond to the region label defined in Figure 4.1c. N.S.: non-statistically significant.

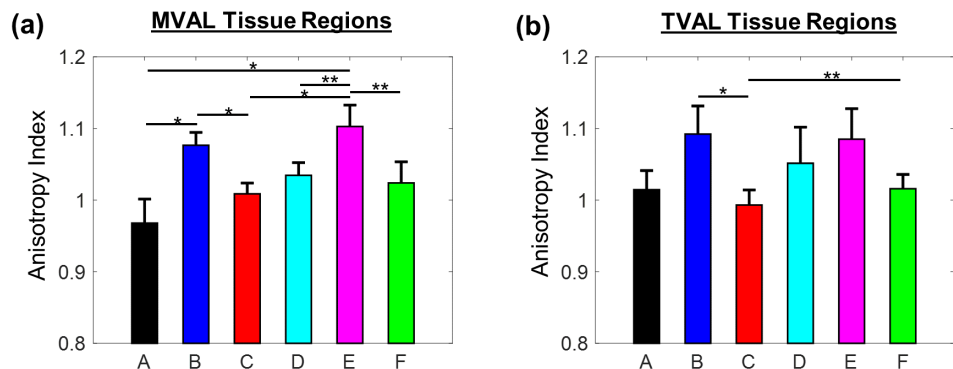


**Figure 4.4.** Mean  $\pm$  SEM of anisotropy index for peak stretch of the six regions of the (a) MVAL and (b) TVAL. The labels (A-F) correspond to the regions defined in Figure 4.1c.

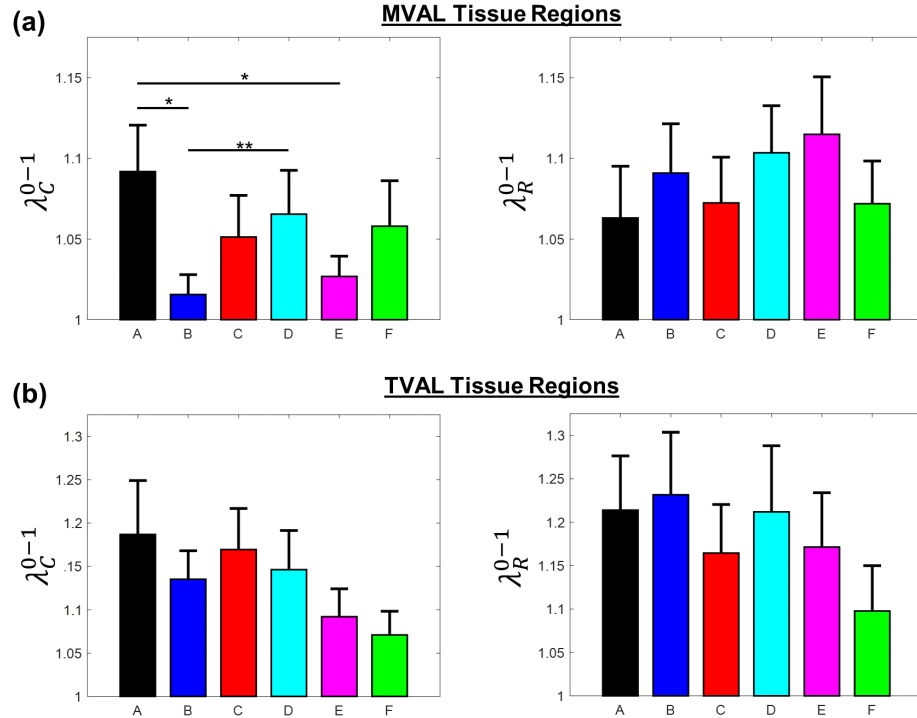


**Figure 4.5.** Mean  $\pm$  SEM of the preconditioning stretches ( $\lambda_C^{0-1}$  and  $\lambda_R^{0-1}$ ) of (a) the six MVAL tissue regions and (b) the six TVAL tissue regions under equibiaxial loading in both the C (left) and R (right) directions. (\*) denotes statistically significant ( $p < 0.05$ ) difference between groups and (\*\*) denotes nearly statistically significant ( $0.05 < p < 0.10$ ) difference between groups; otherwise, not statistically significant ( $p > 0.10$ ).

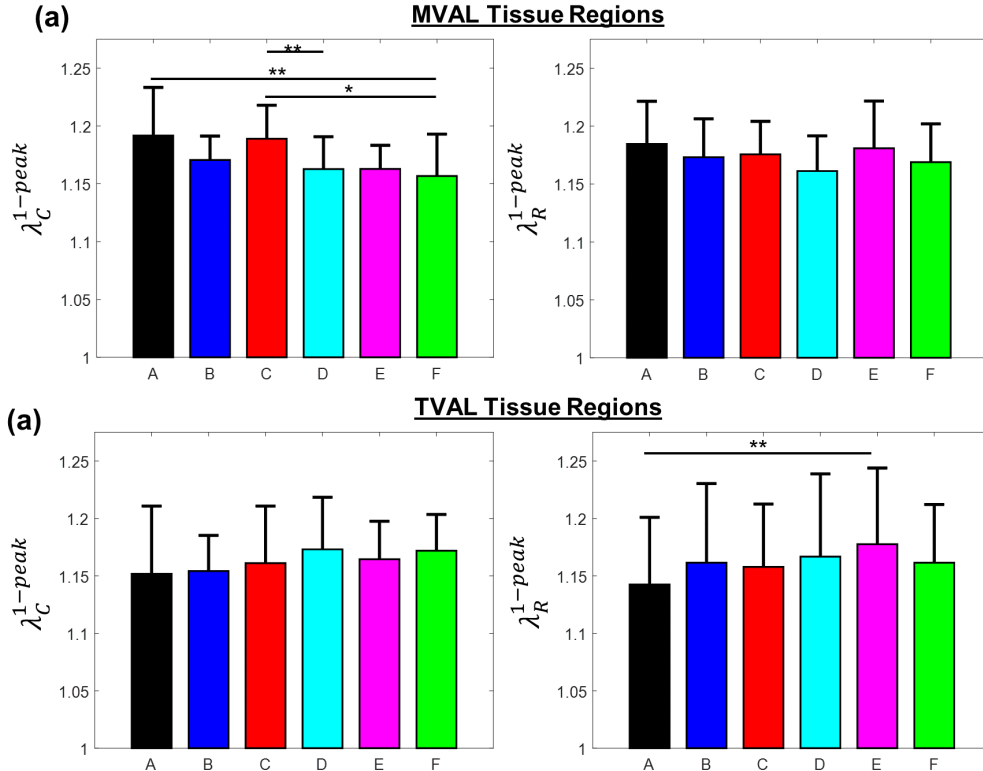


**Figure 4.6.** Mean  $\pm$  SEM of the mechanical stretches ( $\lambda_C^{1-peak}$  and  $\lambda_R^{1-peak}$ ) of all six (a) MVAL and (b) TVAL tissue regions in both the C (left) and R (right) directions under the equibiaxial loading. (\*) denotes statistically significant ( $p<0.05$ ) difference and (\*\*) denotes nearly statistically significant ( $0.05<p<0.10$ ) difference between groups; otherwise, not statistically significant ( $p>0.10$ ).

Three main trends were observed for all loading ratios ( $T_{C,max} : T_{R,max} = 1:1, 0.75:1, 1:0.75, 0.5:1$ , and  $1:0.5$ ) in our biaxial mechanical testing results as described below. (1) We found that the central regions had a greater difference in the total tissue stretch between the circumferential and radial directions than the edge regions for the MVAL (region B:  $p=0.034$ , region E:  $p=0.017$ ) and TVAL (region B:  $p=0.162$ , region E:  $p=0.189$ ). (2) By analyzing the *anisotropy index (AI)*, we found the central regions were more anisotropic than the edge regions for the MVAL (statistically significant difference comparing B-A:

$p=0.016$ , B-C:  $p=0.010$ , and E-A:  $p=0.010$ , and nearly statistically significant difference in D-E:  $p=0.072$ , and E-F:  $p=0.096$ ). This trend was also observed in the TVAL regions (statistically significant difference comparing B-C:  $p=0.048$ , and nearly statistically significant difference in E-C:  $p=0.070$ ). (3) It was found that the *mechanical stretches* in the circumferential direction of the MVAL were higher in regions near the annulus (regions A, B, and C) than those in regions near the free edge (regions D, E, and F) (circumferential direction,  $0.036 < p < 0.703$ ; radial direction,  $0.136 < p < 0.842$ ). This trend was not observed for the TVAL as the *mechanical stretches* were mainly uniform across the entire leaflet (circumferential direction,  $0.496 < p < 0.910$ ; radial direction,  $0.050 < p < 0.930$ ). Specifically, the *mechanical stretches* in the circumferential direction were 1.122-1.155 and 1.122-1.142 for the MVAL and TVAL tissue regions, respectively, whereas the *mechanical stretches* in the radial direction were 1.128-1.150 and 1.112-1.144 for the MVAL and TVAL tissue regions, respectively (Table 4.1 and Table 4.2).

**Table 4.1.** Total tissue stretch, anisotropy index, preconditioning stretch, mechanical stretch from biaxial mechanical tests, and the engineering strain from stress relaxation tests for each MVAL region. Values are reported as mean (SEM).

		A (n=13)	B (n=13)	C (n=13)	D (n=12)	E (n=13)	F (n=13)
Total Tissue Stretch at Peak Loading	$\lambda_C^{0-peak}$	1.301 (0.043)	1.189 (0.021)	1.250 (0.030)	1.239 (0.029)	1.194 (0.021)	1.224 (0.037)
	$\lambda_R^{0-peak}$	1.259 (0.038)	1.280 (0.035)	1.261 (0.030)	1.281 (0.032)	1.317 (0.043)	1.253 (0.034)
Anisotropy Index: $\lambda_R^{0-peak} / \lambda_C^{0-peak}$		0.977 (0.034)	1.076 (0.018)	1.010 (0.015)	1.036 (0.018)	1.103 (0.030)	1.030 (0.030)
Preconditioning Stretch	$\lambda_C^{0-1}$	1.114 (0.029)	1.036 (0.013)	1.073 (0.026)	1.087 (0.028)	1.048 (0.013)	1.080 (0.029)
	$\lambda_R^{0-1}$	1.085 (0.033)	1.113 (0.031)	1.094 (0.029)	1.126 (0.030)	1.138 (0.036)	1.094 (0.027)
$T_{C,max} : T_{R,max} = 1:1$	$\lambda_C^{1-peak}$	1.155 (0.017)	1.136 (0.013)	1.154 (0.011)	1.129 (0.006)	1.128 (0.014)	1.122 (0.010)
	$\lambda_R^{1-peak}$	1.150 (0.012)	1.139 (0.012)	1.142 (0.010)	1.128 (0.008)	1.147 (0.014)	1.134 (0.010)
$T_{C,max} : T_{R,max} = 0.75:1$	$\lambda_C^{1-peak}$	1.290 (0.044)	1.169 (0.021)	1.240 (0.030)	1.224 (0.028)	1.184 (0.021)	1.215 (0.036)
	$\lambda_R^{1-peak}$	1.259 (0.039)	1.262 (0.037)	1.262 (0.030)	1.287 (0.034)	1.315 (0.044)	1.254 (0.034)
$T_{C,max} : T_{R,max} = 1:0.75$	$\lambda_C^{1-peak}$	1.305 (0.043)	1.189 (1.247)	1.247 (0.030)	1.240 (0.029)	1.191 (0.021)	1.224 (0.038)
	$\lambda_R^{1-peak}$	1.250 (0.038)	1.277 (0.034)	1.252 (0.027)	1.281 (0.030)	1.315 (0.043)	1.247 (0.033)
$T_{C,max} : T_{R,max} = 0.5:1$	$\lambda_C^{1-peak}$	1.133 (0.019)	1.120 (0.013)	1.131 (0.012)	1.102 (0.006)	1.105 (0.014)	1.104 (0.010)
	$\lambda_R^{1-peak}$	1.148 (0.013)	1.137 (0.012)	1.140 (0.011)	1.138 (0.011)	1.137 (0.016)	1.137 (0.011)
$T_{C,max} : T_{R,max} = 1:0.5$	$\lambda_C^{1-peak}$	1.157 (0.018)	1.136 (0.014)	1.156 (0.012)	1.127 (0.005)	1.122 (0.014)	1.124 (0.010)
	$\lambda_R^{1-peak}$	1.132 (0.014)	1.126 (0.012)	1.125 (0.011)	1.114 (0.013)	1.133 (0.014)	1.119 (0.010)
Engineering Strain in Stress Relaxation Tests ( $\epsilon = L/L_0$ )	C	0.275 (0.054)	0.203 (0.033)	0.277 (0.034)	0.371 (0.060)	0.171 (0.040)	0.211 (0.035)
	R	0.283 (0.034)	0.348 (0.035)	0.276 (0.080)	0.371 (0.086)	0.440 (0.090)	0.473 (0.065)

\*Variation in the sample size (n) was due to tests in which tissue data was not successfully acquired, such as tissue tearing or tissue insufficiently large, as typically observed for the edge regions.

**Table 4.2.** Tissue total stretch, anisotropy index, preconditioning stretch, mechanical stretch from biaxial mechanical tests, and the engineering strain from stress relaxation tests for each TVAL region. Values are reported as mean (SEM).

		A (n=13)	B (n=13)	C (n=13)	D (n=12)	E (n=13)	F (n=10)
Total Tissue Stretch at Peak Loading	$\lambda_C^{0-peak}$	1.367 (0.064)	1.310 (0.033)	1.358 (0.054)	1.345 (0.049)	1.272 (0.035)	1.255 (0.033)
	$\lambda_R^{0-peak}$	1.387 (0.064)	1.430 (0.076)	1.348 (0.059)	1.414 (0.079)	1.379 (0.072)	1.275 (0.053)
Anisotropy Index: $\lambda_R^{0-peak} / \lambda_C^{0-peak}$		1.019 (0.027)	1.086 (0.039)	0.993 (0.021)	1.054 (0.051)	1.083 (0.043)	1.013 (0.020)
Preconditioning Stretch	$\lambda_C^{0-1}$	1.187 (0.062)	1.135 (0.033)	1.169 (0.047)	1.147 (0.045)	1.092 (0.032)	1.071 (0.027)
	$\lambda_R^{0-1}$	1.214 (0.063)	1.232 (0.072)	1.164 (0.056)	1.212 (0.076)	1.171 (0.063)	1.098 (0.052)
$T_{C,max} : T_{R,max} = 1:1$	$\lambda_C^{1-peak}$	1.152 (0.257)	1.154 (0.183)	1.161 (0.247)	1.173 (0.228)	1.164 (0.193)	1.172 (0.197)
	$\lambda_R^{1-peak}$	1.142 (0.258)	1.161 (0.285)	1.158 (0.249)	1.167 (0.288)	1.178 (0.287)	1.161 (0.232)
$T_{C,max} : T_{R,max} = 0.75:1$	$\lambda_C^{1-peak}$	1.146 (0.282)	1.146 (0.185)	1.159 (0.262)	1.159 (0.221)	1.156 (0.197)	1.158 (0.205)
	$\lambda_R^{1-peak}$	1.132 (0.273)	1.147 (0.280)	1.160 (0.271)	1.156 (0.290)	1.179 (0.291)	1.150 (0.240)
$T_{C,max} : T_{R,max} = 1:0.75$	$\lambda_C^{1-peak}$	1.146 (0.279)	1.148 (0.181)	1.154 (0.253)	1.163 (0.227)	1.157 (0.181)	1.161 (0.197)
	$\lambda_R^{1-peak}$	1.129 (0.270)	1.151 (0.286)	1.150 (0.259)	1.149 (0.289)	1.169 (0.285)	1.143 (0.231)
$T_{C,max} : T_{R,max} = 0.5:1$	$\lambda_C^{1-peak}$	1.131 (0.280)	1.136 (0.186)	1.149 (0.255)	1.147 (0.226)	1.140 (0.191)	1.146 (0.196)
	$\lambda_R^{1-peak}$	1.133 (0.266)	1.153 (0.287)	1.159 (0.261)	1.158 (0.296)	1.175 (0.293)	1.152 (0.233)
$T_{C,max} : T_{R,max} = 1:0.5$	$\lambda_C^{1-peak}$	1.143 (0.283)	1.148 (0.182)	1.162 (0.261)	1.165 (0.229)	1.160 (0.189)	1.158 (0.188)
	$\lambda_R^{1-peak}$	1.123 (0.267)	1.144 (0.280)	1.146 (0.271)	1.142 (0.283)	1.164 (0.269)	1.131 (0.227)
Engineering Strain in Stress Relaxation Tests ( $\epsilon = L/L_0$ )	C	0.431 (0.044)	0.395 (0.074)	0.517 (0.228)	0.334 (0.036)	0.276 (0.029)	0.400 (0.050)
	R	0.327 (0.084)	0.369 (0.077)	0.345 (0.044)	0.466 (0.058)	0.489 (0.185)	0.344 (0.161)

\*Variation in the sample size (n) was due to tests in which tissue data was not successfully acquired, such as tissue tearing or tissue insufficiently large, as typically observed for the edge regions

#### 4.3.3 Stress relaxation testing results

A general trend of anisotropic exponential decays in the normalized membrane tension was found for both the MVAL and TVAL tissue regions (Fig. 4.7 and Fig. 4.8). Average values of the prescribed engineering strain are summarized in Table 4.1 for the MVAL regions and Table 4.2 for the TVAL regions. For the MVAL, all regions were observed to have a similar stress decay, except for region F, which decayed slightly more in the circumferential direction (Fig. 4.7). As for the TVAL, decays in the membrane tension magnitude were observed to be similar across all regions (Fig. 4.8). Comparing between the MVAL and the TVAL, an approximately 20-25% decay in stress reduction was observed for the MVAL tissue regions, whereas approximately 15-20% stress reduction was found across all TVAL tissue regions.

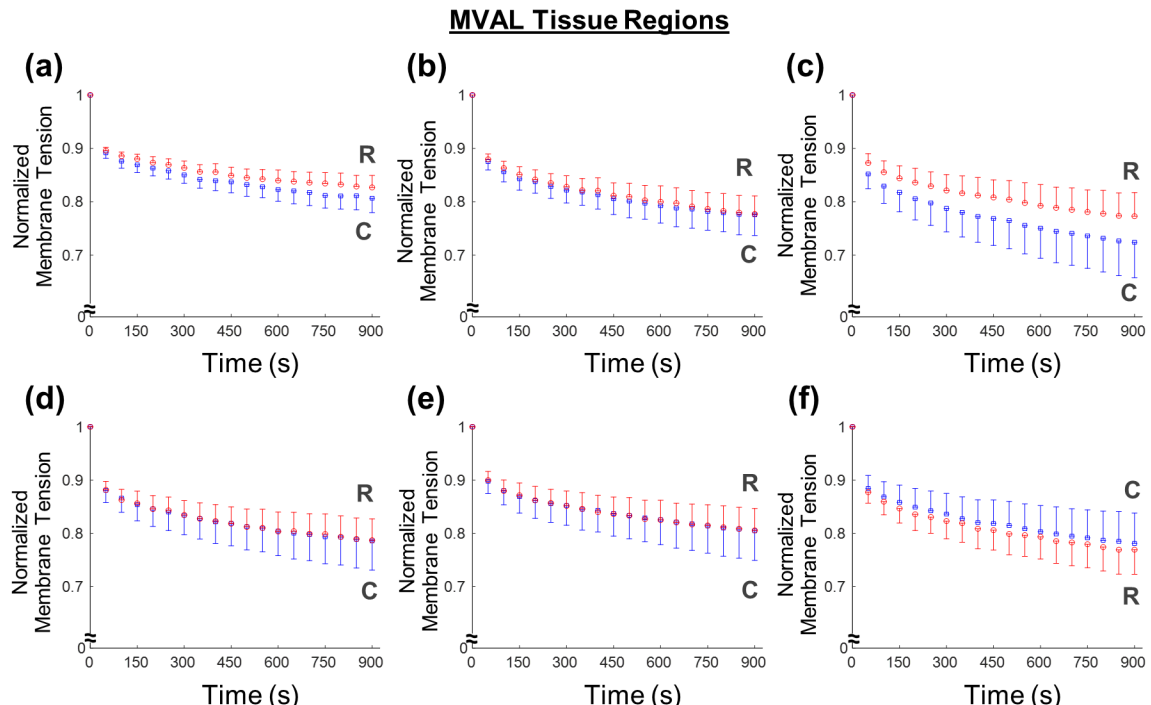


**Figure 4.7.** Mean  $\pm$  SEM of the normalized membrane tension versus time results from the stress relaxation testing for all the six MVAL tissue regions.

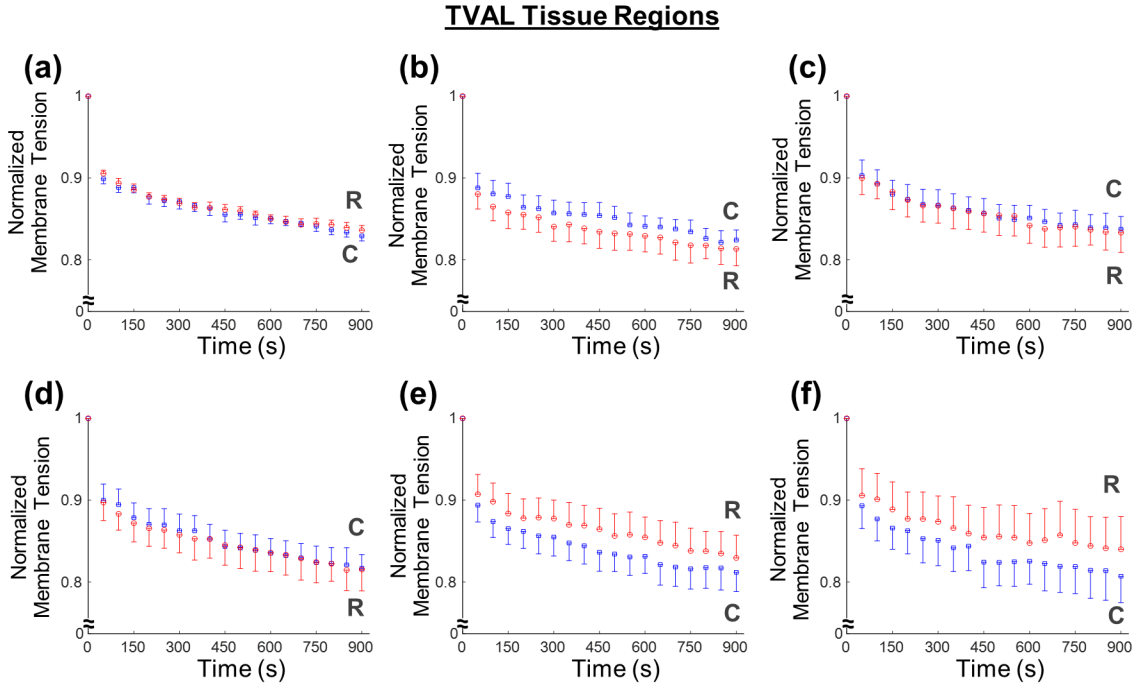


**Figure 4.8.** Mean  $\pm$  SEM of the normalized membrane tension versus time results from the stress relaxation testing for all the six TVAL tissue regions.

## 4.4 Discussion

### 4.4.1 Overall findings and comparisons with previous work

Biaxial mechanical characterization of the six regions of the MVAL and TVAL allowed for comparisons of the leaflet tissue's spatially-varied mechanical properties. It was found that the central regions (region B and region E, cf. Fig. 4.1c) of both leaflets had a more distinct difference in the *peak tissue stretches*, but this difference was found to be statistically significant only for the MVAL. The mechanical properties and material anisotropy for the MVAL tissue regions characterized in this study agree with previous work considering the central belly region [115]. However, from our statistical analyses for the TVAL, we found that the *p*-values of the material anisotropy for the central regions were much lower than those for the edge regions, suggesting a more distinct difference in

the *peak tissue stretches* for the TVAL central regions, which agrees with previous investigations [48].

The observation of the belly regions being more anisotropic was supported when comparing the *AIs* between any two tissue regions. Statistically significant differences in the *AI* were found to be more pronounced for the MVAL tissue regions, especially when comparing the central regions (B and E) to the majority of edge regions (A, C, and D). In contrast, statistically significant differences were only found for the TVAL between regions B and C as well as between regions E and C. This novel finding suggests there is a noticeable regional variance in the mechanical behaviors of the MVAL and TVAL, typically when comparing the central belly regions to those edge regions as closer to the free edge and commissures of the valve.

From our analyses of the *mechanical stretches* for the MVAL and TVAL tissue regions, a general trend was observed with the circumferential stretches being larger in regions closer to the annulus than those near the free edge for the MVAL. Although other regional comparisons for the TVAL did not yield observable trends, the regional variances in tissue's stretch response suggest spatially-varied mechanical behaviors of the atrioventricular heart valve leaflets.

Lastly, regional variance was exemplified through stress relaxation testing. Our results indicated a general trend of anisotropic, exponential decaying in the stress magnitude for the MVAL and TVAL tissue regions. The stress decay was reflective of previous studies considering the bulk leaflet tissues, especially in those central belly regions [45, 54, 116]. Moreover, a fair amount of variation in stress decay was also observed between the six

tissue regions. The general trend of greater stress decay in the MVAL regions compared to the TVAL regions suggests that the MVAL regions may have greater stress-relaxation potential than the TVAL regions.

#### 4.4.2 Study limitations

General study limitations for our biaxial testing framework have been discussed in our previous work [111]: (i) shear stress was neglected from our calculations due to its negligibility, which is typical for biaxial testing protocols, and (ii) the freezing effect on the AHV mechanical behaviors has not been extensively investigated and is an assumption from studies involving other soft tissues. In addition, there were two specific limitations for this study. First, the effective loaded region in this study was much smaller than our previous investigation (6.5 mm versus 4.5 mm) and, to our knowledge, there is no study showing the effect of specimen loaded size on the characterized mechanical behavior of the leaflets. Further investigation may be warranted on the specimen size effect to determine the optimal testing size for the most accurate mechanical characterization of the MV and TV leaflet regions, as currently underway in our lab. Secondly, a hold time of 15-minutes was considered for the stress relaxation testing in this study. An ongoing study from our group and other previous investigations have shown that a holding time of approximately 4 hours may be warranted to observe the *full pattern* of the stress relaxation behavior; still, the majority of stress reduction occurs within the first 900 seconds [45, 54, 116]. In addition, our stress relaxation results have shown that the 15-minute period is sufficient to observe regional similarities/differences in the stress reduction behaviors (Fig. 4.6 and Fig. 4.7).

#### **4.4.3 Concluding remarks**

This research has, *for the first time*, examined the regional variance and similarity of the mechanical properties of the MVAL and TVAL. The biaxial mechanical testing results in this study have demonstrated a significant difference in the material anisotropy when comparing the central tissue regions to the edge regions. Variance was observed in the *mechanical stretch* across the six tissue regions with greater extensibility observed near the annulus of the MVAL. Our stress relaxation results have further showed an anisotropic, exponential stress decay trend with variations in the stress reduction between tissue regions. Our novel experimental findings could provide a better understanding of the spatially-varying mechanics of the leaflets and open the door to future refinement of computational models for accurate prediction of diseased or surgically-intervened conditions, where tissue heterogeneity plays an essential role in the valve function.

## CHAPTER 5. PSFDI SYSTEM DEVELOPMENT

### 5.1 Introduction to Collagen Fiber Quantification Techniques

Collagen fibers compose the ECM in tissues such as tendons, arteries, HV leaflets, and skin. In collagenous tissues, the fibers are arranged in specific architectures to support the functional requirements of the material [117-119]. Due to the relationship between tissue mechanical function and collagen fiber organization, significant efforts have been dedicated to quantifying the collagen fiber architectures (CFAs) in various tissues [91, 120, 121]. These research studies have traditionally analyzed static tissues, i.e., tissues not subjected to external mechanical loading. For example, existing studies have reported the static orientation and spread of collagen fibers throughout the domain of the sclera, meniscus, and murine lung, among others [122-124]. However, these static quantifications are fundamentally incomplete for understanding the tissue mechanical function, because collagen networks will change in response to mechanical loading [125-127]. Thus, complete description of CFA and function requires quantification of changes to fiber networks under applied mechanical loading. The combined structural and mechanical description of dynamic CFA is essential for improved comprehension of the structure-function relationship in healthy tissues, and to improve understanding of structural and functional degradation in diseased tissues.

Unfortunately, existing imaging techniques are generally incapable of providing this rigorous quantification. To explore the capabilities and shortcomings of existing imaging modalities, current fiber architectural quantification methods are reviewed below, with emphasis on their capacity for wide-field examination of dynamic fiber architectures in loaded tissues (Table 5.1).

**Table 5.1.** Comparison of collagen fiber quantification techniques [68, 72, 73, 128-130].

	<b>polarized Spatial Frequency Domain Imaging (pSFDI)</b>	<b>Quantitative-Polarized Light Microscopy (Q-PLM)</b>
<b>Imaging Time</b>	Order of minutes, potentially shorter with improved hardware and lower resolution	Single image capture in seconds, usually requires images at various polarizations
<b>Capture Method</b>	Series of images, arbitrary magnification	Arbitrarily magnified image capture
<b>Field of View (FOV)</b>	Varies by lens, as large as desired, typically order of cm	Varies by lens (typically order of $\mu\text{m-mm}$ )
<b>Resolution</b>	Dictated by pixel-size of images and number of polarization states captured	Varies by magnification & sample thickness
<b>Contrast Mechanism</b>	Birefringence of collagen fiber structure, reflectance-based	Birefringence of collagen fiber structure, transmission-based
	<b>Small Angle Light Scattering (SALS)</b>	<b>Second Harmonic Generation (SHG) Imaging</b>
<b>Imaging Time</b>	Order of hours, depends on size and desired resolution	Single image capture on order of minutes
<b>Capture Method</b>	Rasterized scanning with image capture at each raster point	Second harmonic frequency generation and capture at each pixel of final image
<b>FOV</b>	As large as desired, typically cm-scale due to time limitations	Initial images on order of $\mu\text{m}$ , reconstructed images on order of $100\mu\text{m}$
<b>Resolution</b>	Dependent upon depth-averaged light diffusion and incident beam size	High resolution, capable of resolving individual collagen fibrils
<b>Contrast Mechanism</b>	Anisotropic light scattering by fibrous structures extracted from transmitted light signatures	Birefringent molecular hyperpolarizability among fibers/fibrils alongside frequency doubling nonlinear phenomena

The above values present a baseline of the capabilities of these imaging modalities, as each technique has been customized and extended for specific applications, leading to a variety of FOVs, imaging resolutions, and image acquisition times. For example, although PLM is typically used to examine samples on a microscopic scale, similar techniques were recently applied via the addition of quarter-wave plates to examine dynamic collagen

structures over a cm-scale in milliseconds, albeit with lower resolution [131]. In another recent custom application, a commercial SHG device was integrated with a mechanical testing system to examine changes to collagen fibril structures under load [132, 133]. However, this quantification was depth-limited to the superficial 60  $\mu\text{m}$  of the tissue and was not able to interrogate large tissue regions with spatially-varied microstructures due to imaging time and FOV constraints.

We examined the techniques listed while considering the goal of quantifying dynamic CFA over large tissue domains, and were impressed by the capabilities offered by the pSF DI modality. The technique can be conceptualized as a reflectance combination of polarized light imaging and Spatial Frequency Domain Imaging (SF DI), a planar projection method utilizing structured illumination to probe tissue properties [77, 79]. Through the projection of varied spatial frequency patterns, pSF DI can obtain aggregated information about tissue structures above a desired depth in the tissue [134]. In terms of microstructural quantifications, this technique: (i) is designed for quantitative analysis of collagen fiber orientation and degree of alignment, (ii) examines a cm-scale FOV in the order in the order of minutes for analysis of complex and spatially-varied tissue microstructures, (iii) allows depth discernment for quantification of multilayered samples, (iv) permits analysis of native, unfixed and non-chemically altered tissues, and (v) captures reflected light, encouraging modularity with external systems.

To provide quantification of dynamic collagen architecture, our group developed a system based on the integration of a pSF DI instrument with a commercial biaxial tester. The integrated system is capable of depth-modulated rapid quantification of collagen fiber orientation and degree of alignment throughout the spatial domain of a tissue sample.

Additionally, the system can examine samples at arbitrary desired biaxial loading states, rendering an essential tool for opto-mechanical analysis of membrane tissues, such as the heart valve leaflets, arteries, skin and others. The system has been validated through combined mechano-structural testing on tendon tissues with a known fiber architecture [135] and further utilized in testing on the heart valve leaflets to demonstrate analytical capabilities for multilayered tissues with spatially and depth-varied collagen architectures at physiologically relevant loading states. The specific details of the integrated system and the fundamentals it relies upon are described in the following sections.

## 5.2 Methods

### 5.2.1 Theory of birefringent collagen scattering

When subjected to polarized illumination, collagen fibers exhibit birefringence, i.e., a refractive response that depends upon the polarization and propagation of the incident light. More specifically, collagen fibers manifest *structural* birefringence, i.e., a birefringence arising from the cylindrical shape of the fibers. The structural birefringence of the fibers can be captured via a *co-polarization* imaging approach—a reflectance-based imaging methodology wherein light approaching a sample and reflected light from the sample are forced to pass through the same linear polarizer with angle  $\theta_{polarizer}$ . This co-polarized imaging system can be easily realized with several simple optical components (Fig. 5.1a), including a light projector, a linear polarizer, and a CCD camera.

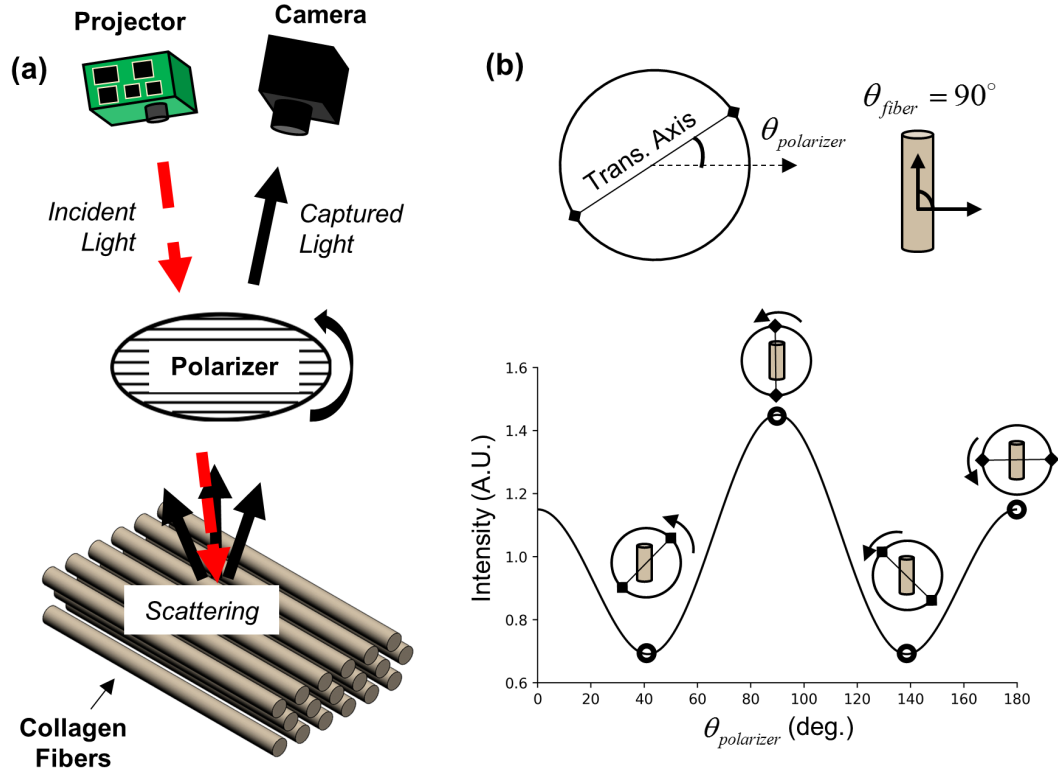


**Figure 5.1.** (a) Schematic of a co-polarized pSFDI system, showing the **optical components** and *passage of light*, including scattering from the fibrous tissue microstructure. (b) Illustration of the birefringent reflected intensity response with an example fiber with orientation angle  $\theta_{fiber}=90^\circ$  and a polarizer angle  $\theta_{polarizer}$  defined on the polar axis with the same reference.

By rotating the polarizer in a co-polarized imaging system through a  $0^\circ$ - $180^\circ$  range and capturing the corresponding reflected intensity associated with each  $\theta_{polarizer}$ , the birefringence of the collagen structure manifests in the varied reflected light intensity. This birefringent intensity variation is depicted for an example fiber with an orientation angle  $\theta_{fiber}$  of  $90^\circ$  (Fig. 5.1b). The bimodal intensity response is periodic over a  $180^\circ$  range, due to symmetry in linear polarization, and has a *global maximum* where  $\theta_{polarizer}=\theta_{fiber}$  with corresponding offset *local maximum* where  $\theta_{polarizer}=\theta_{fiber}\pm90^\circ$ . Simply put, the peaks in reflected intensities occur when the polarizer transmission axis is parallel to and

perpendicular to the fiber orientation angle. Quantitatively, the birefringent reflected intensity of a group of collagen fibers (Fig. 5.1b) can be described by the following 3-term Fourier cosine series:

$$\frac{I_{out}}{\tau_{sys}} = a_0 + a_2 \cos[2(\theta_f - \theta_p)] + a_4 \cos[4(\theta_f - \theta_p)]. \quad (5.1)$$

Equation (5.1), derived based on a formal Stokes/Mueller approach in **Appendix C**, describes the reflected intensity of a group of fibers as a function of the  $\theta_{polarizer}$ , where  $\tau_{sys}$  is the bulk systemic coefficient encompassing non-birefringent intensity modifiers, such as the aperture of the camera, and  $a_0$ ,  $a_2$ , and  $a_4$  are the three Fourier coefficients. Specifically,  $a_0$  describes the average reflected light from the sample, whereas  $a_2$  and  $a_4$  represent the optical anisotropies arising from the birefringence within the sample.

For complex clusters of collagen fibers with varied in-plane polar orientations, the magnitudes of the optical anisotropies provide a means of examining the dispersion of the fibers, which is reflected in the degree of optical anisotropy (*DOA*) in the sample:

$$DOA = \frac{a_2 + a_4}{a_0 + a_2 + a_4}, \quad (5.2)$$

Although the *DOA* metric is not a perfect indicator of collagen fiber dispersion, as the observed optical anisotropy can be impacted by other factors [79], the *DOA* can still provide valuable comparative information about the spatial dispersion of collagen fibers throughout a sample, and can permit microstructural comparisons between loaded and unloaded tissue samples, as explored in *Section 5.3*. Together, Eqns. (5.1) & (5.2) provide the fundamental theory relating the birefringent optical response of a collagenous tissue to

the mean fiber orientation  $\theta_{fiber}$  and the approximate fiber dispersion via *DOA*. In the pSF DI theory, these relationships are used to extract spatial collagen structural information from a tissue sample's optical response. The practical implementation of the pSF DI structural quantification method will be discussed further in *Section 5.2.3*.

### 5.2.2 Spatial frequency domain imaging (SF DI) theory

pSF DI employs the spatial frequency domain imaging (SF DI) theory to control the effective imaging depth of our system's microstructural quantifications. SF DI allows specification of the effective penetration depth,  $\delta_{eff,AC}$ , of the measurements via control of the *spatial frequency*  $f_x$  of the projected light pattern:

$$\delta_{eff,AC} \approx \frac{1}{2\pi f_x}, \quad (5.3)$$

By regulating the incident light's spatial frequency, we can produce spatial maps of the predicted material properties, encoding only information above a desired effective penetration depth, according to Eq. (5.3). These depth-controlled images are known as *AC images*. In the SF DI demodulation process, these depth-controlled AC images are generated along with full-optical-thickness images, denoted as the *DC images*. Although the use of SF DI for depth-modulated imaging has been well-explored in literature [136-138], we provide a thorough analysis of Eq. (5.3) and the derivation of the DC and AC penetration depth formulae in **Appendix C**.

### **5.2.3 Polarized spatial frequency domain imaging system**

The pSFDI (polarized SFDI) imaging technique combines the ability of co-polarized imaging to quantify birefringent fiber structures with the depth-discrimination capabilities of SFDI. Our group has integrated the traditional pSFDI system with a mechanical testing system to form a novel opto-mechanical system capable of quantifying wide-field load-driven changes in a tissue sample's collagen microstructure. Our pSFDI system utilizes an LED-driven, micromirror-based pattern projection system (Texas Instruments, Dallas, TX) with projection wavelength of 490 nm (cyan) and a 5 Megapixel CCD camera (Basler, Germany) with lens of  $f/1.9$  and exposure time of 50 ms. For controlled rotational polarization, the system employs a nanoparticle linear polarizer with diameter 25 mm mounted into a rotational servo motor with 0.1° resolution (Thorlabs, Newton, NJ). These components are fixed to a vertical breadboard using a combination of purpose-built 3D-printed components and standard optics mounting hardware (Fig. 5.2).

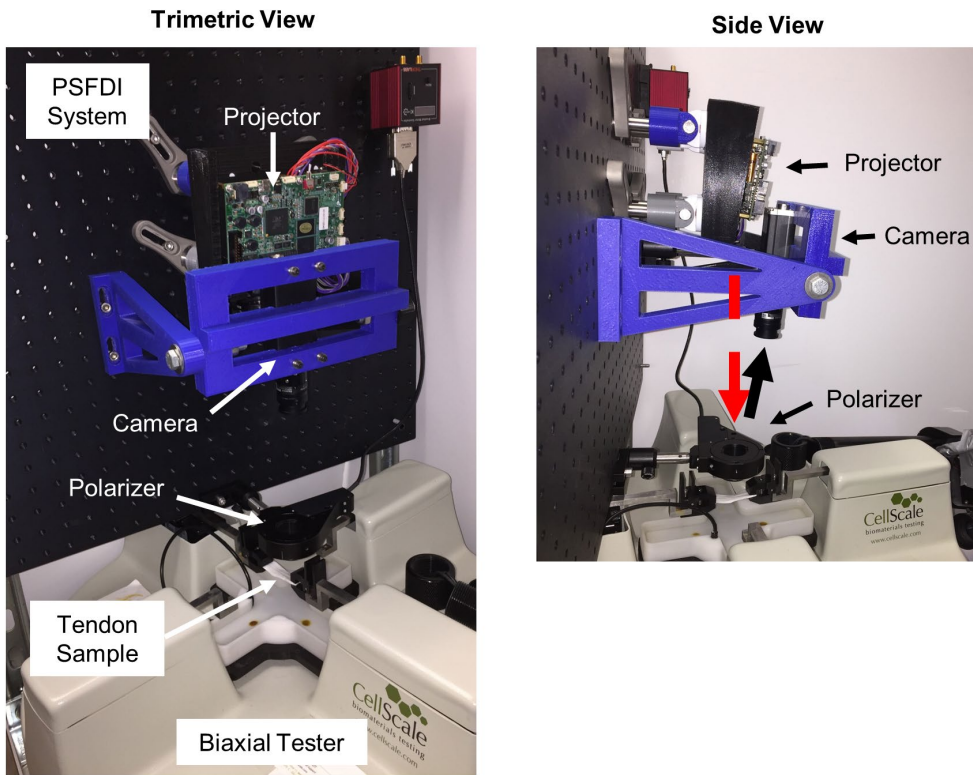


**Figure 5.2.** Trimetric and side views of the integrated pSF DI and biaxial testing system.

Arrows in the side view indicate the passage of light through the system.

For all dynamic testing, the pSF DI system was positioned vertically above a commercial biaxial testing system (CellScale, Ontario, Canada) and calibrated to the tissue size to create the integrated opto-mechanical imaging system. During testing, the projection-system projects 3 phase-shifted images sequentially through a polarizer at angle  $\theta_{polarizer}$  and onto a tissue sample. For each projected image, the light reflects from the sample and passes through the same polarizer before capture by the camera. This projection-capture sequence is repeated at each of 37 discrete polarization increments ( $5^\circ$  increments from  $0^\circ$  to  $180^\circ$ , including both endpoints). The coordination of image projection, image capture, and polarizer rotation is accomplished through a custom LabView program (Austin, TX). After testing, the phase-shifted images are first smoothed via convolution with a normalized  $5 \times 5$  uniform kernel, or convolution matrix, and are then combined at each pixel

and polarization state according to DC and AC convention from SFDI theory (cf. **Appendix C** for more details). At each pixel in the resultant DC and AC images, the intensity is fit with respect to  $\theta_{polarizer}$  using a moving least-squares (MLS) model [139]. This fitting allows the extraction of  $\theta_{fiber}$  as the polarization angle where the MLS model fit intensity is maximized, according to Eq. (5.1). Utilizing the extracted  $\theta_{fiber}$  arrays to compute the cosine terms in Eq. (5.1), linear curve fitting is then performed via the normal equation to extract the three Fourier term coefficients ( $a_0$ ,  $a_2$ ,  $a_4$ ) at each pixel. These coefficients are further applied to Eq. (5.2) to compute the *DOA* image. These data analysis processes were repeated in full for both DC and AC datasets, with the effective penetration depth of the AC images computed using Eq. (5.3). All data analyses were implemented via in-house Python programs.

#### 5.2.4 Analyzing the CFA in soft tissues

All tissues used in the following studies were obtained from a USDA-certified abattoir (Country Home Meat Co., Edmond, OK). The tissues were frozen for storage purposes and thawed prior to testing and sample selection.

##### Verification Test – Bovine Tendon Tissues

First, to validate the microstructural predictions by the developed pSFDI system, “static” testing on bovine tendon samples at varied planar orientations was performed. In the interior region of bovine tendon, collagen fibers exhibit a strong preferential alignment along the longitudinal tendon axis [140]. To evaluate the efficacy of the system’s microstructural predictions, the quantified collagen fiber orientations of tendon samples were compared to the expected preferential orientation as previously mentioned. In brief,

three thin tissue samples were excised from the central region of bovine tendons, with care taken to exclude the synovial sheath membrane enclosing the tendon. The samples were then placed at varied planar orientations, sandwiched between two microscope slides in a 3D-printed container, and mounted to the pSF DI system. Samples were imaged with a spatial frequency  $f_x=0.20 \text{ mm}^{-1}$ . Because the orientation prediction capability of the system was the focus of this group, we considered only the DC, or full-depth, image results from this study.

#### *Quantification of Dynamic Changes in the CFA – Bovine Tendon Tissues*

Next, deformation-controlled tensile testing was performed to examine the load-dependent changes in the collagen fiber microstructures. Specifically, a strip of tissue, with a thickness of 1.25 mm, a width of 15 mm, and a length of 40 mm, was extracted from the central region of a bovine tendon, with the strip length corresponding to the tendon axis. The tendon sample was then mounted to the biaxial testing system subject to various uniaxial strains (0%, 1%, 2% and 3%), while the CFA of the tendon tissue sample was quantified by pSF DI imaging with a spatial frequency  $f_x=0.27 \text{ mm}^{-1}$ .

#### *Quantifications of Depth-Discrimination and Dynamic Changes in the CFA – Porcine Mitral Valve Anterior Leaflet (MVAL) Tissues*

Heart valve leaflets, such as the MVAL, exhibit spatially-varied CFAs with complex layer-dependent microstructures [60, 141]. Therefore, dynamic testing on porcine MVAL tissue samples was performed to predict a more complex collagen fiber architecture using our developed pSF DI system and to examine the depth-discrimination feature of the SF DI imaging. Two studies were considered to examine the microstructures of the MVAL tissue

samples: (i) *Study A*, to examine how the collagen fiber structures in response to varied biaxial loads, and (ii) *Study B*, to analyze the CFA across different MVAL tissue layers.

In each study, anterior leaflet tissue samples were excised from the MV and mounted to the biaxial tester using BioRakes to create an effective testing region of 10 x 10 mm. The tissue was mounted ensuring circumferential and radial directions were aligned with the testing *x*- and *y*-axes, respectively. Sample tissues were then preconditioned to restore their *in vivo* functional condition, using a standard force-controlled preconditioning protocol with a maximum force of 1000 mN applied in both the circumferential and radial directions, based on an assumed maximum physiological membrane tension of 100 N/m [43, 48] and a 10 mm effective edge length.

In *Study A*, an MVAL sample with a thickness of 0.75 mm was examined. After the above-mentioned preconditioning step, the tissue sample was subjected to variety of biaxial loads:  $F_C:F_R=1000\text{mN}:1000\text{mN}$ ,  $1000\text{mN}:250\text{mN}$ , and  $250\text{mN}:1000\text{mN}$ , where  $F_C$  and  $F_R$  are the forces applied in the circumferential and radial directions, respectively. A spatial frequency  $f_x=0.27 \text{ mm}^{-1}$  was adopted for all tests in *Study A* with only the DC, or full-depth, image results reported.

In *Study B*, an MVAL sample with a thickness of 0.87 mm was subjected to mechanical preconditioning and then examined with spatial frequencies of  $0.71 \text{ mm}^{-1}$ ,  $0.42 \text{ mm}^{-1}$ ,  $0.24 \text{ mm}^{-1}$ , and  $0.20 \text{ mm}^{-1}$  (*corresponding to AC imaging depths of 225, 375, 650, and 800  $\mu\text{m}$ , respectively, based on Eq. (5.3)*). The sample was then loaded with  $F_C:F_R=1000 \text{ mN}:1000 \text{ mN}$ , and the pSFDI imaging was repeated using the same set of spatial frequencies mentioned above. Both AC and DC image results were compiled and reported.

## 5.3 Results

### 5.3.1 Collagen microstructural imaging for bovine tendon tissues

The fiber orientations for various bovine tendon samples are presented in Figure 5.3.

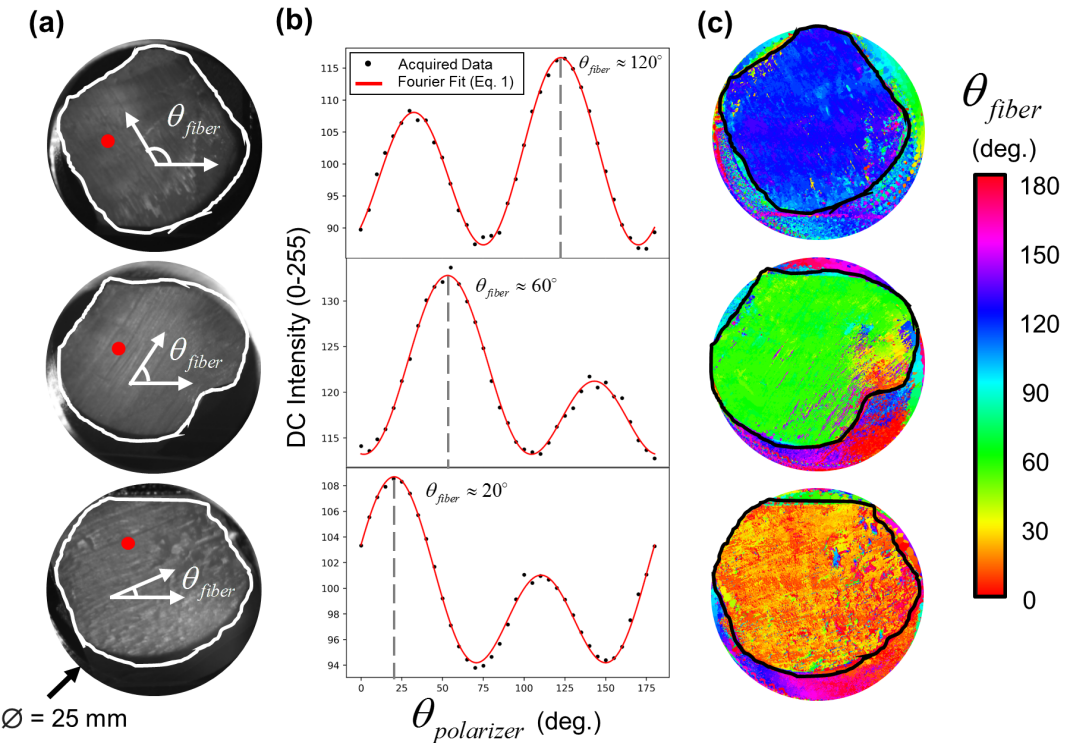


**Figure 5.3.** Microstructural quantifications from the pSF DI system. (a) DC images for 3 bovine tendon tissue samples, with expected  $\theta_{fiber}$  according to the tendon's preferential axial direction, i.e.,  $120^\circ$ ,  $60^\circ$ , and  $20^\circ$ . Red circles indicate single pixel locations where: (b) DC intensity responses, together with the 3-term Fourier series fit (Eq. (5.1)) for quantifying the  $\theta_{fiber}$ , are presented. (c) Colormaps of the predicted  $\theta_{fiber}$  associated with each tendon tissue sample.

Several key findings can be extracted from these plots. Principally, we observed that the Fourier cosine series (Eq. (5.1)) is able to accurately describing the birefringent reflected intensity of collagenous tissues with an arbitrary fiber orientation (Fig. 5.3b). Secondly,

the pixelwise  $\theta_{fiber}$  predictions (Fig. 5.3c) are in a very good agreement with the longitudinal axis of the tendon. These “static” imaging results validated the pSF DI system we developed and further prompted our investigation into the effects of external loading on the tendon tissue’s microstructure. The system predictions of the dynamic CFA for a strip of bovine tendon subjected to various uniaxial loads are shown in Figure 5.4.

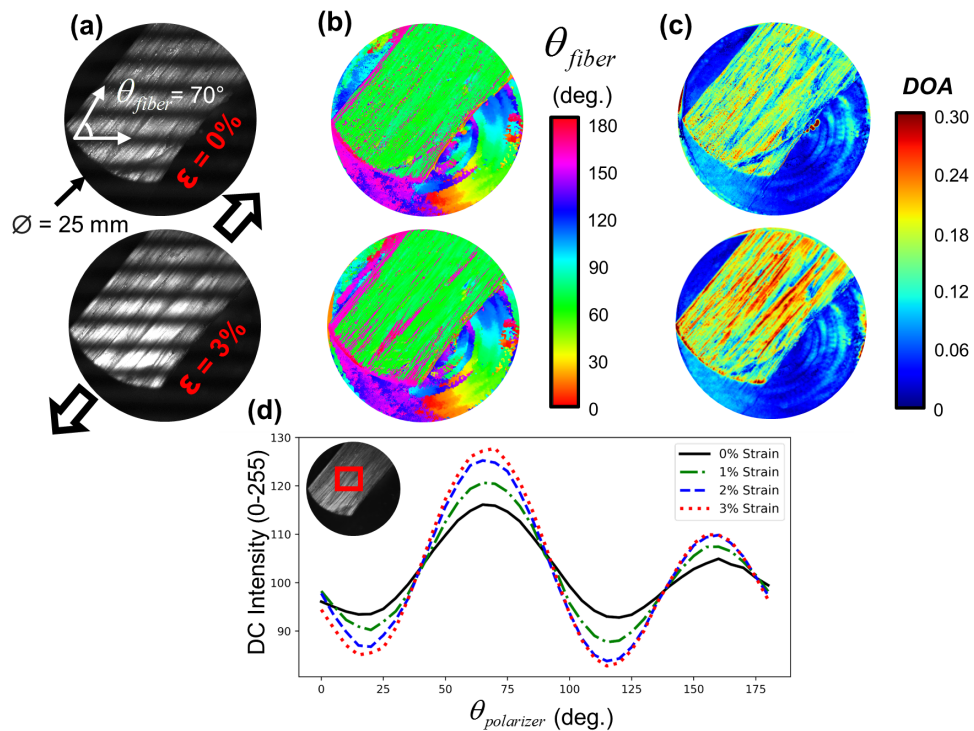


**Figure 5.4.** Dynamic microstructural quantifications from the integrated biaxial-pSF DI system. (a) Experimental raw images of bovine tendon tissue specimen (thickness = 1.25 mm), and predictions of (b)  $\theta_{fiber}$  and (c) DOA at 0% and 3% uniaxial strains. (d) DC intensity responses, obtained by spatially averaging over the region outlined in red, considering 0%, 1%, 2%, and 3% uniaxial strains.

The predominant fiber orientations in the uniaxially-loaded tendon fell along the tendon longitudinal axis at approximately  $70^\circ$ , as shown in Figure 5.4b. Unlike the fiber orientation

predictions, the predicted *DOA* changed markedly, increasing heterogeneously across the tissue domain (Fig. 5.4c). The optical signal averaged over a bulk region of the tissue is presented in Figure 5.4d, where the increased strain corresponds to an increase in the magnitude of the optical birefringence. This increased birefringence is captured in the corresponding increase in average *DOA*; For example, the *DOA* values extracted from the optical responses (Figure 5.4d) were 0.127, 0.163, 0.196, and 0.2127 for the 0%, 1%, 2%, and 3% loading states, respectively. The clear and expected *DOA* increase with increased tissue loading supports its use to indicate fiber dispersion and recruitment in tissues. As tissues are loaded, fiber families are expected to exhibit a more uniform alignment in the direction(s) of applied loading [7, 63, 142, 143]; our system dynamically quantifies this phenomenon through the *DOA* metric.

### 5.3.2 Collagen microstructural imaging for MV leaflet tissues

We used our system to further analyze MVAL tissue samples under various biaxial loads, and the results, which are *the first of their kind*, are shown in Figure 5.5.

Our results indicate that the collagen fiber architecture of the MVAL tissue sample is both spatially complex and highly load-dependent. Specifically, in the unloaded state, the fibers were generally aligned in an extended U-shape—tracing an arc from the annulus on the left, toward the coaptation point, and back to the annulus on the right. This microstructure has been well-catalogued in heart valve leaflets [72, 144, 145]. Moreover, the unloaded *DOA* was relatively spatially uniform, falling into a range of 0.02-0.08 throughout the tissue. However, we observed drastic and spatially-varied changes in both the predicted fiber orientations and *DOA* with applied loading (Fig. 5.5c, Fig. 5.5d, and Fig. 5.5e),

dependent upon the direction and the magnitude of the load. To draw insights from the complex dynamic microstructures quantified in the MVAL sample, we plotted the bimodal distributions of the  $\theta_{fiber}$  and  $DOA$  over the tissue domain for each loading ratio (Fig. 5.6).

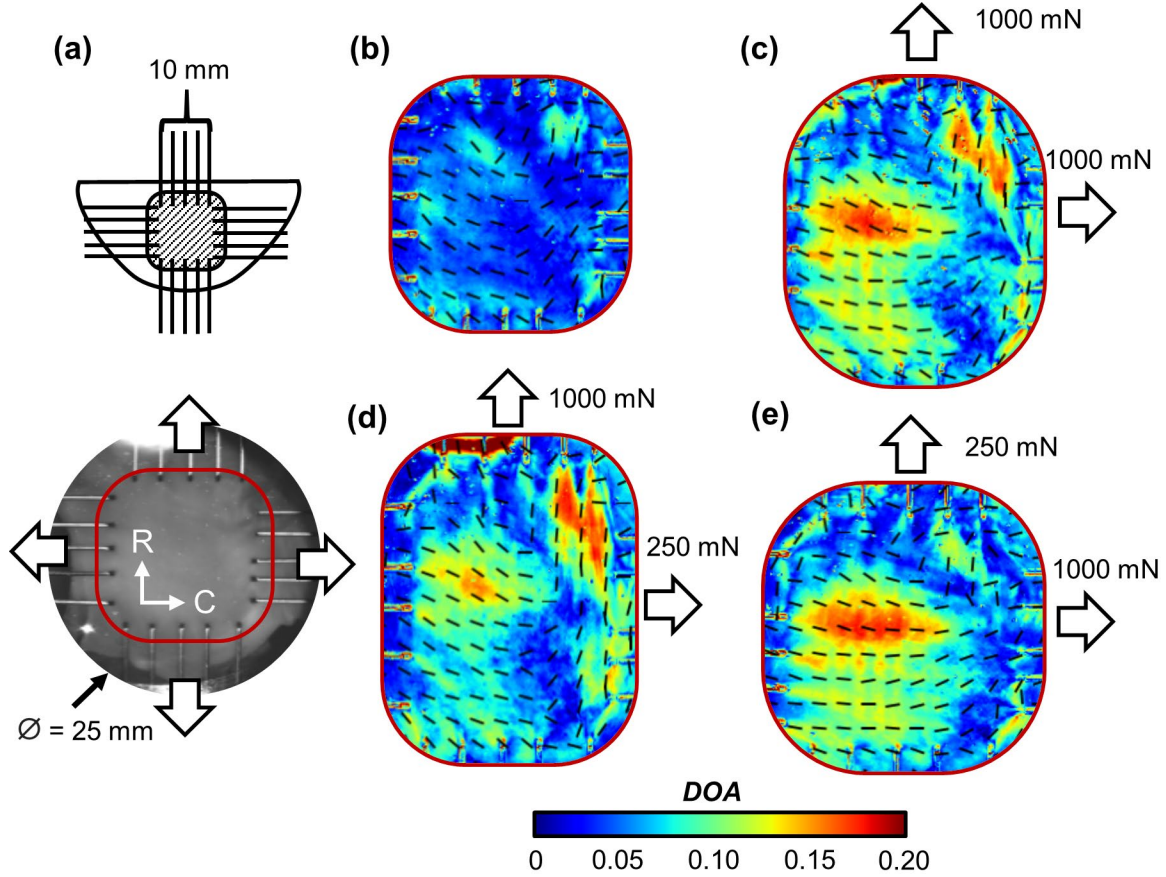


**Figure 5.5.** Dynamic microstructural quantifications from the integrated biaxial-pSF DI system. (a) Schematic of the porcine MVAL specimen (thickness = 0.75 mm) mounted to the BioTester and the DC image showing the biaxially-loaded region. (C: Circumferential, R: Radial). Predictions of  $\theta_{fiber}$  (vector field) and  $DOA$  for the MVAL tissue (b) after preconditioning, and (c-d) under various biaxial loads.

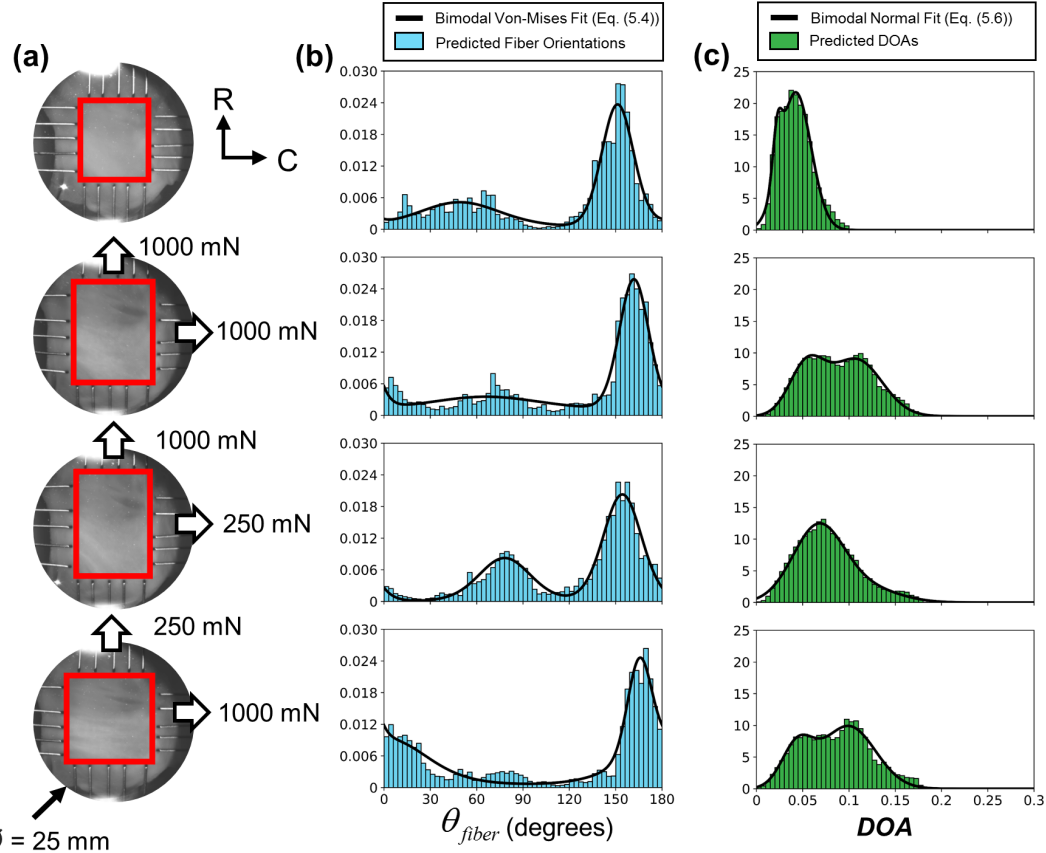


**Figure 5.6.** Distributions of the  $\theta_{fiber}$  and  $DOA$  predictions from MVAL testing in Figure 5.5. (a) Testing image of the MVAL with the region of interest (ROI) outlined in red and loading labelled. Histograms of (b) the  $\theta_{fiber}$  distributions with the corresponding bimodal von Mises distribution fit (Eq. (5.4)) and (c) the  $DOA$  distributions with the corresponding bimodal normal distribution fit (Eq. (5.6)). The parameters of the fit are summarized in Table 5.2), where the distributions were obtained from all the pixels in the ROI.

Both the  $\theta_{fiber}$  and  $DOA$  distributions for the MVAL tissue sample exhibited a salient bimodal character, regardless of loading state (Fig. 5.6b,c). Based on these observations, and previous studies suggesting the presence of multiple fiber families in heart leaflets [118], we used bimodal models to quantify the  $\theta_{fiber}$  and  $DOA$  distributions. For the fiber orientation, a bimodal  $\pi$ -periodic von Mises distribution was used in the fitting, as a more

tractable alternative to a wrapped bimodal normal distribution. The distribution is described by:

$$\hat{f}(\theta_{fiber} | \mu_1, \kappa_1, \mu_2, \kappa_2, w) = w g(\theta_{fiber} | \mu_1, \kappa_1) + (1-w) g(\theta_{fiber} | \mu_2, \kappa_2), \quad (5.4)$$

and

$$g(\theta_{fiber} | \mu, \kappa) = \frac{1}{180^\circ I_0(\kappa)} e^{\kappa \cos[2(\theta_{fiber} - \mu)]} \quad (5.5)$$

where  $(\mu_1, \kappa_1)$  and  $(\mu_2, \kappa_2)$  are the parameters associated with the first von Mises distribution and the second von Mises distribution, respectively,  $I_0$  is the zeroth-order Bessel function, and  $w \in [0,1]$  is the mixing parameter.  $\kappa$ , the dispersion parameter with range  $[0,1]$ , can be considered analogous to  $1/\sigma^2$ , where  $\sigma$  is the standard deviation of a corresponding normal distribution.

Similarly, the predicted *DOA* was fit by a bimodal normal distribution:

$$\bar{f}(DOA | \bar{\mu}_1, \bar{\sigma}_1, \bar{\mu}_2, \bar{\sigma}_2, \bar{w}) = \bar{w} h(DOA | \bar{\mu}_1, \bar{\sigma}_1) + (1-\bar{w}) h(DOA | \bar{\mu}_2, \bar{\sigma}_2), \quad (5.6)$$

and

$$h(DOA | \bar{\mu}, \bar{\sigma}) = \frac{1}{\sqrt{2\pi\bar{\sigma}^2}} e^{-\frac{(DOA - \bar{\mu})^2}{2\bar{\sigma}^2}} \quad (5.7)$$

where  $(\bar{\mu}_1, \bar{\sigma}_1)$  and  $(\bar{\mu}_2, \bar{\sigma}_2)$  are the parameters associated with the two mixing normal distributions, respectively, and  $\bar{w} \in [0,1]$  is the mixing parameter.

The  $\theta_{fiber}$  and  $DOA$  measured frequencies (Fig. 5.6) were both normalized prior to fitting with their respective probability distribution functions. The fitting parameters, along with the coefficient of determination for each model fit ( $R^2$ ) and the tissue stretches are presented for each loading ratio in Table 5.2.

**Table 5.2.** Bulk distributions of the CFA in the MVAL (cf. Fig. 5.5 and Fig. 5.6). Bimodal fiber orientation and  $DOA$  fitting are described by Eqns. (5.4) & (5.6), respectively.

FIBER ORIENTATION VON MISES DISTRIBUTION FIT						
$F_C:F_R$	$\mu_1$ (deg.)	$\kappa_1$ (x10 <sup>-3</sup> )	$w$	$\mu_2$ (deg.)	$\kappa_2$ (x10 <sup>-3</sup> )	$R^2$
<b>0 mN:0 mN</b>	49.063	0.347	0.401	151.199	2.42	0.908
<b>1000 mN:1000 mN</b>	66.038	0.148	0.416	161.794	2.84	0.936
<b>250 mN:1000 mN</b>	78.135	0.917	0.360	154.321	1.66	0.943
<b>1000 mN:250 mN</b>	3.005	0.386	0.666	165.323	4.32	0.938
DOA BIMODAL NORMAL DISTRIBUTION FIT						
$F_C:F_R$	$\bar{\mu}_1$	$\bar{\sigma}_1$	$\bar{w}$	$\bar{\mu}_2$	$\bar{\sigma}_2$	$R^2$
<b>0 mN:0 mN</b>	0.0226	0.0049	0.0922	0.0424	0.0166	0.993
<b>1000 mN:1000 mN</b>	0.0544	0.0189	0.3747	0.1078	0.0279	0.990
<b>250 mN:1000 mN</b>	0.0665	0.0275	0.8066	0.1174	0.0348	0.993
<b>1000 mN:250 mN</b>	0.0442	0.0169	0.2788	0.0995	0.0291	0.980
TISSUE DEFORMATION						
$F_C:F_R$	$\lambda_C$	$\lambda_R$				
<b>0 mN:0 mN</b>	1.0	1.0				
<b>1000 mN:1000 mN</b>	1.169	1.268				
<b>250 mN:1000 mN</b>	1.060	1.311				
<b>1000 mN:250 mN</b>	1.241	1.113				

As shown in Figure 5.6 and Table 5.2, the orientation distributions varied substantially with the applied loading ratio. For example, when  $F_C:F_R=250$  mN:1000 mN, the distributions moved toward the radial tissue direction to support the radially-concentrated loading, with the smaller peak rotating from 66.1° under equibiaxial loading to 78.2°, and

the larger peak rotating from  $161.8^\circ$  to  $154.3^\circ$ . Similarly, when  $F_C:F_R=1000\text{ mN}:250\text{ mN}$  the peaks moved toward the circumferential tissue direction, with the smaller peak adjusting from  $66.1^\circ$  under equibiaxial loading to  $2.9^\circ$  under circumferentially-concentrated loading and the larger peak adapting from  $161.8^\circ$  to  $165.2^\circ$  under this circumferential-preferred loading state.

As for the the *DOA* distributions, the most straightforward result is the general increase in *DOA* from the unloaded state to all loaded states. We also found that when the orientation distributions demonstrated two apparently distinct peaks, the *DOA* distributions generally exhibited either a single peak or two peaks with similar means. Conversely, in loading states where the orientation distributions coalesced, the *DOA* distributions separated. For example, when the  $F_C:F_R=250\text{ mN}:1000\text{ mN}$  the orientation exhibited two distinct groupings, but the *DOA* was apparently unimodal. However, when the  $F_C:F_R=1000\text{ mN}:250\text{ mN}$  the orientation distribution became nearly unimodal and the corresponding *DOA* distribution exhibited two distinct peaks. This curious pattern holds for the  $F_C:F_R=1000\text{ mN}:1000\text{ mN}$  and  $F_C:F_R=0\text{ mN}:0\text{ mN}$  distributions as well, albeit with smaller magnitudes.

A uniform result across each loading ratio as observed from this study is the tissue microstructural affinity for the circumferential direction. For each loading state, the center of the larger fiber distribution fell between  $151^\circ$  and  $4^\circ$ . Although the exact position changed with the loading ratio, the more prevalent fiber family was *always* oriented along the circumferential tissue direction. The *DOA* distributions affirmed the circumferential proclivity of the tissue microstructure; the average *DOA* over the ROI was 0.085 for  $F_C:F_R=1000\text{ mN}:250\text{ mN}$ , but decreased to 0.078 under  $F_C:F_R=250\text{ mN}:1000\text{ mN}$ . That is,

for equivalent biaxial loading magnitudes, we generally observed more aligned fibers when the loading prejudice was in the circumferential tissue direction rather than the radial direction. This circumferential inclination manifests in the tissue stretches as well, with stretches of 26.80% in the radial direction but only 16.87% in the circumferential direction under the equibiaxial load ( $F_C:F_R=1000$  mN:1000 mN). The extensive circumferential affinity in tissue microstructure will be discussed further in relation to heart valve tissue mechanical properties in *Section 5.4.2*.

*Remark:* It should be noted that the assumption of bimodal microstructural distributions was made *a-priori* to allow quantifications of the  $\theta_{fiber}$  and *DOA* distributions of the MVAL tissue sample, as well as their dependence on the applied loads. While other models may more completely represent the population distributions, these bimodal models suffice for our demonstrative purposes.

### 5.3.3 Quantified transmural CFA for the MVAL tissues

The microstructure of an MVAL sample at various depths was also analyzed according to (Eq. (C.14)). Before assessing the imaging results, it's important to understand the layered structure of the MVAL. A cross-sectional histological view of the MVAL morphology is shown in Figure 5.7a, where collagen fibers are stained in blue, and each layer is labeled with its respective thickness [146]. In this study, we examined an MVAL with a thickness of 0.87 mm from the atrialis-side at various imaging depths as shown in Figure 5.7b. We imaged the unloaded tissue at each penetration depth (Fig. 5.7b), then applied an equibiaxial load of  $F_C:F_R=1000$  mN:1000 mN and repeated the pSFDI imaging (Fig. 5.7c).

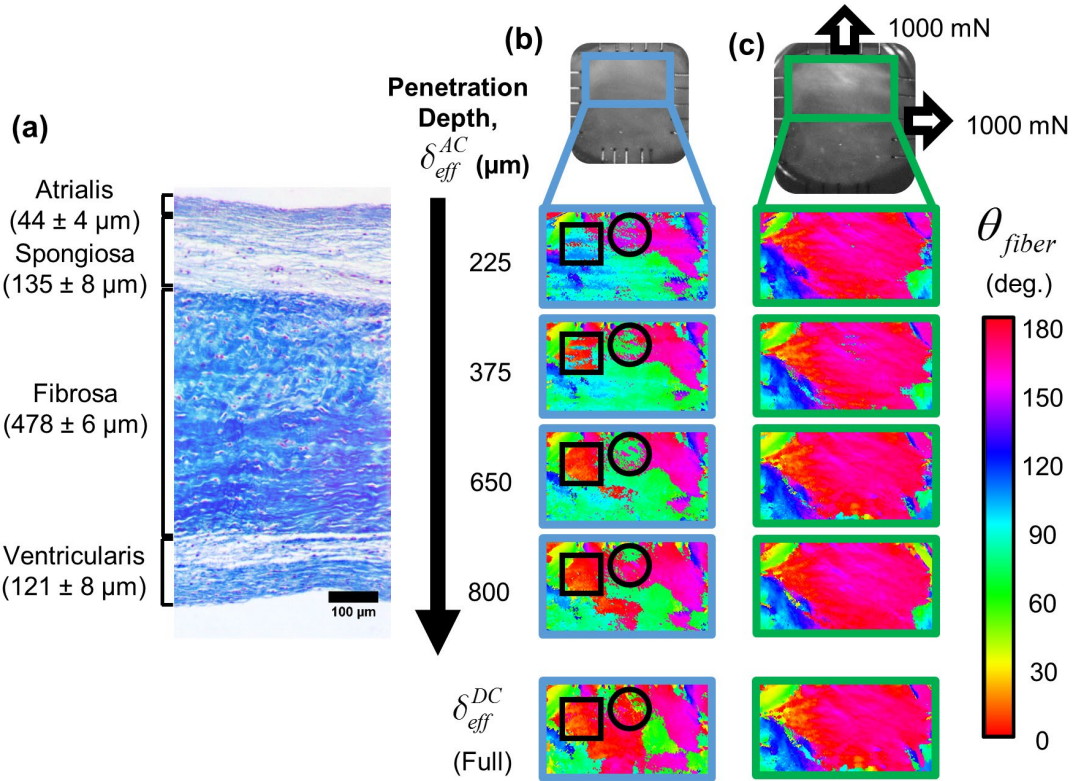


**Figure 5.7.** Depth-modulated microstructural predictions from the integrated biaxial-pSF DI system. (a) Histological image illustrating the 4 morphologically distinct layers of a typical porcine MVAL tissue sample (image modified from [147]). Predictions of  $\theta_{fiber}$  from the AC intensities for a porcine MVAL tissue sample (thickness=0.87 mm) at various penetration depths associated with different spatial frequencies ( $f_x$ ) determined based on Eq. (5.3): (b) after preconditioning, and (c) under equibiaxial loading of 1000 mN. Predictions from the DC intensities are included to compare orientation predictions extracted from the full optical thickness.

In the unloaded state, the fiber orientations showed substantial depth-variance (Figure 5-7a). For example, the predicted fiber orientation changes from  $\sim 90^\circ$  at the shallowest imaging depth ( $225 \mu\text{m}$ ) to  $\sim 0^\circ$  as the imaging depth increases (the black square). Similar depth-dependent orientations can be observed in the upper-central region of the unloaded

test (the black circle), where the predominant fiber orientation changes from  $\sim 160^\circ$  to a mixture of  $\sim 0^\circ$  and  $\sim 70^\circ$  fiber orientations as the imaging depth increases. These results indicate that the spatial organization of collagen fibers may be different in the uppermost atrialis layer from the inferior fibrosa layer for an unloaded MVAL. In contrast, these depth-dependent differences become indiscernable when the MVAL tissue was subjected to the biaxial loading (Fig. 5.7c). Specifically, the fiber orientation quantifications in the loaded tissue are nearly independent of imaging depth, for the range of the examined spatial frequencies. This novel finding suggests that, while unloaded fiber orientations vary with tissue layers, the fiber orientations in the biaxially-loaded MVAL ( $F_C:F_R = 1000 \text{ mN}:1000 \text{ mN}$ ) are uniform throughout the atrialis and fibrosa layers.

## 5.2.4 Discussion

### 5.4.1 Evaluation of the integrated system's capabilities

This study has demonstrated the capability of an integrated biaxial-pSF DI system to quantify the collagen microstructures of soft tissues under various mechanical loading conditions. First of all, we found that although the fiber orientation predictions for the bovine tendon samples were mainly accurate (Fig. 5.3). Still, we observed some local irregularities due mainly to rough sample surfaces rather than any systemic prediction biases. For example, the thin streaks of incorrect predictions for the tissues in Figure 5.3 correspond to regions where the collagen fiber bundles on the tissue surface were not compressed against the microscope slide. These surface irregularities caused specular reflections, resulting in the incorrect fiber predictions. The systemic preference for a smooth sample surface is manifest further in the dynamic uniaxial testing on bovine tendon (Fig. 5.4). Specifically, orientation predictions for the loaded tissue in Figure 5.4b

contained striations of incorrect predictions of  $\sim 160^\circ$  along the direction of applied force, seemingly caused by heterogeneous loading throughout the tissue. We observed that loading caused collagen fiber bundles to be nonuniformly recruited and form an uneven surface geometry, generating abnormal reflections and subsequent incorrect predictions. This observation is supported by the *DOA* measurements for the loaded tissue, which show substantial spatial differences in fiber recruitment. This unfortunate systemic dependence on a smooth surface could be easily improved by using a larger spatial smoothing kernel in the analysis, at the cost of prediction resolution, or submerging the testing samples in a bath to reduce the magnitude of the difference in index of refraction between the tissue and the surrounding media, as implemented in the MVAL tissue imaging experiments.

Fortunately, the surface effects found in the tendon analysis did not persist into the study of the MVAL microstructure due to the smooth leaflet surface and the PBS bath. However, because the MVAL were kept hydrated in a solution bath during testing, we observed pointwise irregularities in the MVAL predictions due to impurities drifting on the surface of the PBS solution. We also saw some specular reflections from the surface of the PBS, but these “bright spots” were typically outside of the tissue domain (Fig. 5.5a), and could be relocated via adjusting the incidence angle of the projected light. In addition to capturing collagen fiber architecture throughout the tissue domain, our system was able to monitor the changes in local fiber networks in response to the varied applied loads. This novel capability is a powerful tool for providing new insight into tissue fiber microstructures. For example, dynamic fiber distributions across the MVAL have been quantified and analyzed (Fig. 5.5 and Fig. 5.6) for the first time, yielding a better understanding of the fiber architectural behaviors within the MVAL subjected to mechanical loading. We expect that

subsequent studies will similarly shed light on a variety of previously impenetrable phenomena by examining the dynamic microstructures of a variety of collagenous tissues.

In the spatial frequency study (*Study B*), we noticed the appearance of some banding in the image of the unloaded tissue at the higher spatial frequencies (Fig. 5.7b). Since one of the purposes of demodulating the 3 phase-shifted initial images into the AC image is to ensure a uniform illumination, no indication of the incident light projection should appear in the resultant images. These bands did not appear at lower spatial frequencies, nor in the loaded tissue predictions (Fig. 5.7c). We suspect these bands were caused by a systemic flaw manifesting only at high spatial frequency and weak sample birefringence. While our captured intensities encode predominantly information from the sample, there is a small amount of light that is reflected from the surface of the polarizer and captured by the camera. For larger spatial frequencies and more reflective samples, this minor reflection error is negated by the signal from the tissue. However, at high spatial frequencies, the minor reflection can cause the intensity skew in the captured images from sinusoidal, leading to banding in the AC combined images. These errors could be remedied in future studies by systemic normalizations and improved calibrations, like those described in the recent paper by Goth. *et al.* (2019), or by restricting the incident spatial frequency to a given range [148]. Despite the appearance of these bands, our system was able to capture the changes to microstructure that accompany loading throughout the thickness of the MVAL. This capacity has numerous applications in the analysis of a variety of layered tissues, such as skin tissue, arteries, gastrointestinal wall, and others.

### **5.4.2 Relationship between CFA and tissue mechanics in the MVAL**

Our study revealed the complexity of load-dependence in MVAL tissue microstructure; these quantified microstructural behaviors can shed light on many of the phenomena observed in mechanical studies on the MV leaflets, such as the material anisotropy, nonlinearity, and the observed spatial variations [147, 149, 150]. Our study revealed that, although the collagen fibers in the MVAL are not perfectly oriented in the circumferential direction, the fibers demonstrate a predominant circumferential orientation even under preferential loading in the radial direction (Fig. 5.6d). This circumferential tendency corresponds to the higher circumferential stiffness in the mechanical response of the heart valve leaflets, contributing to the tissue material's anisotropy. In terms of the spatial differences in tissue microstructures, our study demonstrated that the microstructures of the MVAL tissue sample were generally spatially heterogenous regardless of the applied loads (Fig. 5.5). The observed microstructural heterogeneity in the MVAL echoes the previous findings of mechanical differences across different MVAL regions [149]. In addition to the material anisotropy and the regional variance, ongoing studies are using this integrated system to examine the microstructural basis for the nonlinear mechanical response of the heart valve leaflets. Preliminary results suggest that after a large amount of deformation and fiber realignment, indicated by the toe-region of the mechanical curve, the CFA reaches a “terminal” point and will adjust no further. This cessation of microstructural change corresponds to a rapid stiffening in the tissue mechanics, thus enforcing the observed nonlinear mechanical curves (manuscript in preparation). As demonstrated by this pilot study, quantifying the load-dependent microstructure in membranous tissues like the MVAL can allow explanation of the tissue mechanics from a

microstructural basis. This deeper comprehension of the microstructure behind the tissue's mechanical properties will be essential for improving the understanding of the diseased tissue states and for enriching computational models of the heart valve function [151].

### **5.4.3 Concluding remarks**

This study contributes to the fields of biological tissue imaging and biomechanics. Our contributions can be summarized as follows: (1) development of a novel integrated pSFDI with biaxial mechanical testing system for dynamic microstructural quantification, (2) validation of the system through imaging on static and dynamic bovine tendon tissue samples, and (3) presentation of the local and bulk microstructural properties of collagen fibers in an MVAL sample under a variety of loading conditions, providing examples of the unique and extensive microstructural quantification capabilities of the integrated system. Following this presentation of results, we provided a transparent assessment of the strengths and weaknesses of the system. Finally, we indicated future paths to improve the system capabilities alongside research extensions and investigations we believe will improve the diagnosis and treatment of collagenous tissue diseases through fundamental engineering mechanics study.

## CHAPTER 6. CONCLUSION

### 6.1 Summary of Thesis Contributions

The mechanical responses of each of the two MV and three TV leaflets have been quantified and reported. Additionally, the effects of various testing parameters – including loading rate, testing temperature, and species – on the mechanical responses of the leaflets has been investigated. To provide context for the mechanical behaviors, the distributions of the chordae tendineae, the leaflet thicknesses, and the leaflet compositions were also quantified and presented. Subsequently, the spatial variance in the mechanical properties of the MVAL and TVAL was examined; results showed heterogeneous mechanical properties in both anterior leaflets. This observation prompted further investigation into the microstructural basis for the spatially-varied mechanical behaviors. Through literature review, existing collagen fiber quantification techniques were found to be inadequate for characterizing the desired dynamic and spatially-varied CFA in the HV tissues. To characterize this dynamic CFA, a pSFDI system was developed and assessed through testing on bovine tendon samples before integration with a biaxial mechanical tester. Preliminary dynamic CFA predictions for MVAL tissues were obtained through integrated testing, and bimodal fiber orientation and *DOA* distributions were quantified and modeled.

This research has quantified the MV and TV leaflet mechanics, informing reproduction of healthy tissue behaviors in both computational models and replacement biomaterials. The system developed in this study allows improved analysis of the mechanics-microstructure relationship in collagenous materials, serving as a tool for future investigations.

## 6.2 Recommendations for Future Work

### 6.2.1 Microstructure and mechanics studies

As mentioned in *Section 5.1*, no existing studies have quantified the microstructure of the TV leaflets. Our group seeks to remedy this omission via investigation of the regionally-varied microstructure of the TV leaflets through dynamic pSF DI followed by histological methods. This analysis will provide quantification and comparison of three essential properties of the TV leaflets: (1) the dynamic CFA, as obtained through the combined pSF DI-mechanical testing results, (2) the bulk mechanical response over the belly region of the leaflet under multiple loading protocols, as obtained from the biaxial tester, and (3) the depth-varied microstructural composition, as obtained from histological image processing. Representative results from the combined mechanical-structural quantification for the TVSL are presented in Figure 6.1. The results show that, although fiber alignment tends to prefer the circumferential direction, the distribution is highly nonuniform. Like the MVAL sample from *Section 5.3.2*, we found dynamic CFA in the TVSL demonstrated directionally-dependent properties. Specifically, we saw higher *DOA* with circumferential-prejudiced loading (Fig. 6.1d), compared to similar loading concentrated in the radial-direction (Fig. 6.1c). In addition to these analyses, we conducted histology on three tissue samples extracted from different regions of the TVSL. We expect this combined quantification technique will improve understanding of spatial variance in the TV leaflets and the mechanics-microstructure relationships. Our ongoing project seeks to perform and publish similar analyses for all the three TV leaflets.

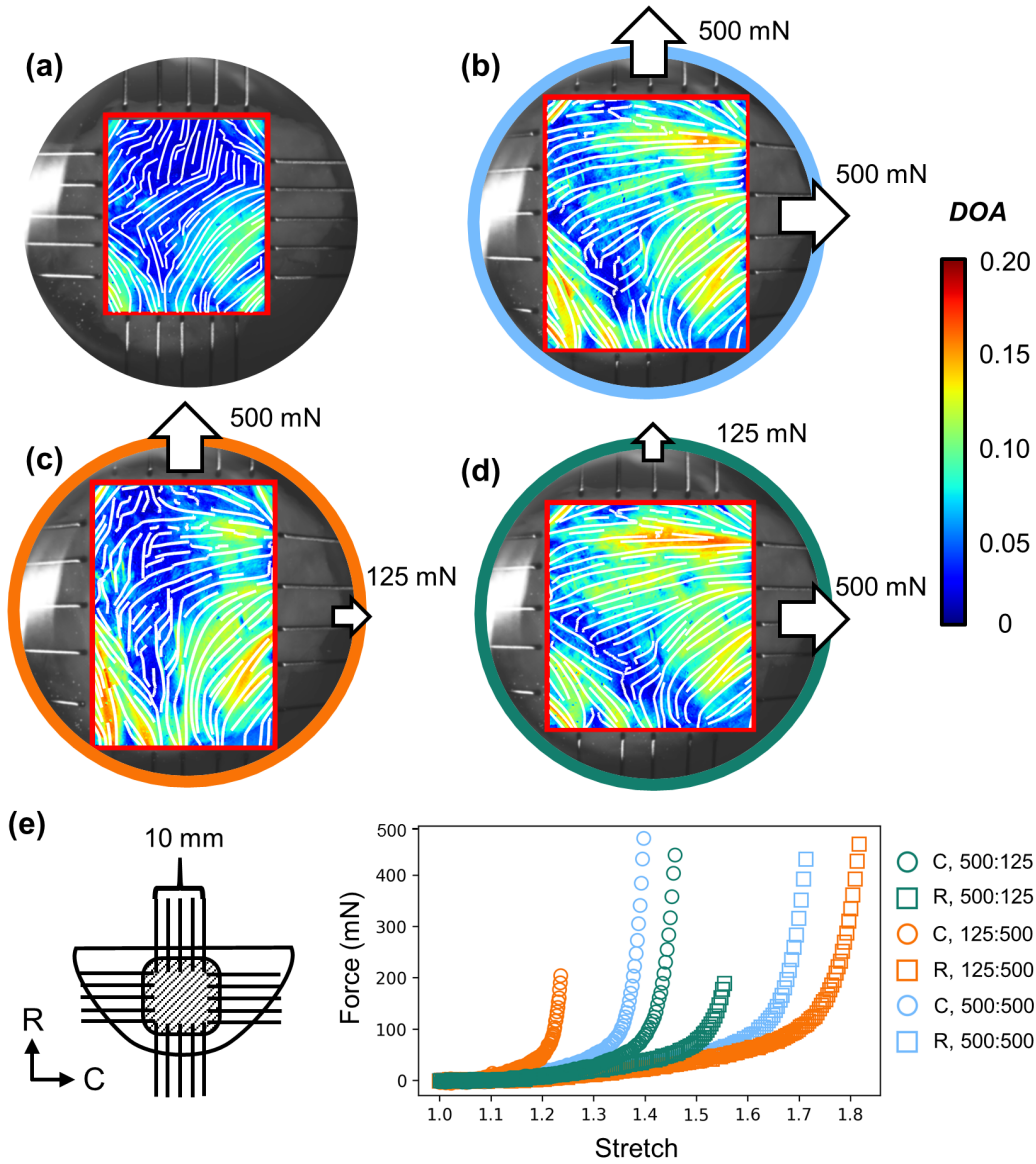


**Figure 6.1.** (a-d) CFA predictions and (e) mechanical response curves for a TVSL tissue specimen subjected to loading ratios ( $F_C:F_R$ , mN) of (a) 0:0, after preconditioning, (b) 500:500, (c) 125:500, and (d) 500:125. White streamlines show  $\theta_{fiber}$ , while DOA is represented via colormap. Note that tissues were imaged at the maximum load of each mechanical curve.

In addition to further analysis of the TV leaflets, future valuable studies could examine further effects of varying the different biaxial mechanical testing parameters. Despite the

many studies presented in this thesis, we still have little understanding of how testing procedures such as freezing, PBS immersion, and effective loaded region size affect the observed mechanical properties of the leaflet tissues. These and similar effect studies could provide scope to the works presented herein and help to elucidate the *in vivo* mechanical behaviors of the valve tissues.

### **6.2.2 Biomaterials testing**

To complement studies on the mechanical properties and microstructures of the atrioventricular leaflets, our group seeks to analyze biomaterials used in the design of replacement bioprosthetic heart valves. Thanks to the dynamic CFA quantification system, we expect new perspectives on the biomechanical similarity of the heart valve replacement materials could be gained. Typically, chemically-fixed bovine pericardial tissue is used as a biomaterial for heart valve replacement (*cf. Section 2.1.3*) [152, 153]. An ongoing study seeks to examine how the various treatment parameters, including fixation time, tissue loading at fixation, and chemical concentration, among others, affect the dynamic CFA in the pericardial tissues. Furthermore, we plan to compare CFAs in these fixed tissues to those of native leaflets to understand how the mechanics and CFA of the artificial material differ, potentially causing functional disparities between native and replacement valves.

### **6.1.2 Interval imaging project**

Our group seeks to understand how the CFA changes in the heart valve leaflets throughout the physiological loading cycle. Rather than examining the tissue at the mechanical endpoints, we recently developed software to examine the tissue at multiple intervals throughout the loading domain, as depicted in Figure 6.2. We expect this interval analysis

will allow elucidation of the microstructural basis for the observed nonlinearity in the tissue mechanical response, among other findings. Through this new software development, we can obtain 10 discrete CFA quantifications throughout the mechanical loading curve in a 20-minute test. With this improved data acquisition rate, novel investigations into tissue mechanics and microstructures become feasible.

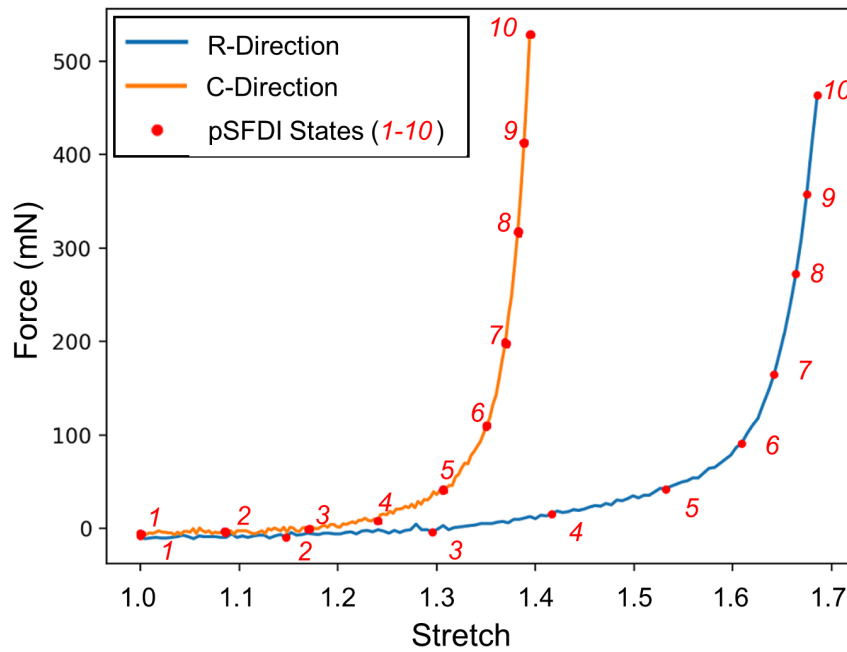


**Figure 6.2.** Depiction of CFA quantification at 10 distinct kinematic states over the physiological mechanical loading interval for a representative heart valve leaflet tissue.

### 6.2.3 Machine learning approaches to relate tissue CFA to mechanics

Machine learning approaches have recently shown promise in predicting tissue mechanical response from microstructures [154]. This capability has important applications in selection of biomaterials for use in synthetic heart valves and for biomaterials synthesis in other fields. We believe the quantitative CFA metrics supplied by the integrated-pSF DI system could provide valuable and novel inputs for predicting the mechanics-

microstructure relationship. However, machine learning models require large datasets to develop sufficient accuracy and generalizability. To increase the data output of our system, we have implemented measures such as the interval testing described previously (*cf.* *Section 6.2.2*) and are examining algorithmic methods for training broadly accurate algorithms on smaller datasets. We are excited to uncover the further details on the relationships between mechanics and microstructures through these algorithmic approaches.

## APPENDIX A: NOMENCLATURE AND SYMBOLS

<b>Class</b>	<b>Abbreviation</b>	<b>Description</b>
Organs	HV	Heart Valve
	MV	Mitral Valve
	TV	Tricuspid Valve
Leaflets	MVAL	Mitral Valve Anterior Leaflet
	MVPL	Mitral Valve Posterior Leaflet
	TVAL	Tricuspid Valve Anterior Leaflet
	TVPL	Tricuspid Valve Posterior Leaflet
	TVSL	Tricuspid Valve Septal Leaflet
Tissue Microstructure	CFA	Collagen Fiber Architecture
	DOA	Degree of Optical Anisotropy
	ECM	Extracellular Matrix
	GAG	Glycosaminoglycan
	PG	Proteoglycan
	VIC	Valvular Interstitial Cells
Mechanics	AI	Anisotropy Index
	PK	Piola-Kirchhoff
Directions	C	Circumferential direction
	R	Radial direction
Imaging Parameters	FOV	Field of View
	ROI	Region of Interest
Imaging Techniques	SALS	Small-Angle Light Scattering
	SFDI	Spatial Frequency Domain Imaging
	SHG	Second Harmonic Generation
	PLM	Polarized Light Microscopy
	pSFDI	Polarized Spatial Frequency Domain Imaging
	Q-PLM	Quantitative Polarized Light Microscopy

Mechanical Loading	$T$	Applied Membrane Tension
	$\mathbf{P}$	1 <sup>st</sup> -Piola-Kirchhoff (1 <sup>st</sup> -PK) Stress Tensor
	$\mathbf{S}$	2 <sup>nd</sup> -Piola-Kirchhoff (2 <sup>nd</sup> -PK) Stress Tensor
	$\boldsymbol{\sigma}$	Cauchy Stress Tensor
Sample Deformation	$\mathbf{C}$	Right Cauchy-Green Deformation Tensor
	$\mathbf{d}_I$	Displacement of Node $I$
	$\mathbf{E}$	Green Strain Tensor
	$\mathbf{F}$	Deformation Gradient Tensor
	$J$	Jacobian; Determinant of the Deformation Tensor
	$\lambda_{C,R}$	Principal Stretch in the Circumferential (C) or Radial (R) Direction
	$\lambda_{C,R}^{0-peak}$	Peak Stretch in the Circumferential or Radial Direction
	$\lambda_{C,R}^{0-1}$	Preconditioning Stretch in the Circumferential or Radial Direction
	$\lambda_{C,R}^{1-peak}$	Mechanical Stretch in the Circumferential or Radial Direction
	$\mathbf{x}_I$ 's	Undeformed Fiducial Marker Coordinates Prior to Loading
Sample Geometry	$L$	Effective Edge Length of Loaded Region
	$t_s$	Sample Thickness
Light Properties	$f_x$	Spatial Frequency of Projection Pattern
	$I$	Captured Light Intensity
	$\vec{S}$	Stokes Vector of Polarized Light
	$\theta_{polarizer}$	Linear Polarization Axis of Light
Sample Optical Properties	$\delta$	Birefringent Sample Phase Retardance
	$D$	Birefringent Sample Diattenuation
	$\mu_s'$	Sample Reduced Scattering Coefficient
	$\mu_a$	Sample Absorption Coefficient
	$R$	Reflectance of a Sample
	$\theta_{fiber}$	Planar Collagen Fiber Orientation in a Sample
System Optical Properties	$\delta_{eff}^{DC,AC}$	Effective Penetration Depth of Optical Signal (DC or AC)
	$\mathbf{M}$	Mueller Matrix of Polarized Light Transport

	$\tau_{sys}$	System Parameter Containing Non-Birefringent Optical Modifiers
Optical Fitting	$a_{0,2,4}$	Fourier Fitting Coefficients
Distribution Fitting	$\mu_{1,2}$	Mean of the First and Second Distributions
	$P$	Mixing Parameter of the Bimodal Distributions
	$\sigma_{1,2}$	Standard Deviation of the First and Second Distributions
Other	SEM	Standard Error of the Mean
	VHD	Valvular Heart Disease

## APPENDIX B: STATISTICAL ANALYSIS OF BIAXIAL TESTING DATA

We present statistical analyses for the equibiaxial protocol ( $T_{C,\max}:T_{R,\max} = 1:1$ ) of 3 different experimental groups, as described in *Section 3.2.3*: (1) the loading rate effect study, (2) the temperature effect group, and (3) the species effect group. We consider tissue responses in the circumferential and radial directions separately in the statistical analysis of each of these studies. For each of these experimental groups, three different stretch measures are examined, as described in detail in *Section 3.2.7*.

For each leaflet within the loading rate effect group, the statistical analysis of stretch in each direction for each valve leaflet of MVAL, MVPL, TVAL, TVPL, and TVSL is presented in its respective figure (Figs. B.1-B.5). The statistical analysis results from the loading-rate group for the mitral and tricuspid valve leaflets are presented in Table B.1 and Table B.2, respectively. Similarly, our statistical analysis results associated with the temperature effect group are presented in Figures B.6-B.10, and in Table B.3 and Table B.4. As for the species group, the statistical analysis results for the MVAL and TVAL tissues are presented in Table B.5 and Table B.6, respectively.

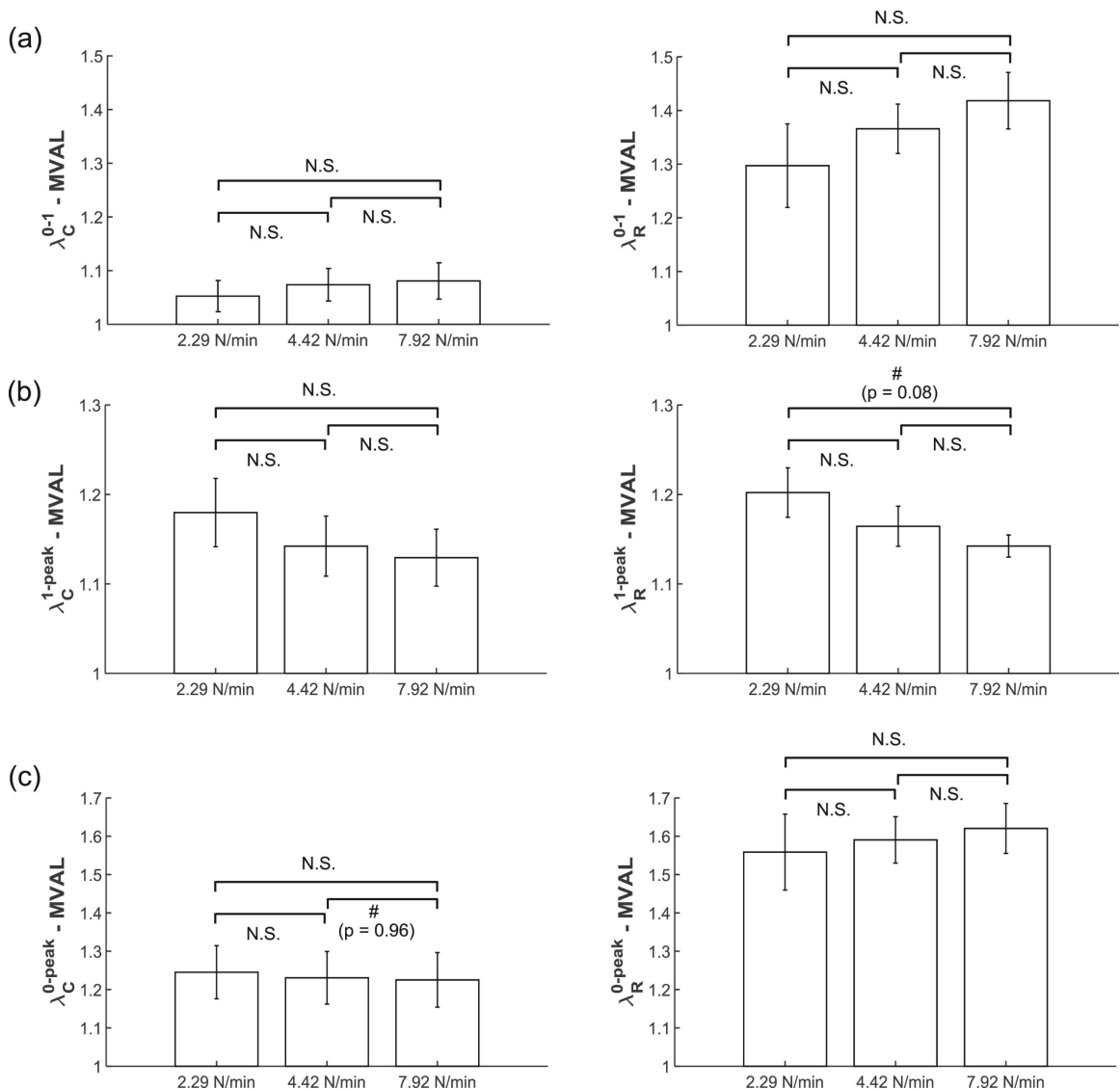


**Figure B.1.** Statistical analyses of the MVAL from the loading rate effect group (n=6), with plots showing trends in (a) the preconditioning stretches, (b) mechanical stretches, and (c) the peak stretches. All bars show mean  $\pm$  SEM. (N.S.: no statistically significant difference,  $p>0.10$ , #: nearly statistically significant difference,  $p<0.10$ , and \*: statistically significant difference,  $p<0.05$ )

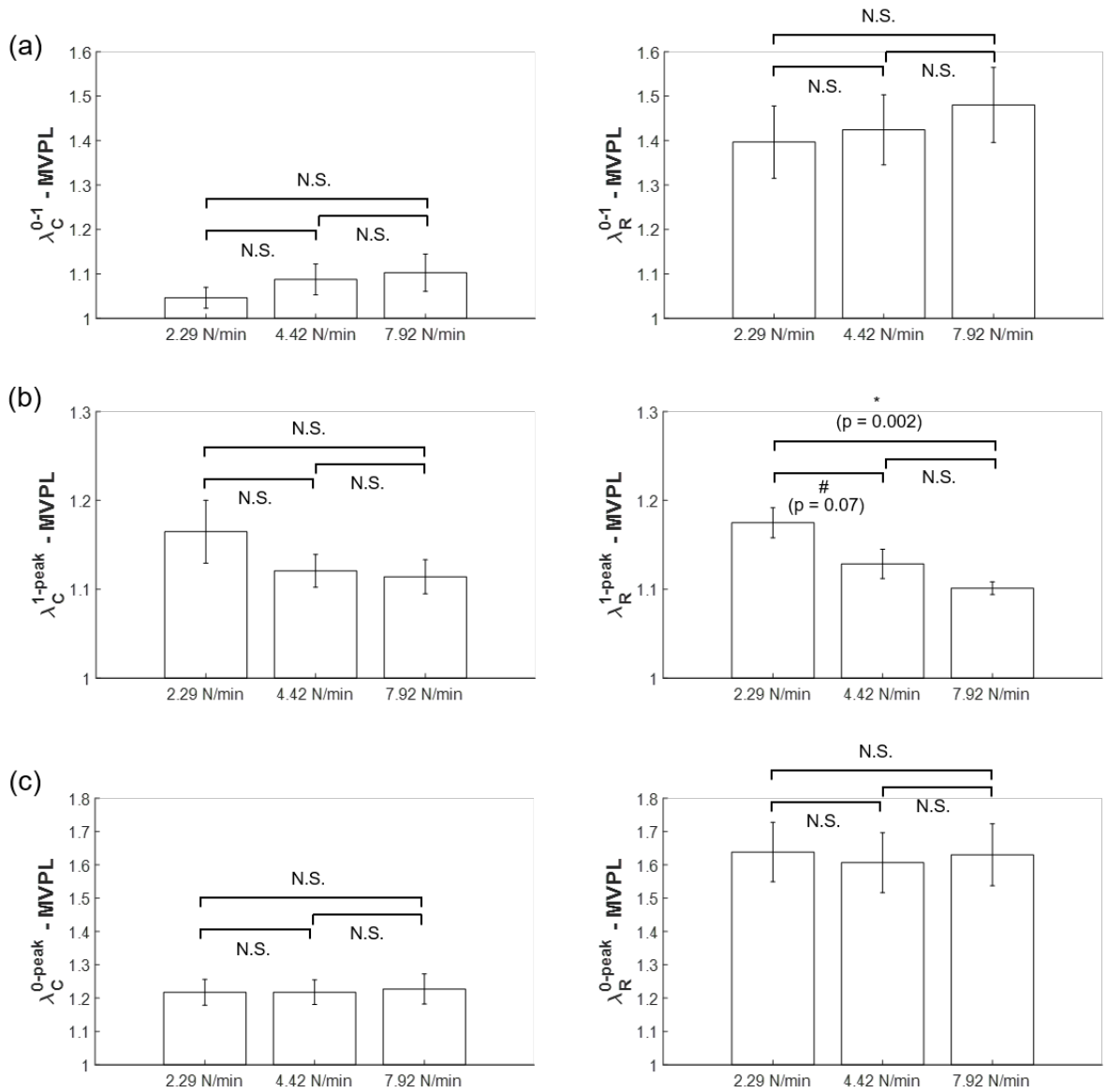


**Figure B.2.** Statistical analyses of the MVPL from the loading rate effect group (n=6), with plots showing trends in (a) the preconditioning stretches, (b) mechanical stretches, and (c) the peak stretches. All bars show mean  $\pm$  SEM. (N.S.: no statistically significant difference,  $p>0.10$ , #: nearly statistically significant difference,  $p<0.10$ , and \*: statistically significant difference,  $p<0.05$ )

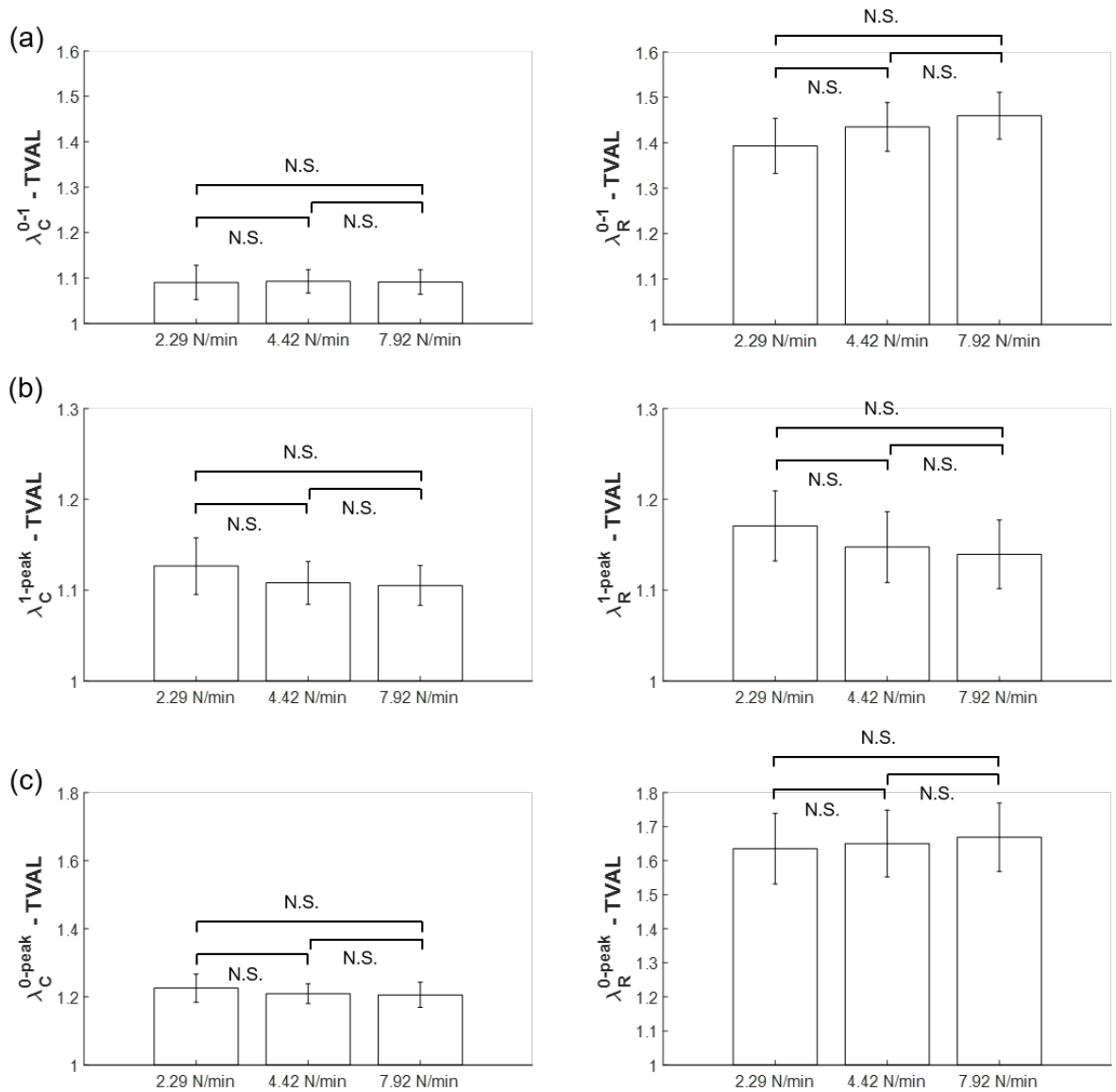


**Figure B.3.** Statistical analyses of the TVAL from the loading rate effect group ( $n=6$ ), with plots showing trends in (a) the preconditioning stretches, (b) mechanical stretches, and (c) the peak stretches. All bars show mean  $\pm$  SEM. (N.S.: no statistically significant difference,  $p>0.10$ )

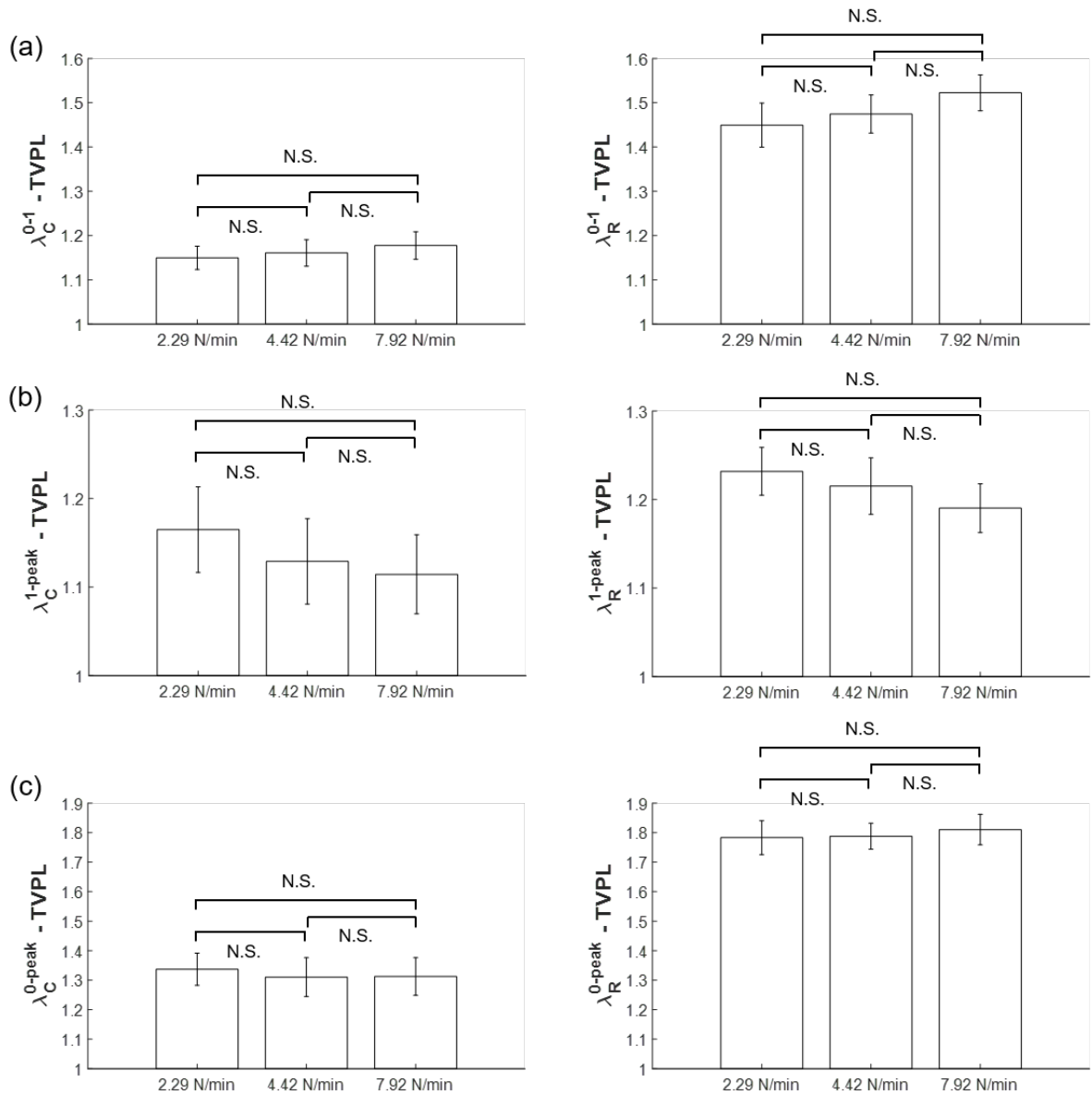


**Figure B.4.** Statistical analyses of the TVPL from the loading rate effect group ( $n=6$ ), with plots showing trends in (a) the preconditioning stretches, (b) mechanical stretches, and (c) the peak stretches. All bars show mean  $\pm$  SEM. (N.S.: no statistically significant difference,  $p>0.10$ )

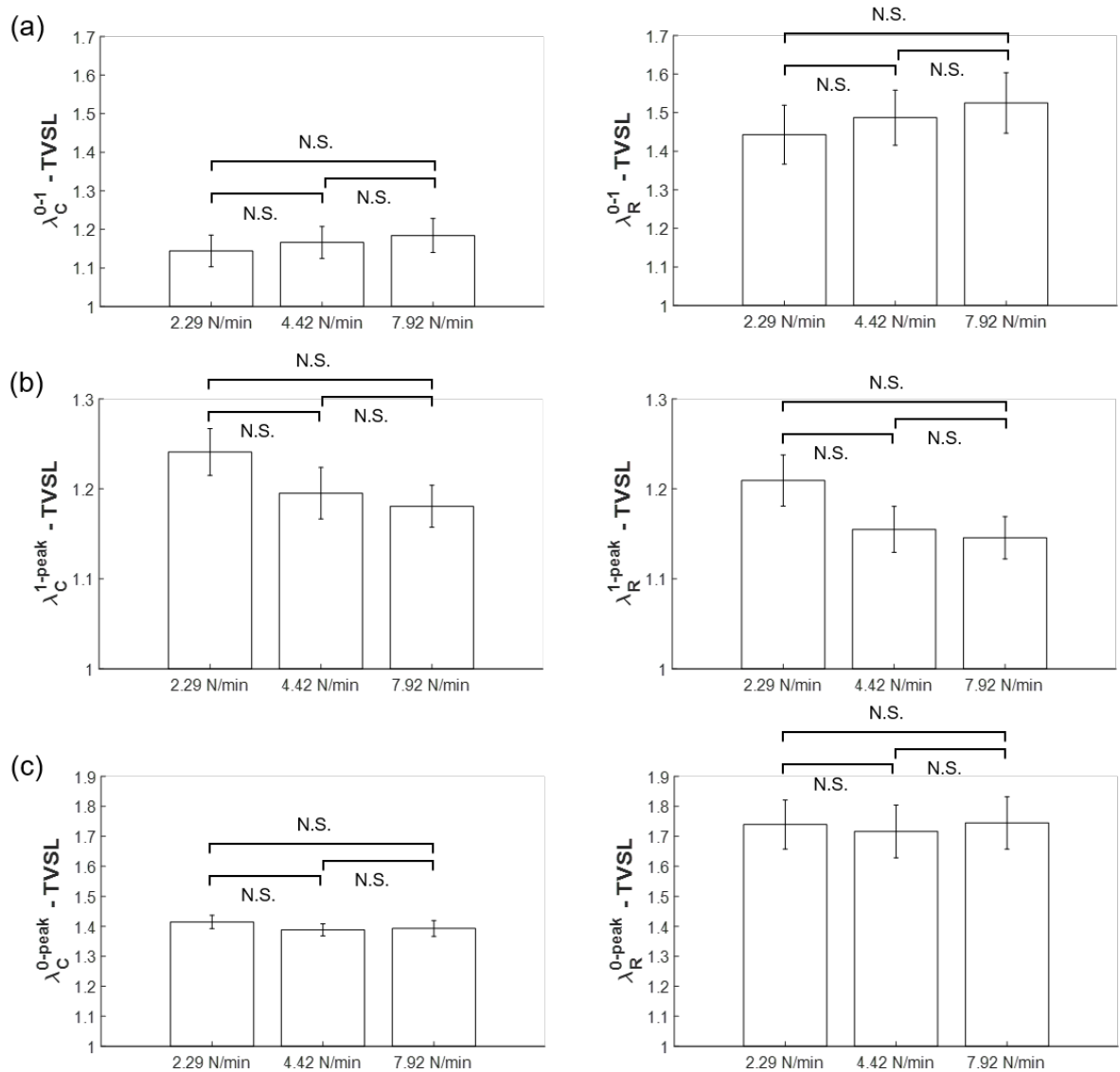


**Figure B.5.** Statistical analyses of the TVSL from the loading rate effect group (n=6), with plots showing trends in (a) the preconditioning stretches, (b) mechanical stretches, and (c) the peak stretches. All bars show mean  $\pm$  SEM. (N.S.: no statistically significant difference,  $p>0.10$ )

**Table B.1.** Statistical analysis of the loading rate effect group on the preconditioning ( $\lambda_C^{0-1}$  and  $\lambda_R^{0-1}$ ), mechanical ( $\lambda_C^{1-peak}$  and  $\lambda_R^{1-peak}$ ), and the peak stretches ( $\lambda_C^{0-peak}$  and  $\lambda_R^{0-peak}$ ) of the MVAL and MVPL tissues (n=6). Quantities are presented as mean  $\pm$  SEM.

<b>MVAL</b>						
<b>Circ.</b>	<b>2.29 N/min</b>	<b>4.42 N/min</b>	<b>7.92 N/min</b>	<b>p value (2.29-4.42)</b>	<b>p value (4.42-7.92)</b>	<b>p value (2.29-7.92)</b>
$\lambda_C^{0-1}$	1.053 $\pm$ 0.029	1.074 $\pm$ 0.030	1.081 $\pm$ 0.034	0.624	0.879	0.539
$\lambda_C^{1-peak}$	1.180 $\pm$ 0.038	1.142 $\pm$ 0.034	1.129 $\pm$ 0.032	0.479	0.785	0.334
$\lambda_C^{0-peak}$	1.245 $\pm$ 0.069	1.231 $\pm$ 0.069	1.225 $\pm$ 0.071	0.884	0.956	0.844
<b>Rad.</b>	<b>2.29 N/min</b>	<b>4.42 N/min</b>	<b>7.92 N/min</b>	<b>p value (2.29-4.42)</b>	<b>p value (4.42-7.92)</b>	<b>p value (2.29-7.92)</b>
$\lambda_R^{0-1}$	1.297 $\pm$ 0.078	1.366 $\pm$ 0.046	1.418 $\pm$ 0.053	0.464	0.472	0.227
$\lambda_R^{1-peak}$	1.202 $\pm$ 0.028	1.164 $\pm$ 0.022	1.142 $\pm$ 0.012	0.315	0.408	0.077
$\lambda_R^{0-peak}$	1.559 $\pm$ 0.099	1.590 $\pm$ 0.061	1.620 $\pm$ 0.065	0.789	0.744	0.614
<b>MVPL</b>						
<b>Circ.</b>	<b>2.29 N/min</b>	<b>4.42 N/min</b>	<b>7.92 N/min</b>	<b>p value (2.29-4.42)</b>	<b>p value (4.42-7.92)</b>	<b>p value (2.29-7.92)</b>
$\lambda_C^{0-1}$	1.046 $\pm$ 0.023	1.088 $\pm$ 0.035	1.103 $\pm$ 0.042	0.349	0.787	0.268
$\lambda_C^{1-peak}$	1.165 $\pm$ 0.035	1.121 $\pm$ 0.019	1.114 $\pm$ 0.019	0.295	0.808	0.235
$\lambda_C^{0-peak}$	1.218 $\pm$ 0.039	1.218 $\pm$ 0.037	1.227 $\pm$ 0.045	0.999	0.871	0.873
<b>Rad.</b>	<b>2.29 N/min</b>	<b>4.42 N/min</b>	<b>7.92 N/min</b>	<b>p value (2.29-4.42)</b>	<b>p value (4.42-7.92)</b>	<b>p value (2.29-7.92)</b>
$\lambda_R^{0-1}$	1.397 $\pm$ 0.081	1.424 $\pm$ 0.079	1.480 $\pm$ 0.084	0.812	0.639	0.492
$\lambda_R^{1-peak}$	1.175 $\pm$ 0.017	1.129 $\pm$ 0.016	1.101 $\pm$ 0.007	0.077	0.159	0.0024
$\lambda_R^{0-peak}$	1.638 $\pm$ 0.089	1.606 $\pm$ 0.090	1.630 $\pm$ 0.093	0.807	0.859	0.951

**Table B.2.** Statistical analysis of the loading rate effect on the preconditioning, mechanical, and peak stretches of the TVAL, TVPL, and TVSL tissues (n=6) (mean  $\pm$  SEM)

TVAL						
Circ.	2.29 N/min	4.42 N/min	7.92 N/min	p value (2.29-4.42)	p value (4.42-7.92)	p value (2.29-7.92)
$\lambda_C^{0-1}$	1.090 $\pm$ 0.038	1.093 $\pm$ 0.026	1.091 $\pm$ 0.027	0.954	0.966	0.982
$\lambda_C^{1-peak}$	1.127 $\pm$ 0.031	1.108 $\pm$ 0.024	1.105 $\pm$ 0.022	0.647	0.929	0.587
$\lambda_C^{0-peak}$	1.226 $\pm$ 0.041	1.210 $\pm$ 0.029	1.206 $\pm$ 0.037	0.758	0.936	0.728
Rad.	2.29 N/min	4.42 N/min	7.92 N/min	p value (2.29-4.42)	p value (4.42-7.92)	p value (2.29-7.92)
$\lambda_R^{0-1}$	1.393 $\pm$ 0.061	1.435 $\pm$ 0.054	1.459 $\pm$ 0.052	0.618	0.747	0.424
$\lambda_R^{1-peak}$	1.171 $\pm$ 0.039	1.147 $\pm$ 0.039	1.140 $\pm$ 0.038	0.678	0.888	0.576
$\lambda_R^{0-peak}$	1.635 $\pm$ 0.104	1.650 $\pm$ 0.098	1.668 $\pm$ 0.101	0.919	0.899	0.823
TVPL						
Circ.	2.29 N/min	4.42 N/min	7.92 N/min	p value (2.29-4.42)	p value (4.42-7.92)	p value (2.29-7.92)
$\lambda_C^{0-1}$	1.150 $\pm$ 0.026	1.161 $\pm$ 0.030	1.178 $\pm$ 0.031	0.780	0.708	0.506
$\lambda_C^{1-peak}$	1.165 $\pm$ 0.048	1.129 $\pm$ 0.048	1.114 $\pm$ 0.045	0.610	0.829	0.461
$\lambda_C^{0-peak}$	1.337 $\pm$ 0.054	1.310 $\pm$ 0.066	1.312 $\pm$ 0.064	0.763	0.983	0.776
Rad.	2.29 N/min	4.42 N/min	7.92 N/min	p value (2.29-4.42)	p value (4.42-7.92)	p value (2.29-7.92)
$\lambda_R^{0-1}$	1.449 $\pm$ 0.050	1.474 $\pm$ 0.043	1.523 $\pm$ 0.040	0.712	0.433	0.281
$\lambda_R^{1-peak}$	1.232 $\pm$ 0.027	1.215 $\pm$ 0.032	1.190 $\pm$ 0.028	0.700	0.567	0.306
$\lambda_R^{0-peak}$	1.783 $\pm$ 0.057	1.788 $\pm$ 0.044	1.810 $\pm$ 0.052	0.947	0.746	0.729
TVSL						
Circ.	2.29 N/min	4.42 N/min	7.92 N/min	p value (2.29-4.42)	p value (4.42-7.92)	p value (2.29-7.92)
$\lambda_C^{0-1}$	1.144 $\pm$ 0.041	1.166 $\pm$ 0.041	1.184 $\pm$ 0.044	0.712	0.773	0.521
$\lambda_C^{1-peak}$	1.241 $\pm$ 0.026	1.195 $\pm$ 0.029	1.181 $\pm$ 0.023	0.264	0.701	0.115
$\lambda_C^{0-peak}$	1.414 $\pm$ 0.023	1.388 $\pm$ 0.020	1.393 $\pm$ 0.027	0.404	0.888	0.549
Rad.	2.29 N/min	4.42 N/min	7.92 N/min	p value (2.29-4.42)	p value (4.42-7.92)	p value (2.29-7.92)
$\lambda_R^{0-1}$	1.443 $\pm$ 0.076	1.487 $\pm$ 0.071	1.525 $\pm$ 0.078	0.682	0.725	0.469
$\lambda_R^{1-peak}$	1.209 $\pm$ 0.029	1.155 $\pm$ 0.026	1.146 $\pm$ 0.024	0.186	0.796	0.117
$\lambda_R^{0-peak}$	1.739 $\pm$ 0.081	1.716 $\pm$ 0.088	1.745 $\pm$ 0.087	0.853	0.823	0.9613

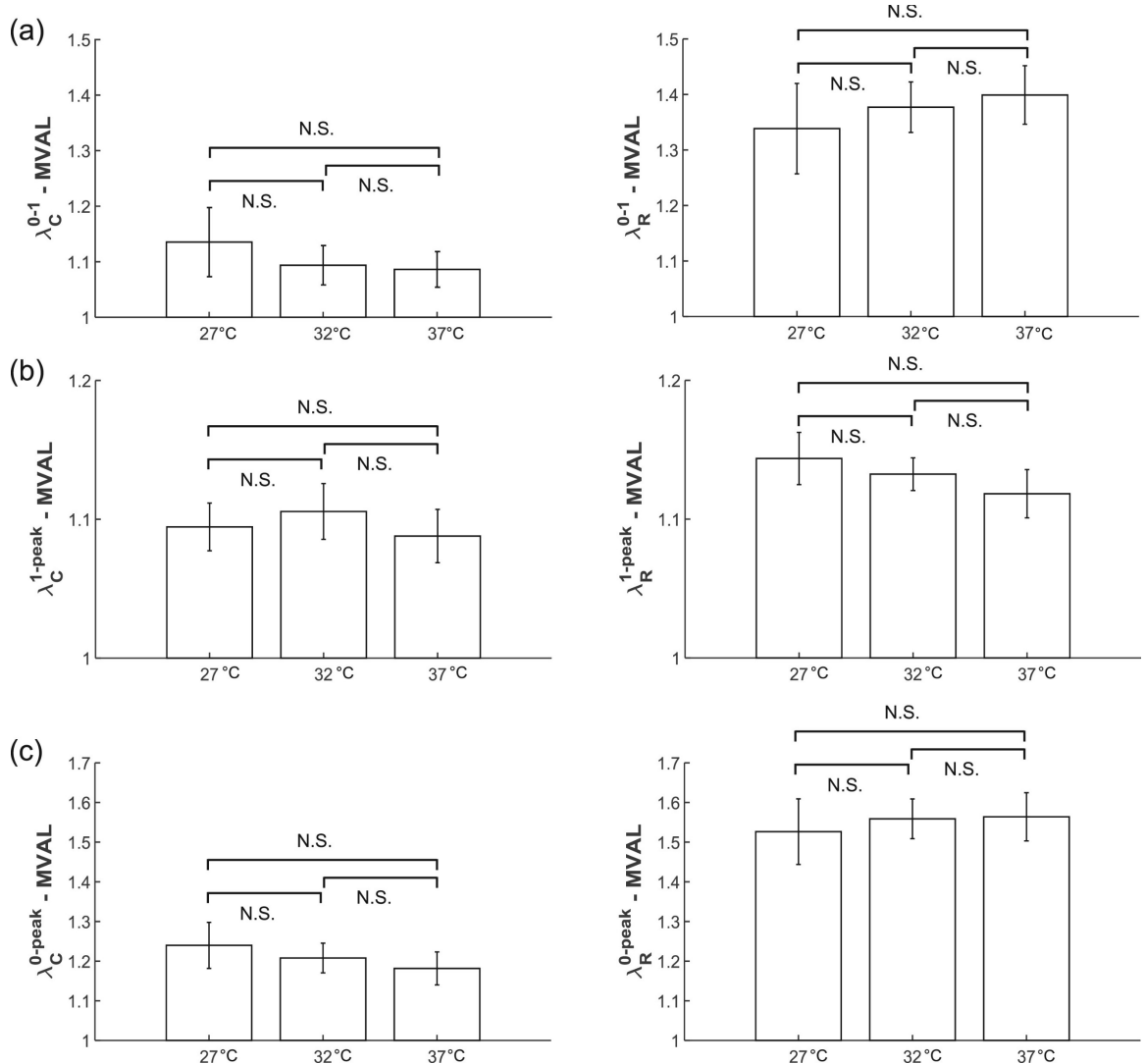


**Figure B.6.** Statistical analyses of the MVAL from the temperature effect group (n=6), with plots showing trends in (a) the preconditioning stretches, (b) mechanical stretches, and (c) the peak stretches. All bars show mean  $\pm$  SEM. (N.S.: no statistically significant difference,  $p>0.10$ )

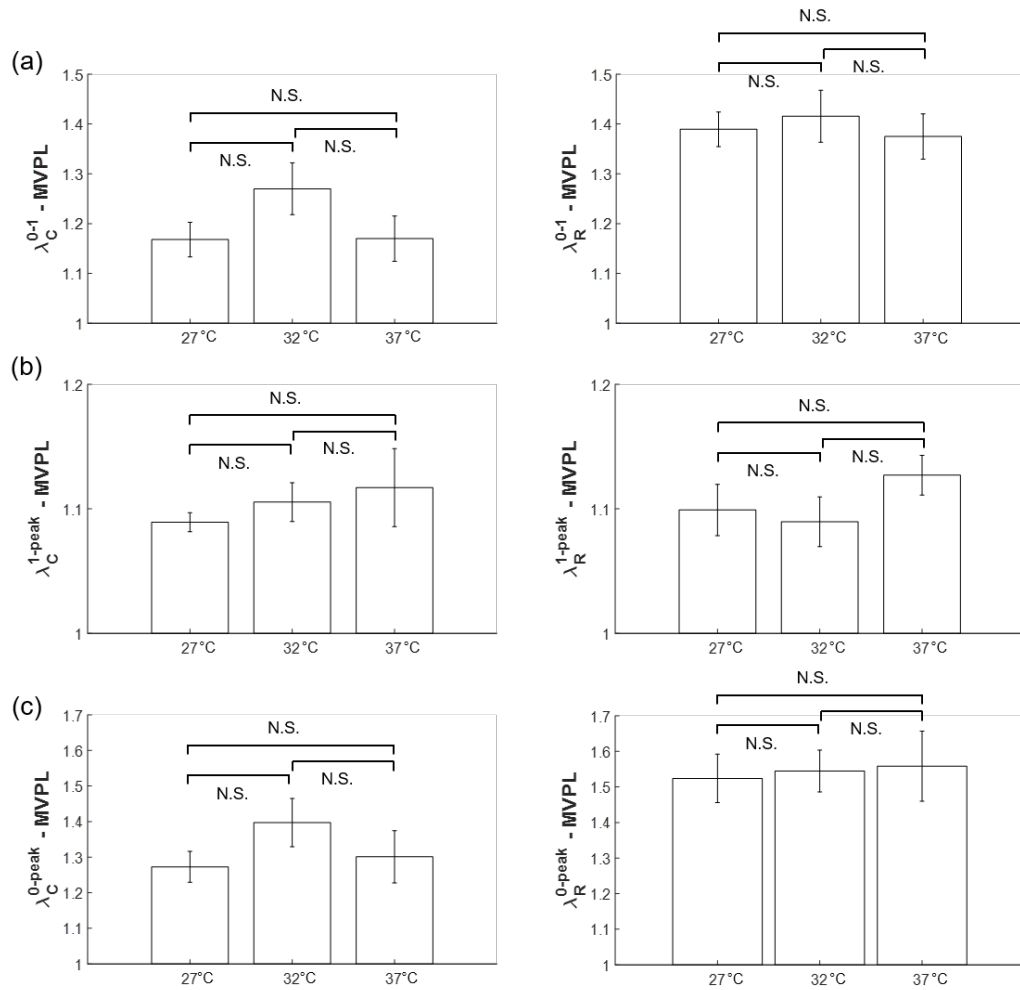


**Figure B.7.** Statistical analyses of the MVPL from the temperature effect group ( $n=6$ ), with plots showing trends in (a) the preconditioning stretches, (b) mechanical stretches, and (c) the peak stretches. All bars show mean  $\pm$  SEM. (N.S.: no statistically significant difference,  $p>0.10$ )

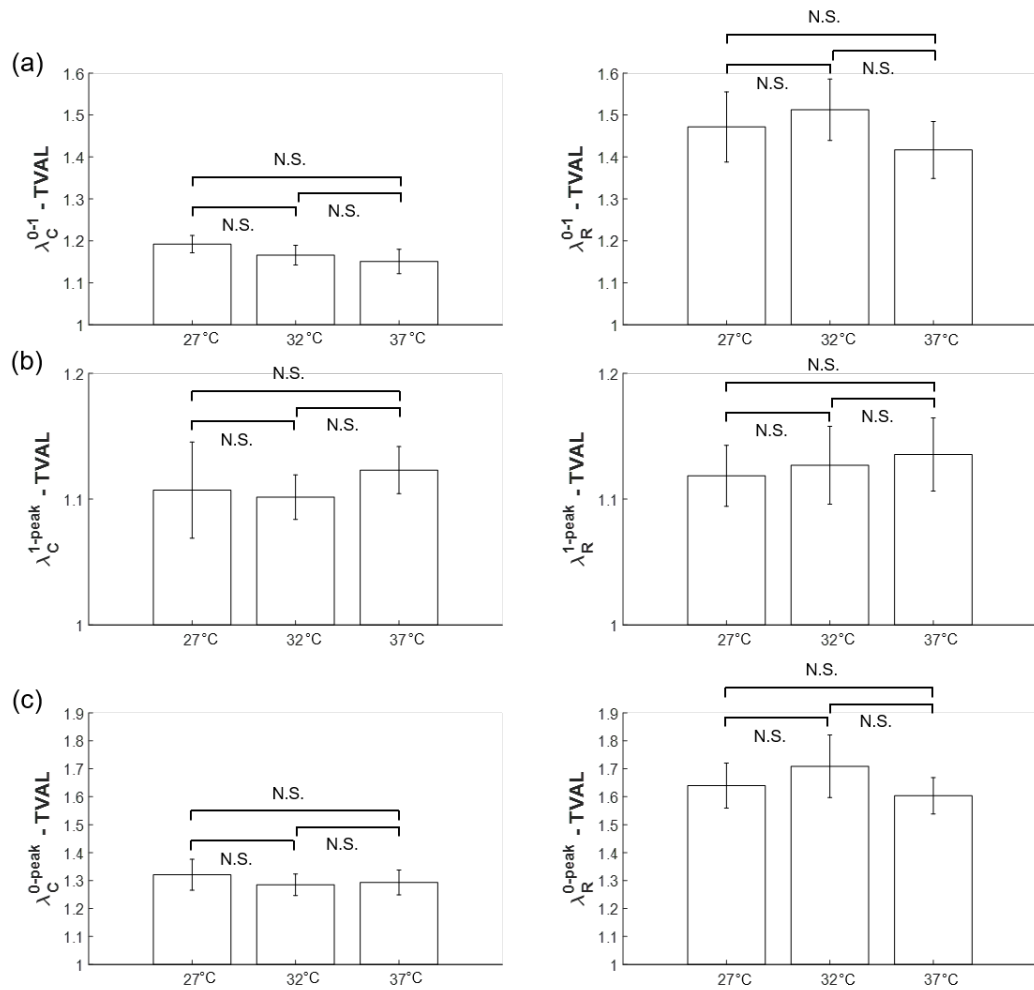


**Figure B.8.** Statistical analyses of the TVAL from the temperature effect group (n=6), with plots showing trends in (a) the preconditioning stretches, (b) mechanical stretches, and (c) the peak stretches. All bars show mean  $\pm$  SEM. (N.S.: no statistically significant difference,  $p>0.10$ )

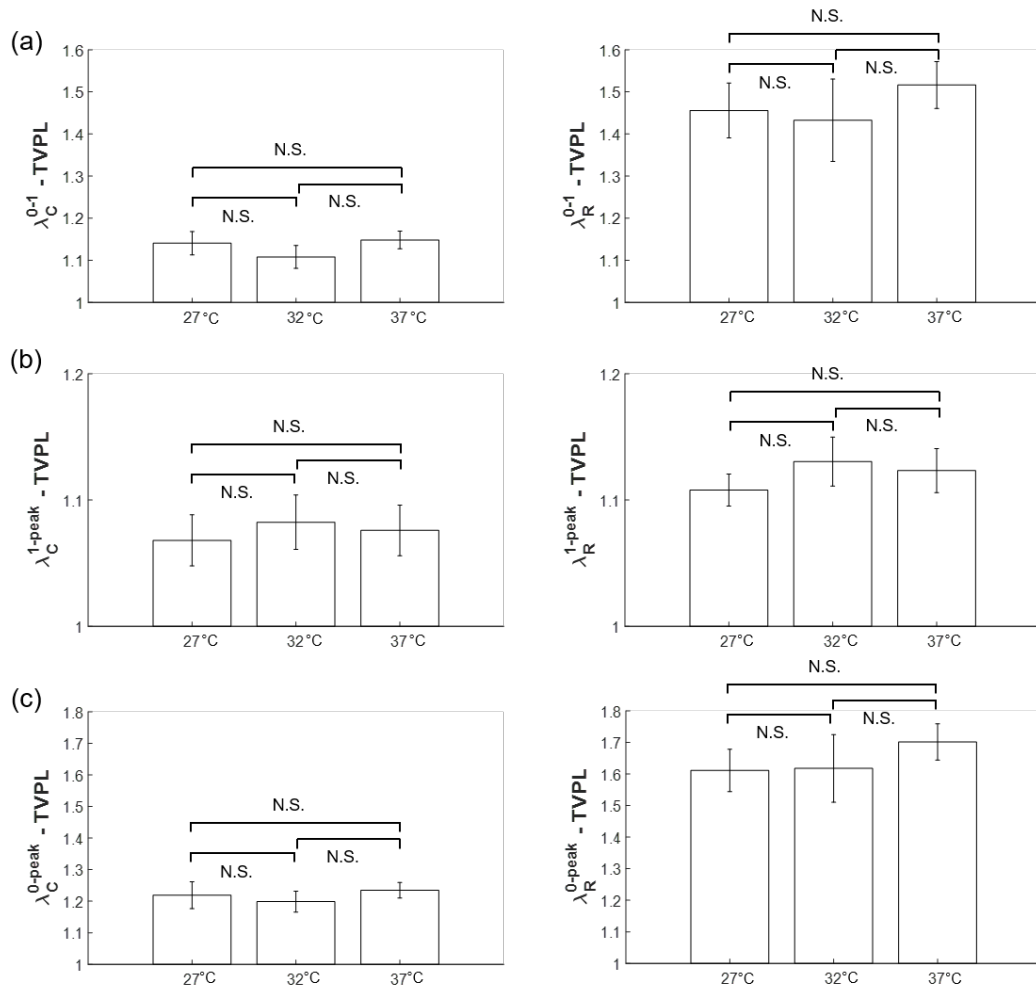


**Figure B.9.** Statistical analyses of the TVPL from the temperature effect group ( $n=6$ ), with plots showing trends in (a) the preconditioning stretches, (b) mechanical stretches, and (c) the peak stretches. All bars show mean  $\pm$  SEM. (N.S.: no statistically significant difference,  $p>0.10$ )

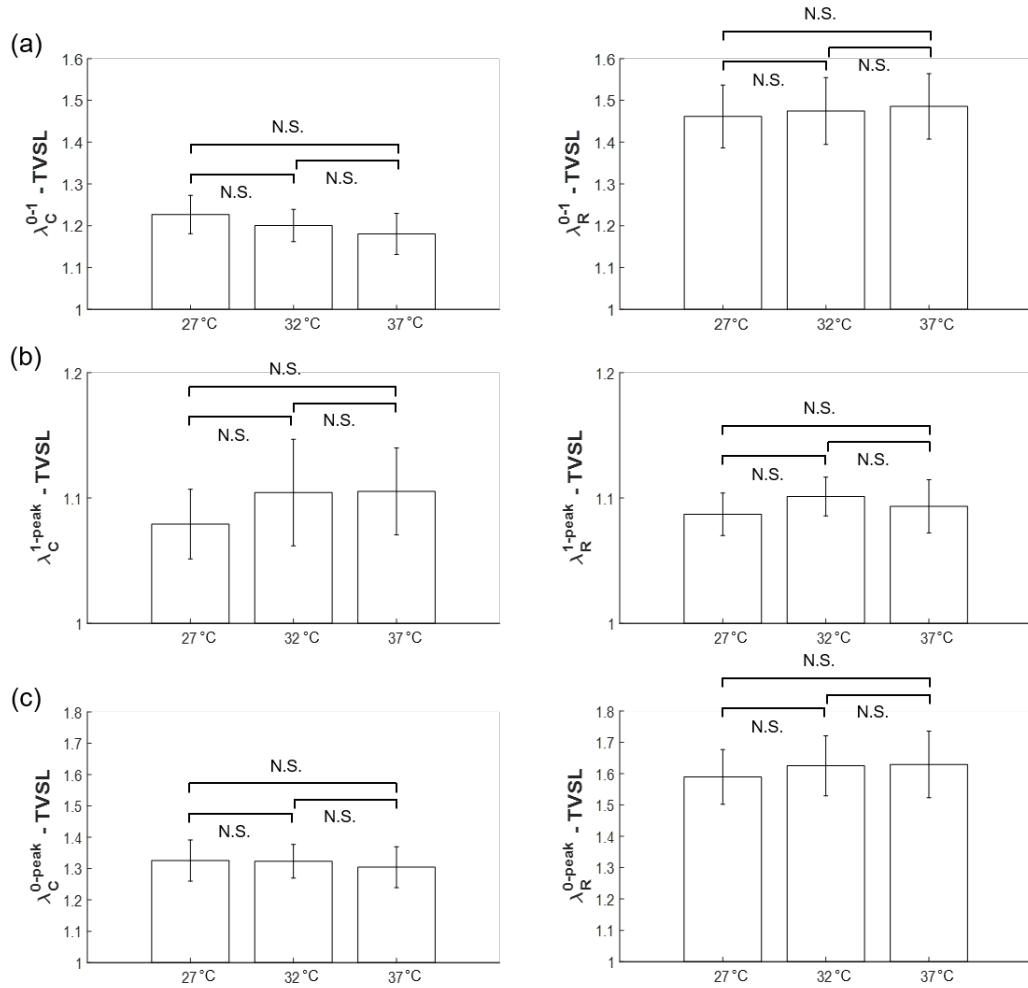


**Figure B.1.** Statistical analyses of the TVSL from the temperature effect group (n=6), with plots showing trends in (a) the preconditioning stretches, (b) mechanical stretches, and (c) the peak stretches. All bars show mean  $\pm$  SEM. (N.S.: no statistically significant difference,  $p>0.10$ )

**Table B.3.** Statistical analysis of the temperature effect group on the preconditioning ( $\lambda_C^{0-1}$  and  $\lambda_R^{0-1}$ ), mechanical ( $\lambda_C^{1-peak}$  and  $\lambda_R^{1-peak}$ ), and peak stretches ( $\lambda_C^{0-peak}$  and  $\lambda_R^{0-peak}$ ) of the MVAL and MVPL tissues (n=6). All quantities are presented as mean  $\pm$  SEM.

MVAL						
Circ.	27 °C	32 °C	37 °C	p value (27-32)	p value (32-37)	p value (27-37)
$\lambda_C^{0-1}$	1.046 $\pm$ 0.023	1.088 $\pm$ 0.035	1.103 $\pm$ 0.042	0.349	0.787	0.268
$\lambda_C^{1-peak}$	1.165 $\pm$ 0.035	1.121 $\pm$ 0.019	1.114 $\pm$ 0.019	0.295	0.808	0.235
$\lambda_C^{0-peak}$	1.218 $\pm$ 0.039	1.218 $\pm$ 0.037	1.227 $\pm$ 0.045	0.999	0.871	0.873
Rad.	27 °C	32 °C	37 °C	p value (27-32)	p value (32-37)	p value (27-37)
$\lambda_R^{0-1}$	1.397 $\pm$ 0.081	1.424 $\pm$ 0.079	1.480 $\pm$ 0.084	0.812	0.639	0.492
$\lambda_R^{1-peak}$	1.175 $\pm$ 0.017	1.129 $\pm$ 0.016	1.101 $\pm$ 0.007	0.142	0.159	0.106
$\lambda_R^{0-peak}$	1.638 $\pm$ 0.089	1.606 $\pm$ 0.090	1.630 $\pm$ 0.093	0.807	0.859	0.951
MVPL						
Circ.	27 °C	32 °C	37 °C	p value (27-32)	p value (32-37)	p value (27-37)
$\lambda_C^{0-1}$	1.168 $\pm$ 0.035	1.270 $\pm$ 0.052	1.170 $\pm$ 0.045	0.134	0.178	0.973
$\lambda_C^{1-peak}$	1.089 $\pm$ 0.008	1.105 $\pm$ 0.016	1.117 $\pm$ 0.031	0.370	0.749	0.410
$\lambda_C^{0-peak}$	1.273 $\pm$ 0.044	1.397 $\pm$ 0.068	1.301 $\pm$ 0.074	0.154	0.358	0.749
Rad.	27 °C	32 °C	37 °C	p value (27-32)	p value (32-37)	p value (27-37)
$\lambda_R^{0-1}$	1.389 $\pm$ 0.072	1.412 $\pm$ 0.059	1.375 $\pm$ 0.087	0.816	0.733	0.899
$\lambda_R^{1-peak}$	1.099 $\pm$ 0.072	1.090 $\pm$ 0.020	1.127 $\pm$ 0.016	0.747	0.175	0.385
$\lambda_R^{0-peak}$	1.524 $\pm$ 0.068	1.545 $\pm$ 0.059	1.558 $\pm$ 0.099	0.820	0.908	0.779

**Table B.4.** Statistical analysis of the temperature effect on the preconditioning, mechanical, and peak stretches of TVAL, TVPL, and TVSL tissues (n=6) (mean  $\pm$  SEM).

TVAL						
Circ.	27 °C	32 °C	37 °C	p value (27-32)	p value (32-37)	p value (27-37)
$\lambda_C^{0-1}$	1.192 $\pm$ 0.021	1.166 $\pm$ 0.023	1.151 $\pm$ 0.029	0.421	0.695	0.275
$\lambda_C^{1-peak}$	1.107 $\pm$ 0.038	1.102 $\pm$ 0.018	1.123 $\pm$ 0.019	0.739	0.427	0.716
$\lambda_C^{0-peak}$	1.321 $\pm$ 0.055	1.285 $\pm$ 0.039	1.293 $\pm$ 0.044	0.610	0.895	0.706
Rad.	27 °C	32 °C	37 °C	p value (27-32)	p value (32-37)	p value (27-37)
$\lambda_R^{0-1}$	1.472 $\pm$ 0.084	1.513 $\pm$ 0.073	1.417 $\pm$ 0.068	0.719	0.360	0.623
$\lambda_R^{1-peak}$	1.119 $\pm$ 0.084	1.513 $\pm$ 0.073	1.417 $\pm$ 0.068	0.719	0.360	0.623
$\lambda_R^{0-peak}$	1.640 $\pm$ 0.080	1.709 $\pm$ 0.112	1.603 $\pm$ 0.065	0.627	0.435	0.733
TVPL						
Circ.	27 °C	32 °C	37 °C	p value (27-32)	p value (32-37)	p value (27-37)
$\lambda_C^{0-1}$	1.141 $\pm$ 0.028	1.108 $\pm$ 0.027	1.148 $\pm$ 0.021	0.421	0.268	0.832
$\lambda_C^{1-peak}$	1.068 $\pm$ 0.020	1.082 $\pm$ 0.022	1.076 $\pm$ 0.020	0.636	0.831	0.786
$\lambda_C^{0-peak}$	1.219 $\pm$ 0.043	1.199 $\pm$ 0.033	1.235 $\pm$ 0.025	0.711	0.403	0.760
Rad.	27 °C	32 °C	37 °C	p value (27-32)	p value (32-37)	p value (27-37)
$\lambda_R^{0-1}$	1.456 $\pm$ 0.065	1.433 $\pm$ 0.098	1.515 $\pm$ 0.056	0.847	0.474	0.497
$\lambda_R^{1-peak}$	1.108 $\pm$ 0.013	1.130 $\pm$ 0.019	1.123 $\pm$ 0.017	0.352	0.791	0.487
$\lambda_R^{0-peak}$	1.611 $\pm$ 0.067	1.618 $\pm$ 0.107	1.701 $\pm$ 0.057	0.960	0.507	0.330
TVSL						
Circ.	27 °C	32 °C	37 °C	p value (27-32)	p value (32-37)	p value (27-37)
$\lambda_C^{0-1}$	1.227 $\pm$ 0.046	1.201 $\pm$ 0.039	1.804 $\pm$ 0.049	0.670	0.753	0.505
$\lambda_C^{1-peak}$	1.079 $\pm$ 0.028	1.104 $\pm$ 0.043	1.105 $\pm$ 0.035	0.630	0.987	0.569
$\lambda_C^{0-peak}$	1.326 $\pm$ 0.066	1.323 $\pm$ 0.054	1.305 $\pm$ 0.065	0.979	0.829	0.825
Rad.	27 °C	32 °C	37 °C	p value (27-32)	p value (32-37)	p value (27-37)
$\lambda_R^{0-1}$	1.462 $\pm$ 0.075	1.475 $\pm$ 0.080	1.486 $\pm$ 0.078	0.907	0.924	0.829
$\lambda_R^{1-peak}$	1.087 $\pm$ 0.017	1.101 $\pm$ 0.016	1.093 $\pm$ 0.021	0.550	0.770	0.820
$\lambda_R^{0-peak}$	1.589 $\pm$ 0.087	1.625 $\pm$ 0.096	1.629 $\pm$ 0.107	0.787	0.978	0.777

**Table B.5.** Statistical analysis results of the species effect group on the preconditioning (

$\lambda_C^{0-1}$  and  $\lambda_R^{0-1}$ ), mechanical ( $\lambda_C^{1-peak}$  and  $\lambda_R^{1-peak}$ ), and peak stretches ( $\lambda_C^{0-peak}$  and  $\lambda_R^{0-peak}$ ) of the MVAL tissue (n=6). All quantities are presented as mean  $\pm$  SEM.

Circ.	Porcine (P)	Adult Ovine (AO)	Juvenile Ovine (JO)	p value (P-AO)	p value (AO-JO)	p value (P-JO)
$\lambda_C^{0-1}$	1.086 $\pm$ 0.032	1.149 $\pm$ 0.057	1.196 $\pm$ 0.087	0.355	0.662	0.262
$\lambda_C^{1-peak}$	1.088 $\pm$ 0.019	1.113 $\pm$ 0.014	1.073 $\pm$ 0.075	0.314	0.614	0.854
$\lambda_C^{0-peak}$	1.181 $\pm$ 0.042	1.280 $\pm$ 0.069	1.270 $\pm$ 0.094	0.248	0.929	0.409
Rad.	Porcine (P)	Adult Ovine (AO)	Juvenile Ovine (JO)	p value (P-AO)	p value (AO-JO)	p value (P-JO)
$\lambda_R^{0-1}$	1.399 $\pm$ 0.053	1.443 $\pm$ 0.105	1.449 $\pm$ 0.102	0.717	0.967	0.372
$\lambda_R^{1-peak}$	1.118 $\pm$ 0.017	1.146 $\pm$ 0.031	1.074 $\pm$ 0.012	0.446	0.052	0.059
$\lambda_R^{0-peak}$	1.564 $\pm$ 0.061	1.654 $\pm$ 0.123	1.552 $\pm$ 0.104	0.527	0.542	0.925

**Table B.6.** Statistical analysis results of the species effect group on the preconditioning (

$\lambda_C^{0-1}$  and  $\lambda_R^{0-1}$ ), mechanical ( $\lambda_C^{1-peak}$  and  $\lambda_R^{1-peak}$ ), and peak stretches ( $\lambda_C^{0-peak}$  and  $\lambda_R^{0-peak}$ ) of the TVAL tissue (n=6). All quantities are presented as mean  $\pm$  SEM.

Circ.	Porcine (P)	Adult Ovine (AO)	Juvenile Ovine (JO)	p value (P-AO)	p value (AO-JO)	p value (P-JO)
$\lambda_C^{0-1}$	1.151 $\pm$ 0.029	1.379 $\pm$ 0.084	1.463 $\pm$ 0.095	0.028	0.522	0.010
$\lambda_C^{1-peak}$	1.123 $\pm$ 0.019	1.071 $\pm$ 0.016	1.023 $\pm$ 0.007	0.065	0.021	0.0005
$\lambda_C^{0-peak}$	1.293 $\pm$ 0.044	1.476 $\pm$ 0.044	1.495 $\pm$ 0.096	0.090	0.880	0.084
Rad.	Porcine (P)	Adult Ovine (AO)	Juvenile Ovine (JO)	p value (P-AO)	p value (AO-JO)	p value (P-JO)
$\lambda_R^{0-1}$	1.417 $\pm$ 0.068	1.601 $\pm$ 0.052	1.657 $\pm$ 0.076	0.057	0.555	0.040
$\lambda_R^{1-peak}$	1.137 $\pm$ 0.029	1.073 $\pm$ 0.014	1.038 $\pm$ 0.018	0.077	0.147	0.016
$\lambda_R^{0-peak}$	1.606 $\pm$ 0.064	1.716 $\pm$ 0.046	1.716 $\pm$ 0.061	0.181	0.999	0.239

## APPENDIX C: DERIVATIONS OF PSFDI FUNDAMENTAL EQUATIONS

### C.1 Derivation of pSFDI reflected intensity (Eq. (5.1)) from birefringent scattering theory

In this section, we describe the polarization of light as it passes through the pSFDI system, in the process deriving the Fourier cosine series form used to fit the reflected intensity curves (Eq. (5.1)) and relating sample optical properties to the Fourier fitting terms.

To illustrate changes to light polarization in the pSFDI system, we employ a standard Stokes/Mueller approach wherein the intensity and polarization state of light is contained within a 4x1 Stokes vector  $\vec{S}$ . The first element of  $\vec{S}$  denotes the light intensity and the subsequent 3 elements represent the light polarization. In the system, the action of each optical component is represented by a corresponding Mueller matrix ( $M^{4x4}$ ). At each interface, the incident Stokes vector is multiplied by the component's Mueller matrix to yield a modified Stokes vector describing the light after interaction. Due to the simplicity of the Stokes/Mueller formalism, the optical behavior of any system can be condensed via multiplication of sequential Mueller matrices to reduce to a single system matrix. For example, the entire polarization behavior of the pSFDI system can be condensed into a single expression, considering a local reference frame and a polarization angle of  $\theta_p$ :

$$\vec{S}_{out} = M_{pSFDI}(\theta_f, \theta_p) \vec{S}_{in}, \quad (C.1)$$

In this representation,  $\vec{S}_{in}$  and  $\vec{S}_{out}$  denote the Stokes vectors of the incident and output light, respectively, and  $M_{pSFDI}(\theta_f, \theta_p)$  is the Mueller matrix describing the behavior of the

pSFDI system with polarizer transmission axis at  $\theta_p$  and sample with fiber angle of  $\theta_f$ . To derive the full behavior of the pSFDI system, we can decompose the Mueller matrix into constituent components:

$$\mathbf{M}_{pSFDI}(\theta_f, \theta_p) = \mathbf{M}_{pol}(-\theta_p) \mathbf{M}_{sample}(\theta_f) \mathbf{M}_{pol}(\theta_p) \quad (C.2)$$

where  $\mathbf{M}_{pol}(\theta_p)$  denotes the Mueller matrix of the linear polarizer at angle  $\theta_p$ , and  $\mathbf{M}_{sample}(\theta_f)$  is the Mueller matrix of reflection from the fibrous sample considering fibers with angle  $\theta_f$ . Note, as light passes through the polarizer the second time,  $\theta_f$  is reversed to account for the reflected reference frame. For mathematical simplicity, we can modify the previous equation by adopting the rotating polarizer as our reference to yield a new Mueller form for the pSFDI system:

$$\vec{S}_{out} = \mathbf{M}_{pol} \mathbf{M}_{sample}(\theta_f, \theta_p) \mathbf{M}_{pol} \vec{S}_{in}, \quad (C.3)$$

To solve this equation, we must quantify the Mueller matrices of the linear polarizer ( $\mathbf{M}_{pol}$ ), oriented along the  $x$ -axis, and the fibrous sample ( $\mathbf{M}_{sample}$ ) with fibers/optical anisotropy aligned along the same direction:

$$\mathbf{M}_{pol} = \frac{1}{2} \begin{bmatrix} 1 & 1 & 0 & 0 \\ 1 & 1 & 0 & 0 \\ 0 & 0 & 0 & 0 \\ 0 & 0 & 0 & 0 \end{bmatrix}, \text{ and } \mathbf{M}_{sample} = R \begin{bmatrix} 1 & D & 0 & 0 \\ D & 1 & 0 & 0 \\ 0 & 0 & \sqrt{1-D^2} \cos(\delta) & \sqrt{1-D^2} \sin(\delta) \\ 0 & 0 & \sqrt{1-D^2} \sin(\delta) & \sqrt{1-D^2} \cos(\delta) \end{bmatrix}, \quad (C.4)$$

where  $R$  is the average reflectance from the sample, and  $D$  and  $\delta$  are the sample diattenuation and phase retardance, respectively, arising from the fiber geometry and

considering principal diattenuation and retardance axes aligned with the  $x$ - and  $y$ -directions, respectively.

When examining rotations of the sample fibers from the polarizer's reference frame, we first note that increases in the fiber angle ( $\theta_f$ ) are equivalent to rotations of the  $\mathbf{M}_{sample}$  by an angle of  $\theta_f$ . Furthermore, we observe that polarizer rotation by  $\theta_p$  can be equivalently represented by rotations to  $\mathbf{M}_{sample}$  by an angle of  $-\theta_p$ , when viewed from the polarizer's reference frame. These observations lead to a modified Mueller form:

$$\begin{aligned}\mathbf{M}_{sample}(\theta_f, \theta_p) &= \mathbf{R}_{rot}(\theta_p)\mathbf{R}_{rot}(-\theta_f)(\mathbf{M}_{sample})\mathbf{R}_{rot}(\theta_f)\mathbf{R}_{rot}(-\theta_p), \\ &= \mathbf{R}_{rot}(-(\theta_f - \theta_p))(\mathbf{M}_{sample})\mathbf{R}_{rot}(\theta_f - \theta_p),\end{aligned}\quad (\text{C.5})$$

where  $\mathbf{R}_{rot}$  is the planar rotation matrix:

$$\mathbf{R}_{rot}(\theta) = \begin{bmatrix} 1 & 0 & 0 & 0 \\ 0 & \cos(2\theta) & \sin(2\theta) & 0 \\ 0 & -\sin(2\theta) & \cos(2\theta) & 0 \\ 0 & 0 & 0 & 1 \end{bmatrix}, \quad (\text{C.6})$$

Using these forms, and assuming unpolarized incident light ( $\vec{S}_{in} = [1, 0, 0, 0]^T$ ), we can solve

Eqn. (C.5) for  $\vec{S}_{out}$ :

$$\vec{S}_{out} = \tau_{sys} \begin{bmatrix} \frac{3}{2} + \frac{1}{2}\sqrt{1-D^2} \cos(\delta) + 2D \cos(2(\theta_f - \theta_p)) + \frac{1}{2}[1 - \sqrt{1-D^2} \cos(\delta) \cos(4(\theta_f - \theta_p))] \\ \frac{3}{2} + \frac{1}{2}\sqrt{1-D^2} \cos(\delta) + 2D \cos(2(\theta_f - \theta_p)) + \frac{1}{2}[1 - \sqrt{1-D^2} \cos(\delta) \cos(4(\theta_f - \theta_p))] \\ 0 \\ 0 \end{bmatrix}, \quad (\text{C.7})$$

where  $\tau_{sys}$  is a systemic coefficient encompassing the sample reflectance  $R$ , the polarizer attenuation, the aperture of the camera, and other non-birefringent optical modifiers. The first term of  $\vec{S}_{out}$  describes the intensity  $I_{out}$  captured by pSF DI system; with term substitution,  $I_{out}$  can be readily represented as a 3-term Fourier cosine series:

$$I_{out} = \tau_{sys} [a_0 + a_2 \cos(2(\theta_f - \theta_p)) + a_4 \cos(2(\theta_f - \theta_p))], \quad (C.8)$$

This final form of  $I_{out}$ , as mentioned in the main text in *Section 5.2.1* (Eq. (5.1)), allows quantification of sample fiber orientation via Fourier fitting of experimental intensity data. However, it is important to note how the sample optical properties, i.e.,  $D$  and  $\delta$ , are incorporated into the Fourier coefficients:

$$a_0 = 1 + \frac{1}{2} [1 + \sqrt{1 - D^2} \cos(\delta)], \quad a_2 = 2D, \quad \text{and} \quad a_4 = \frac{1}{2} [1 - \sqrt{1 - D^2} \cos(\delta)]. \quad (C.9)$$

Given this representation, and the recognition that  $a_0 + a_4 = 2$ , it follows that the diattenuation and sample retardance can be easily expressed in terms of the Fourier coefficients through algebraic manipulation of (C.8) and (C.9):

$$D = \frac{a_2}{a_0 + a_4}, \quad \text{and} \quad \delta = \cos^{-1} \left( \frac{a_0 - 3a_4}{\sqrt{(a_0 + a_4)^2 - a_2^2}} \right), \quad (C.10)$$

By clarifying the relationships between sample diattenuation and retardance and the three Fourier terms, we establish the basis and validity of the Fourier approximation provided in Eq. (5.1) in *Section 5.2.1*.

Remark: The light reflection at the sample interface was neglected in the Mueller formulation described in Eq. (C.5). Because the Mueller matrix of a fibrous sample  $\mathbf{M}_{sample}$  is equivalent in both transmission and reflection modes, leading to the same form of  $I_{out}$ , it is trivial to consider reflection of the light coordinate system at the sample interface. If interested, the reader is encouraged to follow the aforementioned formulaic approach with inverted  $\mathbf{R}_{rot}$  to consider reflection at the sample interface, and note the same form for  $I_{out}$

## C.2 Illustration of AC image penetration depth relationship (Eq. (5.2)) from the SFDI theory

SFDI is a near-infrared planar imaging technique that enables rapid quantification of tissue properties over a broad FOV. Although SFDI has been widely used toward quantification of tissue optical properties and oxygenation biomarkers [136-138], our study implements SFDI to modulate the depth of our microstructural investigations [155]. Our implementation of SFDI entails projection of three spatially-modulated unidimensional sinusoidal intensity patterns over a large region (cm-scale). The patterns share the desired spatial frequency  $f_x$ , but each contain unique linear phase shifts of  $0^\circ$ ,  $120^\circ$ , and  $240^\circ$ . The reflected images from each projection pattern are then sequentially captured by a CCD camera and denoted as pixelwise  $I_{0^\circ}$ ,  $I_{120^\circ}$ , and  $I_{240^\circ}$ , named according to the phase shift of the projection. Then, the pixel-wise intensities extracted from the images are combined according to two conventions: DC intensity  $I_{DC}$  which provides equal weighting for each reflected photon, capturing the conventional diffuse reflectance image, and AC Intensity  $I_{AC}$ , which emphasizes the differences between  $I_{0^\circ}$ ,  $I_{120^\circ}$ , and  $I_{240^\circ}$ , thus neglecting highly diffuse photons:

$$I_{DC} = \frac{I_{0^\circ} + I_{120^\circ} + I_{240^\circ}}{3}, \text{ and } I_{AC} = \frac{\sqrt{2} \left( (I_{0^\circ} - I_{120^\circ})^2 + (I_{120^\circ} - I_{240^\circ})^2 + (I_{0^\circ} - I_{240^\circ})^2 \right)}{3}. \quad (\text{C.11})$$

Due to photon absorption and scattering events within the sample, both DC and AC spatial intensity maps, or images, predominantly contain information above an effective penetration depth ( $\delta_{eff}^{DC}$  and  $\delta_{eff}^{AC}$ , respectively). These two penetration depths correspond to the positions where the intensity of electromagnetic radiation inside a sample falls to  $1/e \approx 37\%$  of its incident value, with the light attenuation rate described by the Beer-Lambert law. Like typical planar projections, the  $\delta_{eff}^{DC}$  exhibits a simple dependence on strictly sample optical properties:

$$\delta_{eff}^{AC} \approx \frac{1}{\sqrt{3\mu_a(\mu_a + \mu_s')}} , \quad (\text{C.12})$$

More concretely, the DC penetration is solely limited by the photons' ability to penetrate the sample and is quantified by the tissue bulk optical properties, i.e.,  $\mu_a$ , the absorption coefficient, and  $\mu_s'$ , the reduced scattering coefficient. This simple dependence renders the DC convention ineffective for interrogating a given tissue sample at varied imaging depths, because the effective depth of the DC image has no dependence on the projected pattern. Conversely, the  $\delta_{eff}^{AC}$  exhibits dependence on both tissue optical properties *and* the spatial frequency  $f_x$  of the incident projection pattern:

$$\delta_{eff}^{AC} \approx \frac{1}{\sqrt{3\mu_a(\mu_a + \mu_s') + (2\pi f_x)^2}} , \quad (\text{C.13})$$

This multivariate depth dependence arises from two factors: (i) AC intensity's propensity to capture reflected photons that retain the incident spatial pattern, as reflected in the form of Eqn. (C.11), and (ii) the dependence of the rate of signal attenuation on the spatial frequency of the incident pattern (Fig. C.1a and Fig. C.1b).

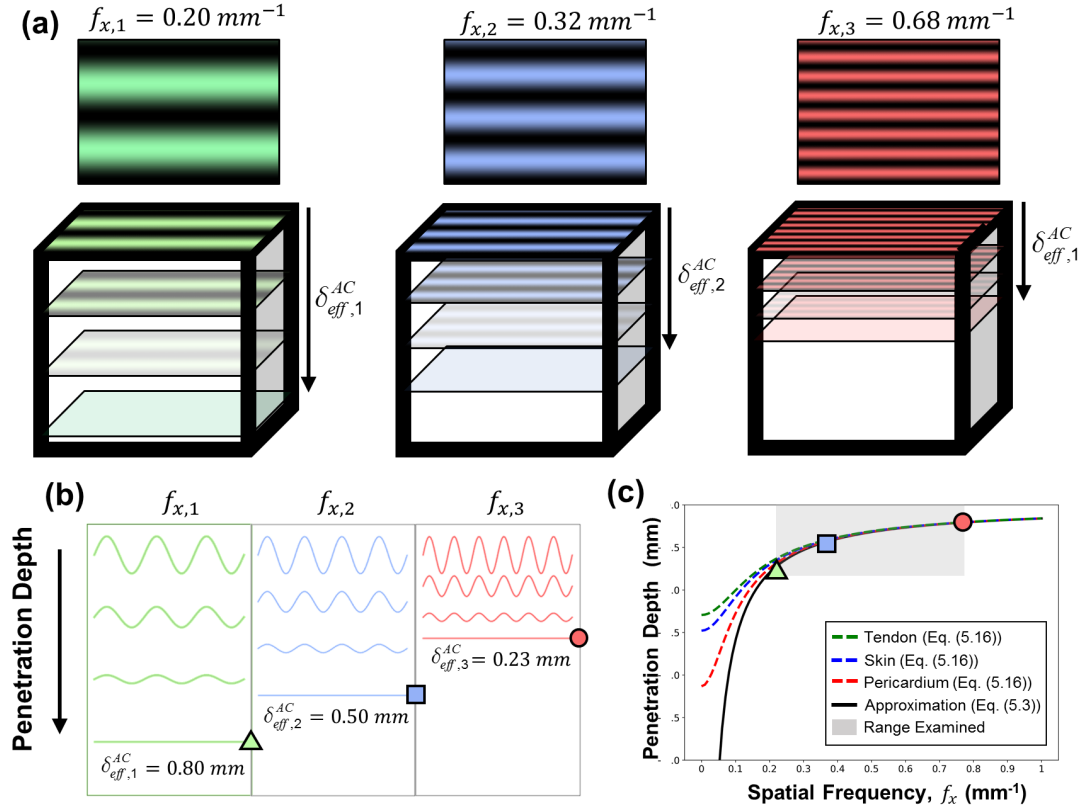


**Figure C.1.** Diagrams exploring the relationship between  $f_x$  and  $\delta_{eff}^{AC}$ . The varied attenuation of three spatial frequency ( $f_{x,1-3}$ ) intensity patterns showing the AC penetration depths ( $\delta_{eff,1-3}^{AC}$ ) according to Eq. (C.14) from the (a) trimetric and (b) side view. (c) Plot comparing estimated penetration depths from the exact model (Eq. (C.13)) for selected tissues [156, 157] and the approximate model (Eq. (C.14)), highlighting the  $f_x$  range used in this study (Fig. 5.7).

Furthermore, at high spatial frequencies relative to the tissue optical properties, the AC penetration depth depends solely on the spatial frequency of the incident pattern:

$$\delta_{\text{eff}}^{\text{AC}} \approx \frac{1}{2\pi f_x}, \quad (\text{C.14})$$

This equation provides the approximate image penetration depth *independent* of the sample's optical properties. If shown to be valid for a class of tissues with known ranges of bulk optical properties, this valuable simplification allows command of image penetration depth via control of the  $f_x$  of the projected pattern. For example, to examine the validity of the imaging depth approximation for the HV leaflets analyzed in this study, we compared Eqns. (C.13) & (C.14) graphically using previously-obtained optical properties of  $\mu_a=0.07 \text{ mm}^{-1}$  and  $\mu_s'=3.00 \text{ mm}^{-1}$  for tendon tissues,  $\mu_a=0.08 \text{ mm}^{-1}$  and  $\mu_s'=1.96 \text{ mm}^{-1}$  for skin tissues, and  $\mu_a=0.03 \text{ mm}^{-1}$  and  $\mu_s'=2.19 \text{ mm}^{-1}$  for pericardial tissues (Fig. C.1c) [156, 157]. Note that the tissue optical properties used in this example are taken from similar tissues, because valve leaflet properties were not found in existing literature. As shown in the figure, the approximation for imaging depth proves valid over the SF ranges projected. In this study, we utilize the simpler approximation, Eq. (C.14), to examine unloaded and loaded HV leaflet tissue at a variety of penetration depths.

## APPENDIX D: BIAXIAL MECHANICAL TESTING PROCEDURES

In this appendix, we present a rigorous description of the mechanical testing procedures used to obtain the mechanical responses presented in Chapter 3 and Chapter 4.

### D.1 Tissue Acquisition and Preparation

The first step in the mechanical testing process is the acquisition of an appropriate heart; for these studies, porcine and ovine hearts were used. When dissecting the heart, the atria are first excised and disposed of to access the atrioventricular valves (Fig. D.1a). Then, axial incisions are made at the posterior commissure of the MV and the postero-septal commissure of the TV (Fig. D.1a and Fig. D.1b). The incisions are continued through the ventricles toward the heart apex to open the valves (Fig. D.1c and Fig. D.1d).

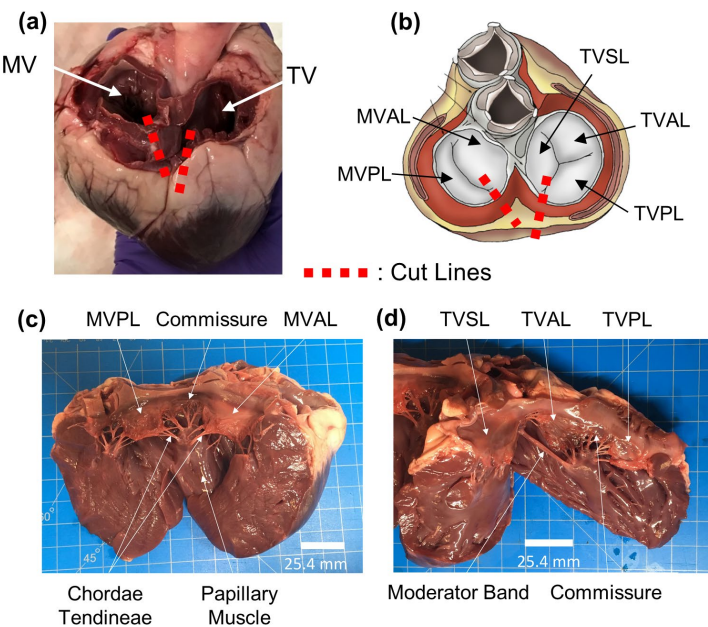


**Figure D.1.** Depictions of the appropriate cut line positions on (a) a porcine heart with atria removed and (b) a schematic of the atrioventricular heart valves. (c, d) show the mitral and tricuspid valves, respectively, fully opened and allowing leaflet excision.

The leaflets are then excised from the opened valves through: (i) severing the attached chordae tendineae near their leaflet attachment, (ii) grasping the leaflet and holding it taught orthogonal to the ventricular surface, and (iii) slicing the leaflet along the annular attachment from commissure to commissure, taking care to preserve the intact leaflet tissue(s) in their entirety. Once excised, the principal directions of the extracted tissue can be established by noting that the leaflet cut edge coincides with the circumferential direction of the tissue. With these directions considered, the desired testing sample can be sectioned from the tissue. This procedure can vary by study but should result in an arbitrary number ( $1, \dots, n$ ) of square tissue samples. The circumferential direction of each tissue sample should be indicated by marks placed along the circumferential axis at the edge midpoints (Fig. D.2b and Fig. D.2e), and the sample should be uniquely labelled.

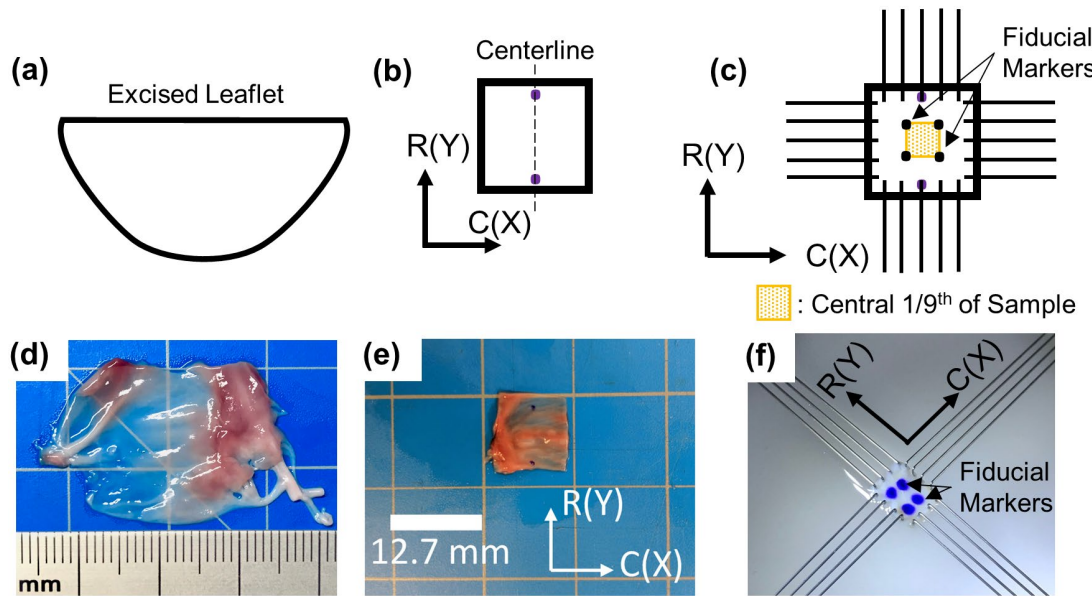


**Figure D.2.** Illustrations of the sample sectioning and mounting procedures for leaflet tissues. (a-c) show schematic representations of the excised leaflet, the sample sectioning and marking process, and the sample mounting procedure, respectively, while (d-f) show images from the same respective procedures. Small ticks in (d) show mm.

The thickness of each sample should be captured via placement onto an incompressible tool with a uniform thickness and flat surface, and the use of calipers to measure the combined thickness of sample and tool. The measurement accuracy can and should be refined by repeating the measurement at multiple sample regions, typically three, then averaging the measurements before subtracting the tool's thickness. With sample thicknesses recorded, the marked samples may be stored in labelled individual containers in a standard refrigerator (4 °C) but should be tested within 2 days of excision.

## D.2 Tissue Mounting

Tissue samples are mounted onto the biaxial tester using BioRakes (Cellscape, Canada), where the rake size is determined by the sample edge length; typically, the difference between the sample edge length and the width of the rake (edge tine – edge tine) should be 1500 µm or larger for proper mounting. To mount the tissue, the sample is first placed on a larger square of rubber backing material. The backing square is then used to mount the sample onto the biaxial tester such that the circumferential and radial tissue directions correspond to the  $x$ - and  $y$ -directions of the biaxial tester, respectively. The rakes are sequentially pushed through the tissue and into the backing material, typically with the edge of spatula tool. Subsequent removal of the backing material leaves the tissue suspended and supported by the rakes. Four fiducial markers are then placed onto the sample at the vertices of a square representing the central 1/9<sup>th</sup> of the mounted region (Fig. D.2c). Two marker types have been used; the study presented in Chapter 3 used glass beads, with diameters of 300-500 µm, carefully glued onto the tissue, whereas the regional study presented in Chapter 4 employed a surgical pen to create the fiducial markers. Although the glass beads provide a more robust measurement, the use of the surgical pen-based

markings for the regional study was required by the smaller sample size (4.5 mm active region). After the application of fiducial markers, the tissue is prepared for testing.

*Remark:* The tissue mounting process is as much a skill as it is a procedure. Like all skills, practice is required to mount a tissue effectively for obtaining accurate material properties.

### **D.3 Biaxial Testing Procedures**

This thesis presented the results of various biaxial mechanical studies – the baseline/force-controlled study, the strain-rate effect study, the temperature effect study, the species/donor age study, the regional variance in mechanical response study, and the stress relaxation study. In this section, biaxial mechanical testing procedures are separated into two groups: (i) uniform procedures across studies and (ii) study-distinct procedures.

#### **D.3.1 Study agnostic tools and utilities**

The Labjoy testing interface includes several standard, broadly-required commands and properties for navigating the tissue mounting and testing process (Fig. D.3).

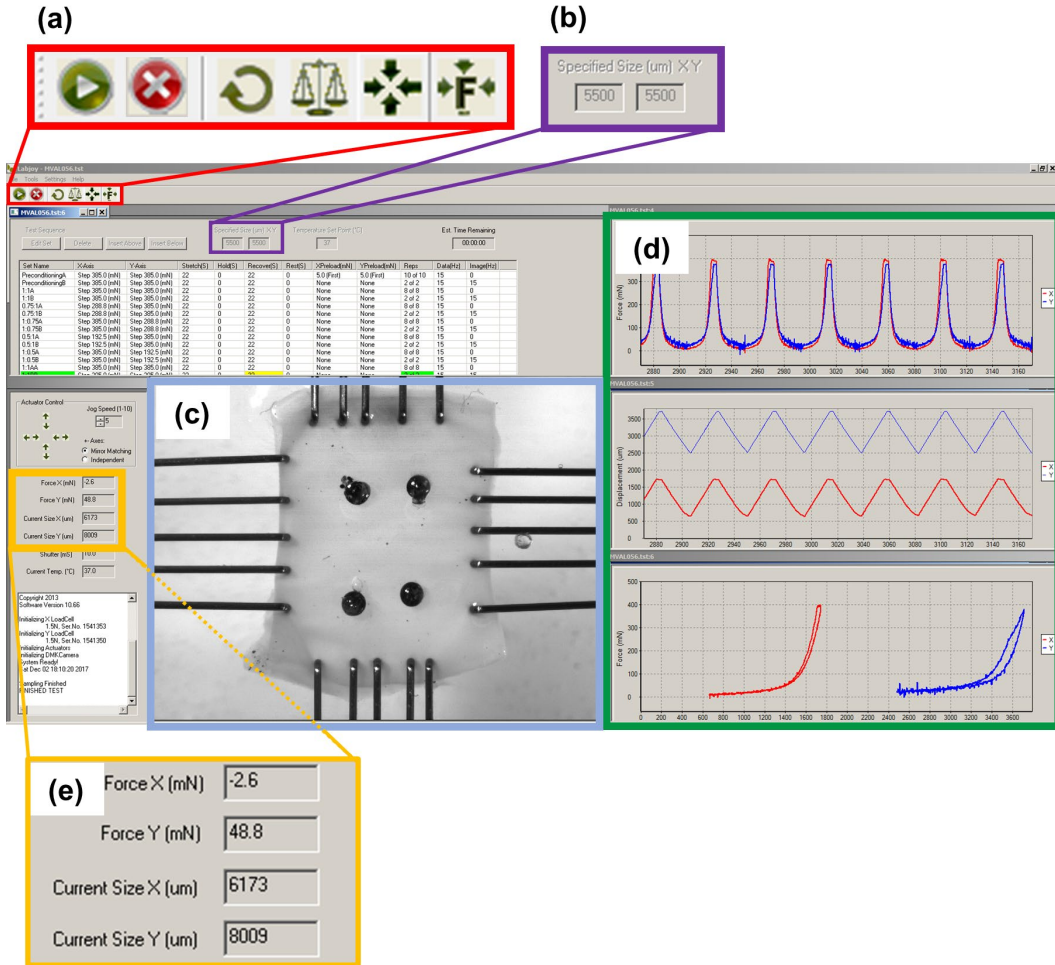


**Figure D.3.** Decomposition of the LabJoy testing graphical interface. (a) Shows, from left to right, the *Start*, *Stop*, *Reset Actuators*, *Zero Load Cells*, *Move to Size*, and *Move to Force* buttons, while (b) highlights input boxes for specification of desired size in x, y directions. (c) includes a dynamic overhead visualization of the testing sample, while (d) encloses real-time graphs of the sample temporal applied forces and deformations, and (e) displays outputs of the current sample applied forces and sizes in the x- and y-directions.

Briefly, the essential interface commands include:

- *Start the Test*: Starts the currently loaded testing sequence.
- *Stop the Test*: Stops the currently running test.
- *Reset Actuators*: Resets the actuators to their “home”, fully-retracted state.
- *Zero Load Cells*: Calibrates the load cells by using the current load as a Tare, or zero-load, reference state.
- *Move to Size*: Moves the tines to the *Specified Size* in the *x*- and *y*-directions.
- *Move to Force*: Prompts for forces in the *x*- and *y*-directions, then adjusts the actuators until the desired force is sustained by the load cells.

Important properties for the biaxial tester interface include:

- *Specified Size (x,y)*: Allow specification of the user-desired sample sizes.
- *Current Force (x,y)*: Provides a readout of the current applied force in *x*- and *y*-directions, determined from the load cells.
- *Current Size (x,y)* : Provides a readout of the current “sample size”, as determined from the distance between tines.

In addition to these, the LabJoy interface will also display the current tissue state (Fig. D.3c), along with graphs of the tissue loading and deformation (Fig. D.3d). These indicators improve ability to assess the test in real-time and to stop tests that have incurred errors, such as tines slipping or markers delaminating from the tissue surface. After testing, digital image correlation methods were employed through the LabJoy software to capture the marker nodal deformations. These nodal deformations were then used to compute the tissue stretches, as described in *Section 3.2.4*.

### D.3.2 Study specific testing procedures

Study-specific procedures were implemented through template (.tmt) files inside of Labjoy, the proprietary software for the CellScale biaxial tester. During testing, templates are rendered into test files (.tst), which describe the testing parameters and sequence. An example of the test file from the baseline/force-controlled testing is shown in Figure D.4.

**Example Test File (.tst)**

(a) Settings Configuration

```

BEGIN_FILE
    Version 1.0
    Collection CellScaleBiaxial

BEGIN_BLOCK

BEGIN_DEVICES
1 Biotestex5000 COM4 AutoDetectCOM LoadcellX 150 29.8435 LoadcellY 150 29.5697 Temperature 37
    PreloadEx 2 25 25 6 5 3 100

BEGIN_CAMERAS
1 DMKCameras USB 10 10 PixPerUmPerZoom 0.305 Maxfps 15

BEGIN_DISPLAYS
1 Video 1 Live_Video 836 627 262 347 FixedAspectRatio

BEGIN_CHARTS
1 Force_mN FAuto 0 500 Time_S Scroll 0 300 Position 600 0 ShowLegend
    Series 1 X (255,0,0) 2
    Series 2 Y (0,0,255) 2
2 Displacement_um FAuto 0 400 Time_S Scroll 0 300 Position 600 350 ShowLegend
    Series 1 X (255,0,0) 2
    Series 2 Y (0,0,255) 1
3 Force_mN FAuto 0 500 Displacement_um FAuto 0 400 Position 600 700 ShowLegend
    Series 1 X (255,0,0) 2
    Series 2 Y (0,0,255) 2

BEGIN_HARDWAREOTS
TemperatureSetPoint 37
PreloadSettingsEx2 2 25 25 6 5 3 100
IdleCurrent 0
SyncPulseDivisor -1
CameraType DMKCamera
CameraShutter 10
CameraGain 10

BEGIN_CONTROLS
Timestamp_Seconds
SampleSizeX_um 5500
SampleSizeY_um 5500
NumTrueStrainSegments 10
NumDataAveragingPoints 1
SizeAdjustWithPreload
SoftLimits 50 60000 50 60000
SoftForceLimits2 1475 1475
TemperatureWarnings 1 1
ResetWarning 1
OutputColumns SetName Cycle Time_S Temperature XSize_um YSize_um XDisplacement_um
YDisplacement_um XForce_mN YForce_mN

```

(b) Testing Sequence Configuration

```

BEGIN_MULTISET
Name XMode XFunction XUnits XMagnitude XPreloadType XPreloadMag YMode YFunction YUnits YMagnitude YPreloadType
YPreloadMag StretchDurationSec RecoveryDurationSec HoldTimeSec RestTimeSec NumReps DataFreqHz ImageFreqHz

PreconditioningA Force Step mN 385 First 5 Force Step mN 385 First 5 22 22 0 0 10 15 0
PreconditioningB Force Step mN 385 None 0 Force Step mN 385 None 0 22 22 0 0 2 15 15
1:1A Force Step mN 385 None 0 Force Step mN 385 None 0 22 22 0 0 8 15 0
1:1B Force Step mN 385 None 0 Force Step mN 385 None 0 22 22 0 0 2 15 15
0.75:1A Force Step mN 288.75 None 0 Force Step mN 385 None 0 22 22 0 0 8 15 0
0.75:1B Force Step mN 288.75 None 0 Force Step mN 385 None 0 22 22 0 0 2 15 15
1:0.75A Force Step mN 385 None 0 Force Step mN 288.75 None 0 22 22 0 0 8 15 0
1:0.75B Force Step mN 385 None 0 Force Step mN 288.75 None 0 22 22 0 0 2 15 15
0.5:1A Force Step mN 192.5 None 0 Force Step mN 385 None 0 22 22 0 0 8 15 0
0.5:1B Force Step mN 192.5 None 0 Force Step mN 385 None 0 22 22 0 0 2 15 15
1:0.5A Force Step mN 385 None 0 Force Step mN 192.5 None 0 22 22 0 0 8 15 0
1:0.5B Force Step mN 385 None 0 Force Step mN 192.5 None 0 22 22 0 0 2 15 15
1:1AA Force Step mN 385 None 0 Force Step mN 385 None 0 22 22 0 0 8 15 0
1:1BB Force Step mN 385 None 0 Force Step mN 385 None 0 22 22 0 0 2 15 15

```

**Figure D.4.** Example test file from the baseline/force-controlled biaxial mechanical study

(cf. *Section 3.3.1*). (a) highlights the settings applied to the entire test, such as the testing temperature, camera settings, and display settings, while (b) contains the specific details for the testing sequence.

The precise modifications made to the testing template to develop the various biaxial mechanical testing procedures used in this study are included below:

- *Loading-Rate Effect Study (cf. Section 3.3.2):* Each tissue in this study group required three separate tests, using templates like the one above at different testing velocities. Inside LabJoy, the velocities were dictated as 3, 4, and 5, from a 1-10 scale. By examining the ensuing loads, we observed the velocities of 3, 4, and 5 were correlated with average loading rates of 2.29 N/min, 4.42 N/min, and 7.92 N/m, respectively.
- *Temperature Effect Study (cf. Section 3.3.3):* Similarly, each tissue in the temperature effect study required three separate tests, using templates like the one shown above. The tests were conducted with the PBS solution at 27 °C, then 32 °C, and finally 37 °C, with the solution heated between tests and the preconditioning protocol performed to begin each test.
- *Species and Donor Age Study (cf. Section 3.3.4):* The only varying factor in this study was the size of the testing specimen. Because juvenile ovine leaflets were much smaller than their adult ovine counterparts, which were in turn smaller than comparable porcine tissues, a range of specimen sizes – typically from 6500 µm to 5500 µm – were used to capture the mechanical responses of these tissues.
- *Regional Variance in Biaxial Mechanical Response Study (cf. Section 4.3.2):* A similar template was used to conduct this study, with the chief difference being the smaller sample size (~4500 µm) implemented via the *Specified Size* and *Move to Size* functionality within LabJoy.

- *Regional Variance in Stress Relaxation Study (cf. Section 4.3.3):* The testing sequence (Fig. D.4b) used in this study was unique and disparate. Briefly, this study included a preconditioning protocol followed by a *Move to Force* step to determine the tissue deformation at maximum physiological load. Then, the biaxial deformations were used to build a displacement-controlled testing sequence, where the tissue was stretched to maximum load and held for a 30-minute period while the temporal biaxial forces were captured, allowing for calculation of the stress-relaxation response of the tissue samples.

## APPENDIX E: PSFDI TESTING AND DATA ANALYSIS PROCEDURES

While the theoretical basis for the pSFDI procedure is presented in Chapter 5, this appendix includes details of the practical application of this technology, and discusses the steps needed to acquire collagen fiber architecture data from the pSFDI system. Briefly, this appendix is broken up into three sections: (i) the system calibration and preparation, (ii) the system testing procedure, and (iii) the post-processing/data analysis steps.

### E.1 pSFDI System Calibration

The calibration procedure for the pSFDI system assumes proper assembly of the device and appropriate placement of the distinct optical components. In this case, the two system components which will require calibration prior to testing are the digital light processor (DLP) (DLP4500EVM, Texas Instruments, TX, USA) and the camera lens (HF35XA-1, Fujinon, Fujifilm, Tokyo, Japan). The DLP device's projector lens must be focused in order to project a resolved image at the focal distance of the object (Fig. E.1).

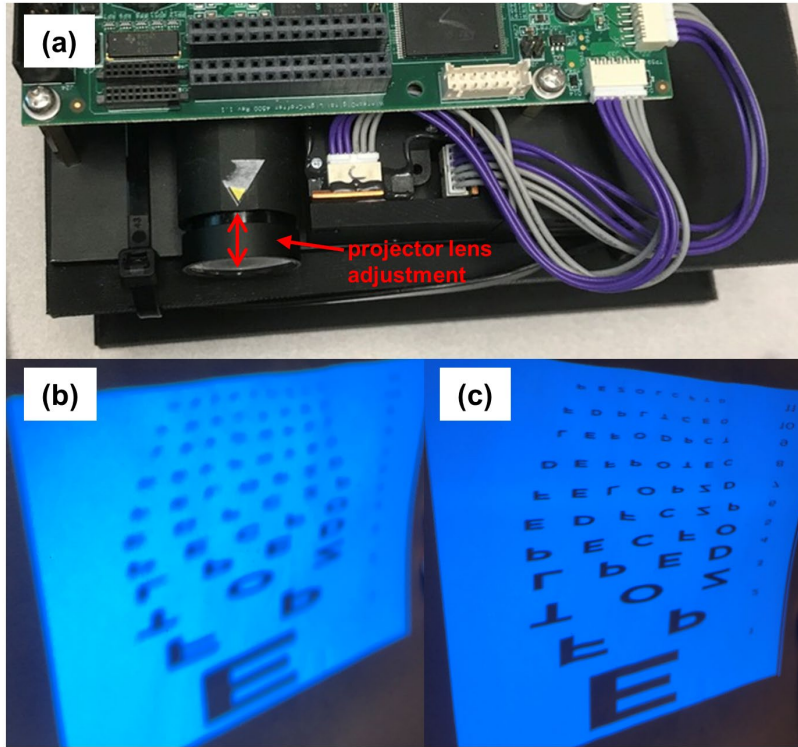


**Figure E.1.** Calibration of the DLP projector lens. (a) shows the projection focal distance adjustment via linear translation of the lens, while (b,c) depict examples of unresolved and properly resolved projections, respectively, of an example image.

The appropriate calibration of the projector lens is important to maintain resolved spatial frequency patterns in the projected images. Typically, the DLP projection can be resolved adequately by examining the illuminated sample and tuning the projector lens until the spatial frequency appears resolved.

Unlike the DLP adjustment, the camera lens adjustment requires the camera visualization software to visualize the effects of the adjustments; for Basler cameras, like the one used in these studies, this software is called *Pylon*. The camera lens should be adjusted while the software is displaying the real-time images captured by the camera. An example of the lens adjustment and the corresponding change in the captured image is shown (Fig. E.2).

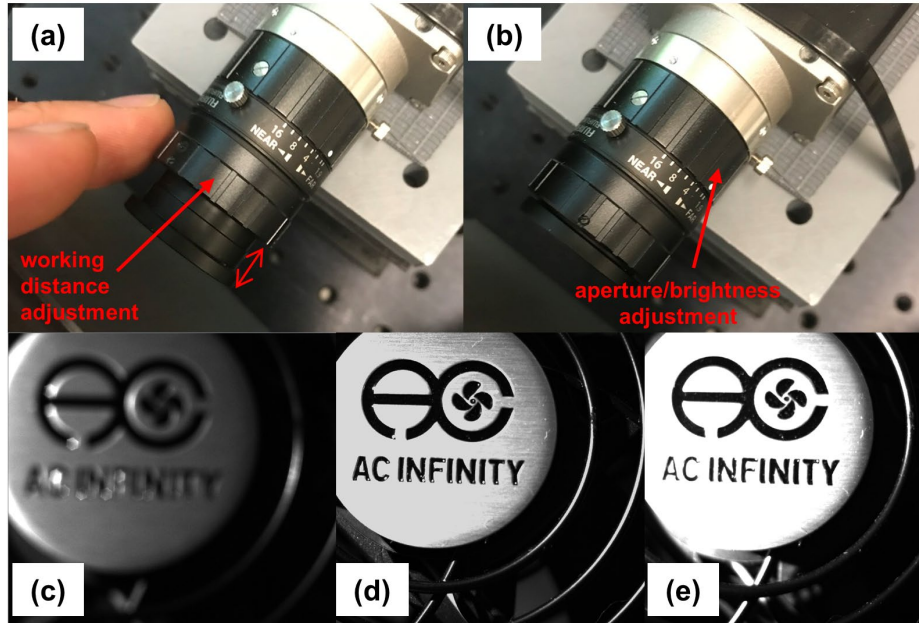


**Figure E.2.** Calibration of the camera lens. (a) shows the working distance adjustment ring of the lens, while (b) shows the aperture adjustment ring, permitting control of image brightness. (c) depicts an underexposed and unresolved image, (d) shows a properly resolved and illuminated image, and (e) depicts a resolved but overexposed image.

The camera lens has two adjustment rings: the working distance adjustment ring and the aperture adjustment ring. The working distance adjustment allows control of the resolution of the image, while the aperture dictates the amount of light the lens accepts and the apparent brightness of the image. Appropriate calibration of the lens working distance and lens aperture is essential for obtaining accurate fiber architectures from a tissue sample, as poorly-focused images (Fig. E.2c) degrade prediction resolution and over or underexposed images (Fig. E.2c and Fig. E.2e) cause incorrect fiber architecture predictions.

## E.2 pSF DI System Testing

This section presents the pSF DI testing controls for a non-integrated system; Recently, testing control systems that integrate with the biaxial tester functionality have been

developed, but these controls were not used in the results presented in this thesis, and are therefore not presented in this appendix. Briefly, the pSFDI system control interface for the non-integrated system is shown in Figure E.3.

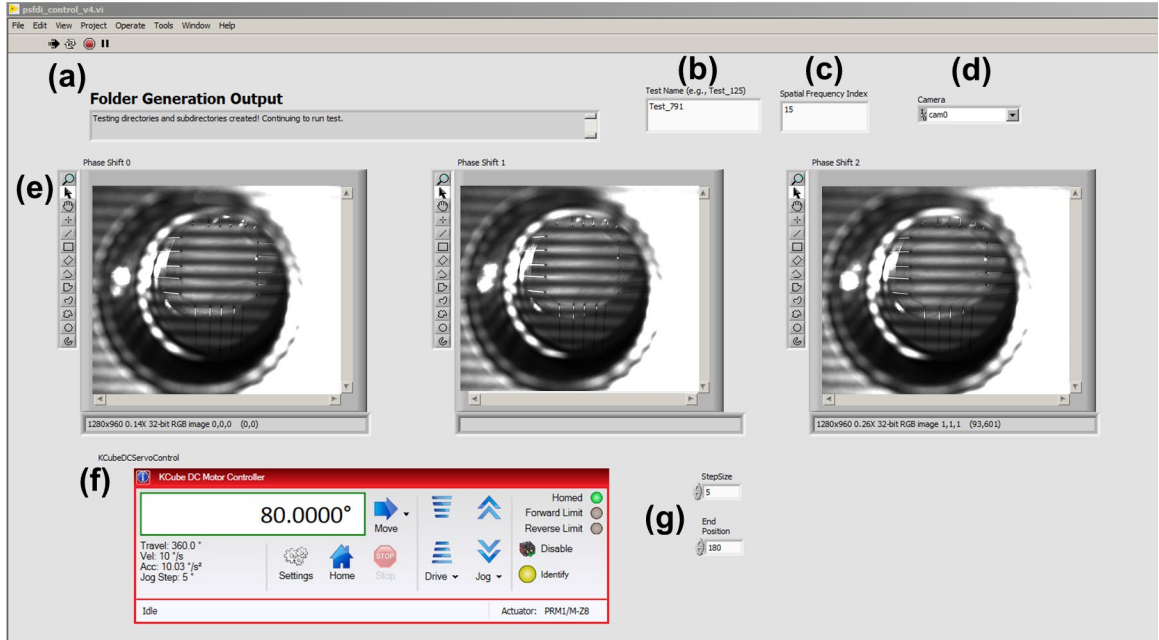


**Figure E.3.** Image of the LabVIEW testing control program interface. (a) shows output of the automated testing folder generation, while (b, c, d) show the boxes allowing input of the test name, spatial frequency, and camera, respectively. (e) displays the real-time testing images at each phase shift, and (f) shows the state of the rotational polarizer mount, while (g) allows input of step size and final polarizer angle (typically 5° and 180°, respectively).

The LabVIEW testing control program, named *psfdi\_control\_v4.vi* inside of the LabVIEW project *PSFDI.lvproj*, allows the user to examine the microstructure of a tissue. The program requires inputs of the desired *Test Name*, *Spatial Frequency* (at discrete steps indexed from 0-21, cf. Table E1), *Camera* (if multiple are connected to the desktop, e.g. for biaxial tester camera), *Step Size* (degrees between imaging), and *End Position* (final degree measure for test). Typically, the test name and spatial frequency are the only

parameters modified on a test-by-test basis. The spatial frequencies are denoted by indexed values from 0-21, corresponding to spatial frequencies and imaging depths (according to Eq. (5.3)) as shown in Table E1.

**Table E.1.** Spatial frequency index values, with corresponding penetration depths and *actual* spatial frequency values. Index values are input to the testing script to permit control of *actual* spatial frequency and subsequent penetration depth.

Index	Depth (mm)	SF (mm-1)
1	0.10	1.592
2	0.13	1.273
3	0.15	1.061
4	0.18	0.909
5	0.20	0.796
6	0.23	0.707
7	0.25	0.637
8	0.28	0.579
9	0.30	0.531
10	0.33	0.490
11	0.35	0.455
12	0.38	0.424
13	0.40	0.398
14	0.45	0.354
15	0.50	0.318
16	0.55	0.289
17	0.60	0.265
18	0.65	0.245
19	0.70	0.227
20	0.75	0.212
21	0.80	0.199
0	Full Optical Thickness	No Pattern

In addition to inputs, the Labview interface includes displays of the real-time images acquired (Fig. E.3e) and the state of the rotational polarizer mount (Fig. E.3f), in addition

to the result of the folder generation, which can prevent users from overwriting data through an error message. These displays allow real-time assessment of the validity of a pSF DI test, and a rapid feedback for testing errors.

### E.3 pSF DI Post-Processing and Data Analysis

A variety of Python programs have been developed to analyze the pSF DI tests. These programs perform a few vital functions: (i) serialization of the image data, (ii) computation, smoothing, and storage of the DC and AC intensities for each test according to Eq. (C.11), (iii) curve fitting for the intensities according to Eq. (5.1) in order to extract the fitting parameters ( $a_0, a_2, a_4$ ), along with the fiber orientation ( $\theta_{fiber}$ ) and *DOA* for each test, and storage of the fitting parameters, (iv) plotting fiber orientation and *DOA* predictions and intensity curves over the full sample region, (v) permitting input of a region of interest (ROI) to allow cropping, and storing the ROI, and (vi) plotting and storing histograms and illustrations of the cropped region over the ROI. Briefly, these functions have been broken into two discrete analysis steps, due to the need for user input to define the appropriate crop region. In the analysis, **Step 1** performs functions (i-iv) and **Step 2** handles functions (v-vi) for a specific test. These data analysis programs are reduced into a simple user interface via a *Jupyter Notebook* program in the custom PSF DI repository (analyze\_tests.ipynb, Fig. E.4).

#### Step 1: Image serialization and curve fitting

- Provide lists of the tests you would like to crop, along with their corresponding spatial frequency

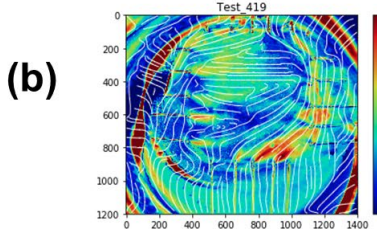
In [5]:

```
#### User modifies here
# Define the list of the tests you want to analyze
test_list1 = ['Test_419']
spat_freq1 = [15]

#####
%matplotlib inline
from psfdi.run import main as run
run(test_list1, spat_freq1)

Smoothed DC and AC data is loaded for Test_419
Orientations and DOA predictions are loaded for Test_419
Creating visual of pixel graph locations
Plotting the cosine curve fitting results, DOA predictions, and orientation predictions
```

(a)



(b)

All tests processed successfully!

Out[5]: 0

#### Step 2: Crop the region of interest for the test

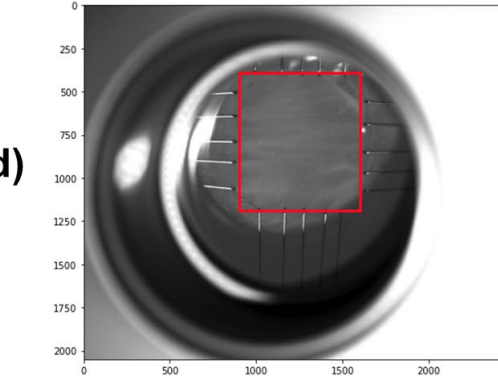
Note: Make sure the step 1 has been run previously for all tests you wish to crop

In [1]:

```
# List the tests you would like to run cropping for here
# Recall that you will only need to crop the first test in an interval test
test_list = ['Test_419']
# Provide the tab name that these tests are stored in in the google sheet
# (usually Interval_Testing or Tricuspid Leaflet Study)
gsheet_tab = 'Interval Testing'

#####
%matplotlib inline
from psfdi.manual_crop import crop as crop
crop(test_list, gsheet_tab)
```

(c)



(d)

**Figure E.4.** Image of the data analysis interface. (a) denotes the user input box to specify lists of the test names and spatial frequencies of the tests to be analyzed during **Step 1** of the analysis, while (b) shows the corresponding **Step 1** output, including indications of the program state and resulting figures. (c) displays the input for **Step 2** of the analysis, and (d) provides an interactive textual cropping tool for the user to specify the region of interest.

The steps can be run concurrently for different tissue samples by opening multiple instances of the *analyze\_tests.ipynb* file. Dependent upon the desktop, **Step 1** usually takes approximately 10 minutes to complete, while **Step 2** takes roughly 1 minute for a user to crop a test, and another 10 seconds to compute and plot the histogram analyses. Example results of the **Step 1** analysis for a TV posterior leaflet tissue are included in Figure E.5.

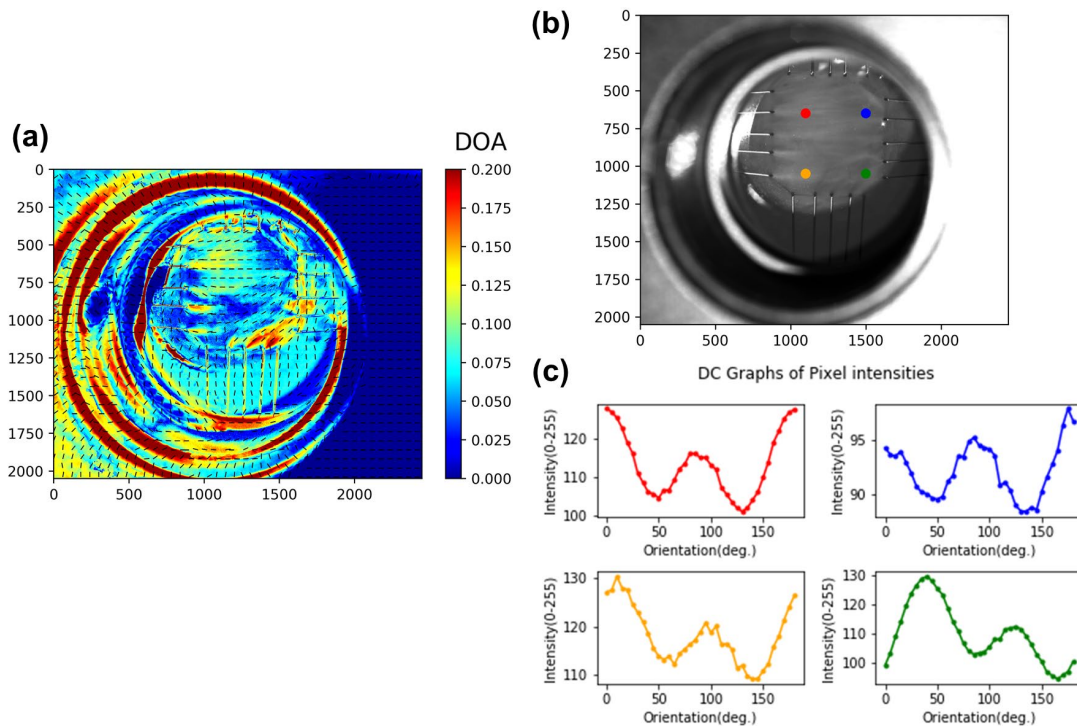


**Figure E.5.** Results from **Step 1** of the analysis for a TVPL tissue under equibiaxial loading. (a) shows the fiber orientations (—) on a background of *DOA*, while (b, c) illustrate

4 spatial points and the DC intensity curves (Intensity vs Polarization angle) at these points.

The curves shown in Figure E.5c describe the basis for the fiber architecture predictions, and the full spatial view shown in Figure E.5a helps to assess spatial variance in the predictions. Similarly, the establishment of a valid region of interest in **Step 2** of the analysis permits further assessment of the fiber architecture distributions (Fig. E.6).

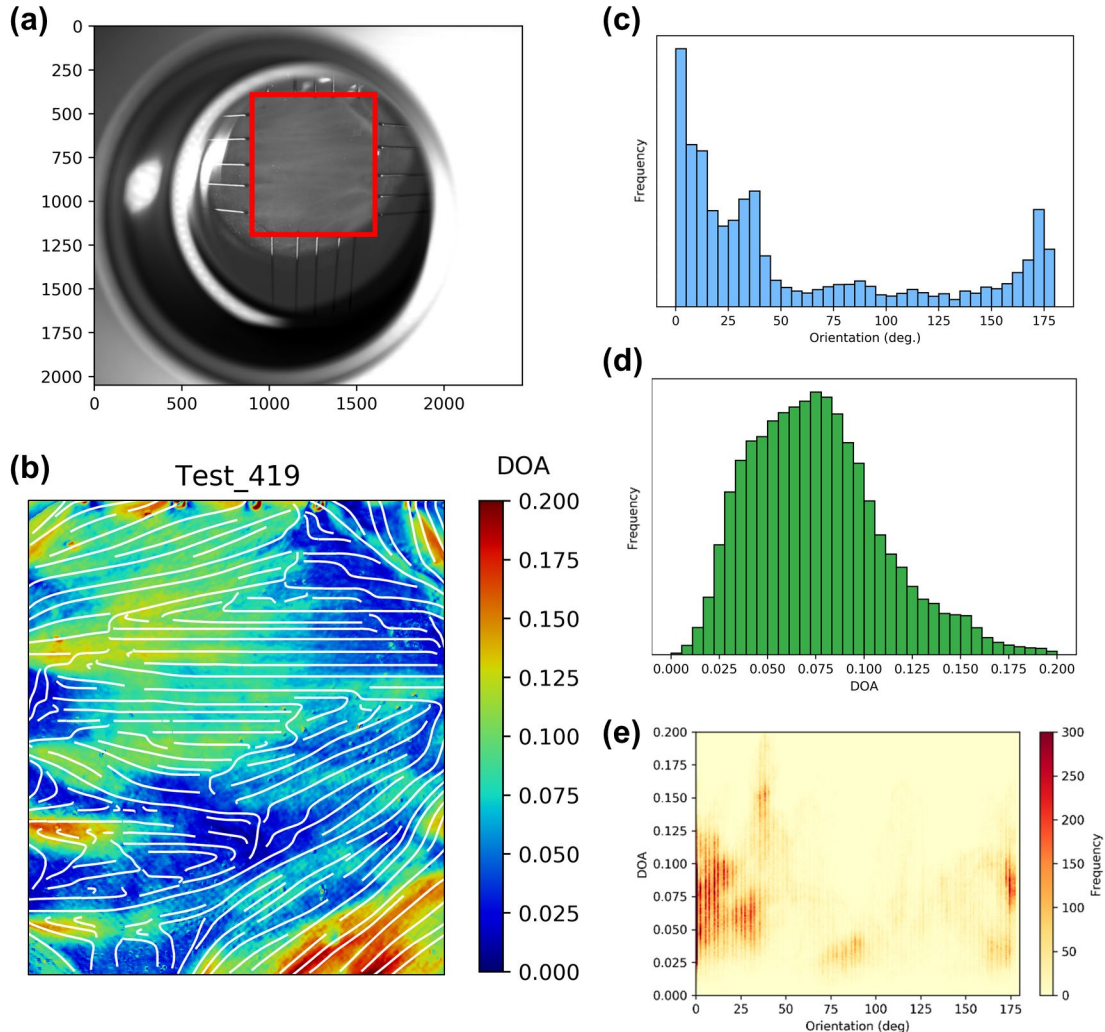


**Figure E.6.** Results from **Step 2** of the analysis for a TVPL tissue under equibiaxial loading. (a) denotes the sample's region of interest (ROI) over a combined DC image, while (b) shows the fiber orientations (white lines) on a background of *DOA*. (c,d) show histograms of the fiber orientation and *DOA*, respectively, while (e) shows the combined distributions of fiber orientation and *DOA*.

As depicted in the above figure, a variety of analyses are possible through establishing an ROI for the tissue. Specifically, the different histograms allow analysis of the distributions of the collagen fiber architectural metrics, while the fiber tracing plot allows improved visualizations of the collagen fiber architectures throughout the tissue domain.

## REFERENCES

1. Nkomo, V.T., Gardin, J.M., Skelton, T.N., Gottdiener, J.S., Scott, C.G., and Enriquez-Sarano, M., Burden of Valvular Heart Diseases: A Population-Based Study. *The Lancet*, 2006. **368**(9540): pp. 1005-1011.
2. Rosenhek, R., Iung, B., Tornos, P., Antunes, M.J., Prendergast, B.D., Otto, C.M., Kappetein, A.P., Stepinska, J., Kaden, J.J., and Naber, C.K., Esc Working Group on Valvular Heart Disease Position Paper: Assessing the Risk of Interventions in Patients with Valvular Heart Disease. *European Heart Journal*, 2011. **33**(7): pp. 822-828.
3. Iung, B. and Vahanian, A., Epidemiology of Valvular Heart Disease in the Adult. *Nature Reviews Cardiology*, 2011. **8**(3): pp. 162.
4. Jones, J.M., O'kane, H., Gladstone, D.J., Sarsam, M.A., Campalani, G., MacGowan, S.W., Cleland, J., and Cran, G.W., Repeat Heart Valve Surgery: Risk Factors for Operative Mortality. *The Journal of Thoracic and Cardiovascular Surgery*, 2001. **122**(5): pp. 913-918.
5. Wang, Q. and Sun, W., Finite Element Modeling of Mitral Valve Dynamic Deformation Using Patient-Specific Multi-Slices Computed Tomography Scans. *Annals of biomedical engineering*, 2013. **41**(1): pp. 142-153.
6. Lee, C.-H. and Sacks, M.S., Fibers to Organs: How Collagen Fiber Properties Modulate the Closing Behavior of the Mitral Valve, in *Structure-Based Mechanics of Tissues and Organs*. 2016, Springer. pp. 365-381.
7. Lee, C.-H., Rabbah, J.-P., Yoganathan, A.P., Gorman, R.C., Gorman, J.H., and Sacks, M.S., On the Effects of Leaflet Microstructure and Constitutive Model on

- the Closing Behavior of the Mitral Valve. *Biomechanics and modeling in mechanobiology*, 2015. **14**(6): pp. 1281-1302.
8. Cheung, D.Y., Duan, B., and Butcher, J.T., Current Progress in Tissue Engineering of Heart Valves: Multiscale Problems, Multiscale Solutions. *Expert Opinion on Biological Therapy*, 2015. **15**(8): pp. 1155-1172.
  9. Mol, A., Smits, A.I., Bouten, C.V., and Baaijens, F.P., Tissue Engineering of Heart Valves: Advances and Current Challenges. *Expert Review of Medical Devices*, 2009. **6**(3): pp. 259-275.
  10. Sodian, R., Hoerstrup, S.P., Sperling, J.S., Martin, D.P., Daebritz, S., Mayer Jr, J.E., and Vacanti, J.P., Evaluation of Biodegradable, Three-Dimensional Matrices for Tissue Engineering of Heart Valves. *Asaio Journal*, 2000. **46**(1): pp. 107-110.
  11. Booth, C., Korossis, S., Wilcox, H., Watterson, K., Kearney, J., Fisher, J., and Ingham, E., Tissue Engineering of Cardiac Valve Prostheses I: Development and Histological Characterization of an Acellular Porcine Scaffold. *The Journal of Heart Valve Disease*, 2002. **11**(4): pp. 457-462.
  12. Xue, Y., Sant, V., Phillipi, J., and Sant, S., Biodegradable and Biomimetic Elastomeric Scaffolds for Tissue-Engineered Heart Valves. *Acta Biomaterialia*, 2017. **48**: pp. 2-19.
  13. Levine, R.A., Triulzi, M., Harrigan, P., and Weyman, A., The Relationship of Mitral Annular Shape to the Diagnosis of Mitral Valve Prolapse. *Circulation*, 1987. **75**(4): pp. 756-767.
  14. Salgo, I.S., Gorman III, J.H., Gorman, R.C., Jackson, B.M., Bowen, F.W., Plappert, T., St John Sutton, M.G., and Edmunds Jr, L.H., Effect of Annular Shape on Leaflet

- Curvature in Reducing Mitral Leaflet Stress. *Circulation*, 2002. **106**(6): pp. 711-717.
15. Gorman III, J.H., Jackson, B.M., Enomoto, Y., and Gorman, R.C., The Effect of Regional Ischemia on Mitral Valve Annular Saddle Shape. *The Annals of Thoracic Surgery*, 2004. **77**(2): pp. 544-548.
  16. Mihaljevic, T., Lam, B.-K., Rajeswaran, J., Takagaki, M., Lauer, M.S., Gillinov, A.M., Blackstone, E.H., and Lytle, B.W., Impact of Mitral Valve Annuloplasty Combined with Revascularization in Patients with Functional Ischemic Mitral Regurgitation. *Journal of the American College of Cardiology*, 2007. **49**(22): pp. 2191-2201.
  17. Lam, J., Ranganathan, N., Wigle, E., and Silver, M., Morphology of the Human Mitral Valve. *Circulation*, 1970. **41**(3): pp. 449-458.
  18. Silver, M., Lam, J., Ranganathan, N., and Wigle, E., Morphology of the Human Tricuspid Valve. *Circulation*, 1971. **43**(3): pp. 333-348.
  19. Ranganathan, N., Lam, J., Wigle, E., and Silver, M., Morphology of the Human Mitral Valve: II. The Valve Leaflets. *Circulation*, 1970. **41**(3): pp. 459-467.
  20. Klabunde, R., *Cardiovascular Physiology Concepts*. 2011: Lippincott Williams & Wilkins.
  21. Axel, L., Papillary Muscles Do Not Attach Directly to the Solid Heart Wall. *Circulation*, 2004. **109**(25): pp. 3145-3148.
  22. Kahlert, P., Plicht, B., Schenk, I.M., Janosi, R.-A., Erbel, R., and Buck, T., Direct Assessment of Size and Shape of Noncircular Vena Contracta Area in Functional Versus Organic Mitral Regurgitation Using Real-Time Three-Dimensional

- Echocardiography. *Journal of the American Society of Echocardiography*, 2008. **21**(8): pp. 912-921.
23. Kihara, T., Gillinov, A.M., Takasaki, K., Fukuda, S., Song, J.M., Shiota, M., and Shiota, T., Mitral Regurgitation Associated with Mitral Annular Dilation in Patients with Lone Atrial Fibrillation: An Echocardiographic Study. *Echocardiography*, 2009. **26**(8): pp. 885-889.
24. Gabbay, U. and Yosefy, C., The Underlying Causes of Chordae Tendinae Rupture: A Systematic Review. *International journal of cardiology*, 2010. **143**(2): pp. 113-118.
25. Rajamannan, N.M., Myxomatous Mitral Valve Disease Bench to Bedside: Ldl-Density-Pressure Regulates Lrp5. *Expert review of cardiovascular therapy*, 2014. **12**(3): pp. 383-392.
26. Nobuyoshi, M., Arita, T., Shirai, S.-i., Hamasaki, N., Yokoi, H., Iwabuchi, M., Yasumoto, H., and Nosaka, H., Percutaneous Balloon Mitral Valvuloplasty: A Review. *Circulation*, 2009. **119**(8): pp. e211-e219.
27. Tang, G.H., David, T.E., Singh, S.K., Maganti, M.D., and Borger, M.A., Tricuspid Valve Repair with an Annuloplasty Ring Results in Improved Long-Term Outcomes. *Circulation*, 2006.
28. Webb, J.G., Wood, D.A., Ye, J., Gurvitch, R., Masson, J.-B., Rodés-Cabau, J., Osten, M., Horlick, E., Wendler, O., and Dumont, E., Transcatheter Valve-in-Valve Implantation for Failed Bioprosthetic Heart Valves. *Circulation*, 2010. **121**(16): pp. 1848.

29. Tamburino, C., Ussia, G.P., Maisano, F., Capodanno, D., La Canna, G., Scandura, S., Colombo, A., Giacomini, A., Michev, I., and Mangiafico, S., Percutaneous Mitral Valve Repair with the Mitraclip System: Acute Results from a Real World Setting. *European Heart Journal*, 2010. **31**(11): pp. 1382-1389.
30. Chandrashekhar, Y., Westaby, S., and Narula, J., Mitral Stenosis. *The Lancet*, 2009. **374**(9697): pp. 1271-1283.
31. McCarthy, P.M., Bhudia, S.K., Rajeswaran, J., Hoercher, K.J., Lytle, B.W., Cosgrove, D.M., and Blackstone, E.H., Tricuspid Valve Repair: Durability and Risk Factors for Failure. *The Journal of Thoracic and Cardiovascular Surgery*, 2004. **127**(3): pp. 674-685.
32. Akins, C.W., Buckley, M.J., Daggett, W.M., Hilgenberg, A.D., Vlahakes, G.J., Torchiana, D.F., and Madsen, J.C., Risk of Reoperative Valve Replacement for Failed Mitral and Aortic Bioprostheses. *The Annals of Thoracic Surgery*, 1998. **65**(6): pp. 1545-1552.
33. Fung, Y., On the Foundations of Biomechanics. *Journal of Applied Mechanics*, 1983. **50**(4b): pp. 1003-1009.
34. Fung, Y.-c., Perrone, N., and Anliker, M. Biomechanics, Its Foundations and Objectives. in *Symposium on Biomechanics, its Foundations and Objectives (1970: University of California, San Diego)*. 1972. NJ, Prentice-Hall.
35. Sauren, A., Van Hout, M., Van Steenhoven, A., Veldpaus, F., and Janssen, J., The Mechanical Properties of Porcine Aortic Valve Tissues. *Journal of Biomechanics*, 1983. **16**(5): pp. 327-337.

36. Broom, N., The Stress/Strain and Fatigue Behaviour of Glutaraldehyde Preserved Heart-Valve Tissue. *Journal of Biomechanics*, 1977. **10**(11-12): pp. 707-724.
37. Vesely, I. and Boughner, D., Analysis of the Bending Behaviour of Porcine Xenograft Leaflets and of Natural Aortic Valve Material: Bending Stiffness, Neutral Axis and Shear Measurements. *Journal of Biomechanics*, 1989. **22**(6-7): pp. 655-671.
38. May-Newman, K. and Yin, F., Biaxial Mechanical Behavior of Excised Porcine Mitral Valve Leaflets. *American Journal of Physiology-Heart and Circulatory Physiology*, 1995. **269**(4): pp. H1319-H1327.
39. Sacks, M., A Method for Planar Biaxial Mechanical Testing That Includes in-Plane Shear. *Journal of biomechanical engineering*, 1999. **121**(5): pp. 551-555.
40. Sacks, M.S., Biaxial Mechanical Evaluation of Planar Biological Materials. *Journal of Elasticity*, 2000. **61**(1): pp. 199.
41. Billiar, K.L. and Sacks, M.S., Biaxial Mechanical Properties of the Natural and Glutaraldehyde Treated Aortic Valve Cusp-Part I: Experimental Results. *Transactions-American Society of Mechanical Engineers Journal of Biomechanical Engineering*, 2000. **122**(1): pp. 23-30.
42. Stella, J.A. and Sacks, M.S., On the Biaxial Mechanical Properties of the Layers of the Aortic Valve Leaflet. *Journal of biomechanical engineering*, 2007. **129**(5): pp. 757-766.
43. Stella, J.A., Liao, J., and Sacks, M.S., Time-Dependent Biaxial Mechanical Behavior of the Aortic Heart Valve Leaflet. *Journal of Biomechanics*, 2007. **40**(14): pp. 3169-3177.

44. Grashow, J.S., Sacks, M.S., Liao, J., and Yoganathan, A.P., Planar Biaxial Creep and Stress Relaxation of the Mitral Valve Anterior Leaflet. *Annals of biomedical engineering*, 2006. **34**(10): pp. 1509-1518.
45. Grashow, J.S., Yoganathan, A.P., and Sacks, M.S., Biaxial Stress–Stretch Behavior of the Mitral Valve Anterior Leaflet at Physiologic Strain Rates. *Annals of biomedical engineering*, 2006. **34**(2): pp. 315-325.
46. Wells, S.M. and Sacks, M.S., Effects of Fixation Pressure on the Biaxial Mechanical Behavior of Porcine Bioprosthetic Heart Valves with Long-Term Cyclic Loading. *Biomaterials*, 2002. **23**(11): pp. 2389-2399.
47. Pham, T., Sulejmani, F., Shin, E., Wang, D., and Sun, W., Quantification and Comparison of the Mechanical Properties of Four Human Cardiac Valves. *Acta Biomaterialia*, 2017. **54**: pp. 345-355.
48. Khoiy, K.A. and Amini, R., On the Biaxial Mechanical Response of Porcine Tricuspid Valve Leaflets. *Journal of biomechanical engineering*, 2016. **138**(10): pp. 104504.
49. Marciniak, A., Glover, K., and Sharma, R., Cohort Profile: Prevalence of Valvular Heart Disease in Community Patients with Suspected Heart Failure in Uk. *BMJ open*, 2017. **7**(1): pp. e012240.
50. Stephens, E.H., de Jonge, N., McNeill, M.P., Durst, C.A., and Grande-Allen, K.J., Age-Related Changes in Material Behavior of Porcine Mitral and Aortic Valves and Correlation to Matrix Composition. *Tissue Engineering Part A*, 2009. **16**(3): pp. 867-878.

51. Pham, T. and Sun, W., Material Properties of Aged Human Mitral Valve Leaflets. *Journal of Biomedical Materials Research Part A*, 2014. **102**(8): pp. 2692-2703.
52. Rabbah, J.-P.M., Saikrishnan, N., Siefert, A.W., Santhanakrishnan, A., and Yoganathan, A.P., Mechanics of Healthy and Functionally Diseased Mitral Valves: A Critical Review. *Journal of biomechanical engineering*, 2013. **135**(2): pp. 021007.
53. Rausch, M.K., Famaey, N., Shultz, T.O.B., Bothe, W., Miller, D.C., and Kuhl, E., Mechanics of the Mitral Valve. *Biomechanics and modeling in mechanobiology*, 2013. **12**(5): pp. 1053-1071.
54. Sacks, M.S. and Yoganathan, A.P., Heart Valve Function: A Biomechanical Perspective. *Philosophical Transactions of the Royal Society of London B: Biological Sciences*, 2007. **362**(1484): pp. 1369-1391.
55. Zhang, W., Ayoub, S., Liao, J., and Sacks, M.S., A Meso-Scale Layer-Specific Structural Constitutive Model of the Mitral Heart Valve Leaflets. *Acta Biomaterialia*, 2016. **32**: pp. 238-255.
56. Alavi, S.H., Sinha, A., Steward, E., Milliken, J.C., and Kheradvar, A., Load-Dependent Extracellular Matrix Organization in Atrioventricular Heart Valves: Differences and Similarities. *American Journal of Physiology-Heart and Circulatory Physiology*, 2015. **309**(2): pp. H276-H284.
57. Grande-Allen, K.J. and Liao, J., The Heterogeneous Biomechanics and Mechanobiology of the Mitral Valve: Implications for Tissue Engineering. *Current cardiology reports*, 2011. **13**(2): pp. 113-120.

58. Wiltz, D., Arevalos, C.A., Balaoing, L.R., Blancas, A.A., Sapp, M.C., Zhang, X., and Grande-Allen, K.J., Extracellular Matrix Organization, Structure, and Function, in *Calcific Aortic Valve Disease*. 2013, IntechOpen.
59. Tseng, H. and Grande-Allen, K.J., Elastic Fibers in the Aortic Valve Spongiosa: A Fresh Perspective on Its Structure and Role in Overall Tissue Function. *Acta Biomaterialia*, 2011. **7**(5): pp. 2101-2108.
60. Kramer, K., Ross, C., Babu, A., Wu, Y., Towner, R., Mir, A., Burkhardt, H.M., Holzapfel, G.A., and Lee, C.-H., An Investigation of Layer-Specific Tissue Biomechanics of Porcine Atrioventricular Valve Anterior Leaflets. Available at SSRN 3321895, 2019.
61. Lin, K., Zhang, D., Macedo, M.H., Cui, W., Sarmento, B., and Shen, G., Advanced Collagen-Based Biomaterials for Regenerative Biomedicine. *Advanced Functional Materials*, 2019. **29**(3): pp. 1804943.
62. Pierlot, C.M., Lee, J.M., Amini, R., Sacks, M.S., and Wells, S.M., Pregnancy-Induced Remodeling of Collagen Architecture and Content in the Mitral Valve. *Annals of biomedical engineering*, 2014. **42**(10): pp. 2058-2071.
63. Lee, C.-H., Zhang, W., Liao, J., Carruthers, C.A., Sacks, J.I., and Sacks, M.S., On the Presence of Affine Fibril and Fiber Kinematics in the Mitral Valve Anterior Leaflet. *Biophysical journal*, 2015. **108**(8): pp. 2074-2087.
64. Galhardo, M.S., Caldini, E.G., Battlehner, C.N., and Toledo, O.M.S., Age-Dependent Physiological Changes in the Histoarchitecture of the Articular Cartilage of the Rabbit Mandibular Condyle: A Morphological and Morphometric Study. *Cells Tissues Organs*, 2012. **195**(4): pp. 340-352.

65. Bancelin, S., Nazac, A., Ibrahim, B.H., Dokládal, P., Decencière, E., Teig, B., Haddad, H., Fernandez, H., Schanne-Klein, M.-C., and De Martino, A., Determination of Collagen Fiber Orientation in Histological Slides Using Mueller Microscopy and Validation by Second Harmonic Generation Imaging. *Optics Express*, 2014. **22**(19): pp. 22561-22574.
66. Keikhosravi, A., Liu, Y., Drifka, C., Woo, K.M., Verma, A., Oldenbourg, R., and Eliceiri, K.W., Quantification of Collagen Organization in Histopathology Samples Using Liquid Crystal Based Polarization Microscopy. *Biomedical Optics Express*, 2017. **8**(9): pp. 4243-4256.
67. Williams, R.M., Zipfel, W.R., and Webb, W.W., Interpreting Second-Harmonic Generation Images of Collagen I Fibrils. *Biophysical Journal*, 2005. **88**(2): pp. 1377-1386.
68. Chen, X., Nadiarynk, O., Plotnikov, S., and Campagnola, P.J., Second Harmonic Generation Microscopy for Quantitative Analysis of Collagen Fibrillar Structure. *Nature Protocols*, 2012. **7**(4): pp. 654.
69. Robitaille, M.C., Zareian, R., DiMarzio, C.A., Wan, K.-T., and Ruberti, J.W., Small-Angle Light Scattering to Detect Strain-Directed Collagen Degradation in Native Tissue. *Interface Focus*, 2011. **1**(5): pp. 767-776.
70. Ethier, C.R., Bertin, B., Flanagan, J.G., and Girard, M., Preliminary Small-Angle Light Scattering (Sals) Investigation of Lamina Cribrosa (Lc) Structure in Human Eyes. *Investigative Ophthalmology & Visual Science*, 2012. **53**(14): pp. 3183-3183.
71. Holzapfel, G.A., Collagen in Arterial Walls: Biomechanical Aspects, in *Collagen*. 2008, Springer. pp. 285-324.

72. Sacks, M.S., Smith, D.B., and Hiester, E.D., A Small Angle Light Scattering Device for Planar Connective Tissue Microstructural Analysis. *Annals of Biomedical Engineering*, 1997. **25**(4): pp. 678-689.
73. Joyce, E.M., Liao, J., Schoen, F.J., Mayer Jr, J.E., and Sacks, M.S., Functional Collagen Fiber Architecture of the Pulmonary Heart Valve Cusp. *The Annals of Thoracic Surgery*, 2009. **87**(4): pp. 1240-1249.
74. Anselmo, W., Branchetti, E., Grau, J.B., Li, G., Ayoub, S., Lai, E.K., Rioux, N., Tovmasyan, A., Fortier, J.H., and Sacks, M.S., Porphyrin-Based Sod Mimic Mntnbu Oe-2-Pyp5+ Inhibits Mechanisms of Aortic Valve Remodeling in Human and Murine Models of Aortic Valve Sclerosis. *Journal of the American Heart Association*, 2018. **7**(20): pp. e007861.
75. Anssari-Benam, A., Screen, H.R., and Bucchi, A., Insights into the Micromechanics of Stress-Relaxation and Creep Behaviours in the Aortic Valve. *Journal of the Mechanical Behavior of Biomedical Materials*, 2019. **93**: pp. 230-245.
76. Anssari-Benam, A., Tseng, Y.-T., Holzapfel, G.A., and Bucchi, A., Rate-Dependency of the Mechanical Behaviour of Semilunar Heart Valves under Biaxial Deformation. *Acta Biomaterialia*, 2019.
77. Yang, B., Lesicko, J., Sharma, M., Hill, M., Sacks, M.S., and Tunnell, J.W., Polarized Light Spatial Frequency Domain Imaging for Non-Destructive Quantification of Soft Tissue Fibrous Structures. *Biomedical Optics Express*, 2015. **6**(4): pp. 1520-1533.

78. Sacks, M.S., Smith, D.B., and Hiester, E.D., The Aortic Valve Microstructure: Effects of Transvalvular Pressure. *Journal of Biomedical Materials Research: An Official Journal of The Society for Biomaterials, The Japanese Society for Biomaterials, and the Australian Society for Biomaterials*, 1998. **41**(1): pp. 131-141.
79. Goth, W., Yang, B., Lesicko, J., Allen, A., Sacks, M.S., and Tunnell, J.W. Polarized Spatial Frequency Domain Imaging of Heart Valve Fiber Structure. in *Optical Elastography and Tissue Biomechanics III*. 2016. International Society for Optics and Photonics.
80. Goth, W.A., Rapid Wide-Field Imaging of Soft-Tissue Microstructure. 2019.
81. Shiran, A. and Sagie, A., Tricuspid Regurgitation in Mitral Valve Disease. *Journal of the American College of Cardiology*, 2009. **53**(5): pp. 401-408.
82. O'Rourke, R.A. and Crawford, M.H., Mitral Valve Regurgitation. *Current problems in cardiology*, 1984. **9**(2): pp. 1-52.
83. Waller, B.F., Howard, J., and Fess, S., Pathology of Mitral Valve Stenosis and Pure Mitral Regurgitation—Part I. *Clinical cardiology*, 1994. **17**(6): pp. 330-336.
84. Potter, S., Graves, J., Drach, B., Leahy, T., Hammel, C., Feng, Y., Baker, A., and Sacks, M.S., A Novel Small-Specimen Planar Biaxial Testing System with Full in-Plane Deformation Control. *Journal of Biomechanical Engineering*, 2018. **140**(5): pp. 051001.
85. Dreyfus, G.D., Corbi, P.J., Chan, K.J., and Bahrami, T., Secondary Tricuspid Regurgitation or Dilatation: Which Should Be the Criteria for Surgical Repair? *The Annals of Thoracic Surgery*, 2005. **79**(1): pp. 127-132.

86. Anyanwu, A.C. and Adams, D.H. Functional Tricuspid Regurgitation in Mitral Valve Disease: Epidemiology and Prognostic Implications. in *Seminars in thoracic and cardiovascular surgery*. 2010. Elsevier.
87. Navia, J.L., Nowicki, E.R., Blackstone, E.H., Brozzi, N.A., Nento, D.E., Atik, F.A., Rajeswaran, J., Gillinov, A.M., Svensson, L.G., and Lytle, B.W., Surgical Management of Secondary Tricuspid Valve Regurgitation: Annulus, Commissure, or Leaflet Procedure? *The Journal of Thoracic and Cardiovascular Surgery*, 2010. **139**(6): pp. 1473-1482. e5.
88. Woo, S.L.-Y., Orlando, C.A., Camp, J.F., and Akeson, W.H., Effects of Postmortem Storage by Freezing on Ligament Tensile Behavior. *Journal of Biomechanics*, 1986. **19**(5): pp. 399-404.
89. Stemper, B.D., Yoganandan, N., Stineman, M.R., Gennarelli, T.A., Baisden, J.L., and Pintar, F.A., Mechanics of Fresh, Refrigerated, and Frozen Arterial Tissue. *Journal of Surgical Research*, 2007. **139**(2): pp. 236-242.
90. Foutz, T., Stone, E., and Abrams, J.C., Effects of Freezing on Mechanical Properties of Rat Skin. *American Journal of Veterinary Research*, 1992. **53**(5): pp. 788-792.
91. Liao, J., Joyce, E.M., and Sacks, M.S., Effects of Decellularization on the Mechanical and Structural Properties of the Porcine Aortic Valve Leaflet. *Biomaterials*, 2008. **29**(8): pp. 1065-1074.
92. Pierlot, C.M., Moeller, A.D., Lee, J.M., and Wells, S.M., Biaxial Creep Resistance and Structural Remodeling of the Aortic and Mitral Valves in Pregnancy. *Annals of Biomedical Engineering*, 2015. **43**(8): pp. 1772-1785.

93. Chuong, C.-J. and Fung, Y.-C., Residual Stress in Arteries, in *Frontiers in Biomechanics*. 1986, Springer. pp. 117-129.
94. Fung, Y., Fronek, K., and Patitucci, P., Pseudoelasticity of Arteries and the Choice of Its Mathematical Expression. *American Journal of Physiology-Heart and Circulatory Physiology*, 1979. **237**(5): pp. H620-H631.
95. Humphrey, J.D., Vawter, D.L., and Vito, R.P., Quantification of Strains in Biaxially Tested Soft Tissues. *Journal of Biomechanics*, 1987. **20**(1): pp. 59-65.
96. Billiar, K. and Sacks, M., A Method to Quantify the Fiber Kinematics of Planar Tissues under Biaxial Stretch. *Journal of Biomechanics*, 1997. **30**(7): pp. 753-756.
97. Toma, M., Jensen, M.Ø., Einstein, D.R., Yoganathan, A.P., Cochran, R.P., and Kunzelman, K.S., Fluid–Structure Interaction Analysis of Papillary Muscle Forces Using a Comprehensive Mitral Valve Model with 3d Chordal Structure. *Annals of biomedical engineering*, 2016. **44**(4): pp. 942-953.
98. Ruifrok, A.C. and Johnston, D.A., Quantification of Histochemical Staining by Color Deconvolution. *Analytical and quantitative cytology and histology*, 2001. **23**(4): pp. 291-299.
99. Hosseini, S.M., Wilson, W., Ito, K., and van Donkelaar, C.C., How Preconditioning Affects the Measurement of Poro-Viscoelastic Mechanical Properties in Biological Tissues. *Biomechanics and Modeling in Mechanobiology*, 2014. **13**(3): pp. 503-513.
100. Bernacca, G.M., O'Connor, B., Williams, D.F., and Wheatley, D.J., Hydrodynamic Function of Polyurethane Prosthetic Heart Valves: Influences of Young's Modulus and Leaflet Thickness. *Biomaterials*, 2002. **23**(1): pp. 45-50.

101. Wang, Z., Golob, M.J., and Chesler, N.C., Viscoelastic Properties of Cardiovascular Tissues, in *Viscoelastic and Viscoplastic Materials*. 2016, InTech.
102. Lelovas, P.P., Kostomitsopoulos, N.G., and Xanthos, T.T., A Comparative Anatomic and Physiologic Overview of the Porcine Heart. *Journal of the American Association for Laboratory Animal Science*, 2014. **53**(5): pp. 432-438.
103. Hinton, R.B. and Yutzey, K.E., Heart Valve Structure and Function in Development and Disease. *Annual Review of Physiology*, 2011. **73**: pp. 29-46.
104. Labrosse, M.R., Jafar, R., Ngu, J., and Boodhwani, M., Planar Biaxial Testing of Heart Valve Cusp Replacement Biomaterials: Experiments, Theory and Material Constants. *Acta Biomaterialia*, 2016. **45**: pp. 303-320.
105. Chen, L., Yin, F.C., and May-Newman, K., The Structure and Mechanical Properties of the Mitral Valve Leaflet-Strut Chordae Transition Zone. *Journal of biomechanical engineering*, 2004. **126**(2): pp. 244-251.
106. Ayoub, S., Lee, C.-H., Driesbaugh, K.H., Anselmo, W., Hughes, C.T., Ferrari, G., Gorman, R.C., Gorman, J.H., and Sacks, M.S., Regulation of Valve Interstitial Cell Homeostasis by Mechanical Deformation: Implications for Heart Valve Disease and Surgical Repair. *Journal of The Royal Society Interface*, 2017. **14**(135): pp. 20170580.
107. Huang, H.-Y.S., Balhouse, B.N., and Huang, S., Application of Simple Biomechanical and Biochemical Tests to Heart Valve Leaflets: Implications for Heart Valve Characterization and Tissue Engineering. *Proceedings of the Institution of Mechanical Engineers, Part H: Journal of Engineering in Medicine*, 2012. **226**(11): pp. 868-876.

108. Sacks, M.S., Grashow, J., and Yoganathan, A.P. Viscoelastic Behavior of Heart Valve Tissues under Biaxial Stretch. in *ASME 2004 International Mechanical Engineering Congress and Exposition*. 2004. American Society of Mechanical Engineers.
109. Sacks, M.S., Incorporation of Experimentally-Derived Fiber Orientation into a Structural Constitutive Model for Planar Collagenous Tissues. *Journal of Biomechanical Engineering*, 2003. **125**(2): pp. 280-287.
110. Lee, C.-H., Amini, R., Gorman, R.C., Gorman, J.H., and Sacks, M.S., An Inverse Modeling Approach for Stress Estimation in Mitral Valve Anterior Leaflet Valvuloplasty for in-Vivo Valvular Biomaterial Assessment. *Journal of Biomechanics*, 2014. **47**(9): pp. 2055-2063.
111. Jett, S., Laurence, D., Kunkel, R., Babu, A.R., Kramer, K., Baumwart, R., Towner, R., Wu, Y., and Lee, C.-H., An Investigation of the Anisotropic Mechanical Properties and Anatomical Structure of Porcine Atrioventricular Heart Valves. *Journal of the Mechanical Behavior of Biomedical Materials*, 2018. **87**: pp. 155-171.
112. Huang, S. and Huang, H.-Y.S., Biaxial Stress Relaxation of Semilunar Heart Valve Leaflets During Simulated Collagen Catabolism: Effects of Collagenase Concentration and Equibiaxial Strain State. *Proceedings of the Institution of Mechanical Engineers, Part H: Journal of Engineering in Medicine*, 2015. **229**(10): pp. 721-731.
113. Reddy, J.N., *An Introduction to Continuum Mechanics*. 2013: Cambridge university press.

114. Tadmor, E.B., Miller, R.E., and Elliott, R.S., *Continuum Mechanics and Thermodynamics: From Fundamental Concepts to Governing Equations*. 2012: Cambridge University Press.
115. Jett, S., Laurence, D., Kunkel, R., Babu, A.R., Kramer, K., Baumgart, R., Towner, R., Wu, Y., and Lee, C.-H., Biaxial Mechanical Data of Porcine Atrioventricular Valve Leaflets. *Data in Brief*, 2018, in press.
116. Sacks, M.S., David Merryman, W., and Schmidt, D.E., On the Biomechanics of Heart Valve Function. *Journal of Biomechanics*, 2009. **42**(12): pp. 1804-1824.
117. Kuhn III, C., Boldt, J., King Jr, T.E., Crouch, E., Vartio, T., and McDonald, J.A., An Immunohistochemical Study of Architectural Remodeling and Connective Tissue Synthesis in Pulmonary Fibrosis. *American Review of Respiratory Disease*, 1989. **140**(6): pp. 1693-1703.
118. Driessens, N.J.B., Cox, M.A.J., Bouten, C.V.C., and Baaijens, F.P.T., Remodelling of the Angular Collagen Fiber Distribution in Cardiovascular Tissues. *Biomechanics and Modeling in Mechanobiology*, 2008. **7**(2): pp. 93-103.
119. Balguid, A., Rubbens, M.P., Mol, A., Bank, R.A., Bogers, A.J.J.C., van Kats, J.P., de Mol, B.A.J.M., Baaijens, F.P., and Bouten, C.V.C., The Role of Collagen Cross-Links in Biomechanical Behavior of Human Aortic Heart Valve Leaflets—Relevance for Tissue Engineering. *Tissue engineering*, 2007. **13**(7): pp. 1501-1511.
120. Jeffery, A.K., Blunn, G.W., Archer, C.W., and Bentley, G., Three-Dimensional Collagen Architecture in Bovine Articular Cartilage. *The Journal of Bone and Joint Surgery*, 1991. **73**(5): pp. 795-801.

121. Quantock, A.J., Meek, K.M., Fullwood, N.J., and Zabel, R.W., Scheie's Syndrome: The Architecture of Corneal Collagen and Distribution of Corneal Proteoglycans. *Canadian Journal of Ophthalmology*, 1993. **28**(6): pp. 266-272.
122. Grytz, R., Fazio, M.A., Girard, M.J.A., Libertiaux, V., Bruno, L., Gardiner, S., Girkin, C.A., and Downs, J.C., Material Properties of the Posterior Human Sclera. *Journal of the Mechanical Behavior of Biomedical Materials*, 2014. **29**: pp. 602-617.
123. Fithian, D.C., Kelly, M.A., and Mow, V.C., Material Properties and Structure-Function Relationships in the Menisci. *Clinical Orthopaedics and Related Research*, 1990(252): pp. 19-31.
124. Toshima, M., Ohtani, Y., and Ohtani, O., Three-Dimensional Architecture of Elastin and Collagen Fiber Networks in the Human and Rat Lung. *Archives of Histology and Cytology*, 2004. **67**(1): pp. 31-40.
125. Driessen, N.J., Bouten, C.V.C., and Baaijens, F.P.T., Improved Prediction of the Collagen Fiber Architecture in the Aortic Heart Valve. *Journal of Biomechanical Engineering*, 2005. **127**(2): pp. 329-336.
126. Gibson, T., Kenedi, R.M., and Craik, J.E., The Mobile Micro-Architecture of Dermal Collagen: A Bio-Engineering Study. *British Journal of Surgery*, 1965. **52**(10): pp. 764-770.
127. Kääb, M.J., Ito, K., Clark, J.M., and Nötzli, H.P., Deformation of Articular Cartilage Collagen Structure under Static and Cyclic Loading. *Journal of Orthopaedic Research*, 1998. **16**(6): pp. 743-751.

128. Rieppo, J., Hallikainen, J., Jurvelin, J.S., Kiviranta, I., Helminen, H.J., and Hyttinen, M.M., Practical Considerations in the Use of Polarized Light Microscopy in the Analysis of the Collagen Network in Articular Cartilage. *Microscopy Research and Technique*, 2008. **71**(4): pp. 279-287.
129. Yang, B., Brazile, B., Jan, N.-J., Voorhees, A.P., and Sigal, I.A. Structured Polarized Light Microscopy (Splm) for Mapping Collagen Fiber Orientation of Ocular Tissues. in *Emerging Digital Micromirror Device Based Systems and Applications X*. 2018. International Society for Optics and Photonics.
130. Yang, B., Lesicko, J., Sharma, M., Hill, M., Sacks, M., and Tunnell, J.W. Collagen Fiber Orientation Mapping with Top Layer Discrimination Using Polarized Light Spatial Frequency Domain Imaging on Native Heart Tissue. in *Biomedical Optics*. 2014. Optical Society of America.
131. Wu, X., Pankow, M., Huang, H.-Y.S., and Peters, K., High-Speed Polarization Imaging of Dynamic Collagen Fiber Realignment in Tendon-to-Bone Insertion Region. *Journal of Biomedical Optics*, 2018. **23**(11): pp. 116002.
132. Alavi, S.H., Ruiz, V., Krasieva, T., Botvinick, E.L., and Kheradvar, A., Characterizing the Collagen Fiber Orientation in Pericardial Leaflets under Mechanical Loading Conditions. *Annals of Biomedical Engineering*, 2013. **41**(3): pp. 547-561.
133. Alavi, S.H., Sinha, A., Steward, E., Milliken, J.C., and Kheradvar, A., Load-Dependent Extracellular Matrix Organization in Atrioventricular Heart Valves: Differences and Similarities. *American Journal of Physiology: Heart and Circulatory Physiology*, 2015. **309**(2): pp. H276-H284.

134. Goth, W., Sacks, M.S., and Tunnell, J.W. Interpreting Fiber Structure from Polarization Dependent Optical Anisotropy. in *Imaging, Manipulation, and Analysis of Biomolecules, Cells, and Tissues XV*. 2017. International Society for Optics and Photonics.
135. Kannus, P., Structure of the Tendon Connective Tissue. *Scandinavian Journal of Medicine & Science in Sports*, 2000. **10**(6): pp. 312-320.
136. Mazhar, A., Saggese, S., Pollins, A.C., Cardwell, N.L., Nanney, L.B., and Cuccia, D.J., Noncontact Imaging of Burn Depth and Extent in a Porcine Model Using Spatial Frequency Domain Imaging. *Journal of Biomedical Optics*, 2014. **19**(8): pp. 086019.
137. Cuccia, D.J., Bevilacqua, F.P., Durkin, A.J., Ayers, F.R., and Tromberg, B.J., Quantitation and Mapping of Tissue Optical Properties Using Modulated Imaging. *Journal of Biomedical Optics*, 2009. **14**(2): pp. 024012.
138. Cuccia, D.J., Bevilacqua, F., Durkin, A.J., and Tromberg, B.J., Modulated Imaging: Quantitative Analysis and Tomography of Turbid Media in the Spatial-Frequency Domain. *Optics Letters*, 2005. **30**(11): pp. 1354-1356.
139. Maisuradze, G.G., Thompson, D.L., Wagner, A.F., and Minkoff, M., Interpolating Moving Least-Squares Methods for Fitting Potential Energy Surfaces: Detailed Analysis of One-Dimensional Applications. *The Journal of Chemical Physics*, 2003. **119**(19): pp. 10002-10014.
140. Provenzano, P.P. and Vanderby Jr, R., Collagen Fibril Morphology and Organization: Implications for Force Transmission in Ligament and Tendon. *Matrix Biology*, 2006. **25**(2): pp. 71-84.

141. Vesely, I., The Role of Elastin in Aortic Valve Mechanics. *Journal of Biomechanics*, 1998. **31**(2): pp. 115-123.
142. Billiar, K.L. and Sacks, M.S., A Method to Quantify the Fiber Kinematics of Planar Tissues under Biaxial Stretch. *Journal of Biomechanics*, 1997. **30**(7): pp. 753-756.
143. Anssari-Benam, A., Screen, H.R.C., and Bucchi, A., Insights into the Micromechanics of Stress-Relaxation and Creep Behaviours in the Aortic Valve. *Journal of the mechanical behavior of biomedical materials*, 2019. **93**: pp. 230-245.
144. Lee, C.-H., Amini, R., Sakamoto, Y., Carruthers, C.A., Aggarwal, A., Gorman, R.C., Gorman, J.H., and Sacks, M.S., Mitral Valves: A Computational Framework, in *Multiscale Modeling in Biomechanics and Mechanobiology*. 2015, Springer. pp. 223-255.
145. Hadian, M., Corcoran, B.M., Han, R.I., Grossmann, J.G., and Bradshaw, J.P., Collagen Organization in Canine Myxomatous Mitral Valve Disease: An X-Ray Diffraction Study. *Biophysical journal*, 2007. **93**(7): pp. 2472-2476.
146. Jett, S., Laurence, D., Kunkel, R., Babu, A.R., Kramer, K., Baumwart, R., Towner, R., Wu, Y., and Lee, C.-H., Biaxial Mechanical Data of Porcine Atrioventricular Valve Leaflets. *Data in Brief*, 2018. **21**: pp. 358-363.
147. Jett, S., Laurence, D., Kunkel, R., Babu, A.R., Kramer, K., Baumwart, R., Towner, R., Wu, Y., and Lee, C.H., An Investigation of the Anisotropic Mechanical Properties and Anatomical Structure of Porcine Atrioventricular Heart Valves. *Journal of the mechanical behavior of biomedical materials*, 2018. **87**: pp. 155-171.

148. Goth, W., Potter, S., Allen, A.C., Zoldan, J., Sacks, M.S., and Tunnell, J.W., Non-Destructive Reflectance Mapping of Collagen Fiber Alignment in Heart Valve Leaflets. *Annals of Biomedical Engineering*, 2019 (<https://doi.org/10.1007/s10439-019-02233-0>).
149. Laurence, D., Ross, C., Jett, S., Johns, C., Echols, A., Baumgart, R., Towner, R., Liao, J., Bajona, P., Wu, Y., *et al.*, An Investigation of Regional Variations in the Biaxial Mechanical Properties and Stress Relaxation Behaviors of Porcine Atrioventricular Heart Valve Leaflets. *Journal of Biomechanics*, 2019. **83**: pp. 16-27.
150. May-Newman, K. and Yin, F.C., Biaxial Mechanical Behavior of Excised Porcine Mitral Valve Leaflets. *American Journal of Physiology-Heart and Circulatory Physiology*, 1995. **269**(4): pp. H1319-H1327.
151. Gasser, T.C., Ogden, R.W., and Holzapfel, G.A., Hyperelastic Modelling of Arterial Layers with Distributed Collagen Fibre Orientations. *Journal of The Royal Society Interface*, 2005. **3**(6): pp. 15-35.
152. Kulik, Y.P., Prosthetic Pericardium. 1990, Google Patents.
153. Poirier, N.C., Pelletier, L.C., Pellerin, M., and Carrier, M., 15-Year Experience with the Carpentier-Edwards Pericardial Bioprostheses. *The Annals of Thoracic Surgery*, 1998. **66**(6): pp. S57-S61.
154. Liang, L., Liu, M., and Sun, W., A Deep Learning Approach to Estimate Chemically-Treated Collagenous Tissue Nonlinear Anisotropic Stress-Strain Responses from Microscopy Images. *Acta Biomaterialia*, 2017. **63**: pp. 227-235.

155. Bodenschatz, N., Krauter, P., Liemert, A., Wiest, J., and Kienle, A., Model-Based Analysis on the Influence of Spatial Frequency Selection in Spatial Frequency Domain Imaging. *Applied Optics*, 2015. **54**(22): pp. 6725-6731.
156. Sandell, J.L. and Zhu, T.C., A Review of in-Vivo Optical Properties of Human Tissues and Its Impact on Photodynamic Theory. *Journal of Biophotonics*, 2011. **4**(11-12): pp. 773-787.
157. Shuaib, A., Characterizing Optical Properties in Fibrous Tissues. 2011, University of Missouri--Columbia.